Control and Measurement of Oxygen in Microfluidic Bioreactors

Volker Nock

Department of Electrical and Computer Engineering

A thesis submitted in partial fulfilment of the
requirements for the degree of

Doctor of Philosophy

University of Canterbury
Christchurch, New Zealand
January, 2009

In loving memory of my grandmother

Gertrud Zehnle

19.3.1914 - 26.4.2008

ABSTRACT

Bioartificial Liver (BAL) is a term for medical devices designed to replace natural liver functions. The idea behind the use of artificial livers is to either externally support an injured liver to recovery or bridge a patient with a failing liver to transplantation. Central to all BAL systems is a bioreactor for culturing liver cells. The main function of this reactor is to provide a cell adhesion matrix and supply the necessary nutrient solution. A high cellular oxygen uptake rate combined with low solubility in aqueous media makes oxygen supply to the liver cells the most constraining factor in current reactor designs. Devices with parallel-plate channel geometry promise high efficiency for blood detoxification and liver metabolism. However, due to their specific flow regime oxygen depletion in the medium is a major problem in these devices.

This thesis explores a unique method of controlling and measuring dissolved oxygen in BAL cell-culture bioreactors and lab-on-a-chip devices. Testing is performed using simulations, prototype bioreactor devices and *in-vitro* measurement of dissolved oxygen. Several strategies developed to fabricate the bioreactors and integrate oxygen sensing are presented. Emphasis is placed on techniques that provide compatibility with commonly used microfabrication processes, while allowing for laterally-resolved measurement of oxygen in a re-usable, low-cost setup.

The most significant contribution presented is the development and assessment of the tapered cell-culture bioreactor with integrated PS/PtOEPK oxygen sensor. The combination adopts a unique approach to oxygen control. Bioreactor shape is used to modulate the oxygen supplied to cells via the resulting shear-stress function. By linearly increasing the shear-stress oxygen concentration can be maintained constant over the length of the reactor. Using the integrated oxygen sensor, the resulting concentration profile can be monitored in real-time with high lateral resolution. The advantage of the device over existing techniques is that no additional oxygenation inside the reactor chamber is required to maintain a certain concentration profile and that oxygen

concentration can be mapped *in-situ* without having to introduce further chemicals into the perfusion medium.

This thesis presents a number of other contributions: a grayscale mask process, development of the PS/PtOEPK sensor patterning method and signal optimization regime, demonstration of the multi-stream flow application, an experimental setup for sensor calibration and a process to pattern cell-adhesion proteins simultaneously with the oxygen sensor, a multi-layer BAL prototype and the results of a brief experiment to test an approach using vertically aligned carbon nanotube bundles as fluidic conduits for bile drainage.

ACKNOWLEDGMENTS

The work presented in this thesis has been carried out at the Nanolaboratory at the Department for Electrical and Computer Engineering at the University of Canterbury in Christchurch, New Zealand. Financial support was provided in part by the MacDiarmid Institute for Advanced Materials and Nanotechnology and the University of Canterbury through a Targeted Doctoral Scholarship.

I am especially grateful to the guidance and support by my supervisors Professor Richard Blaikie and Professor Tim David. Through Richard's encouragement and guidance in the world of microfabrication, and by giving me the freedom to develop and explore my own ideas, my experience as a PhD student has been more than enjoyable. Tim in particular I have to thank for introducing me to the fascinating world of bioartificial livers, the beautiful maths of fluid dynamics and for letting me work on the first steps to test his transport model. I thank you both for giving me the opportunity to work with you, it has been a great pleasure.

I would also like to express my gratitude to all the people who have enriched my stay at the department and helped me in so many ways. In particular, I would like to thank Helen Devereux and Gary Turner for keeping the lab running against all the odds; Marjorie Griffiths and Rebekah Hunt for taking my head off all the paperwork; Maan Alkaisi for bringing together the Bionano community; Pieter Kikstra for all his magic solutions to computer problems. My friends, colleagues and fellow labrats, Postdocs and former and current PhD students: Euan Boyd, Florian L'Hostis and Erwin Berthier for making the office such a great place to come to every day and for never complaining about my cheesecake; James Muys, David Melville, Leo Schuler, Stuart Lansley, Matthew Arnold, David Garrett, Mikkel Schøler, Sanitta Thongpang, Khairudin Mohamed, John Foulkes, Lin Ling, Martin Allen, Xianming Liu and Andrew Gross for a great time and all the invaluable help around the lab. My special thanks go to Alexander Boeser, whom I had the pleasure to be working with during his internship and who is partly responsible

for the work reported in Section 4.4, and Fahmi Samsuri for providing and culturing the cells used in Chapter 8.

Furthermore, I would like to thank all the other people I had the pleasure of working with during this thesis, especially John Evans for helping to set up the link to the CSMHS and sorting out the ethical approval; Mathieu Sellier and David Beebe for great discussions on microfluidics and equally great soccer matches; and Wenhui Wang, Ali Ghanbari and Craig Galilee for introducing me to the wonderful world of little worms and bending micropillars.

Finally, thanks to all the people who have made living in New Zealand such a great experience. The extracurricular support team: the Smart family and the Wednesday soccer crew for putting up with my running and efficient German playing style; the crew of the Canterbury University Tramping Club for all the awesome days in the hills and for giving me some of the best inspiration on sunny, cold, wet and wonderful days in the beautiful natural landscapes of New Zealand, there just aren’t many better ways to visualize laminar flow than by watching a glacier.

My good friends and former and current flatmates Sylvia, Andy, Dave, Ivor, Tom and Laura for providing a home away from home; Sharon for her love and patience with my lack of enthusiasm for skiing during those wonderful months; and, last but not least, my family, my parents Alice and Hans Nock, and my brother Matthias, for their endless love and for teaching me the really important things in life, I could not have done this without you!

ABBREVIATIONS

Abbreviations used in this thesis are listed here for easy reference.

AHS	Alginate-entrapped Hepatocyte Spheroid
ALF	acute hepatic failure
AMC	Academic Medical Center
BAL	bio-artificial liver
BC	boundary condition
BLSS	Bioartificial Liver Support System
BMP	bitmap
CCD	charge-coupled device
CFD	computational fluid dynamics
CNT	carbon nanotubes
CSMHS	Christchurch School of Medicine and Health Sciences
CV	central vein
Da	*Damkohler* number
DC	direct current
DI	deionized
DIC	differential interference contrast
DMEM	Dulbecco's Modified Eagle's Medium
DO	dissolved oxygen
EBL	electron beam lithography
ECM	extra cellular matrix
FEM	finite element method
FHF	fulminant hepatic failure
FMB	Flat Membrane Bioreactor
HA	hepatic artery
HF	hydrofluoric acid
HFS	hollow fiber system
HMS	Harvard Medical School

HSC	hepatic stellate cell
HV	hepatic vein
IPA	isopropyl alcohol
JPEG	Joint Photographic Experts Group
LDLT	living donor liver transplantation
LLS	Lobule-like Structure Module
LOC	lab on a chip
LSEC	liver sinusoidal endothelial cells
LSS	liver support system
MARS	Molecular Absorbent and Recirculating System
MELS	Modular Extracorporeal Liver Support
MIBK	methyl isobutyl ketone
MW	molecular weight
NIR	near infrared
OLT	orthotopic liver transplantation
OPTN	Organ Procurement and Transplantation Network
OXY-HFB	Oxygenating Hollow Fiber Bioreactor
PDF	pressure driven flow
PDMS	polydimethylsiloxane
Pe	*Peclet* number
PE	polyethylene
PEB	post exposure bake
PMMA	polymethyl methacrylate
PS	polystyrene
PtOEPK	platinum(II) octaethylporphyrinketone
PUF	Polyurethane Foam Module
PV	portal vein
Re	*Reynolds* number
RF	radio frequency
RFB	Radial Flow Bioreactor
RIE	reactive ion etching

ROI	region of interest
RT	room temperature
SEM	scanning electron microscopy
SHF	subfulminant hepatic failure
TPE	thermoset polyester
UCLA	University of California Los Angeles
US	ultrasound
VACNT	vertically aligned carbon nanotubes

TABLE OF CONTENTS

The most exciting phrase to hear in science, the one that heralds new discoveries, is not 'Eureka!' (I found it!) but 'That's funny...'

Isaac Asimov
1920-1992, Russian-born American
Author and Professor in Biochemistry

CHAPTER 1

Introduction

1.1 OVERVIEW AND OBJECTIVES

Oxygen concentration can modulate cellular functions and depletion of available dissolved oxygen can lead to cell death [1]. Oxygen is the substrate of multicellular life and cells have been found to be able to sense reduced oxygen availability (hypoxia), triggering homeostatic responses, which impact on virtually all areas of biology and medicine [2-4]. Gradients of oxygen concentration are considered to be one of the main parameters controlling metabolic and functional zonation in organs such as the liver [5]. Understanding of this phenomena and the ability to replicate it *in-vitro* are fundamental to the design of cell-culture bioreactors and microfluidic devices for cell-biology studies and in biomedical devices. However, to date, there has not been a great deal of focus on the control and measurement of oxygen concentration in microfluidics-based bioreactors. The work presented in this thesis is targeted towards bio-artificial liver (BAL) bioreactors for the treatment of liver diseases, which provide an additional challenge in form of the large oxygen consumption exhibited by hepatocytes.

Existing parallel-plate bioreactors have great potential for ease of fabrication and system scale-up, however, these rectangular geometries suffer from oxygen depletion problems due to the nature of fluid flow at the micro-scale. Equally, existing oxygen

detection schemes are either difficult to integrate with these devices, do not provide spatially-resolved concentration information or require large amounts of expensive fluorescent dyes. Furthermore, as technology and understanding of biological processes improve, system scale-up becomes more feasible thereby increasing the importance of ease of integration.

The aim of the research presented here is to contribute to a better understanding of oxygen concentrations in microfluidic cell-culture bioreactors. This thesis describes the development, testing and evaluation of a novel toolbox to detect and control the distribution of dissolved oxygen in a microfluidic bioreactor, such as used in BAL systems. In particular, the goal is to provide the necessary means to evaluate the hypothesis of the effect of geometry on the oxygen concentration profile.

1.2 Thesis Contributions

The most significant contribution to the field made by this thesis is the tapered cell-culture bioreactor with integrated PS/PtOEPK oxygen sensor [6]. The combination adopts a novel approach to oxygen control and the results presented demonstrate that this method is feasible. The device has several advantages over existing systems, as are described.
Other major contributions include:

1 *The species transport model* [7]. The modified version of Prof. Tim David's model of platelet transport [8] is used to calculate the specific bioreactor shape corresponding to a desired concentration profile. Computational fluid dynamics simulations were performed, which validate the model predictions for dissolved oxygen [6].

2 *The grayscale mask process* [9]. A novel approach to reducing the turn-over time for prototype grayscale masks has been developed. Resulting devices complement the solutions of the 2D application of the species transport model.

3 *The PS/PtOEPK sensor patterning method and signal optimization* [10]. This has been developed in order to allow for sensor integration with PDMS microfluidic devices and selectively localized cell-culture. It also has applications in areas other than bioreactors, particularly when highly homogeneous or spatially resolved sensor response is required.

4 *The multi-stream flow application* [11]. A novel device has been fabricated for parallel high-throughput flow assays with in-built oxygen measurement in a single bioreactor. Controlling the oxygen concentration of individual streams improves the validity of cell-based experiments and allows to determine the coefficient of diffusion of oxygen in different perfusion media.

Other, more minor, contributions can be found throughout this thesis. These include innovations such as an experimental setup for sensor calibration and a process to pattern cell-adhesion proteins simultaneously with the oxygen sensor. Such developments are by no means unique; however, the approach taken may well be original and of benefit to others in the future.

Also worthy of mention is the BAL prototype, a multi-layer PDMS device demonstrating the feasibility of device scale-up towards a clinically relevant bioreactor size.

Finally, the results of a brief experiment to test an approach using vertically aligned carbon nanotube bundles as fluidic conduits for bile drainage are reported. Results are promising, which makes this a strong candidate for future work.

The following publications have resulted from this work:

- V. Nock, R. J. Blaikie, and T. David, “Microfluidics for Bioartificial Livers”, *New Zealand Medical Journal (2007)*, Vol. 120, No. 1252, pp. 2-3.

- V. Nock, R. J. Blaikie, and T. David, “Micro-patterning of Polymer-based Optical Oxygen Sensors for Lab-on-Chip Applications”, *Proceedings of SPIE (2007)*, Vol. 6799, DOI: 10.1117/12.759023.

- V. Nock and R. J. Blaikie, “Fabrication of optical grayscale masks for tapered microfluidic devices”, *Microelectronic Engineering (2008)*, Vol. 85, No. 5-6, pp. 1077-1082.

- V. Nock, R. J. Blaikie, and T. David, “Patterning, integration and characterisation of polymer optical oxygen sensors”, *Lab on a Chip (2008)*, Vol. 8, No. 8, pp. 1300-1307, DOI: 10.1039/b801879k.

- V. Nock, R. J. Blaikie, and T. David, “Generation and detection of laminar flow with laterally-varying oxygen concentration levels”, *Proceedings of MicroTAS (2008)*, Vol. 1, pp. 299-301.

- V. Nock, R. J. Blaikie, and T. David, “In-situ Optical Oxygen Sensing for Bioartificial Liver Bioreactors”, *Proceedings of ICBME (2008)*, **in press.**

- V. Nock, R. J. Blaikie, and T. David, “Oxygen Control For Bioreactors And In-vitro Cell Assays”, *AIP Conference Proceedings*, **in preparation**.

The work described in this thesis has also been presented in various forms:

- Poster presentation, “Microfluidics for Bioartificial Livers”, *MacDiarmid Institute Student Symposium (Wellington, NZ, October 2005)*.

- Oral presentation, “Microfluidics for Bioartificial Livers”, *MacDiarmid Institute Bionano-Network Meeting (Christchurch, NZ, January 2006)*.

- Oral presentation, “Microfluidics for Bioartificial Livers”, *German-New Zealand Workshop on Nanotechnology (Wellington, NZ, March 2006)*.

- Oral presentation, “Microfluidics for Bioartificial Livers”, *Health Research Society of Canterbury Scientific Meeting, University of Canterbury (Christchurch, NZ, March 2006)*.

- Oral presentation, “Microfluidics for Bioartificial Livers”, *Showcase 2006, University of Canterbury Postgraduate Conference (Christchurch, NZ, October 2006)*, Audience Best Presentation Award.

- Poster presentation, “Microfluidics for Bioartificial Livers”, *Running Hot - Science in New Zealand Conference (Christchurch, NZ, November 2006)*.

- Poster presentation, “Bioartificial Livers - A Place in Therapy?”, *MacDiarmid Institute Student Symposium (Christchurch, NZ, November 2006)*.

- Poster presentation, “Design and Fabrication of a Bioartificial Liver Bioreactor”, *AMN-3 Satellite Meeting on Nano- and Bionano-Technology, Quantum Transport and Quantum Functional Semiconductors NBT-QT (Wellington, NZ, February 2007)*.

- Oral presentation, “Microfluidics for Bioartificial Livers”, *3rd International Conference on Advanced Materials & Nanotechnology AMN-3 (Wellington, NZ, February 2007)*.

- Poster presentation, “Electron Beam Lithography for the Fabrication of Grayscale Masks”, *3rd International Conference on Advanced Materials & Nanotechnology AMN-3 (Wellington, February 2007)*, Runner-up Best Student Poster Award.

- Oral presentation, “Design and Fabrication of a Bioartificial Liver Bioreactor”, *Durmont d’Urville Workshop on Microfluidics (Christchurch, NZ, April 2007)*.

- Oral presentation, “Last Drinks Please! - An Update on Bioartificial Liver Research”, *Showcase 2007, University of Canterbury Postgraduate Conference (Christchurch, NZ, August 2007)*, College of Engineering Best Presentation Award.

- Oral presentation, “Plasma-Patterning of Fluorescence-based Oxygen Sensors”, *33rd International Conference on Micro-and Nano-Engineering MNE (Copenhagen, Denmark, September 2007)*.

- Poster presentation, “Fabrication of Optical Grayscale Masks for Tapered Microfluidic Devices”, *33rd International Conference on Micro-and Nano-Engineering MNE (Copenhagen, Denmark, September 2007)*.

- Poster presentation, “Optical Sensing of Dissolved Oxygen in Bioreactor Devices for Bioartificial Livers”, *MacDiarmid Institute Student Symposium (Hamilton, NZ, November 2007)*.

- Oral presentation, “Micro-patterning of Polymer-based Optical Oxygen Sensors for Lab-on-Chip Applications”, *Microelectronics, MEMS, and Nanotechnology AU07 (Canberra, Australia, December 2007)*.

- Oral presentation, “Integrated Optical Oxygen Sensors for PDMS-based Microfluidic Devices”, *MacDiarmid Institute Bionano-Network Meeting (Christchurch, NZ, January 2008)*.

- Oral presentation, “From Electrons to Liquids - Using Semiconductor Technology to improve Biomedical Devices”, *University of Canterbury NanoLab User Meeting (Christchurch, NZ, April 2008).*

- Oral presentation, “Microfluidics for Bioartificial Livers - How Semiconductor Technology can improve Biomedical Devices”, *Departmental Seminar, Electrical and Computer Engineering, University of Canterbury (Christchurch, NZ, May 2008).*

- Oral presentation, “In-situ Oxygen Gradients for Cell-Culture Bioreactors”, *Health Research Society of Canterbury Scientific Meeting, University of Otago, Christchurch School of Medicine & Health Sciences (Christchurch, NZ, September 2008).*

- Poster presentation, “Generation and detection of laminar flow with laterally varying oxygen concentration levels”, *12th International Conference on Miniaturized Systems for Chemistry and Life Sciences MicroTAS (San Diego, USA, October 2008).*

- Oral presentation, “Beyond Imaging: Applications of Fluorescence Microscopy”, *MacDiarmid Institute Student Symposium (Wellington, NZ, November 2008).*

- Oral presentation, “In-situ Optical Oxygen Sensing for Bioartificial Liver Bioreactors”, *13th International Conference on Biomedical Engineering ICBME (Singapore, December 2008).*

- Accepted for oral presentation, “Graduated Oxygen Levels using Multiple Laminar Streams”, *4th International Conference on Advanced Materials & Nanotechnology AMN-4 (Dunedin, NZ, February 2009)*

The work presented in this thesis has further been reported in the following non-peer reviewed forms:

- “Polymer Optical Oxygen Sensor for Microfluidic Devices” in *Technical Insights: Sensor Technology Alerts (July 2008)*, Frost&Sullivan.

- Photography, “Prototype of a silicone multi-layer Bioartificial Liver Bioreactor”, *University of Canterbury College of Engineering Research Photo Competition 2008 (Christchurch, NZ, November 2008)*, 3rd Prize.

In addition, the author has contributed to the following presentations and paper on work related to, but not directly relevant to this thesis:

- V. Nock, A. Ghanbari, W. Wang, R. J. Blaikie, G. Chase, X. Chen, and C. Hann, "Force pattern characterization of *C. elegans* in motion", *Showcase 2008, University of Canterbury Postgraduate Conference (Christchurch, NZ, September 2008)*, oral presentation, College of Engineering Best Presentation Award.

- A. Ghanbari, V. Nock, W. Wang, R. J. Blaikie, G. Chase, X. Chen, and C. Hann, "Force pattern characterization of *C. elegans* in motion", *15th International Conference on Mechatronics and Machine Vision in Practice (Auckland, NZ, December 2008)*, oral presentation.

- A. Ghanbari, V. Nock, W. Wang, R. J. Blaikie, G. Chase, X. Chen, and C. Hann, "Force pattern characterization of *C. elegans* in motion", *Proceedings of M2VIP (2008)*, pp. 680-685.

1.3 THESIS STRUCTURE

To guide the reader through the thesis an outline of the structure is shown in Fig. 1.1. The illustration compares a natural liver sinusoid and the developed bioreactor device and indicates which parts of the device are covered in which chapter of the thesis. In general, the reader is assumed to have a basic knowledge of semiconductor processing technologies and their application to the fabrication of microfluidic devices, but not a background in fluidic transport phenomena and bio-artificial liver devices. Hence, a review of BALs is presented in this thesis, as well as some fundamental microfluidics phenomena.

Chapter 2 - *Introduction to Bio-Artificial Livers*, introduces essential background concepts, including a brief introduction to liver anatomy, liver diseases and the principles behind treatment of these using BAL devices. An outline of the historical development of BALs is also presented, together with a summary of major engineering challenges relating to BAL bioreactors.

Following this, Chapter 3 - *Theoretical Background*, discusses common flow phenomena at the micro-scale and their application to derive the general transport equation. It further shows how these equations can be applied to yield the relationship between geometry, shear-stress and oxygen concentration. The use of this relationship for passive

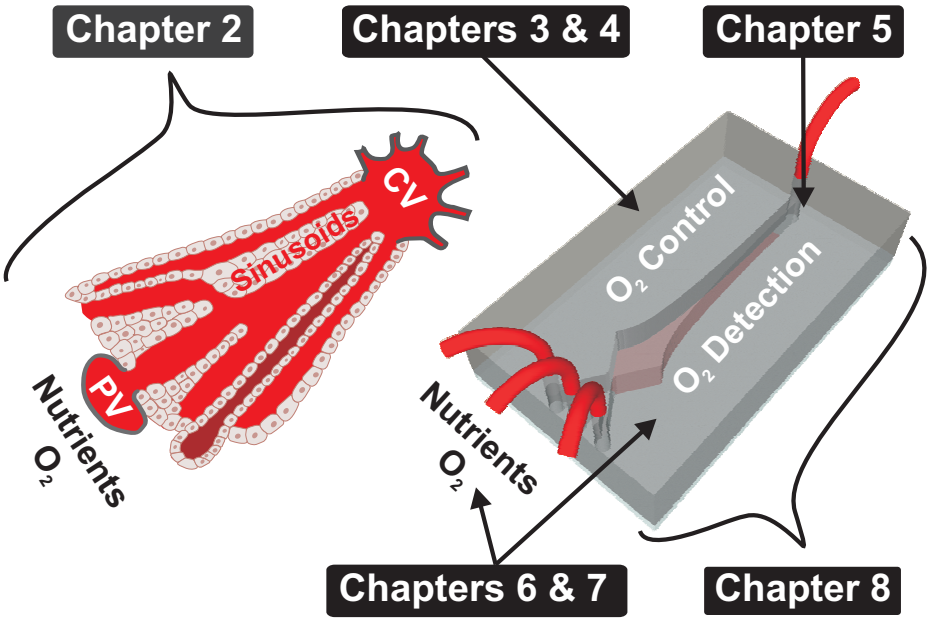

Figure 1.1: *Guideline through this thesis.*

concentration control is demonstrated for the special case of constant oxygen concentration by means of analytical calculation and numerical fluid dynamics simulations.

Chapter 4 - *Bioreactor Design and Fabrication*, and Chapter 5 - *Oxygen Sensor Integration*, cover the fabrication of the two device designs and integration of the oxygen sensing layer into the bioreactor devices. Two novel fabrication processes for tapered microfluidic channels and for polymer matrix-based optical oxygen sensors are introduced.

In Chapter 6 - *Experimental Fluidic Setup*, and Chapter 7 - *Characterisation of Oxygen Measurement*, the developed measurement setup and the sensor calibration procedure for application of the devices to oxygen sensing are discussed in detail. The latter chapter covers sensor use for measurement of both gaseous and dissolved oxygen, as well as methods to optimize the sensor intensity response. In addition, a review of oxygen sensing in the context of the Lab-on-a-chip concept is given and the applicability of the developed processes and devices to on-chip oxygen visualization and detection are described.

Multi-stream parallel flow generation with variable oxygen concentrations and measurement of coefficient of diffusion are demonstrated in this context.

This is followed by the penultimate Chapter 8 - *Cell Integration*, which addresses issues relating to *in-vitro* cell-culture and its potential influence on sensor performance. Oxygen sensing with cells is shown and the chapter finishes by introducing a novel concept of an auxiliary bile drainage system for BAL devices.

A summary of the work presented in this thesis is provided in Chapter 9 - *Conclusions and Future Work*, as are recommendations for future research.

Appendices A, B, C and D cover the detailed derivation of the relationship between oxygen concentration profile and bioreactor shape. The nomogram given in Appendix F illustrates the determination of the dissolved oxygen concentration in an example liquid for a given temperature, salinity and pressure.

The art of medicine consists in amusing the patient while nature cures the disease.

Voltaire
1694-1778, French Philosopher

CHAPTER 2

Introduction to Bio-Artificial Livers

In this chapter the liver as organ is introduced. General function and related diseases are summarized. This is followed by a closer look at the range of different medical treatments available, with particular focus on Bioartificial liver (BAL) systems and their current status. The second part of the chapter discusses engineering challenges related to BALs and relates the research presented in this thesis to current cell-culture and BAL devices.

2.1 THE LIVER

The liver performs more than 500 different functions, all of which are essential to life. The vital organ's unique ability to regenerate, or regrow, cells that have been destroyed by injury or disease has always been a source of fascination to humans.

One of the first accounts of the liver's fascinating regenerative capabilities can be found in greek mythology. In the myth of the titan Prometheus, king of the gods Zeus hides the fire from humans as retribution to a deceit by the titan. Prometheus in return steals the fire from Zeus and returns it to the humans. The angered Zeus then punishes the titan by chaining him to a mountain and having his liver eaten by an eagle. Each day the liver would grow back, making it an endless punishment until the eagle was finally killed by the hero Heracles. Figure 2.1 shows the famous mythological scene as painted by Peter Paul Rubens in the early 17th century.

However, despite this extraordinary capability the liver may undergo irreversible changes that permanently interfere with function and pose a significant threat to survival in form of complete organ failure. Throughout medical history there have been continuous efforts to understand and treat liver failure. A number of strategies and liver support devices have been proposed but success has so far been limited.

The recent advent of and continuing progress in microfabrication has created the possibility to enhance liver support systems to a state far beyond current systems. With fabrication technology reaching biological size scales and by applying the growing knowledge of microfluidic systems it will be possible to closer map the real liver and thereby provide a better environment for liver cell function. In the following sections the anatomy of the liver, its functions as an organ and its diseases will be introduced. Strategies for treatment of liver failure will be discussed, followed by an overview of current existing liver support devices and their shortcomings.

2.1.1 Structure and Physiology

2.1.1.1 Macro-Anatomy

Located in upper right-hand part of the abdomen the liver is the largest organ within the human body, weighing up to 2.5 kg [12]. As a soft organ the liver is susceptible to traumatic injury and being essential for life its removal results in ensured death within a few hours [13]. For external protection it is therefore attached to the diaphragm and sheltered by the rib cage. Of pyramidal shape, the basic liver structure is divided into two main lobes with the right lobe being about six times the size of the left lobe. As depicted in Fig. 2.2, the liver is connected to the gastro-intestinal tract from where it receives portal blood loaded with dissolved foods via the hepatic portal vein. In addition, oxygen-rich arterial blood is supplied from the aorta by means of the hepatic artery.Upon passage through the liver arterial and portal blood drain via hepatic veins into the inferior vena cava and finally the right atrium of the heart. In comparison, the liver shows the fourth highest specific blood perfusion rate of all organs in the human body with a typical rate of ~1000-1400 cm^3/min (up to a maximum of ~5400 cm^3/min [14]) and average pressures of 9 mmHg in the portal vein to 0 mmHg in the hepatic vein [15].

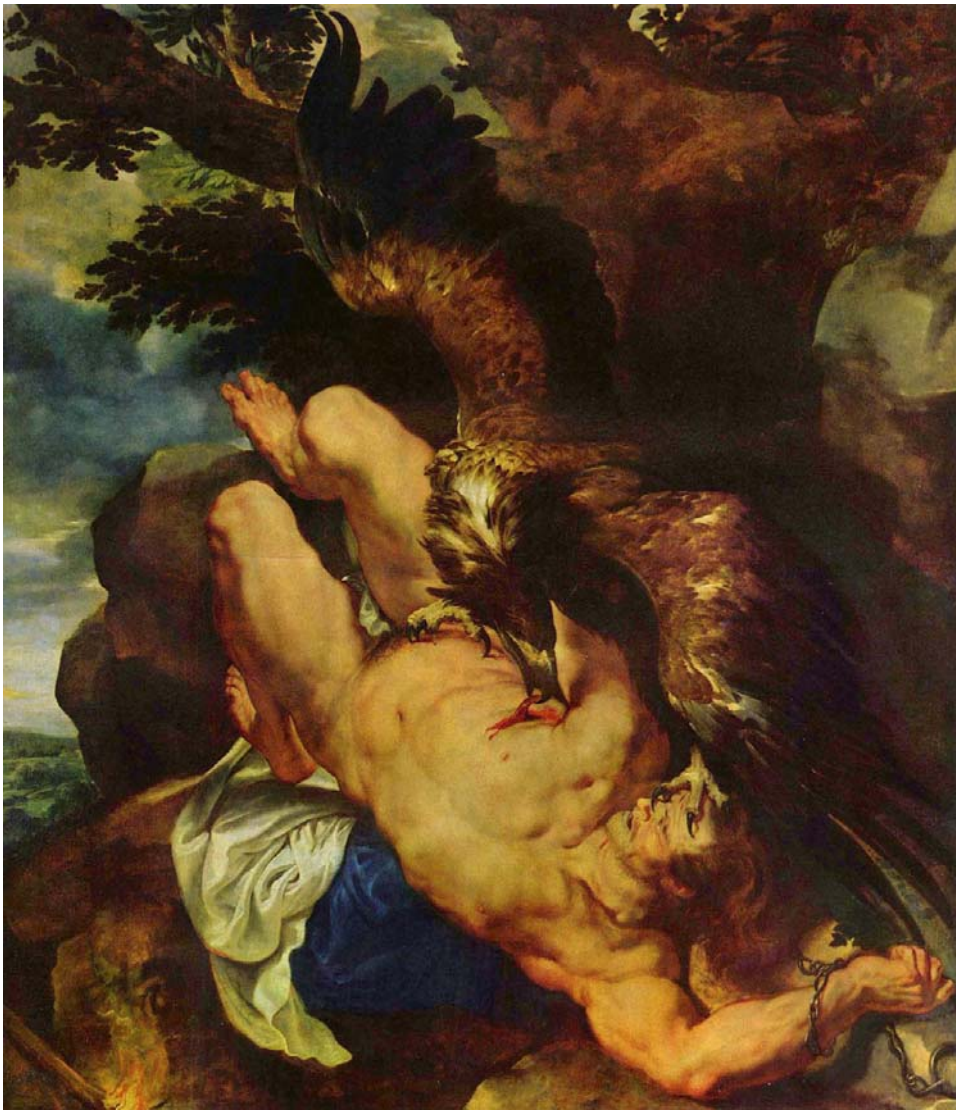

Figure 2.1: *Chained Prometheus, oil on canvas painting by Peter Paul Rubens, 1611-1612.*

Serving as an entrance for both the portal vein and the hepatic artery is the porta hepatis, a fissure at the undersurface of the liver. Once inside, the portal vein and hepatic artery branch forming portal canals where major branches are combined together with those of the bile duct. From branches of these portal canals arterial and portal blood passes into the spaces between liver cords called sinusoids. Through these sinusoids the blood drains into the central hepatic vein (Fig. 2.3). Bile produced by the liver cells is channelled in bile canaliculi and bile ductule which empty into the bile ducts. These individual ducts exit the liver and combine with the cystic duct from the gall bladder to the common bile duct. The

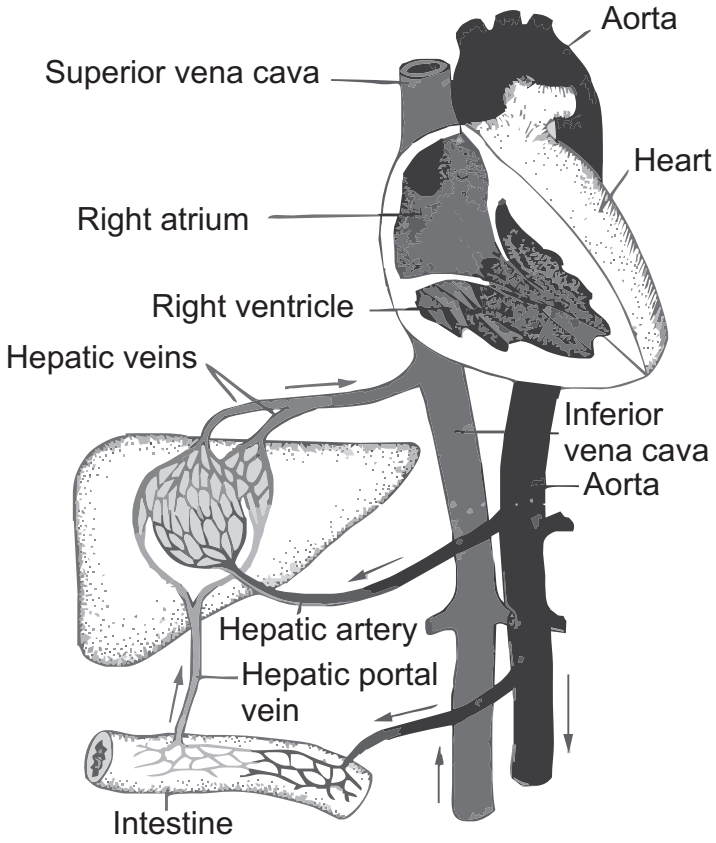

Figure 2.2: *The human liver's hepatic portal and venous drainage system (Adapted from [13]).*

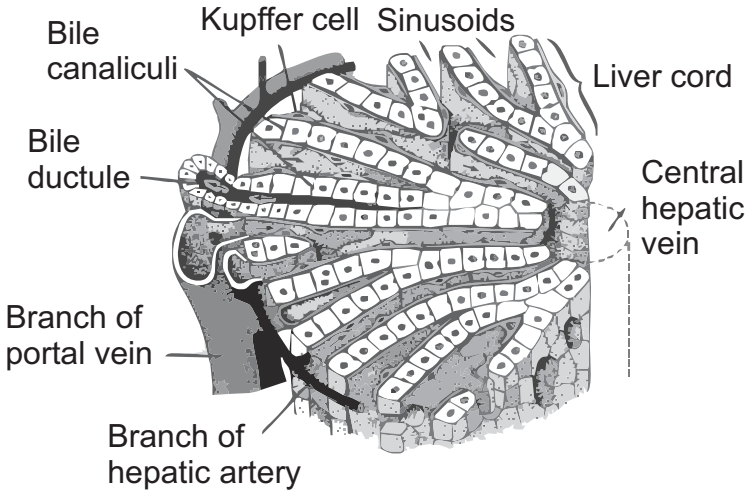

Figure 2.3: *Part of a liver lobule depicting flow of blood from portal canal through sinusoid to the hepatic vein (Adapted from [13]).*

common duct unites with the pancreatic duct at the ampulla of Vater and both empty into the small intestines at the sphincter of Oddi (Fig. 2.4).

In summary, the intricate natural microfluidic system formed by the liver's macro anatomy provides the highest state of cell culture environment for the liver cells. It enables them to simultaneously provide metabolic functions and remove toxins from the blood for delivery into the body's waste system, all modulated via the essential oxygen supplied by the hepatic artery.

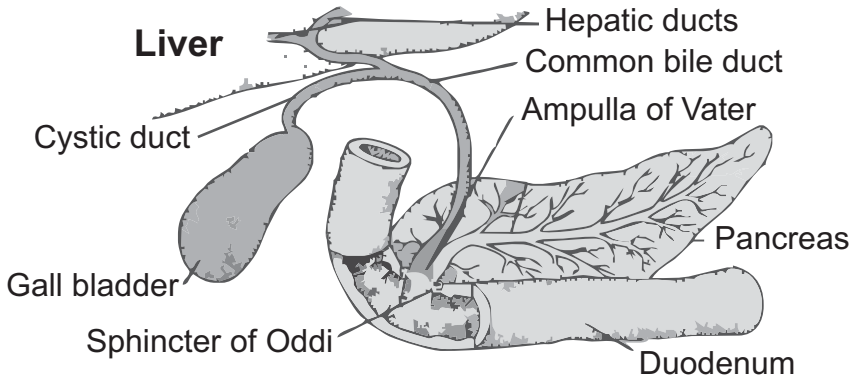

Figure 2.4: *Bile drainage system of the human liver (Adapted from [13]).*

2.1.1.2 Micro-Anatomy

Understanding what makes the liver structure so suited for liver cell function is the key to successful bioengineering of a potential artificial liver and therefore necessitates a closer look at the organ's micro anatomy. Inside the liver, portal canals, hepatic veins and groups of liver cells together form the liver lobule as a basic functional unit. Cylindrical in structure, with a diameter of 0.8 to 2 mm and with a depth of several mm, about 50,000 to 100,000 of these liver lobules make up a human liver [15]. Each lobule is composed of hepatic cellular plates one to two cells thick and arranged around a central vein, as can be seen in Fig. 2.5.

2.1.1.3 Sinusoids

The hepatic planes form the liver sinusoids, through which the blood flows from portal vein and hepatic artery to the central vein. Oxygen-rich arterial blood often enters as far down the sinusoid as 1/3 of its total length away from the interlobular septa, the dense

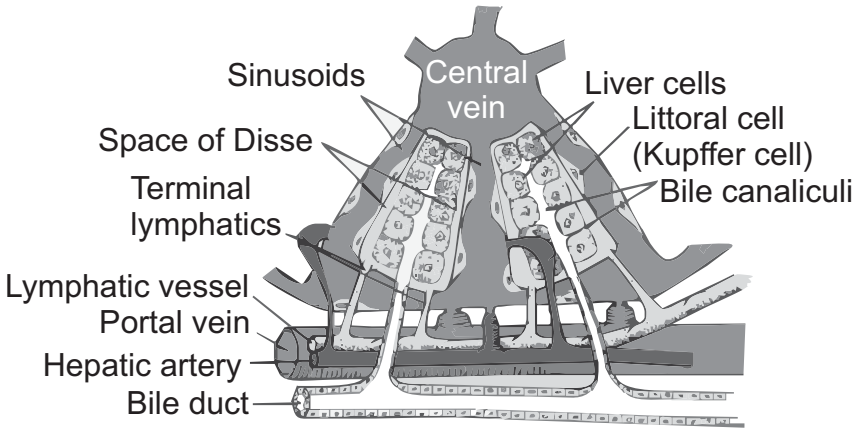

Figure 2.5: *Part of a liver lobule with hepatic plates formed by cords of hepatocytes (Adapted from [15]).*

fibrous tissue supporting the portal canals (see middle sinusoid in Fig. 2.5). With an average length of 500 µm, the sinusoid diameter varies from slightly more than 4 µm in zone 1 at the portal tract to around 5.5 µm in zone 3 near the hepatic venule [16]. In comparison, the diameter of red blood cells (erythrocytes) is an average of 7.8 µm. As a result, sinusoidal walls, made up by porous endothelial cells, as well as the blood cells have to distort to allow passage through the sinusoids. This process of "forced sieving" or "endothelial massage" is thought to facilitate the exchange of metabolites between blood and liver cells. Furthermore, tapering of the sinusoids is complemented by a gradient in diameter and frequency of pores or fenestrae as they are also called. In the direction of blood flow towards the central vein the porosity of the sinusoid wall increases as the diameter of fenestrae decreases but their frequency increases [16]. Regulation of dietary lipids is shown as one example of fenestrae function in Fig. 2.6. Here a large lipoprotein, the chylomicron, is blocked from entering the space of Disse while its smaller remnants are able to pass and thus get in direct contact with the hepatocytes.

2.1.1.4 Cellular Level

On the cellular level the human liver consists of five main cell types. Whereas the first four of them are of different lineage and usually classified as sinusoidal cells, the last one is the actual liver cell, the hepatocyte. All together they create an integrated functional

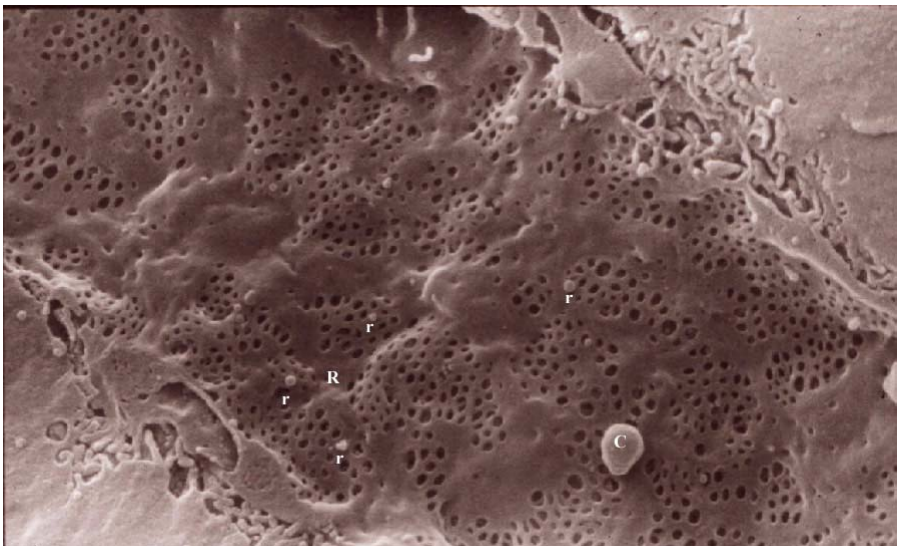

Figure 2.6: *Scanning electron micrograph showing fenestrated endothelial lining of a sinusoid wall. A chylomicron (C) is prevented from accessing the space of Disse while its smaller remnants (r) fit through the pores (from [17]).*

system, which allows the liver to perform its role as multifunctional organ in the body [16]:

Liver Sinusoidal Endothelial Cells (LSEC)

Endothelial cells provide the inner lining of the sinusoids, thereby preventing direct contact between hepatocytes and blood cells, platelets and the largest of colloids circulating in the blood. However, contrary to those in capillaries, LSECs have fenestrae which are not occluded by a basement membrane and thereby provide what is also termed as the "liver sieve" [16]. The fenestrae in the liver sinusoids range from numerous (5-20 /μm^2) small openings (mean diameter 0.175 µm, range 0.1 to 0.3 µm) to rare (<0.1 /μm^2) large openings (0.3 to 1 µm diameter) [14] and allow plasma access to the space of Disse behind.

Kupffer Cells

Supplementing the endothelial cells inside the sinusoids are Kupffer cells, tissue macrophages capable of recognizing and destroying bacteria, endotoxins and other foreign macromolecules in the blood.

Hepatic Stellate Cells of Ito

Located outside the sinusoid in the space of Disse, the hepatic stellate cells of Ito (HSC) act as storage for fat soluble Vitamin A in form of retinyl esters. Furthermore, they activate to myofibroblasts and synthesize collagen when retinol depleted [12].

Pit Cells

Like the Kupffer cells, Pit cells are natural killer cells or large granular lymphocytes located intrasinusoidally attacking neoplastic or tumor cells.

Hepatocytes - The Liver Cells

Polyhedral in shape and with a typical diameter of 18 µm, hepatocytes or main liver cells account for about 60 % of liver substance or 80 % of liver cell population [14]. As shown in Fig. 2.7 hepatocytes are separated from blood-carrying sinusoids by endothelial cells and the space of Disse, which itself drains into the lymphatics. The outer plasma membrane facing the space of Disse forms microvilli, increasing the surface area manyfold [13]. At their contact line adjacent hepatocytes form intercellular spaces, the bile canaliculi, used to transport bile away into the bile drainage system and eventually the small intestines.

Inside the hepatocyte cell mitochondria provide chemical energy, as well as synthesis of glucogen and the enzymes cause deanimation and urea synthesis. The endoplasmatic reticulum in turn synthesizes the specific liver proteins for blood coagulation, while the ribosomes on its margin synthesize the enzyme necessary for the utilization of glucose obtained from glucogen [13].

2.1.2 Liver Functions

Playing an important role in such vital tasks as molecule synthesis, detoxification, waste product disposal and general metabolism makes the liver a truly complex multifunctional organ. Over 5000 different functions have currently been assigned to the liver, with the main functions performed by the liver distinguished into:

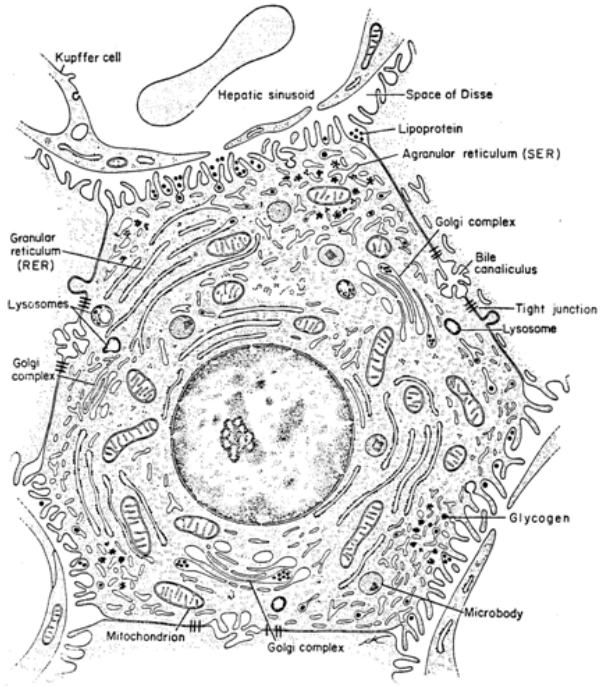

Figure 2.7: *Drawing of a hepatocyte with part of Kupffer cell and sinusoid (Adapted from [13]).*

(i) *vascular* functions for storage and filtration of blood;

(ii) *metabolic* functions concerned with the majority of metabolic systems in the body;

(iii) *secretory* and *excretory* functions responsible for formation of bile flow through bile ducts into gastrointestinal tract.

The following section will introduce the individual functions described above in greater detail.

2.1.2.1 Functions of the Hepatic Vascular System

One of the main vascular functions of the liver is to act as a blood reservoir. As mentioned before, the typical flow rate for blood through the liver is ~1450 ml/min with around 1100 ml entering via the portal vein and an approximately further 350 ml from the hepatic artery. This corresponds to almost 29 % of the overall resting cardiac output. In normal pressure situations the blood volume in the liver including hepatic veins and hepatic sinusoids amounts to 450 ml, about 10 % of the total blood volume. In high pressure

situations as much as 0.5 to 1 l of extra blood can be stored [15].

The second important vascular function is blood cleansing. Various gut bacteria, endotoxins and foreign macromolecules are picked up by the blood, mainly while flowing through intestinal capillaries. Macrophages like Kupffer cells line the sinusoids and digest these bacterias upon contact. It is estimated that less than 1 % of bacteria contained in the portal blood manage to pass through the liver and on into the rest of the circulation system.

A further auxiliary function and direct result of blood vessel porosity in the liver is the formation of large quantities of lymphatic fluid. Both fluid and proteins passing through into the space of Disse are drained by lymphatic vessels as depicted in Fig. 2.5. This leads to the liver supplying nearly half of all lymphatic fluid produced in the body at resting conditions [15].

2.1.2.2 Metabolic Functions

As also described in [15], the most important metabolic functions of the liver can be further subdivided into carbohydrate, fat, protein and miscellaneous metabolisms. In the following a summary of functions regarding each metabolism is given.

Carbohydrate Metabolism

The specific functions carried out by the liver in carbohydrate metabolism are:

(i) storage of glycogen;

(ii) conversion of galactose and fructose to glucose;

(iii) gluconeogenesis;

(iv) formation of other important compounds from intermediate products of carbohydrate metabolism.

In general, the liver acts as a glucose buffer by storage and release, thereby maintaining a normal concentration of glucose in the blood. Should the glucose level fall too low amino acids are converted into glucose raising the concentration back to normal (gluconeogenesis).

Fat Metabolism

While many cells in the body can perform fat metabolism, the following functions mainly take place in the liver:

(i) supply of energy by oxidation of fatty acids;

(ii) formation of most lipoproteins;

(iii) synthesis of cholesterol and phospholipids;

(iv) conversion of carbohydrates and proteins to fat.

Protein Metabolism

Compared to carbohydrate and fat metabolism, protein metabolism is certainly the most important metabolic function of the liver since it can not be replaced by any other part of the body. In fact, loss of all liver protein metabolic functions results in death within a few days. Briefly the main functions of the liver are:

(i) deanimation of amino acids;

(ii) formation of urea for removal of ammonia from body fluids;

(iii) formation of ~90 % of all plasma proteins;

(iv) interconversions among amino acids and other compounds important to metabolic processes (such as non-essential amino acids for example).

Deanimation of amino acids in particular is essential for their conversion into energy, carbohydrates or fat and almost all deanimation takes place in the liver. Ammonia produced by the deanimation process and bacteria in the gut are removed by formation of urea. Absence of this function leads to a rapid rise in the ammonia concentration in the plasma, followed by hepatic coma and eventually death.

Miscellaneous Metabolic Functions

Besides the main metabolic functions described above the liver performs a variety of further functions related to the metabolism. Given below is an example of four miscellaneous functions:

(i) Storage of vitamins with capacity for up to 10 months of vitamin A, 3 to 4 months of vitamin D and 1 to several years of vitamin B_{12};

(ii) formation of substances utilized in blood coagulation process (requires vitamin K to be present);

(iii) storage of iron in form of ferritin (provides an iron buffer system for blood); and

(iv) chemical detoxification and excretion of various drugs, hormones and other substances such as calcium.

2.1.2.3 Secretory and Excretory Functions - Bile

Hepatocytes in the liver secret around 600-1200 ml of bile per day into the intestinal tract. The major constituents of the bile thereby are bile acids, cholesterol, water, bilirubin and other organic substances. Once introduced into the intestines, acids contained in the bile aid in emulsifying large fat particles into several smaller ones. While these can be attacked more easily and broken down by lipases, the acids also assist in transporting and absorbing digested fat end products to and through the intestinal mucosal membrane. Bile further serves as a means to excrete waste products from blood, in particular cholesterol and bilirubin, a pigment created by degradation of hemoglobin during the destruction of old red blood cells.

2.1.3 Diseases of the Liver

Being such a multifunctional organ a variety of diseases are linked to the liver and affect it both directly and indirectly. Although, compared to other organs, the liver has the unique ability to regenerate and regrow after loss of more than 70 % of its substance, the human body can not substitute its functions in case of total liver failure. In general, a large number of liver diseases are associated with jaundice indicating increased levels of bilirubin in the blood. While being a standard product of hemoglobin breakup, excess levels of the pigment can be caused by abnormal levels of red blood cell destruction, impaired uptake or transport, defective conjugation of bilirubin and drug-impaired difficulties in canalicular excretion for example [13]. A condition in which the liver is

damaged beyond self-regeneration and ceases to function is termed liver failure. Due to the liver's importance to human survival, those diseases that ultimately lead to a complete liver failure are the most serious.

Depending upon the time span between the onset of symptoms, such as jaundice, and cessation of liver function failures are classified into:

(i) Subfulminant Hepatic Failure (SHF, within 2-8 weeks);

(ii) Fulminant Hepatic Failure (FHF, within 2 weeks);

(iii) Acute Hepatic Failure (ALF, within 48 hours).

In contrary to the rare acute cases the process of liver failure is most often either chronic or occurs gradually over several years. Common causes of hepatic failure include hepatitis, liver inflammation, by virus or occasionally poisons, autoimmunity or hereditary conditions, with Hepatitis C being the most common cause worldwide [18]. Another particularly widespread reason for failure is Cirrhosis, the replacement of dead liver cells by and formation of fibrous tissue in the liver. This is usually a result of excessive alcohol consumption, viral hepatitis or general contact with liver-toxic chemicals. A third major cause is auto-immune liver disease, including autoimmune hepatitis, primary biliary cirrhosis and primary sclerosing cholangitis, which accounted for 29 % of all liver transplantations in the United Kingdom in 2000 [19]. Further less common diseases include hereditary hemochromatosis, Wilson's disease and hepatocellular carcinoma or liver cancer. Figure 2.8 shows the major causes for liver failure by diagnosis for 17,922 people registered as awaiting transplantation with the Organ Procurement and Transplantation Network (OPTN) in the United States as of September 2005 [20].

2.1.4 Liver Failure Treatment

The most effective treatment for irreversible liver failure as of today is Orthotopic Liver Transplantation (OLT). In this procedure a failed liver is removed from the patient's body and a healthy liver from a recently deceased human donor is transplanted into the same location. From the first successful transplantation in a human being reported in 1968 [19]

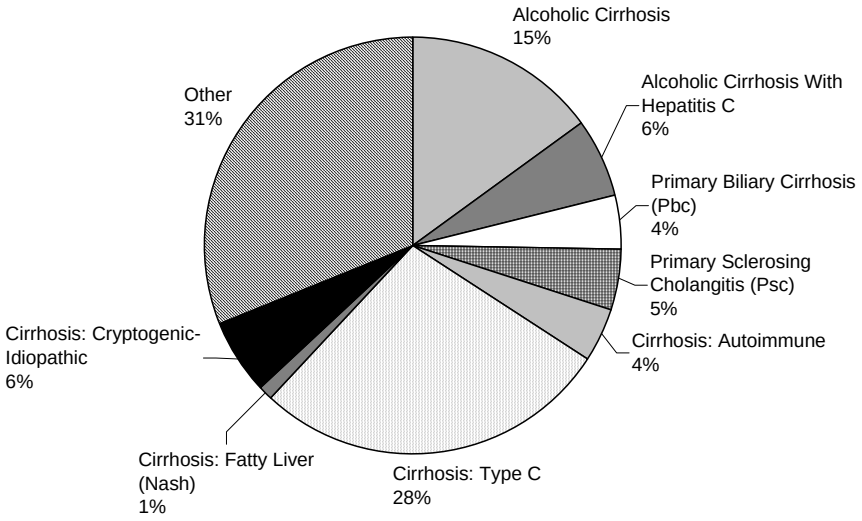

Figure 2.8: *Diagnosis by disease for liver transplantation in the United States September 2005.*

the number of livers transplanted annually in the US has risen to 6,500 in 2007 [20]. When compared to the almost 20,000 patients currently waiting for transplantation it becomes obvious that a severe shortage of donor livers exists.

Other alternative options to OLT have therefore emerged in the form of Living Donor Liver Transplantation (LDLT) [21], the use of marginal [22], domino [23] and split livers [24]. In LDLT part of a donor's healthy liver is surgically removed and inserted into a recipient, while the donor liver recovers to its previous size. Originally the procedure was introduced for parents to donate part of their liver as replacement for the damaged liver of their child, but today even adult-to-adult LDLT is possible to a certain degree. However, not only as with OLT is the procedure accompanied by high costs and shortage of available donors, it also introduces an additional risk for the donor due to the major surgical procedure of removal.

While in general these procedures may help reduce the shortage of donor livers, additional less invasive and more cost-effective options are required. Of the alternatives to whole organ transplantation the four main cellular approaches under investigation are displayed in Fig. 2.9.

Hepatocyte transplantation (Fig. 2.9(a)) is a method where isolated liver cells are injected into the liver or other ectopic sites to engraft and proliferate [26]. The time as to when a clinical benefit occurs can be up to 48 hours, which makes it a possible procedure

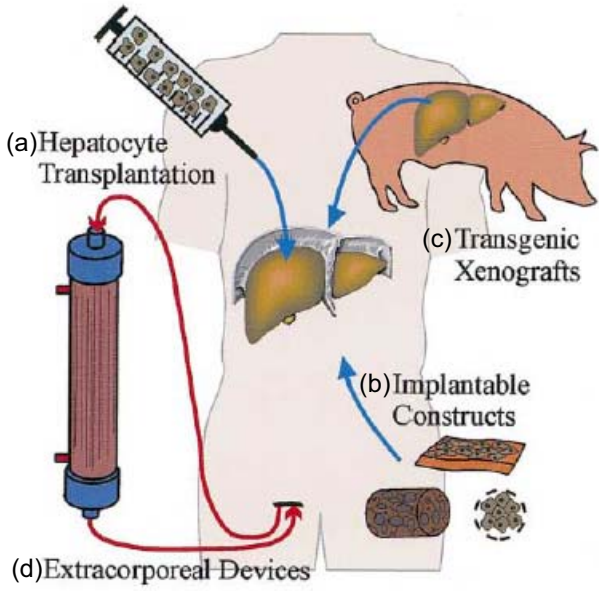

Figure 2.9: *Main alternative approaches to cellular therapies for the treatment of liver disease (Adapted from [25]).*

for treatment of most non-emergency conditions. Best results have been obtained for treating specific metabolic disorders, although long-term function of transplanted hepatocytes is usually not detected [27]. In a related approach implantable constructs (Fig. 2.9(b)) are produced by culturing hepatocytes *ex-vivo* on or in synthetic or biodegradable support scaffolds [28]. The two major types of implantables are hepatocytes in open matrices that allow host tissue ingrowth and hepatocytes encapsulated by a selective membrane, whereas the main advantage of the latter lies in the possible use of non-allogeneic cell sources [27]. Pig livers (Fig. 2.9(c)) are being investigated as the main source for transgenic xenograft and could eventually provide an unlimited supply of transplant livers, however graft rejection continues to be a major problem [29]. A fourth major approach is the development of extracorporeal bioartificial liver (BAL) devices (Fig. 2.9(d)) designed to support or replace a failing liver. Similar in concept to kidney dialysis machines the extracorporeal approach with its principles and systems will be presented in greater detail in the following section.

2.2 LIVER SUPPORT SYSTEMS

The preeminent need for a liver support system (LSS) stems from the large current discrepancy between donor liver demand and supply. But even with an unlimited pool of transplantable livers the desire to find a close-to-ideal match between donor and recipient demands time, which might not be given especially in cases of ALF. Thus a working system able to effectively replace a large spectrum of liver functions could be used for both adjunct and temporary liver support [27]. In the first case the system would deliver longer term adjunct support to a liver with reduced functional capabilities such as chronic deficiency, allowing for endogenous liver regeneration. In the second case a greater spectrum of functions would be replaced over the critical phase of liver failure or the device used to bridge a complete and acute liver failure to OLT. Considering a mortality rate of ~90 % for severe FHF restoring essential liver functions should improve the survival rate, increase the availability of donor livers and avoid expensive transplantation processes [30].

From a historical point of view hepatic coma following liver failure was long thought to originate from small dialyzable toxins accumulating in the blood. Consequentially this led to the development of various systems aiming to remove these toxins. Recently however, and with the rising appreciation of the liver's multifunctional role, the notion that viable hepatocytes should be an essential part of any LSS has gained increased support [31]. As shown in Fig. 2.10, a system can be classified either biological or non-biological depending on whether it uses viable liver cell preparations or artificial kidney dialysis principles as an active component. Systems that use a combination of both are classified as hybrid. Different measures such as neurological improvement and degree of elimination/production of substances are used to assess treatment outcome.

2.2.1 NON-BIOLOGICAL LIVER SUPPORT

Several non-biological approaches to liver support have been explored and their general success is considered limited mainly due to their inability to replace the synthetic and metabolic functions of the liver. The following historical summary of the different approaches is based on the review by Barshes et al. [32].

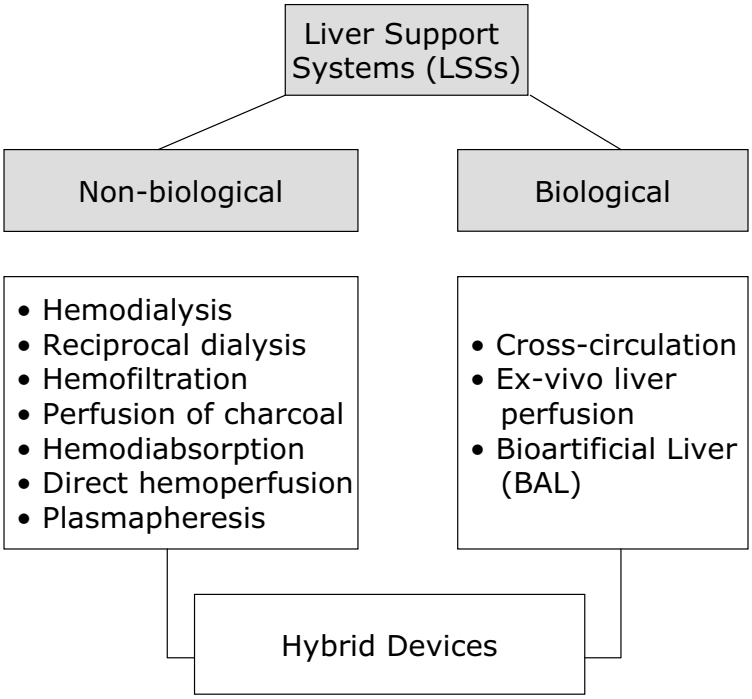

Figure 2.10: *Classification of liver support approaches and examples.*

2.2.1.1 Hemodialysis

One of the first approaches to be used was modified hemodialysis in the mid-1950's due to its successful application in kidney failure. Early trials showed ammonia removal but no survival impact. While the advent of better membranes such as polyacrylonitrile has recently led to more encouraging results, no controlled trials have been reported.

2.2.1.2 Reciprocal (Albumin) Dialysis

A concept introduced in 1976 is that of reciprocal dialysis, where the dialysate composition is used to correct plasma amino acid levels. In 1993 it was combined with an albumin-impregnated membrane containing carrier proteins to facilitate transfer of substances to the dialysate.

2.2.1.3 Hemofiltration

In hemofiltration low-to-middle molecular weight solutes are convectively removed from the blood. Similar in principle to hemodialysis, hemofiltration however is a slower

continuous process that thereby places less strain on a patient's circulatory system. Studies of combined hemofiltration and plasma exchange have shown increased neurological activity and survival.

2.2.1.4 Hemoperfusion

Contrary to filtration, hemoperfusion removes molecules from the blood by perfusion over a sorbent material such as charcoal-based sorbents, synthetic resins or anion exchange resins [32]. While coated charcoal has been most thoroughly tested with good general results, a controlled clinical trial could not show significant survival improvement [31]. In hemodiabsorption or hemodiafiltration charcoal perfusion is combined with a cation exchange resin to form a single access device. This process was used in the BioLogic-DT sorption-suspension dialyzer but also did not yield an improvement in survival [32].

2.2.1.5 Plasmapheresis

A therapy commonly used to treat autoimmune diseases, plasmapheresis or the removal of parts of blood plasma, was first introduced as treatment for FHF in 1968. As result of these early trials only transient improvements and no effect on long-term survival could be observed [31]. More recent studies with high-volume plasma exchange however demonstrated improved survival of patients with drug induced liver failure and plasmapheresis in general is considered to be effective in removal of serum inflammatory mediators not removable by hemodialysis [31].

Two examples of commercially available non-biological liver failure treatment devices both use a variant of albumin dialysis. In the Molecular Absorbent and Recirculating System (MARS®, Gambro AB, [33]) water-soluble and protein-bound toxins are removed from the blood via a albumin treated hollow fiber membrane and a recirculating albumin dialysate cleansing the membrane outside. Prometheus® (Fresenius Medical Care AG), shown in Fig. 2.11, uses fractionated plasma separation and membrane-based high-flux hemodialysis resulting in increased filtration of albumin-bound substances compared to MARS [32]. Analysis of several randomized clinical studies using MARS® did not show an overall benefit contrary to the survival

Figure 2.11: *Prometheus liver support system (From [34]).*

improvements seen in non randomized trials. For Prometheus, substantial decreases in bilirubin, urea, creatinine and ammonium were reported, but other disease and coma scores did not improve [35].

2.2.2 BIOLOGICAL LIVER SUPPORT

Compared to non-biological approaches, purely biological ones show encouraging results but their clinical implementation has proven to be more difficult.

2.2.2.1 Cross Circulation

For a limited number of cases treatment of FHF was attempted by cross-circulating a patient's blood through another healthy human or baboon. Although this led to a decrease

in bilirubin level, neither neurologic status nor survival were increased, whereas the risk for disease transmission is significant for the healthy partner.

2.2.2.2 Ex-vivo Liver Perfusion

The extracorporeal perfusion of a whole or partial liver is a further biological approach showing short-term neurological improvement. Until recently the use of pig livers however did not improve long-term survival and is associated with considerable complications due to rejection of the xenograft and zoonoses, the interspecies transmission of diseases. The use of human livers unsuitable for transplantation and liver slices can alleviate this, but this is again limited due to general shortage in organ supply.

2.2.3 Extracorporeal Systems based on Liver Cell Preparations

Situated between purely biological and non-biological approaches are bioartificial liver systems incorporating preparations of isolated parenchymal liver cells in some form of artificial bioreactor. The main goal pursued with these systems is to provide an environment for cell survival and biochemical/synthetic function combined with *in-vivo* like levels of transport [25] that could bridge the time until a donor organ is available for transplantation. A large variety of different concepts and device designs exist in various stages. The next sections will summarize the current status of BAL systems and discuss major design issues.

2.3 Current Status of Bioartificial Liver Support

2.3.1 Historical Background

The advent of the term “artificial liver” began in the late 1950s with *in-vitro* experiments using fresh liver tissue homogenates, which demonstrated metabolic functions and ammonia to urea conversion. Around 1960 several early BAL devices were introduced for the perfusion of a patient’s blood over liver tissue preparations in a bioreactor [32]. These devices showed only a reduced applicability mainly due to limitations in cellophane membrane technology [31]. The first clinical use of an artificial liver was reported in 1959

by Tokyo University and consisted of cation and anion exchange reactors in combination with a cellophane dialysis membrane and donor animals [32]. A major new series of devices followed the introduction of hepatocyte isolation by enzymatic digestion in 1969 [36]. New techniques such as cuprophane membrane material and synthetic capillaries with cells cultured in extrafiber space were introduced in the 1970s. Conjugation of bilirubin, ureagenesis, protein synthesis and drug metabolism for human hepatocytes were all demonstrated in devices using these technologies [37-39]. Further concepts innovated in the mid to late 1970s were those of plasma separation and high-flow plasma re-circulation with the liver cells placed in the circulatory loop. These developments were followed by the first clinical report on the use of an isolated hepatocyte suspension based system in 1987 [31].

2.3.2 EXISTING BAL SYSTEMS

In the time since 1990 several different systems have been evaluated both in clinical or preclinical trials and *in-vitro* tests. The following summary is based on the recent review by Park and Lee [30].

2.3.2.1 Systems in Clinical Trials

A total of nine BAL systems have undergone clinical trial since 1990. Seven of those are hollow fiber system (HFS), which are summarised in Table 2.1, while the rest are based on porous matrix technology, summarised in Table 2.2. Four [40-42,44] out of the seven HFSs have similar bioreactor configurations and are represented in Table 2.1 by the HepatAssist system.

HepAssist

This system was first developed by Rozga et al. [44] and marketed by Circe Biomedical Inc. It uses microcarrier-attached cryopreserved porcine hepatocytes placed in the extracapillary space of 0.2 μm-pore polysulphone hollow fiber membranes. The patient's plasma flows through the capillaries after passing a column of activated charcoal. A circuit diagram depicting the operation method of the system is shown in Fig. 2.12.

Hollow Fiber Systems				
BAL system	HepatAssist (Arbios) [43,44]	ELAD (Vital Therapies) [45-48]	LSS(MELS) (Charite, Germany) [49-52]	BLSS (Excorp Medical) [53,54]
Bioreactor configuration	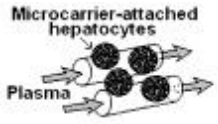	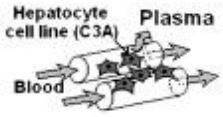	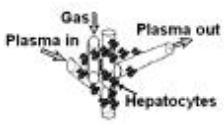	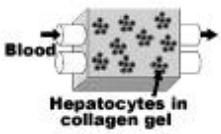
Flow system	Polysulphone 0.2 μm-pore hollow fiber membranes	Hollow fiber and direct plasma through cellulose acetate membrane	Hydrophilic interwoven hollow-fiber membranes, multi-compartment	Cellulose acetate hollow fibers
Shape of cells	Microcarrier attached irregular aggregates	Large aggregates	Tissue-like organoids	Collagen gel entrapped
Hepatocyte source	Cryopreserved porcine ($5\text{-}7x10^9$)	Human cell line C3A (100-400 g)	Discarded human/ porcine (600 g)	Porcine (70-120 g)
Immunological barrier	None	Yes (70-120kD)	None (300kD)	Yes (100kD)
Perfusion (plasma separation rate) [ml/min]	Plasma (50)	Blood (NA)	Plasma (31)	Blood (NA)
Reactor flow rate [ml/min]	400	200	100-200	100-250
Neurological improvement	Yes	Probably	Yes	No
Ammonia removal	18%	-8% (increased)	NA	33%
Bilirubin removal	18%	-20% (increased)	NA	6%

Table 2.1: *Configuration, characteristics and clinical results of hollow fiber BAL systems (Adapted from [30]).*

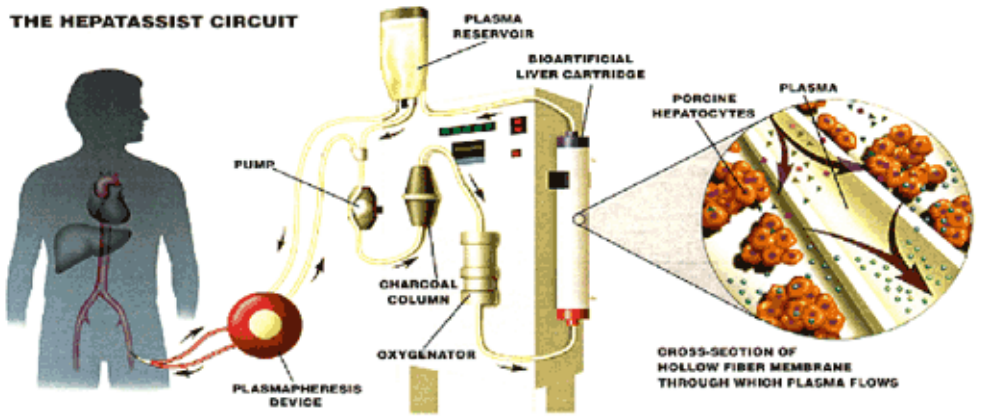

Figure 2.12: *Diagram of the HepatAssist system (Adapted from [43]).*

HepatAssist was extensively tested in Phase II/III clinical trials but did not reach primary endpoint (30-day survival) in the overall study population [43]. An improved second-generation device based on the original system and termed HepatAssist-2 is available from Arbios Systems, Inc. (Los Angeles, USA) for Phase III clinical trials [43].

ELAD

Compared to the other systems, the ELAD or extracorporeal liver assist device is unique as it is the only one to use the human hepatocyte cell line C3A. These cells are derived from the HepG2 human liver cancer cell line and cultured in the extrafiber space of hollow fiber cellulose acetate membranes. Full blood flows through the fibers and plasma is filtered across the membrane to the hepatocytes. The system underwent four clinical trials including a discontinued Phase II trial [48] with inconclusive results since it was introduced by Hepatix/VitaGen. Currently it is under further development by Vital Therapies, Inc. (San Diego, USA).

LSS(MELS)

Gerlach et al. at the Charite University Hospital in Berlin, Germany, introduced the liver support system (LSS) with a novel bioreactor design [49]. As shown in Fig. 2.13, a multitude of independent interwoven hollow fiber capillaries create a three-dimensional matrix seeded with self-assembling hepatocyte aggregates. Both human hepatocytes from discarded donor livers and porcine hepatocytes are used. Plasma enters the reactor via a

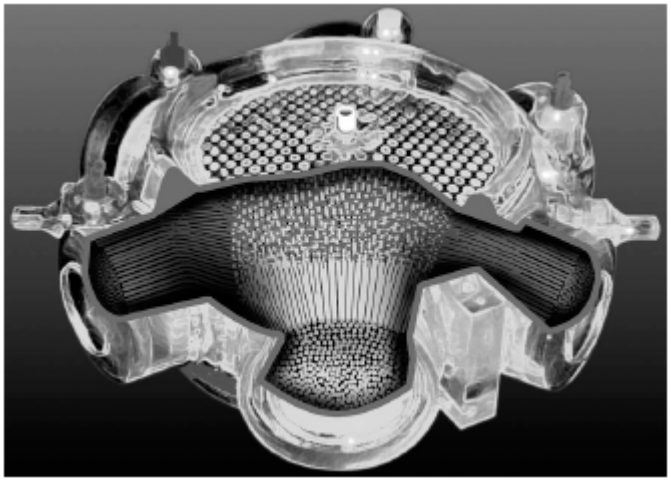

Figure 2.13: *Bioreactor design used in the LSS-BAL (Adapted from [39]).*

first set of fiber membranes closed at one end. After passage through the extracapillary space it exits the reactor via a second set of fibers. A third set of hydrophobic membranes is used to supply oxygen to the cells by diffusion through the membrane. During a Phase I clinical trial using human hepatocytes the LSS was combined with a MARS dialysis device yielding the modular extracorporeal liver support (MELS). Together the systems successfully supported six patients to OLT with improvement in neurological and coagulation states [51]. MELS components are being marketed by Hybrid Organ GmbH (Berlin, Germany) [52].

BLSS

Commercialized by Excorp Medical, Inc. (Minneapolis, USA) the bioartificial liver support system (BLSS) differentiates itself from other HFS by using porcine hepatocytes mixed with a collagen solution. This mixture is then infused into the extracapillary space of cellulose acetate hollow fibers while blood is perfused through the lumen of the fibers. Preliminary results of Phase I clinical trials with BLSS show a decrease in both ammonia and bilirubin but no significant improvements in neurological states. Phase II trials are currently being conducted [55].

Porous Matrix Devices

The bioreactor configuration of the other two BAL systems also in clinical trials (Table 2.2) differs from HFS bioreactors in so far as that porous matrices are used as scaffolds for hepatocyte attachment.

Porous Matrix Systems		
BAL system	RFB-BAL (University of Ferrara, Italy)[56,57]	AMC-BAL (University of Amsterdam, Netherlands)[58]
Bioreactor configuration	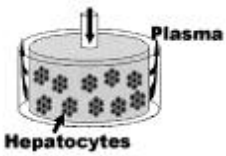	
Flow system	Radial flow, direct perfusion	Nonwoven hydrophilic polyester matrix for cell attachment, hollow fibers for oxygen supply and a spacer between the matrix, direct perfusion
Shape of cells	Aggregates	Small aggregates
Hepatocyte source	Porcine (200 g)	Porcine ($1.2x10^{10}$)
Immunological barrier	None	None
Perfusion (plasma separation rate, ml/min)	Plasma (22)	Plasma (40-50)
Reactor flow rate (ml/min)	200-300	150
Neurological improvement	Yes	Yes
Ammonia removal	33%	44%
Bilirubin removal	11%	31%

Table 2.2: *Characteristics and clinical results of porous matrix BAL systems (Adapted from [30]).*

In the radial flow bioreactor (RFB) developed at the University of Ferrara, Italy, plasma enters the centre of the module and passes through a porous matrix containing hepatocyte aggregates. A 33 % reduction of ammonia and 11 % for bilirubin compared to the initial levels were observed during treatment with the RFB-BAL [57].

The second example in this group is the Academic Medical Center (AMC) BAL developed at the University of Amsterdam, Netherlands [58]. In this device small porcine hepatocytes aggregates are attached to a matrix of nonwoven hydrophilic polyester interspersed with hollow fibers for oxygen supply. Plasma is directly perfused through the matrix. During trials the system successfully supported six out of seven patients to OLT and led to, neurological improvement, as well as 44 % reduction in ammonia and 31 % in bilirubin.

2.3.2.2 Systems in Preclinical and *in-vitro* Tests

The field of other major BAL devices in preclinical trials is divided into four HFSs (Table 2.3), one porous matrix and two encapsulation systems (Table 2.4), and two flat-plate systems (Table 2.5).

LIVERx2000

The first HFS, the LIVERx2000 system developed at the University of Minnesota and Algenix (St. Paul, USA) was approved for clinical trials but no results have been published yet [59]. It uses cellulose-diacetate hollow fibers into which a solution of porcine hepatocyte spheroids in collagen gel is injected. Upon contraction of the gel an oxygenated medium can be recirculated through the fiber lumen to nourish the hepatocytes while the exterior of the capillaries is perfused with whole blood.

LIVERaid

LIVERaid is a second BAL system available from Arbios Systems [43]. It utilizes a proprietary multi-compartment hollow fiber module with fiber-within-a-fiber geometry. The two compartments in the single-cartridge device are filled with porcine liver cells and chemical sorbents thereby providing whole liver functions and blood detoxification.

OXY-HFB

Developed at the Eberhard-Karls University, Germany, the oxygenating hollow fiber bioreactor (OXY-HFB) consists of a furled hollow fiber matt [60]. Porcine hepatocytes are seeded into the extracapillary space onto the surface of the fibers. Medium or plasma enters through the centre of the rolled matt and exits radially outwards and upwards. Oxygen is pumped through the fibers in opposite direction to the plasma flow [61].

LLS

The liver lobule-like structure module (LLS) is one of two BAL systems designed at Kyushu University, Japan [62]. It employes a close-spaced regular arrangement of blood-conducting hollow fiber membranes. Centripetal force is used to create high-density porcine hepatocyte organoids in the space surrounding the fibers.

PUF-HALSS

The second system from Kyushu University is a porous matrix design based on a multicapillary polyether rigid-type polyurethane foam module (PUF). Isocyanate and polyol are used as cell-culture substratum while a cylindrical block of PUF provides a sponge-like macroporous structure with a porosity of 98.8 % [64]. Pores are interconnected and animal hepatocyte spheroids form upon inoculation into the packed-bed module. Plasma flows directly through capillaries created by the pores allowing for good mass transfer to the cells.

UCLA-BAL

In the University of California Los Angeles (UCLA) BAL bioreactor porcine hepatocytes are microencapsulated within biocompatible semipermeable calcium alginate/polylysine sodium alginate composite membranes as shown in Fig. 2.14 [65]. The microcapsules are arranged in a packed-bed configuration and directly perfused with whole blood. Free cell-to-cell interactions are possible within capsules while the membrane provides immuno-isolation from blood components.

Hollow Fiber Systems				
BAL system	LIVERx2000 (Algenix) [59]	LIVERaid (Arbios) [43]	Oxy-HFB (Eberhard Karls University, Germany) [60,61]	LLS-HALSS (Kyushu University, Japan) [62]
Bioreactor configuration	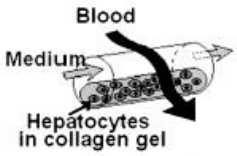	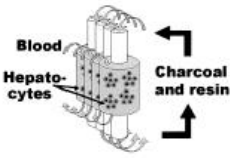	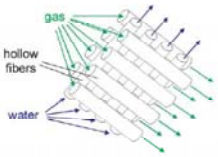	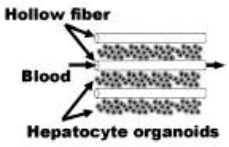
Flow system	Collagen gel encapsulated hepatocytes in cellulose diacetate-based fiber perfused with oxygenated medium, extrafiber space with blood	Multi-compartment hollow fiber within a fiber geometry combining hepatocytes with sorbent based toxin removal	Sheets of oxygenating and integral heat exchange fibers, hepatocytes seeded on fiber surface in extrafiber space perfused with plasma	Hollow fibers acting as blood capillaries with hepatocytes in extra fiber space
Shape of cells	Hepatocyte spheroid suspension in collagen gel	NA	Tissue-like	Organoid
Hepatocyte source	Porcine (60-70 g)	Porcine ($1.5x10^{10}$)	Porcine ($2.5x10^{9}$)	NA
Immunological barrier	Yes (100 kD)	NA	None	NA
Perfusion	Blood	Blood	Plasma	Blood

Table 2.3: *Hollow fiber BAL systems in in-vitro tests.*

AHS-BAL

An optimized version of this system was developed in the form of the alginate-entrapped hepatocyte spheroid (AHS) BAL at Dongguk University, South Korea [66]. Here hepatocytes are cultured in suspension to form spheroids prior to encapsulation, as hepatocyte spheroids were found to show higher liver-specific functions *in-vitro* than dispersed single hepatocytes.

Porous Matrix and Encapsulation Systems			
BAL system	PUF-HALSS (Kyushu University, Japan) [63,64]	UCLA-BAL (UCLA, USA) [65]	AHS-BAL (Dongguk University, South Korea) [66]
Bioreactor configuration	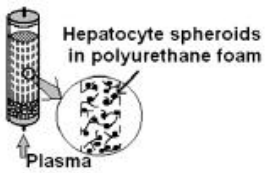	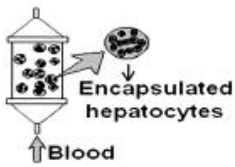	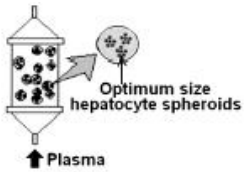
Flow system	Triangular arranged multicapillaries in polyurethane foam packed bed module with interconnecting pores	Microencapsulated hepatocytes within biocompatible semi permeable calcium alginate-polylysine-sodium alginate composite membrane in packed bed configuration	Ca-alginate-entrapped hepatocyte spheroids in packed bed configuration
Shape of cells	Spheroid	Microencapsulated	Microencapsulated spheroids
Hepatocyte source	Porcine (200 g)	Porcine	Porcine
Immunological barrier	None	Yes (NA)	NA
Perfusion	Plasma	Blood	Plasma

Table 2.4: *Porous matrix and encapsulation-based BAL systems in in-vitro tests.*

Flat Membrane Bioreactor Devices

The fourth family of devices, summarised in Table 2.5, is comprised of flat membrane bioreactor (FMB) systems.

FMB1-BAL

In the FMB-BAL system presented by Bartolo et al. [67] hepatocytes are cultured between two layers of collagen. The bottom and top of these layers are enclosed by membranes and structural support. A gas permeable membrane at the bottom allows for

oxygen supply from an integrated gas channel to the cells while a microporous membrane at the top separates the cells from medium flow. An additional permeable membrane is used as the top cover for the medium channel. Sustained albumin production and urea synthesis at a constant rate were shown over a perfusion period of 18 days [67].

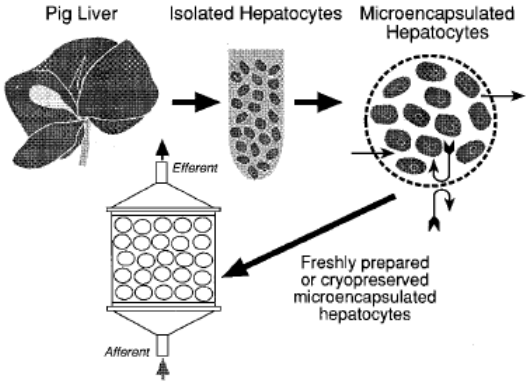

Figure 2.14: *Schematic of the UCLA-BAL process used for hepatocyte encapsulation (Adapted from [65]).*

FMB2-BAL

Shito et al. [68] at the Massachusetts General Hospital developed a further FMB-BAL. In their design a hepatocyte monolayer is seeded onto a glass slide pre-coated with collagen. The slide is placed in a support structure with a gas permeable polyurethane membrane covering the plasma channel. Hepatocytes are directly exposed to plasma flow which is oxygenated via the membrane separating plasma and a gas flow chamber above it. Efficacy of the BAL system for treatment of FHF was demonstrated in rats and resulted in increased animal survival rates [69]. Scale-up of both FMB systems to a clinically relevant surface area is achieved by stacking several individual modules connected in parallel.

2.3.3 Comparison of current BAL systems

A direct performance comparison of the systems presented above is very difficult. Different stages of system development and trial status, as well as variation and complexity of trial-specific parameters such as patient group only allow for a generalized

Flat-Plate Systems		
BAL system	FMB1-BAL (Leibniz Institute for Biotechnology and Artificial Organs, Germany)[67]	FMB2-BAL (Massachusetts General Hospital, USA) [68,69]
Bioreactor configuration	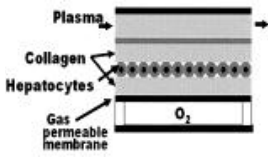	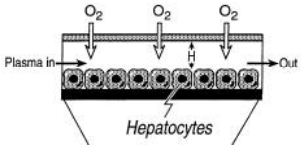
Flow system	Hepatocyte monolayer sandwiched between collagen layers separated from plasma and oxygen channels by membranes	Hepatocyte monolayer on collagen in direct contact to plasma flow oxygenated through membrane from separate channel
Shape of cells	Monolayer	Monolayer
Hepatocyte source	Porcine ($2x10^8$-$4x10^9$cells)	Porcine ($1.39x10^{6)}$
Immunological barrier	Yes (NA)	None
Perfusion	Plasma	Plasma

Table 2.5: *Flat-plate BAL systems in in-vitro tests.*

evaluation. Within the group of BAL devices in clinical trial the first generation HepatAssist system has the disadvantages of smaller relative cell numbers (5% of liver mass compared to 10% for other systems), short treatment time (6-8 h compared to 12-24 h) and mass transfer limited by diffusion through the fiber membrane (compared to direct hepatocyte perfusion with plasma in the RFB, LSS(MELS) and AMC BAL systems).

A further very important factor with major influence on BAL performance is oxygen supply. It is this issue that is addressed in this thesis. Systems with integral oxygenators like LSS(MELS) and AMC-BAL try to eliminate hypoxic space and oxygen gradients inside the bioreactor by use of separate fibers for oxygen transport. This trend towards

Hepatic function and treatment time	Culture method	Current status of application	
		Preclinical	**Clinical**
Long-term and enhanced functions	Liver-like structure		
	3D co-culture		LSS(MELS)
	2D co-culture		
↕	Collagen sandwich	FMB1, FMB2	
	Spheroids or organoids	LLS, AHS, PUF	AMC
	Microencapsulation	AHS	
	Porous matrix	PUF	RFB, AMC
	Extracellular matrix		BLSS, LIVERx2000
Short-term and poor functions	Microcarrier		HepatAssist

Table 2.6: *Application of cell culture techniques to BAL systems.*

integration of separate oxygen or nutrient supply channels to overcome mass transfer limitations is one of the most significant to be observed in the newer preclinical BAL systems. The second trend summarised in Table 2.6 is the use of improved cell culture techniques for prolonged and enhanced liver functions.

2.4 Engineering Challenges in BAL Design

Despite the obvious progress towards a functional BAL seen in the liver support systems presented above, a variety of critical engineering challenges still remain to be addressed. This section discusses three of the main challenges and introduces the proposed research into this context. Table 2.7 shows a summary of engineering constraints as identified by Chan et al. [27] for designing an artificial liver.

One of the first questions for extracorporeal devices is whether to use **Plasma or Whole Blood for Perfusion** of the liver cells. In today's systems this question is largely answered in favour of perfusion with plasma. The use of whole blood is in general simpler

because it does not require additional plasma separation and has an increased oxygen carrying capability compared to plasma. However, it is associated with thrombocytopenia, as well as hemolysis, and heparin anticoagulation medication has to be given, making it unsuitable for patients with invasive intracranial pressure monitoring [32].

Parameter	Desired Value/Property
Minimum functional capacity	1%-10% of liver
Maximum priming volume	1 l
Maximum distance between cells and nutrient supply	1 mm
Maximum size of cell aggregates	100 μm
Scaffold material	Biocompatible and supports hepatocyte differentiated function

Table 2.7: *Design constraints for BALs (Adapted from [27]).*

The second question is **Procurement of Liver Cells**. While primary human hepatocytes would be the natural choice for BAL devices, their availability is limited due to the general organ shortage and *in-vitro* replication of cells and their liver-specific functions have yet to be demonstrated [27]. So far a derivation of HepG2 cancer cells termed C3A are the only human cells reported to be used in an artificial liver device. However, by comparison, adult porcine hepatocytes are suggested to perform at higher levels of liver-specific functions than C3A cells and a risk of transmission of tumourigenic products to the patient exists [27]. Porcine hepatocytes on the other hand are readily available, but their use is being associated with potential hyperacute rejection, inter-species transmission of diseases and liver function mismatch. Investigations are underway as to whether the dedicated breeding of transgenic pigs could solve these problems [27], while stem cells could provide the major source for human liver cells in the future [70]. In the meantime, a recently proposed suicide gen terminated variety of HepG2 (HepG2/tk) shows the potential of higher levels of liver-specific functions and increased safety compared to previous tumorous cell lines [71].

The third and probably most interesting question from an engineering point of view is that of **Cell Culture Technique and Bioreactor Design**. Up until today, the most

widely used bioreactor design for BAL systems is that of hollow fiber configuration introduced in Section 2.3.1. In HFS however, substrate transport limitations prevail due to relatively large fiber diameters and the fiber wall membrane barrier [27]. While the introduction of separate fibers for oxygen and nutrient supply helps to ease this problem, it also significantly increases the complexity of running such a bioreactor [72]. For systems with alternative topology like the flat-plate bioreactor, additional membranes and channels for oxygen supply also increase fabrication complexity. In general, when designing an artificial bioreactor for liver cells the best standard to compare to is the natural environment, the liver. Here hepatocytes exhibit distinctive epithelia polarity, meaning that their plasma membrane is divided into domains with differing functions according to the surrounding cells. Furthermore, they form cell-to-cell communication structures like bile canaliculi, a tight junction and a gap junction, and show highly efficient regeneration and differentiated functions [30].

The main factor influencing the latter is the location of the hepatocytes within the liver structure. Maintenance of this functional heterogeneity depends on various factors, including gradients of hormones, substrates, oxygen and extracellular matrix composition; the relative importance of these individual factors is currently unknown [27].

The high oxygen uptake rate of hepatocytes, combined with its relatively low solubility in aqueous media deprived of oxygen carriers (such as plasma), is considered to be the most constraining parameter in the design of BAL devices [27]. Studies by Allen and co-workers [73,74] on the influence of oxygen tension on hepatocyte function indicate a functional zonation depending on the oxygen gradient through a bioreactor. Figure 2.15 shows a sketch of the hepatic zonation as found along the liver sinusoid. The metabolic activity of hepatocytes creates oxygen and hormone gradients, which lead to regionally dominating metabolic or detoxification functions [73]. The results of Allen et al. suggest that by modifying environmental conditions such as oxygen gradient, hepatocyte metabolism can be modulated towards *in-vivo* behavior. As can be seen in Fig. 2.16, one way to achieve this form of spatial control could be to compartmentalise the bioreactor into separate modules [27]. Another possibility could be to use micropatterning and microfabrication for selective placement of cells in the

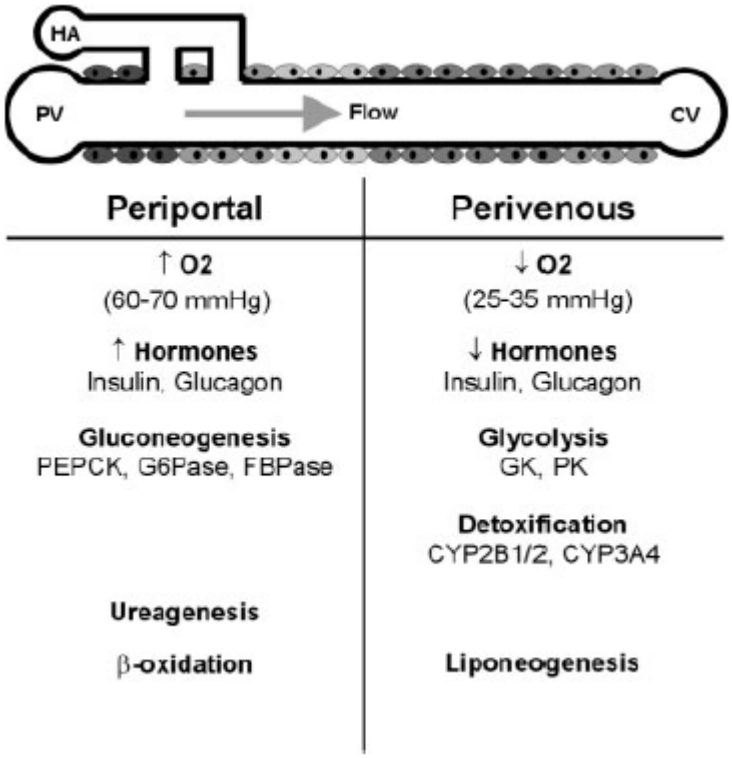

Figure 2.15: *Characteristics of hepatic zonation. Liver functions are categorized depending on cell location into a periportal and a perivenous zone. HA: hepatic artery, PV: portal vein, CV: central vein (Adapted from [73]).*

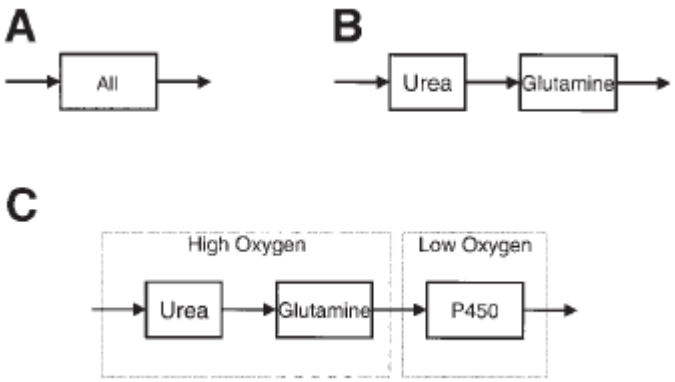

Figure 2.16: *Potential bioreactor designs: (A) single unit, all functions; (B) two subunits for ammonia conversion to urea and glutamine; (C) three subunits with two under high oxygen tension to clear ammonia and a third under low oxygen tension for P450 detoxification (Adapted from* [27]).

device [75,76].

Recent experiments on the stress response of hepatocytes in relation to oxygen concentration have further indicated that cells cultured at perivenous concentrations are more susceptible to anoxia-induced damage than their periportal counterparts [77]. These results, and the everlasting desire to deepen the general understanding of intercellular signaling, have lead to a continuing interest in the development of oxygen transport improvements [78] and high-throughput, physiologically relevant cell-culture and analysis devices [79-81].

2.4.1 Concept of Geometry-Based Oxygen Control

As discussed in the introduction presented in this chapter, BAL devices with cell-culture bioreactors constitute one of the most promising means of treatment for liver diseases. With increasing knowledge of liver functions and their related micro-anatomical phenomena, the importance of being able to recreate these *in-vitro* becomes ever more significant. Although flat-plate bioreactors can be constrained by species transport limitations and require active measures to counteract species depletion, the same physics underlaying these limitations can be used in conjunction with microfabrication and microfluidics technology, to render them into an ideal platform for simplified control of species concentration, such as dissolved oxygen. In addition, and as shown in the following Chapter 3, this particular device category allows reactors to be scaled-up in a biomimetic fashion similar to the liver lobule, where sinusoids are radially arranged around a central blood vessel.

The goal of this thesis is thus to demonstrate passive oxygen control based on bioreactor geometry and integrated oxygen sensing. To achieve this, a “hybrid” bioreactor, based on a tapering design for oxygen control but retaining the previously mentioned fabrication, integration and cell-culture advantages of the flat-plate design, is designed and developed. To visualize the principle used for oxygen control, a schematic of the interconnection between bioreactor geometry and oxygen concentration profile is shown in Fig. 2.17. A comprehensive mathematical derivation of the analytical model is presented in the following Chapter 3 - *Theoretical Background*. In brief, a specific

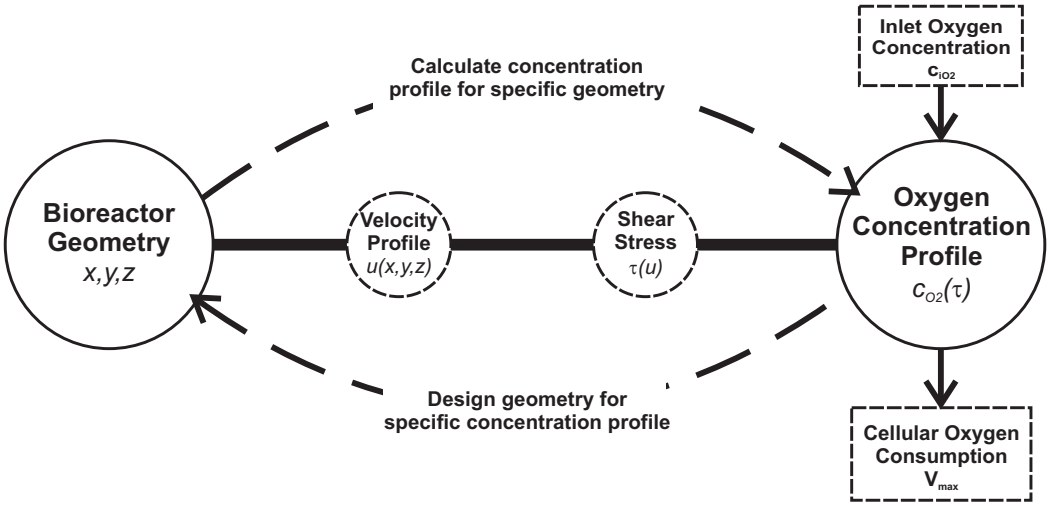

Figure 2.17: *Schematic of the oxygen control principle: Bioreactor geometry is linked to the oxygen concentration profile via the velocity profile and shear stress.*

geometry produces a particular velocity profile based on the laminar flow conditions. This profile is linked to the shear stress through the resulting velocity gradient at the bioreactor wall, which, in turn, influences the oxygen concentration profile via the conservation equation.

For example, a properly designed gradual tapering of the bioreactor height along its length leads to a increasing velocity gradient and shear stress profile, which then helps to maintain a close-to-constant longitudinal oxygen concentration to cells cultured within the device. The existence of this connection allows for both, the calculation of a concentration profile based on the available geometry, as well as the derivation of a geometry based on a desired oxygen concentration profile. The latter case is of great interest for cell-culture bioreactors and BAL devices in particular as it enables one to design constant or custom oxygen concentration gradient bioreactors simply by adjusting the geometry.

Besides the introduction and numerical evaluation of this theory, this thesis also strives to lay the groundwork for a future experimental verification of devices based on this model and their integration for use in a prototype BAL. To facilitate this several significant points have to be addressed, such as device fabrication and interfacing, integration of an oxygen sensor, sensor calibration for use with biological media, cell procurement, seeding and culture, oxygen measurement in culture and comparison to

analytical model, integration of a bile drainage system and device scale-up to a volume relevant to clinical trial. All of these points are introduced in the following chapters of this thesis, with four of them covered comprehensively, paving the way for a future application of devices based on the model.

2.5 SUMMARY

As discussed in this chapter, failure of basic liver function in humans is a serious condition, with a high mortality if left untreated. Major metabolic processes occur in the liver alone and can not be compensated by other organs. Despite the almost mystical self-healing abilities exhibited by the liver, orthopic transplantation remains the most successful treatment method to date. With increasing knowledge of liver macro- and micro-anatomy however, novel medical approaches and devices become feasible. One such promising approach is the use of BALs to bridge a patient to transplantation or support a damaged liver during self-repair. First devices have been shown to increase patient survival in clinical tests, but remain expensive and complicated to run. On the other hand, constant progress in micro fabrication has enabled general biomedical devices to closer and closer resemble size scales observed naturally in micro-anatomy. Several microfluidic liver cell-culture and BAL devices based on this new technology have been proposed. Most, if not all of them, have to rely on special setups to overcome oxygen transport limitations, which lead to increased device complexity and potential failure points.

To avoid the need for separate oxygen supply channels the use of custom-shaped microchannels for the generation of arbitrary oxygen gradients in a bioreactor is proposed in this thesis. In the next chapter analysis of a theoretical model for laminar flow and computational fluid dynamic simulations are used to show that, by modifying wall shear stress in a microchannel, custom concentration gradients of a solute transported by a fluid in the channel can be induced. When applied to the oxygen supply for cells growing on the channel boundary, this could simplify bioreactor construction by overcoming the problem of too low oxygen tension, as found in conventional parallel-plate reactors. Furthermore, if this bioreactor would be employed in an bioartificial liver device it could

provide the zonation described above simply by tailoring the shape of the channel to the desired concentration gradient.

While the applicability of this effect to general cell culture devices and BALs is obvious, it is not limited solely to this task. Selected examples of other applications that could profit from controlled concentrations in microfluidic systems are fluid-based biomedical sensors [82] and passive micromixers [83]. The former are usually located on one of the channel walls and of finite dimension. A geometrically-induced constant concentration of a dissolved analyte over the length of the sensor could potentially increase measurement precision. For the latter induced gradients could help to overcome the laminar flow separation seen in microfluidic channels and thereby facilitate the mixing of different flows.

By medicine life may be prolonged,
yet death will seize the doctor too.

William Shakespeare
1564-1616, English Poet and Playwright

CHAPTER 3

Theoretical Background

This chapter covers the theoretical background of the gradient-generating effect investigated in the proposed research. First, key properties and the fundamental equations used to describe fluid flow at the micro-scale are introduced. Then these equations are used, in combination with Prof. Tim David's theory on platelet transport [8], to derive an analytical model for shear stress dependent species transport. When solved for a desired oxygen concentration this model returns the channel geometry required to produce the corresponding shear stress function. To demonstrate applicability to BAL and cell-culture oxygen supply the model is solved to yield a channel geometry that generates a constant concentration of oxygen at the bottom surface along the overall reactor length. Results obtained with the analytical model are further compared to computational fluid dynamic simulations for a 2D and 3D model geometry.

3.1 KEY PROPERTIES OF MICROFLUIDICS

To simplify the theoretical analysis, only Newtonian fluids are considered. Water is an example of a fluid considered Newtonian under most circumstances; its stress / rate of strain curve is linear and passes through the origin. The constant of proportionality is known as the viscosity. In common terms, this means the fluid continues to flow, regardless of the forces acting on it. For example, water is Newtonian, because it continues to exemplify fluid properties no matter how fast it is stirred or mixed. In

contrast, in a non-Newtonian fluid stirring can leave behind a “hole” that gradually fills up over time or causes the fluid to become thinner, the drop in viscosity causing it to flow more. Blood is an example of non-Newtonian fluid. It is a highly specialized circulating tissue consisting of several types of cells suspended in a fluid medium known as plasma. If the cells are removed, the remaining plasma is mainly composed of water, proteins and inorganic electrolytes and behaves more like a Newtonian fluid. Whilst the BAL devices proposed here could potentially be used with either whole blood or separated plasma, the analysis and design are carried out assuming a Newtonian fluid.

3.1.1 Shear Stress

A viscous fluid moving along a solid boundary, like a channel wall, will incur a shear stress on that boundary. The no-slip condition dictates that the speed of the fluid at the boundary (relative to the boundary) is zero. At some height from the boundary the flow speed must equal that of the bulk fluid. The region between these two points is named the boundary layer. Shear stress is imparted onto the boundary as a result of this loss of velocity. Figure 3.1 shows a schematic of the tangential shear force applied to a certain boundary area. In general, the relationship for the wall shear stress is given by

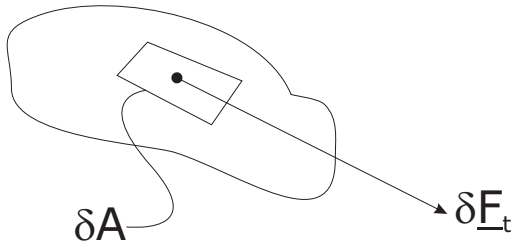

Figure 3.1: *Tangential force on an area.*

$$\tau_w = \lim_{\delta A \to 0} \frac{\delta F_t}{\delta A}. \tag{3.1}$$

For a Newtonian fluid in a two-dimensional microchannel, as displayed in Fig. 3.2, Newton’s law of viscosity can be used to mathematically represent the shear stress by

$$\tau = -\mu \cdot \frac{\partial}{\partial y}\vec{u}\,, \tag{3.2}$$

where τ is the shear stress, μ the fluid viscosity, u the fluid velocity in x-direction and y the position across the channel.

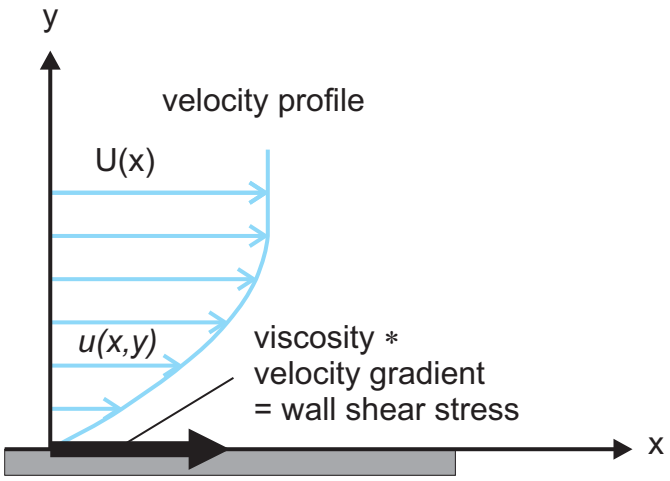

Figure 3.2: *Schematic indicating the wall shear stress (tangential) caused by a liquid moving past a wall.*

3.1.2 VISCOSITY

Serving as a mechanism to transfer kinetic into thermal energy analogous to friction of solid bodies, the viscosity of a fluid μ can be defined as a measure of its resistance to flow, as already described in Equation (3.2) for a simple channel geometry. In general terms the viscosity is defined as

$$[\text{shear stress}] = \mu\,[\text{strain rate}] \tag{3.3}$$

For non-compressible fluids in general, the shear stress is proportional to the rate of change of the shear strain S_{xy}, with components of tensor S_{xy} given by

$$S_{xy} = \mu \cdot \left(\frac{\partial u_x}{\partial y} + \frac{\partial u_y}{\partial x}\right) \tag{3.4}$$

and $u_{x,y}$ components of the velocity vector. The dynamic or shear viscosity parameter μ is related to kinematic viscosity ν by

$$\nu = \frac{\mu}{\rho}, \tag{3.5}$$

where ρ is the density. By definition, the viscosity of a Newtonian fluid depends only on temperature and pressure[1], but not on the forces acting upon it.

3.1.3 The Basic Equations of Fluid Dynamics

To describe fluid flow in a non-deformable control volume Ω, bounded by surface $\partial\Omega$ with n the unit normal outward, the following equations for *Conservation of Mass*, *Momentum* and *Energy* can be formulated using principles of mechanics and thermodynamics [85],

$$\frac{\partial \rho}{\partial t} + \nabla \cdot (\rho \vec{u}) = 0 \tag{3.6a}$$

$$\frac{\partial}{\partial t}(\rho \vec{u}) + \nabla \cdot [\rho \vec{u}\vec{u} - \sigma] = \vec{f} \tag{3.6b}$$

$$\frac{\partial E}{\partial t} + \nabla \cdot [E \cdot \vec{u} - \sigma \vec{u} + \vec{q}] = \vec{f} \cdot \vec{u}, \tag{3.6c}$$

where ρ is the density, $\vec{u}$ is the velocity field and E the total specific energy. In addition, all external forces on the volume are represented by f, $\vec{q}$ is the heat flux vector and σ the stress tensor. For Newtonian fluids the latter is composed of normal components and the viscous stress tensor τ,

$$\sigma = -pI + \tau \tag{3.7}$$

$$\tau = \mu \cdot [\nabla \vec{u} + (\nabla \vec{u})^T] + \zeta (\nabla \vec{u}) I, \tag{3.8}$$

with p being the pressure, I the unit tensor and μ, ζ the first and second viscosity coefficients, respectively. For incompressible fluids the second viscosity coefficient ζ disappears as no changes in volume can occur, leading to Equation (3.4).

1.and on the chemical composition of the fluid if the fluid is not a pure substance.

Since we are interested in the transport (diffusion, convection) of another species (e.g. oxygen) dissolved in a fluid, a mathematical description of this process is required. This description is found in form of the conservation of chemical species equation, which can be written in general vector form as

$$\frac{\partial c}{\partial t} + \nabla \bullet (\vec{u} \cdot c + V_D) = S\,, \tag{3.9}$$

where V_D is the diffusion velocity and S a source term for the species. By applying Fick's Law of Diffusion,

$$V_D = -D \cdot \nabla c\,, \tag{3.10}$$

it follows that

$$\nabla \bullet (V_D) = \nabla \bullet (-D \cdot \nabla c) = -D \cdot \nabla^2 c\,, \tag{3.11}$$

with D a constant diffusion coefficient. Furthermore, noting that $\nabla \bullet \vec{u} = 0$ for an incompressible constant density fluid (Equation (3.6a)),

$$\nabla \bullet (\vec{u} \cdot c) = \vec{u} \bullet \nabla c + c \cdot \nabla \bullet \vec{u} = \vec{u} \bullet \nabla c\,. \tag{3.12}$$

Hence Equation (3.9) can be re-written as

$$\frac{\partial c}{\partial t} + \vec{u} \bullet \nabla c = D \cdot \nabla^2 c + S\,. \tag{3.13}$$

Applying the law of conservation of species to a small Cartesian volume element gives [86]

$$\frac{\partial c}{\partial t} + u_x \cdot \frac{\partial c}{\partial x} + u_y \cdot \frac{\partial c}{\partial y} + u_z \cdot \frac{\partial c}{\partial z} = D \cdot \left(\frac{\partial^2 c}{\partial x^2} + \frac{\partial^2 c}{\partial y^2} + \frac{\partial^2 c}{\partial z^2} \right) + S\,, \tag{3.14}$$

where c is the concentration, u_i the velocities in x,y,z-direction, D the diffusion coefficient and S a term for production or consumption of the species in the volume.

By use of the continuum Equation (3.6a) in combination with Equations (3.7, 3.8),

the momentum Equation (3.6b) can be rearranged to give

$$\rho\left[\frac{\partial}{\partial t}\vec{u} + \vec{u} \bullet \nabla\vec{u}\right] = -\nabla p + \nabla\tau + \vec{f}. \tag{3.15}$$

To complement the laws of conservation, the equation of state for ideal gases,

$$p = \rho RT, \tag{3.16}$$

where $R = C_p - C_v$ as the difference of specific heats, can be used to rewrite the energy Equation (3.6c) to

$$\rho C_v \cdot \frac{DT}{Dt} = -p\nabla\vec{u} + \nabla \cdot [k\nabla T] + \tau\nabla\vec{u}, \tag{3.17}$$

with $D/(Dt) = \partial/(\partial t) + \vec{u} \cdot \nabla$. Combined the system of Equations (3.6a), (3.15), (3.16) and (3.17) is known as the *Navier-Stokes equations*.

3.1.3.1 Simplification for Incompressible Flow

In case of an incompressible fluid $D\rho/(Dt) = 0$ and the equations for Conservation of Mass (3.6a) and Momentum (3.6b) become

$$\nabla \bullet \vec{u} = 0. \tag{3.18}$$

$$\rho\left[\frac{\partial}{\partial t}\vec{u} + \vec{u} \cdot \nabla\vec{u}\right] = -\nabla p + \mu \cdot \nabla^2\vec{u} + \vec{f} \tag{3.19}$$

or for Cartesian coordinates

$$\frac{\partial u_x}{\partial x} + \frac{\partial u_y}{\partial y} + \frac{\partial u_z}{\partial z} = 0 \tag{3.20}$$

and

$$\rho\left(\frac{\partial u_x}{\partial t} + v_x\frac{\partial u_x}{\partial x} + v_y\frac{\partial u_x}{\partial y} + v_z\frac{\partial u_x}{\partial z}\right) = \mu\left[\frac{\partial^2 u_x}{\partial x^2} + \frac{\partial^2 u_x}{\partial y^2} + \frac{\partial^2 u_x}{\partial z^2}\right] - \frac{\partial p}{\partial x} + \rho g_x,$$

$$\rho\left(\frac{\partial u_y}{\partial t}+v_x\frac{\partial u_y}{\partial x}+v_y\frac{\partial u_y}{\partial y}+v_z\frac{\partial u_y}{\partial z}\right)=\mu\left[\frac{\partial^2 u_y}{\partial x^2}+\frac{\partial^2 u_y}{\partial y^2}+\frac{\partial^2 u_y}{\partial z^2}\right]-\frac{\partial p}{\partial y}+\rho g_y,$$

$$\rho\left(\frac{\partial u_z}{\partial t}+v_x\frac{\partial u_z}{\partial x}+v_y\frac{\partial u_z}{\partial y}+v_z\frac{\partial u_z}{\partial z}\right)=\mu\left[\frac{\partial^2 u_z}{\partial x^2}+\frac{\partial^2 u_z}{\partial y^2}+\frac{\partial^2 u_z}{\partial z^2}\right]-\frac{\partial p}{\partial z}+\rho g_z,$$

where gravity has been accounted for as a body force, and the values of g_x, g_y, g_z will depend on the orientation of gravity with respect to the chosen set of coordinates.

3.2 Derivation of Constant Oxygen Concentration

The goal of this derivation is to provide a constant oxygen concentration along the channel boundary. By keeping the concentration constant, areas of low oxygen tension along the channel length can be avoided, which would increase hepatocyte survival and function. Furthermore, this would eliminate the need for separate oxygen supply channels simplifying device fabrication.

To derive the concentration gradient a channel with parallel-plate configuration (as shown in Fig. 3.3) is considered. Assuming flow in the x-direction, no bulk flow reaction

Figure 3.3: *Model of parallel-plate channel.*

($S \equiv 0$) and unlimited width in z-direction, the species transport in the channel can be described by the two-dimensional steady-state convection and diffusion Equation (3.13) [87]

$$\tilde{u}\cdot\frac{\partial \tilde{c}_i}{\partial \tilde{x}}+\tilde{v}\cdot\frac{\partial \tilde{c}_i}{\partial \tilde{y}}=D_i\cdot\left[\frac{\partial^2 \tilde{c}_i}{\partial \tilde{y}^2}+\frac{\partial^2 \tilde{c}_i}{\partial \tilde{x}^2}\right],\qquad i=1,\ldots,N, \tag{3.21}$$

where $\tilde{c}_i$ is the concentration of species i, $\tilde{u},\tilde{v}$ the velocities in x,y-directions respectively and D_i the diffusion rate coefficient for species i.

Only diffusion in y-direction is considered, while dispersion in the flow direction (x-direction) is assumed to be negligible in comparison to the convective contribution [87,88]. To non-dimensionalize the conservation equation the following characteristic scales for mass fraction $c_{i,\infty}$ (initial concentration), length L (e.g. depth of channel) and velocity U_∞ (average velocity) are chosen

$$x = \frac{\tilde{x}}{L}; y = \frac{\tilde{y}}{L}; u = \frac{\tilde{u}}{U_\infty}; u = \frac{\tilde{u}}{U_\infty}; v = \frac{\tilde{v}}{U_\infty}; c_i = \frac{\tilde{c}_i}{c_{i,\infty}}. \tag{3.22}$$

Equation (3.21) can then be rewritten (see Appendix A) as the non-dimensional 'reduced' mass conservation equation

$$u \cdot \frac{\partial c_i}{\partial x} + v \cdot \frac{\partial c_i}{\partial y} = \frac{1}{Pe} \cdot \frac{\partial^2 c_i}{\partial y^2}, \tag{3.23}$$

with the Peclet number, Pe, defined as the ratio of convection to diffusion according to

$$Pe = \frac{U_\infty \cdot L}{D_i}. \tag{3.24}$$

Using the similarity variable η as introduced by David et al. [8,87]

$$\eta = \frac{(Pe \cdot Re)^{1/3} \cdot \sqrt{\tau(x)}}{(9\int_{x_0}^{x} \sqrt{\tau(\gamma)} d\gamma)^{1/3}} \cdot y = \beta(x) \cdot y, \tag{3.25}$$

then, under the assumption of linear velocity profile, Equation (3.23) can be rewritten as a one-dimensional equation (see Appendix B)

$$\frac{\mathrm{d}^2 c}{\mathrm{d}\eta^2} + 3\eta^2 \cdot \frac{\mathrm{d}c}{\mathrm{d}\eta} = 0. \tag{3.26}$$

To solve this ordinary differential equation the boundary conditions have to be determined. A large distance from the surface, in the centre of the sinusoid, the species concentration is

$$\eta \to \infty; \;\; c(\eta) \to c_{\infty}, \tag{3.27}$$

where c_{∞} corresponds to the concentration c_0 in the bulk of the fluid.

Furthermore, at the surface (for $\eta = y = 0$) it can be said, that the reaction rate at the fluid-wall interface balances the rate of diffusion to the surface. For liver cells situated on the surface, the reaction rate or oxygen uptake can be modelled by Michaelis-Menten kinetics [73,74,88]:

$$\frac{D_i \cdot c_{\infty}}{L} \cdot \left.\frac{\partial c}{\partial y}\right|_{y=0} = \frac{D_i \cdot c_{\infty}}{L} \cdot \beta(x) \cdot \left.\frac{\partial c}{\partial \eta}\right|_{\eta=0} = \frac{c(x,0) \cdot \kappa \cdot V_{max}}{K_m + c(x,0)}, \tag{3.28}$$

where D is the diffusion constant, κ is the cell seeding density, V_{max} the cell-dependent maximum oxygen uptake rate, K_m the Michaelis-Menten constant and c the concentration.

It is shown in Appendix C that the solution to Equation (3.26) along with the boundary conditions given by Equations (3.27) and (3.28) is

$$c(\eta) = \frac{c(x,0)}{K_m + c(x,0)} \cdot \frac{Da}{\beta(x)} \cdot \int_0^{\eta} e^{-\gamma^3} d\gamma + c(x,0) \quad , \tag{3.29}$$

where Da is the non-dimensional Damkohler Number defined as

$$Da = \frac{\kappa \cdot V_{max} \cdot L}{D_i \cdot c_{\infty}}. \tag{3.30}$$

To obtain an expression for the concentration on the surface, Equation (3.29) is now solved for $\eta = 0$ (see Appendix D) and

$$c(x,0) = \frac{1}{2} \cdot [(1 - \Delta - K_m) + \sqrt{(\Delta + K_m - 1)^2 + 4 \cdot K_m}] \tag{3.31}$$

is obtained as surface concentration, where

$$\Delta = \frac{Da}{\beta(x)} \cdot \frac{\Gamma(1/3)}{3} \quad . \tag{3.32}$$

Since the goal of this calculation is to obtain a constant concentration of oxygen along the wall, the result for $c(x,0)$

$$c(x,0) = \frac{1}{2} \cdot \left[\left(1 - \frac{Da}{\beta(x)} \cdot \frac{\Gamma(1/3)}{3} - K_m \right) + \sqrt{\left(\frac{Da}{\beta(x)} \cdot \frac{\Gamma(1/3)}{3} + K_m - 1 \right)^2 + 4 \cdot K_m} \right] \tag{3.33}$$

needs to be constant for all x. This in turn requires that $\beta(x)$ remains constant.

Appendix E shows that this requirement is met if the wall shear stress increases linearly with x according to $\tau(x) = a \cdot x + \tau_0$, where a is a constant of proportionality and τ_0 the wall shear stress at $x = 0$. An example of a flow chamber with linear shear stress generated via the chamber shape was shown by Usami et al. [90]. In their work the stress gradient was used to test platelet adhesion, while the theory presented here allows for the derivation of any desired solute concentration. Equation (3.33) also allows the concentration gradient profile at the boundary to be determined for other shear stress gradients or, by numerical inversion, the required stress gradients to produce an arbitrary concentration profile.

3.3 Derivation of Required Channel Geometry

As found by the calculations above, diffusion of oxygen to cells on the channel wall can be kept constant by increasing shear stress in linear proportion to the channel length. In this section the required geometry to achieve this is derived using the previously found results.

3.3.1 Model for the Parallel-Sided Channel

The derivation starts with an infinitely long 2D channel and the Navier-Stokes equation of momentum conservation for stationary incompressible flow,

$$u\frac{\partial u}{\partial x}+v\frac{\partial u}{\partial y}=-\frac{\partial p}{\partial x}+\mu\cdot\left[\frac{\partial^2 u}{\partial x^2}+\frac{\partial^2 u}{\partial y^2}\right], \tag{3.34}$$

where p is the pressure, μ the kinematic viscosity and u, v the fluid velocities in x,y-directions.

Due to the assumption of an infinitely long channel and steady flow regime the velocity in x-direction u is considered to be slowly varying, and therefore

$$\frac{\partial u}{\partial x}\approx 0 \quad \text{and} \quad \frac{\partial^2 u}{\partial x^2}\approx 0\ . \tag{3.35}$$

Using this Equation (3.34) becomes

$$v\frac{\partial u}{\partial y}=-\frac{\partial p}{\partial x}+\mu\frac{\partial^2 u}{\partial y^2}. \tag{3.36}$$

In addition, from the conservation of mass Equation (3.20) $\partial u/\partial x+\partial v/\partial y=0$ it follows that the fluid velocity perpendicular to the channel is constant across the channel width. Since channel walls are parallel and perpendicular velocity at the boundary must be zero, v across the channel equals zero, leading to the equation for *Poiseuille flow*

$$\frac{\mathrm{d}p}{\mathrm{d}x}=\mu\frac{\partial^2 u}{\partial y^2}, \tag{3.37}$$

which represents the balance between the pressure gradient and the viscous nature of the flow.

After integrating Equation (3.37) twice,

$$u(y)=\frac{1}{2\mu}y^2\cdot\frac{\mathrm{d}p}{\mathrm{d}x}+yC_1+C_2, \tag{3.38}$$

and the boundary conditions can be used, as follows, to determine the integration constants. Since the velocity at the boundaries is equal to zero the constants C_1, C_2 can be determined to

$$u(0) = 0 \rightarrow C_2 = 0 \tag{3.39}$$

for $y = 0$ and

$$u(H) = 0 \rightarrow \frac{1}{2\mu} H^2 \frac{dp}{dx} + HC_1 = 0 \rightarrow C_1 = -\frac{1}{2\mu} H \frac{dp}{dx} \tag{3.40}$$

for $y = H$, where H is the channel height.

After inserting these results into equation (3.38) the function for velocity is found to be

$$u(y) = -\frac{1}{2\mu}\frac{dp}{dx}[H \cdot y - y^2] = -\frac{H^2}{2\mu}\frac{dp}{dx}\left[\frac{y}{H} - \frac{y^2}{H^2}\right], \tag{3.41}$$

which is the parabolic velocity distribution typical to *plane Poiseuille flow* (see Fig. 3.4).

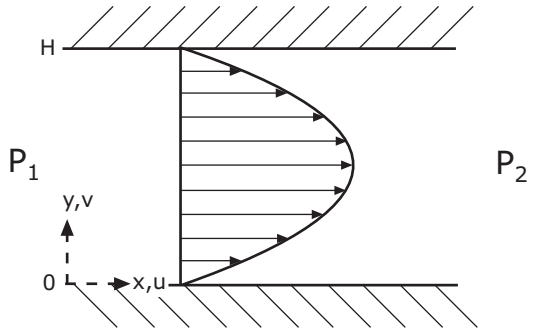

Figure 3.4: *Parabolic velocity distribution for Poiseuille flow in a channel of height H, arrows depicting velocity.*

3.3.2 Model for Tapering Channel

To be used in the equation for velocity (3.41), as determined before for a parallel-sided channel, it is assumed that $\frac{d}{dx}h(x) \ll 1$, i.e. the overall change in shape is small. Prior to substitution into the equation the variables need to be non-dimensionalized according to:

$$\tilde{u}(\tilde{y}) = -\frac{1}{2\mu}\frac{d}{d\tilde{x}}\tilde{p}[\tilde{h}(x)\tilde{y} - \tilde{y}^2], \tag{3.42}$$

with the dimensionless constants defined as follows

$$x = \frac{\tilde{x}}{h_0};\ y = \frac{\tilde{y}}{h_0};\ h(x) = \frac{\tilde{h}(x)}{h_0};\ h_0 = \tilde{h}(\tilde{x}_0);p = \frac{\tilde{p}}{\rho U^2_\infty}. \tag{3.43}$$

The above constants are inserted into Equation (3.42), which, after rearranging, results in

$$u(y) = -\frac{1}{2}\frac{dp}{dx}\cdot\frac{\rho U_\infty \cdot h_0}{\mu}[h(x)y - y^2] = -\frac{Re}{2}\frac{dp}{dx}\cdot[h(x)y - y^2], \tag{3.44}$$

where Re is the Reynolds number defined as the ratio of inertial and viscous effects in the system,

$$Re = \frac{\rho U_\infty \cdot h_0}{\mu}. \tag{3.45}$$

To determine the flow rate the velocity profile is integrated across the channel height leading to

$$Q = \int_0^{h(x)} u(y)dy = \int_0^{h(x)} -\frac{Re}{2}\frac{dp}{dx}\cdot[h(x)y - y^2]dy, \tag{3.46}$$

which results in

$$Q = -\frac{Re}{2}\frac{dp}{dx}\cdot\left[\frac{h(x)y^2}{2} - \frac{y^3}{3}\right]\Bigg|_0^{h(x)} = -\frac{Re}{12}\frac{dp}{dx}\cdot h^3(x). \tag{3.47}$$

Equation (3.47) can be rearranged to find

$$dp/dx = -12Q/(Re\cdot h^3(x)), \tag{3.48}$$

which then is inserted into equation (3.44) to give

$$u(y) = \frac{6Q}{h^3(x)}[h(x)y - y^2]. \tag{3.49}$$

The non-dimensionalised shear stress for laminar flow of an incompressible fluid at the wall of a parallel-plate channel is known to be

$$\tau_w = -\frac{1}{Re}\cdot\left.\frac{\mathrm{d}u}{\mathrm{d}y}\right|_{y=0} = -\frac{1}{Re}\cdot\left.\left(\frac{6Q}{h^2(x)} - \frac{12Q}{h^3(x)}\cdot y\right)\right|_{y=0} = -\frac{6Q}{Re\cdot h^2(x)}. \tag{3.50}$$

From calculations in Section 3.2 it was derived that, to provide a constant oxygen concentration along the wall, the shear stress on the same must increase proportionally with distance x along the sinusoid:

$$\tau_w = ax + \tau_0 = \frac{6Q}{Re\cdot h^2(x)}, \tag{3.51}$$

which corresponds to

$$h^2(x) = \frac{6Q}{Re(ax+\tau_0)} \propto \frac{1}{ax+\tau_0} \tag{3.52}$$

and

$$h(x) = \sqrt{\frac{6Q}{Re(ax+\tau_0)}} \propto \frac{1}{\sqrt{ax+\tau_0}} \tag{3.53}$$

respectively. This result points out, that to keep the concentration constant, the profile of the channel height has to vary proportional to $1/\sqrt{ax+\tau_0}$ along its length, ensuring a linearly increasing shear stress at the wall. Figure 3.5 shows a sketch of such a tapered channel geometry.

3.3.3 Summary of the Theoretical Analysis

The goal of the previous sections was to derive an analytical model of a channel geometry providing a constant oxygen concentration at the channel boundary. It was found that this could be achieved by varying the wall shear stress and an equation relating the required channel width-to-length was obtained as

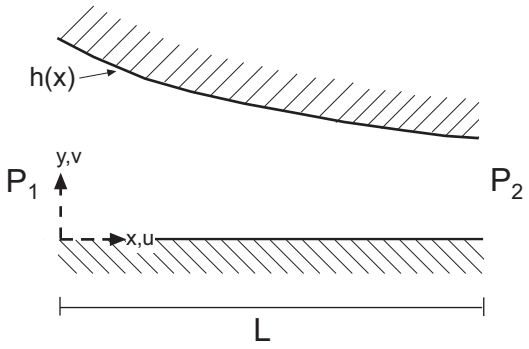

Figure 3.5: *Model of the 2D tapered channel.*

$$h(x) = \sqrt{\frac{6 \cdot Q}{Re \cdot (ax + \tau_0)}}, \tag{3.54}$$

where $h(x)$ is the distance from centre of channel to the wall, Q the flow rate through channel, Re the Reynolds number, a constant of proportionality for the increasing shear stress on the wall, τ_0 the wall shear stress at $x = 0$ and x the distance along channel length. Depending on cell type (oxygen uptake rate, cell seeding density) and channel dimensions (Reynolds number, flow rate) the individual parameters in equation (3.54) can be determined.

3.4 Analytical and Simulation Results

In this section the results obtained from the analytical model are verified using a commercially available finite-element (FEM) simulation software package. Drawing from the geometrical layout derived in Section 3.3.3, FEM simulations using the commercial software package COMSOL Multiphysics [91] were performed. Multiphysics allows the combination of various application modes in one model to create a computational fluid dynamics (CFD) simulation with coupled multiphysics. To visualize the geometrical effect on concentration gradients a 2D flat-plate channel was compared to a simple form of a tapered channel. The results shown here were obtained by coupling the incompressible Navier-Stokes fluid flow application mode with that of convective and diffusive mass transport. Figure 3.6 shows the equations and boundary conditions used in the modelling.

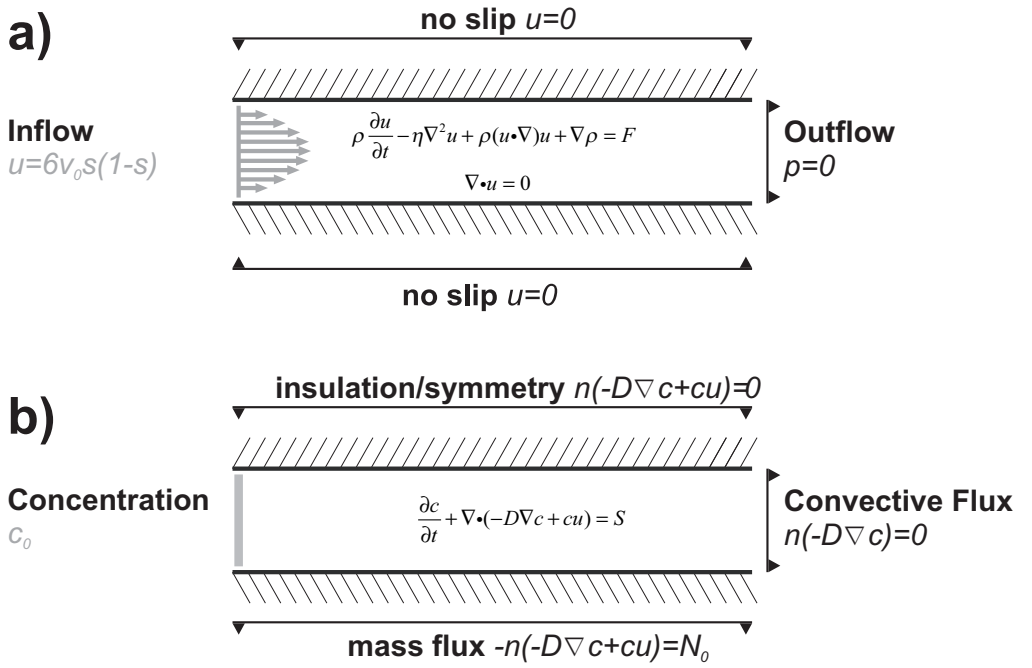

Figure 3.6: *Governing equations and boundary conditions in the finite-element model: (a) momentum balance with incompressible Navier-Stokes equation; (b) mass balance with convection and diffusion equation.*

In the momentum balance part, shown in Fig. 3.6(a), the governing equation is the incompressible Navier-Stokes equation. The upper and lower channel wall BCs are no-slip, meaning the velocity $u = 0$ at the boundaries. On the left side channel entrance a fully-developed parabolic flow profile is assumed, while the right side pressure is set to zero for outflow condition. For the tapered channel a constant velocity profile was set as the boundary conditions on the left side inlet.

Mass balance in Fig. 3.6(b) is governed by the convection and diffusion equation with the reaction part $S = 0$ in the channel domain. The concentration at the left side channel entrance is assumed to be constant c_0, while convective flux is the boundary conditions at the channel exit and insulation/symmetry at the upper channel boundary. This means that there is no oxygen transport over the upper boundary. Oxygen consumption of hepatocytes present on the lower channel boundary is modelled via negative mass flux according to Michaelis-Menten kinetics [88]. The flux term N_0 is defined as:

$$N_0 = -\frac{\kappa \cdot V_{max} \cdot c(x,0)}{K_m + c(x,0)}, \tag{3.55}$$

where κ is the cell seeding density, V_{max} the cell-dependent oxygen uptake rate, K_m the Michaelis-Menten constant and $c(x,0)$ the oxygen concentration at the lower boundary. During simulation negative concentrations can occur as a result of numerical noise, discontinuous concentrations, an incorrect reaction term or mesh resolution. Two avoid negative concentration the flux term on the boundary was modified to be

$$N_0 \cdot (c > 0). \tag{3.56}$$

Physical parameters used in the simulation are from experimental data for rat hepatocytes [88], with the hepatocyte seeding density $\kappa = 10^9 hepatocytes/m^2$, the oxygen uptake rate of the hepatocytes $V_{max} = 3.8 \cdot 10^{-16} mol/s/hepatocyte$, the diffusivity of oxygen in water/plasma $D_{O_2} = 2 \cdot 10^{-9} m^2/s$, and the Michaelis-Menten constant $K_m = 6.62 \cdot 10^{-3} mol/m^3$. Also, in the mass transport application mode the inlet concentration on the left boundary is set to $c_0 = 1.892 \cdot 10^{-1} mol/m^3 = 3.0272 mg/l$, as given in [88], a value which corresponds to oxygen in physiological salines such as plasma and is lower than the solubility in pure water at atmospheric pressure and room temperature (9.1 mg/l at 20ºC, see Appendix F). Density and viscosity of the fluid were modelled to be, as for water, $\rho = 1 \cdot 10^3 kg/m^3$ and $\mu = 1 \cdot 10^{-3} kg/(m \cdot s)$ respectively. To reduce calculation time, the channel length of 5.4 cm in the x-direction was scaled-down by a factor of 100 in the two-dimensional model.

3.4.1 Parallel vs. Tapered Channel in 2D

Steady-state simulation results [7] for a parallel-plate (A) and a tapered channel based on a *Bezier*-curve upper boundary (B) are shown in Fig. 3.7. The arrows in both plots illustrate the flow profile with the typical parabolic shape for laminar flow at a Reynolds Number of *Re* = 3 corresponding to a channel length of 75 mm and depth of 200 µm for the parallel-plate design and 200-150 µm for the tapered design. Analyte concentration is illustrated by color, with red denoting areas of high concentration and dark blue those with zero concentration. When comparing the results for the two geometries the effect of the

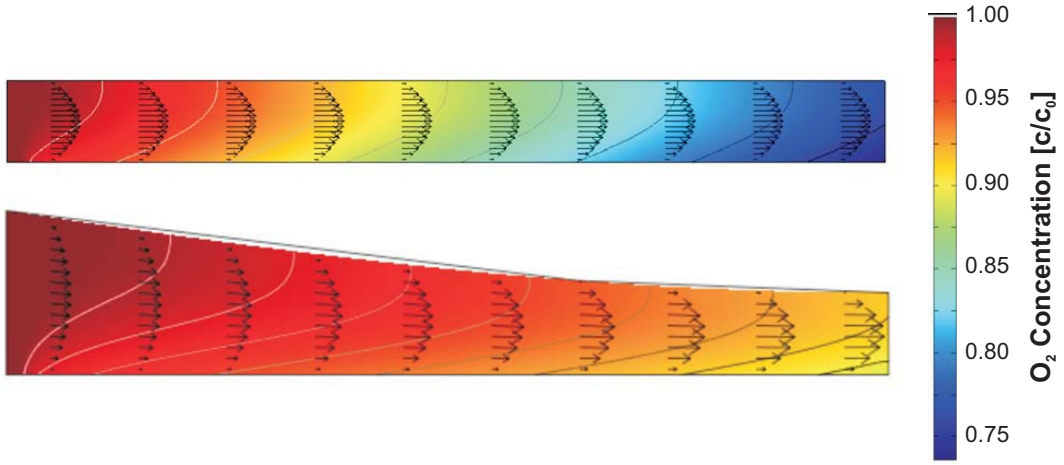

Figure 3.7: *Steady-state concentration gradients and flow profile for: (A) a parallel-plate; and (B) a tapered channel. Arrows denote the flow profile, colors the local concentration from red/high to blue/low (geometry not to scale).*

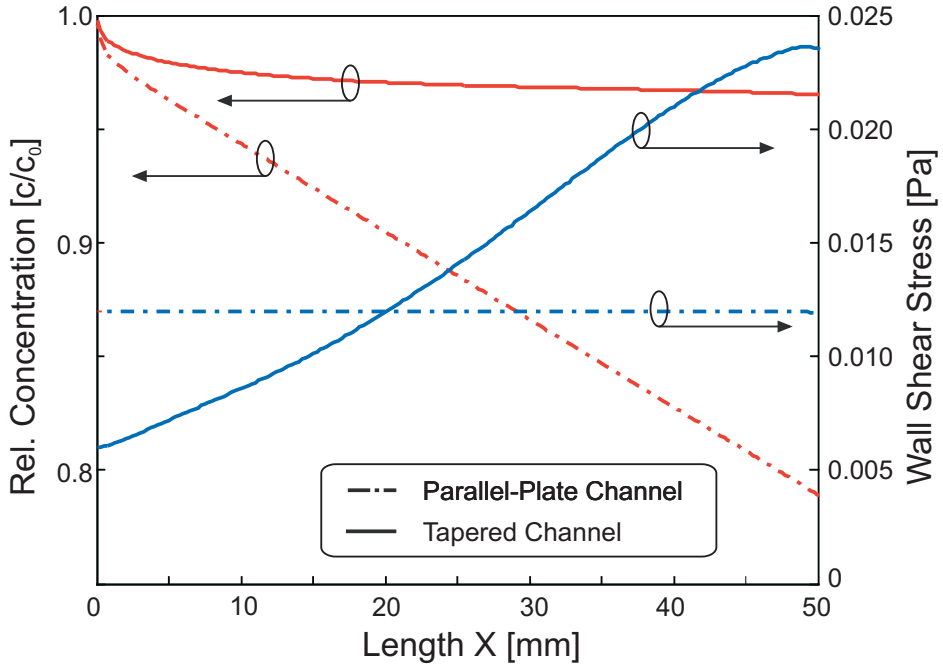

Figure 3.8: *Comparison of relative oxygen concentration (red) and wall shear stress (blue) for parallel-plate and tapered channel designs.*

tapered channel derived earlier can be observed. This becomes even more apparent when the concentrations on the lower boundaries of both channels are plotted together. In Fig. 3.8 the relative concentration and wall shear stress on the lower channel surface are

plotted versus channel length. For the parallel-plate channel (broken line) the wall shear stress (bottom graph) is constant over the length due to the constant height of the channel. However, the oxygen concentration (top graph) decreases around 25 % from entrance to channel exit. For the tapered channel with a non-optimized shape (full line) the wall shear stress increases almost linearly over the reactor length. While, as predicted by theory, the surface concentration remains almost constant, decreasing only around 2 % over the total length relative to the bulk concentration at the channel entrance. This modelling shows that, as predicted by the analysis, channel geometry-induced wall shear stress control allows the surface oxygen concentration to be controlled.

3.4.2 Analytical Model vs. Finite Element Simulation in 2D

To investigate the applicability of the model derived in Section 3.2, both analytical solution and finite element simulation were applied to the case of a parallel-plate channel geometry as given in Fig. 3.3. For the analytical model Mathematica [92] was used to encode the equations, while FEM was performed using Multiphysics as described above. Results were combined and plotted using Matlab [93]. The dimensions for the 2D model were given as channel height H = 140 µm, channel length (in x-axis) X = 75 mm with physical parameters again taken from [88]. In Fig. 3.9 the oxygen concentration on the lower boundary of the parallel-plate channel as obtained by both analytical (full line) and FEM model (broken line) is compared. Results are plotted for three different cases of Reynolds number: $Re = 0.07$ corresponds to an average fluid velocity of $U_{0.07} = 4.76 \cdot 10^{-6} m/s$, $Re = 0.7$ to $U_{0.7} = 4.76 \cdot 10^{-4} m/s$ and $Re = 7$ to $U_7 = 4.76 \cdot 10^{-2} m/s$.

It can be seen from Fig. 3.9 that the analytical model compares well with the FEM simulations for high Re conditions. However, for Reynolds numbers equal to and lower than 0.7 the discrepancies between the analytical solution and the FEM result increase and the analytical model can no longer be used to predict the oxygen concentration. This is mainly due to the boundary condition (Equation (3.27), $\eta \to \infty;\ c(\eta) \to c_\infty$) used in the derivation of the model. Hereby it is assumed that the concentration of the dissolved species e.g. oxygen, approaches the bulk or entrance concentration at a large distance

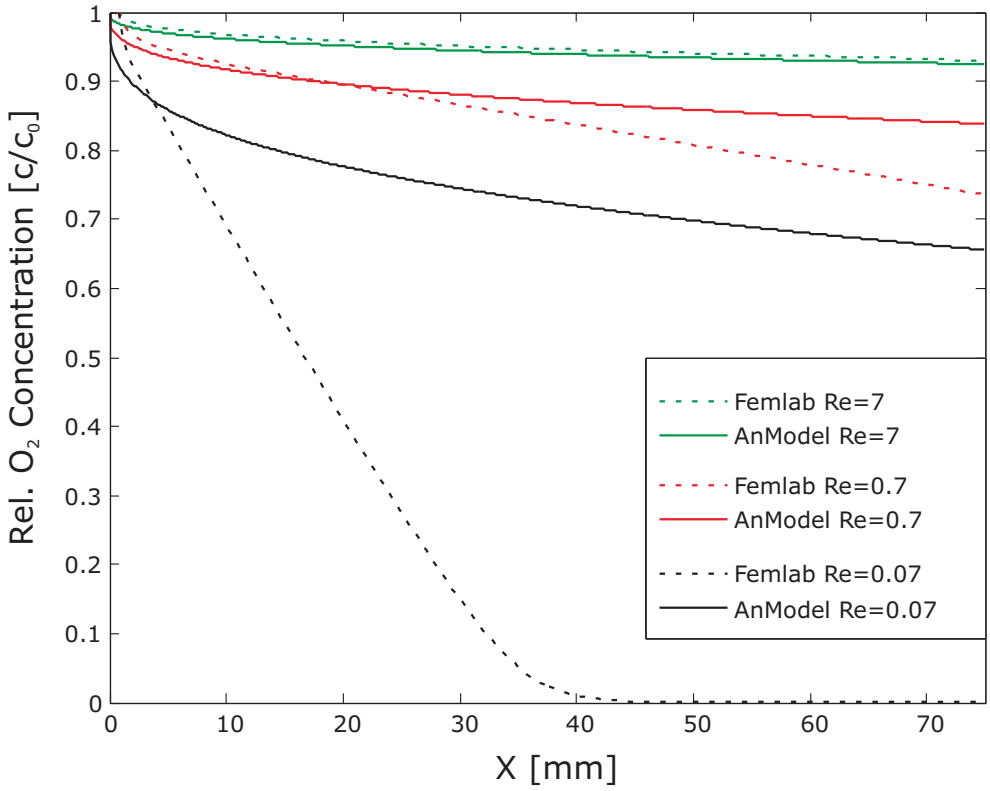

Figure 3.9: *Comparison of oxygen concentrations on the lower boundary of the parallel-plate channel obtained by analytical (full line) and finite element (dashed line) modelling for Reynolds numbers Re = 0.07, 0.7 and 7.*

from the lower boundary, for example the middle of the channel. When looking at the FEM result for the oxygen distribution in the parallel-plate channel at $Re = 0.07$ (Fig. 3.10) it becomes obvious that the boundary condition is no longer valid.

To determine a lower limit of the model in terms of flow conditions the behavior for further Reynolds numbers was investigated in more detail. Figure 3.11 compares oxygen concentration along the device length for different values of *Re* ranging from 70 to 1.4. As can be seen, within the dimensions of the particular geometry and for flow conditions of $1.4 < Re \leq 70$ the analytical model compares well with the results obtained via FEM simulation. In summary, numerical verification of the analytical model demonstrates its usefulness as a starting point for device design. However, for extreme values of *Re*, FEM simulations give better guidance and should be used in general to fine-tune the final device geometry.

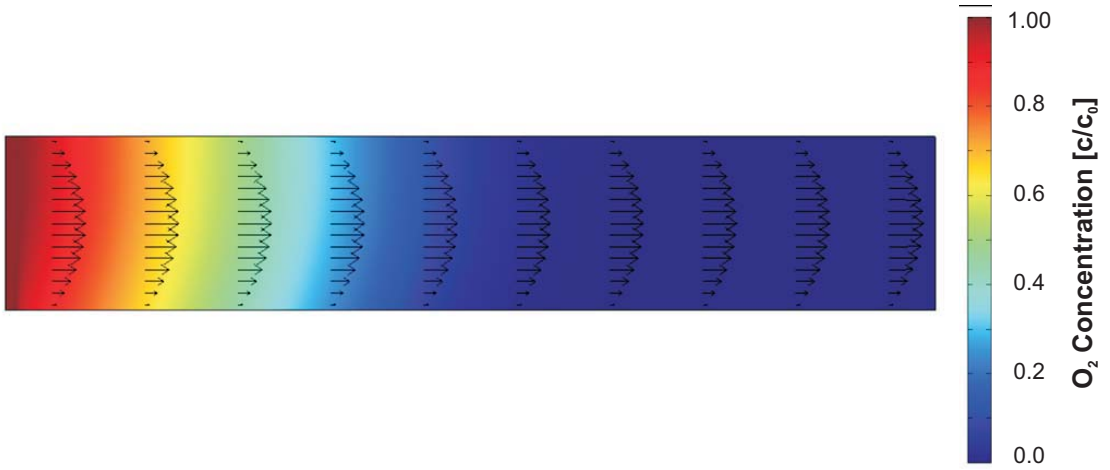

Figure 3.10: *FEM result for the oxygen distribution in the parallel-plate channel at Re = 0.07 (geometry not to scale).*

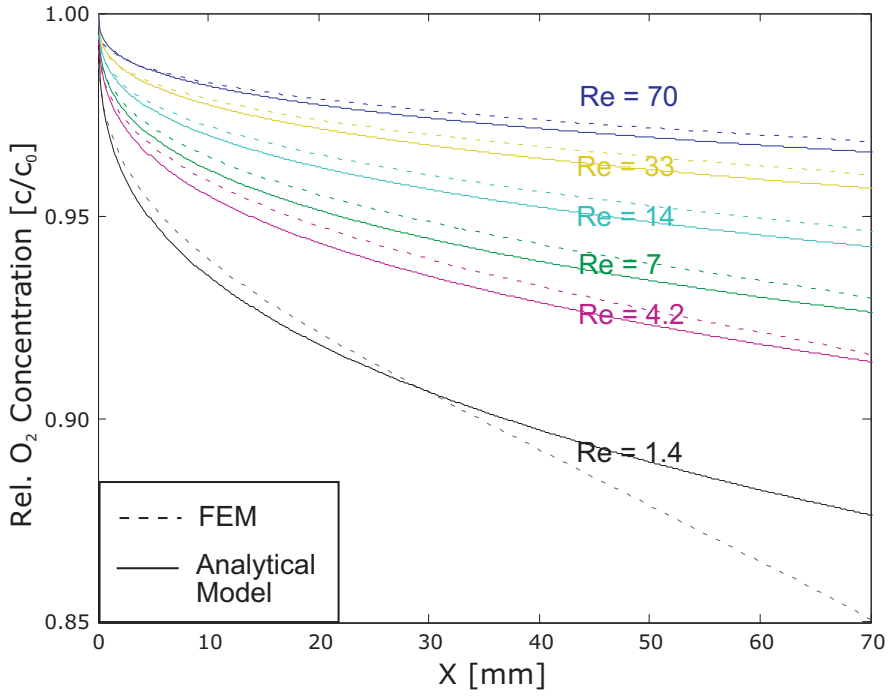

Figure 3.11: *Relative oxygen concentration on the lower boundary along channel length for Reynolds numbers from 1.4 to 70 in the parallel-plate reactor. Both analytical (full line) and simulation results (dashed line) are shown.*

3.4.3 Simulation Results for the Three-dimensional Bioreactor

Similar to the tapered depth model investigated above, the analytical derivation can be used to design a three-dimensional geometry with constant oxygen concentration [6]. Problems with the fabrication of the vertically tapered design, described in detail in the following Chapter 4, ultimately lead to the derivation of this laterally-tapered geometry[1]. Again, the wall shear stress was designed to increase linearly along the channel length. However, this time the linear increase was obtained by tapering the width of the channel rather than the depth. The function of channel width derived for this design corresponds to the height function for the two-dimensional case and is given by

$$y = 2 \cdot W_{entrance} \cdot \frac{L_{total}}{L_{total} - x}\,, \tag{3.57}$$

where y is the distance from the centre axis x, $2 \cdot W_{entrance}$ the initial width at the entrance for $x = 0$, L_{total} the total length of the reactor and x the position along the axis.

The initial geometry function was evaluated in MATLAB and exported as a geometry element into Multiphysics as an geometry element. This element was then used to create a two-dimensional footprint and the final three-dimensional geometry by extrusion of the footprint along the z axis. Using internal symmetries only half of the model has to be solved, which is shown in Fig. 3.12(a) for the oxygen concentration in the reactor and an inlet flow rate of 8 µl/min. Boundary conditions and governing equations used in the model were the tree-dimensional versions of those introduced in Fig. 3.6. Cells were simulated to cover the entire lower boundary up to the widest point depicted by a dotted line in the inset in Fig. 3.12(b).

Simulation results for the wall shear stress and oxygen concentration along the centre line of the lower boundary are plotted in (b) and (c) of Fig. 3.12, respectively. Inlet flow rate was used as parameter for the simulation and results are given for flow rates of 0.8, 4, 8 and 40 µl/min. As can be seen from the wall shear stress graph (Fig. 3.12(b)), the geometry leads to an almost linear increase in stress in the region were the cells are

1.Using planar microfabrication it is much simpler to create laterally-tapered structures than vertically-tapered ones.

modelled. For 40 µl/min, the highest flow rate shown, the wall shear stress value peaks at 0.7 dyn/cm^2, which is significantly lower than physiological values observed to influence hepatocyte function [94]. At the same time, relative oxygen concentration remains almost constant over the length of the reactor, dropping to about 90% at the outlet for a flow rate of 40 µl/min. This indicates that the lateral design is a valid substitute for the initial vertically tapered geometry, while allowing for significantly easier fabrication of devices based on this design.

3.5 SUMMARY

By combining the Navier-Stokes description of laminar flow with the law of the conservation of species a two-dimensional model for solute transport inside a microchannel has been derived. A non-dimensionalized version of this model was solved by applying it to a theoretical parallel-plate channel geometry seeded with liver cells and a general solution for the species concentration inside the channel was obtained. This general form indicates that the special solution for constant oxygen concentration along the channel boundary can be found by employing an initial geometry providing linearly increasing wall shear stress. The two-dimensional shape function of this required geometry was consecutively derived from the solution and found to be proportional to the inverse square root of the shear stress. For comparison a channel with the derived vertically tapering shape was successively implemented and simulated using FEM software to confirm the model predictions. The analytical model was found to follow the CFD simulation results for a large range of Reynolds numbers and fluid shear stresses. Further, fully three-dimensional simulations of a horizontally tapered reactor shape showed the same effect as observed for the initial geometry due to laminar flow being predominant inside the device. Following derivation and flow characterisation of the designed reactors, the next chapter will discuss the fabrication of fluidic devices based on the particular geometries described above.

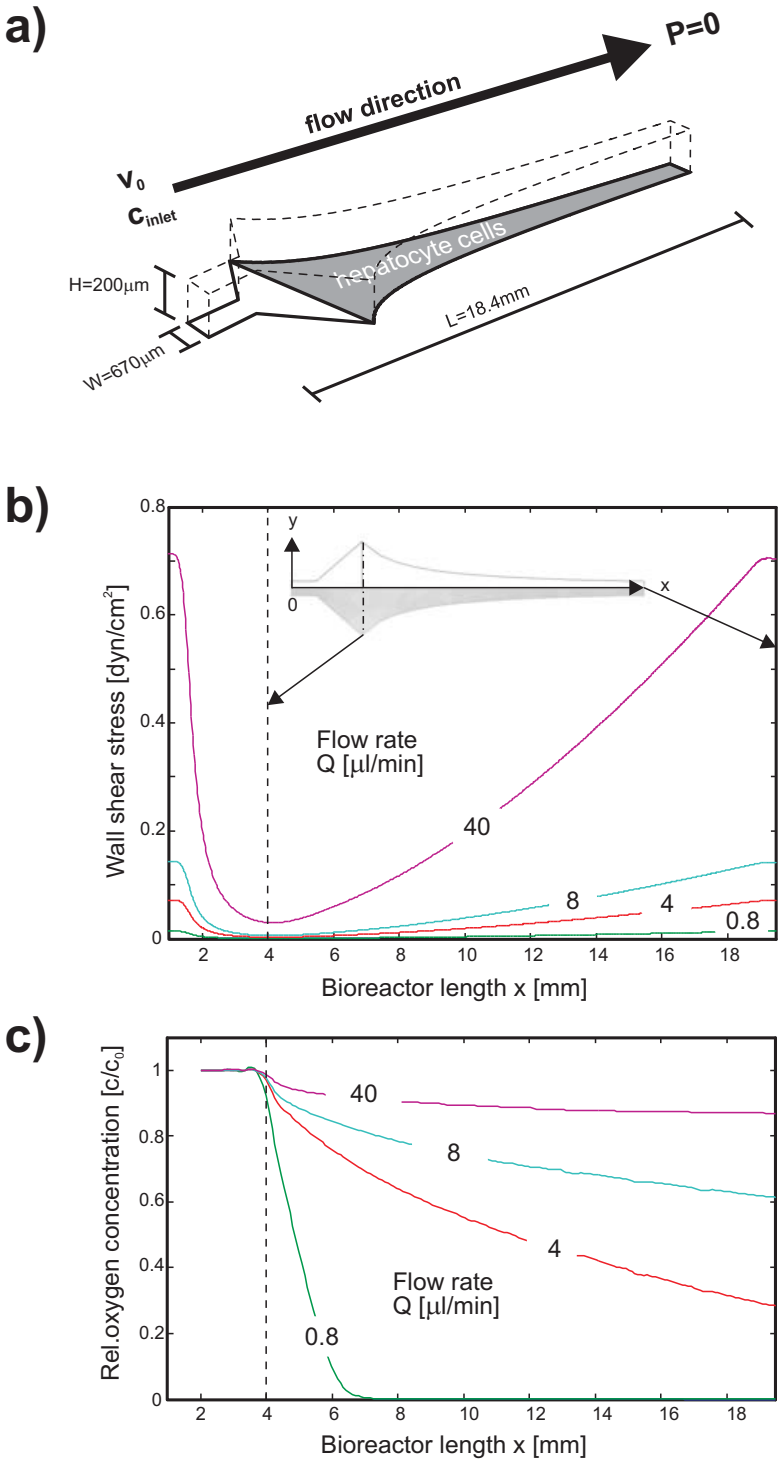

Figure 3.12: *Simulated flow and transport characteristics for a 3D model of the linearly increasing wall shear stress bioreactor. Dimensions of the bioreactor, cell-culture area and flow direction are shown in (a). The wall shear stress and relative* oxygen *concentration along the centre line on the lower boundary are plotted in (b) and (c), respectively.*

Any sufficiently advanced technology is indistinguishable from magic.

Arthur C. Clarke
1917-2008, British Author,
Inventor and Futurist

CHAPTER 4

Bioreactor Design and Fabrication

In this chapter two different bioreactor designs and their respective fabrication technologies are described. The first section introduces the general methods used and the main differences between the two designs. The following two sections each focus on one of the bioreactor designs. For each design the fabrication process and related issues are discussed in detail. The last section utilizes the chosen design to explore strategies for potential system scale-up.

4.1 DESIGN CONSIDERATIONS

To reproduce the size scales found in the liver, the natural environment for the hepatocyte cell, microfabrication technology has to be employed to fabricate artificial bioreactor devices used as a matrix for support of cellular function. Whilst originally developed for the production of microelectronic chips, microfabrication technologies have been adopted, with some application specific additions and modifications, to produce increasingly complex networks of micro-sized fluidic channels.

The combination of fabrication, functionalization and use of these channel networks, reservoirs and interfacing structures together with active parts, such as pumps and valves, and sensors is summarized in the field of microfluidics. While years of process development in the microelectronics industry have produced a pool of mature fabrication

technologies, their adaption to the fabrication of fluidic devices is not without problems. One of the most fundamental limitations in the standard microelectronics process chain of material deposition, lithographic pattern transfer and structural change by selective etching is its layer-based nature. To achieve the high precision necessary for electronics, materials are deposited in ultra smooth layers and structured laterally by use of photoresists. Structuring beyond the horizontal axes, with the exception of vertical vias, is practically non-existent in microelectronics fabrication. In microfluidics, and to a certain extend in micro-optics, vertically tapered structures on the other hand, can yield some very interesting properties and applications such as the shear-based transport phenomena discussed in the previous chapter.

A device incorporating a vertically tapered version of the bioreactor shape would have the advantage to allow for direct comparison of experimental results with the analytical model derived in the previous chapter. Due to this, vertical structuring was initially investigated for bioreactor fabrication. Grayscale lithography, a variation of standard binary lithography modified to allow for vertical structuring by a single exposure, was used to develop a device fabrication process. This initial design (Design A) is based on a change in reactor depth over reactor length to obtain a wall-shear stress change. Due to the complexity of this process and rough surface features of device molds produced with grayscale lithography a second design (Design B) was later developed. This Design B is based on a constant depth with tapering width and can be fabricated using standard single-layer binary lithography. However, direct comparison of experimental results obtained from Design B with the proposed two-dimensional analytical model is not possible due to the approximations used in the derivation of the model. In this case the results of the full three-dimensional fluid dynamics simulation have to be used for comparison and to account for boundary effects. The following discusses development of a fabrication process for both bioreactor designs and the potential of system scale-up towards a full bioartificial liver device using Design B.

4.2 Constant Width, Tapering Depth Bioreactor

The reactor shape of Design A is derived from the results provided by the analytical model. Cell seeding will be facilitated on the bottom surface of the channel and the taper of the channel depth is chosen to provide constant oxygen concentration on the bottom surface over the channel length. Figure 4.1 shows a 3D rendering of Design A as used in FEMLAB to simulate fluid flow and species transport. The target channel geometry for the prototype is 500 µm wide, tapering from 200 µm at the input end to 150 µm at the output end.

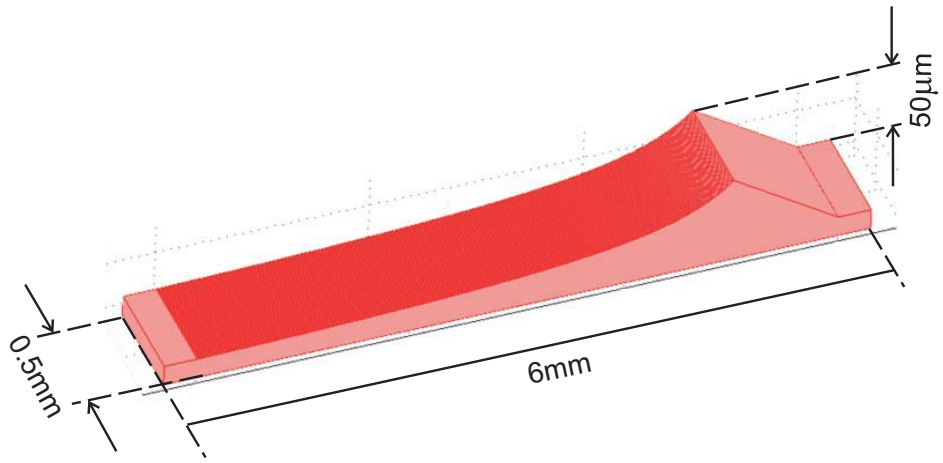

Figure 4.1: *COMSOL model of the vertically tapered Design A (geometry not to scale).*

4.2.1 Fabrication of the Mold

Soft lithography and replica moulding of polydimethylsiloxane (PDMS) [95] is used to create the microfluidic systems. Therefore, a master mould incorporating the tapered channel profile should be fabricated in photoresist using graytone (or grayscale) lithography on a standard mask aligner [96]. To achieve this flood exposure through graytone masks will be undertaken with a conventional contact/proximity aligner (Süss MA6). The masks themselves are written on a glass substrate pre-coated with tungsten, and polymethyl methacrylate (PMMA) as electron beam resist, using the Raith 150 electron beam lithography (EBL) system.

4.2.1.1 Grayscale Lithography

The idea behind graytone lithography is to use an optical mask to modulate light intensity passing through to photoresist beneath. In projection lithography this is achieved by the use of mask patterns close to or below the resolution limit of the projection system. As illustrated in Fig. 4.2, if the pixels on the mask and their spacing are larger than the resolution of the lithography system (a) the diffraction orders are collected according the numerical aperture and the pixels are reconstructed on the photoresist. However, if pixels

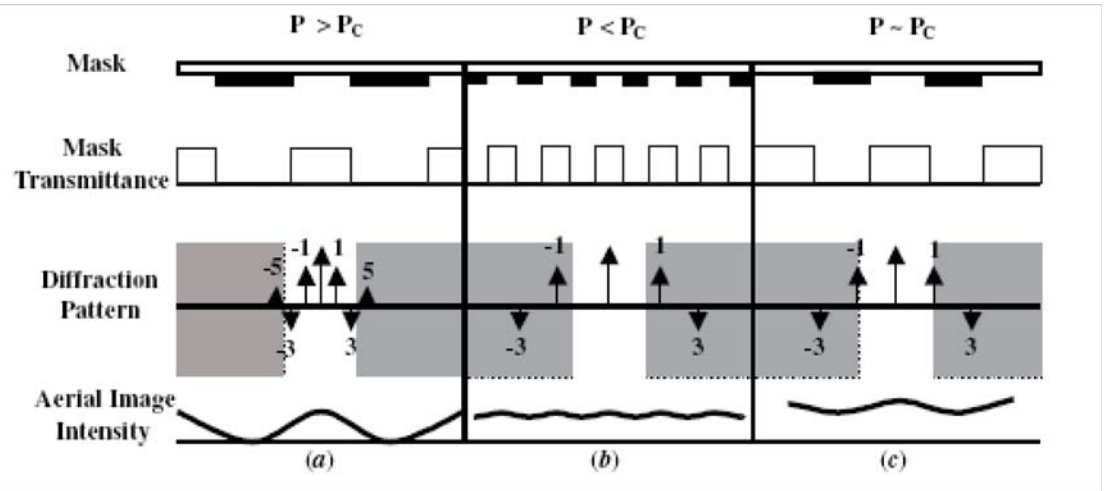

Figure 4.2: *Behavior of diffracted light assuming the critical pitch P_C is the smallest pitch where the numerical aperture accepts the first diffraction order. Orders in the shaded region are not accepted by the system (from [97]).*

and spacing are below the resolution limit (b) only the zeroth spatial diffraction order is captured on the resist. For a constant pitch $P<P_C$ a square unit cell can be defined with side length P. Here P_C is the critical pitch for collecting the first diffracted order from the structure,

$$P_C = \frac{\lambda}{NA}, \tag{4.1}$$

where λ is the wavelength and NA the numerical aperture of the exposure system [97]. The modulation of intensity passing through the mask is then dependent on the area fill of

this unit cell, which in turn is dependent on the number of primary pixels covering the unit cell.

Figure 4.3 illustrates the bottom-up pattern design for a mask fabricated and designed based on this approach. A primary sub-pixel of side length a is used to fill a unit cell of side length P according to the desired fill factor and corresponding intensity modulation. The unit cell is then instanced and multiplied to create the overall pattern. Assuming a resolution limit P_C of >1 µm (Süss MA6 Mask Aligner in vacuum mode) and a primary pixel side length a of 100 nm, 10x10 or 100 different levels of intensity can theoretically be realized on the mask. The background in Fig. 4.3 is a micrograph of an actual grayscale mask after development of PMMA resist. Implementation of the mask design is either in

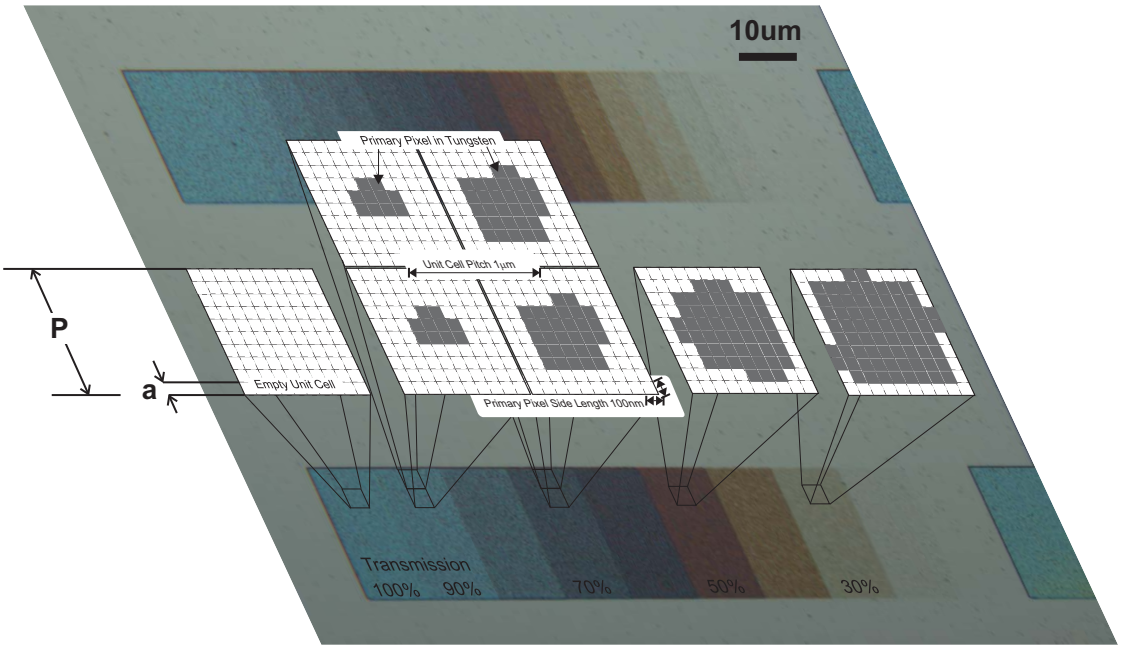

Figure 4.3: *Illustration of the grayscale mask pattern layout: A primary pixel of side length* a *is used to fill the unit cell (*P*) and create a large-scale pattern of defined intensity modulation.*

the commercial software package L-Edit Pro (Tanner Inc.) or alternatively in the Raith software package. A primary pixel is used to create unit cells with filling factors from 100 to 0 % transmission. These unit cells are then instanced and multiplied to create larger patterns with a desired fill factor. Finally an arbitrarily sloped profile is then achieved by

arranging a succession of areas with increasing or decreasing fill factors. When calibrated with the resist contrast function, the correlation between these areas of different fill factors and developed resist depth leads to the final structure.

4.2.1.2 Optical Grayscale Mask Fabrication Process

Based on the inhouse capabilities at the UC Nanofabrication Laboratory a novel optical grayscale mask fabrication process was developed [9]. Large scale binary channel patterns were combined on the final mask with smaller, high-resolution grayscale features in a two step process. Figure 4.4 outlines the major process steps required to obtain a complete grayscale mask. In all cases standard 25x75 mm glass microscope slides and 22x22 mm glass coverslips of thickness No. 2 (ESCO) were used.

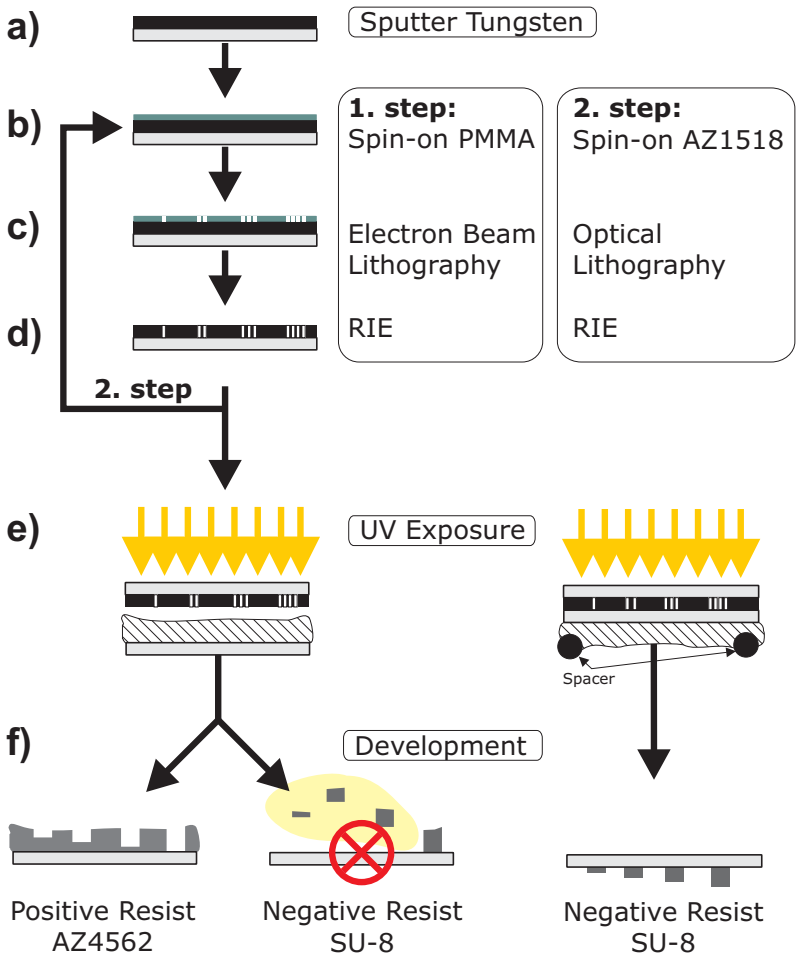

Figure 4.4: *Schematic of the complete grayscale mask fabrication process.*

The substrates were first cleaned using acetone, methanol and IPA consecutively before blow drying with nitrogen gas. A 100 nm thick absorber layer of tungsten was sputter-deposited in 300 W DC argon plasma using an Edwards Auto500 DC/RF magnetron sputtering system (Fig. 4.4(a)). For grayscale features PMMA (4% HMW in xylene) was spun onto the tungsten at 4000 rpm for 1 min (Fig. 4.4(b)). This was followed by a 90 s softbake at 180°C on a hotplate. For electron beam exposure samples were loaded into a Raith150 Electron Lithography system.

Grayscale mask patterns were prepared using the internal Raith software package and exposed at a typical dose of 60 $\mu As/cm^2$, as indicated in Fig. 4.4(c). After exposure, samples were developed in 3:1 IPA:MIBK for 30 s, rinsed with IPA and blow dried with nitrogen gas. Prior to pattern transfer, PMMA was hardbaked for 5 min at 100°C on a hotplate. Samples were then placed in an Oxford PlasmaLab 80Plus and the resist pattern was transferred into the tungsten layer via RIE (Fig. 4.4(d)). Typical process parameters for the RIE etch were 80 sccm SF_6 gas flow rate, 0.15 torr etching pressure and 200 W power for 15 s at a temperature of 313 K. Remaining resist was stripped by immersing the samples in acetone and applying ultrasound. Finally samples were rinsed with methanol, followed by IPA and blow drying in nitrogen gas. In a second step larger patterns of channels were integrated on mask with the grayscale features by repeating steps (b) to (d) in AZ1518 positive photoresist and aligning the optical photolithography to the underlaying features. Samples processed accordingly were used as masks in optical grayscale lithography.

Figure 4.5 shows an example of a grayscale test pattern written on the Raith EBL system. A glass cover slip was used as substrate with a covering layer of 100 nm thick sputter-deposited tungsten. The pattern was written into PMMA resist and successively etched into the tungsten via Reactive Ion Etching. The inset in the right top corner shows a micrograph of the mask after development and hardbaking of PMMA resist. The main image shows a micrograph of the same mask in transmission after RIE and stripping of PMMA.

In Fig. 4.6 a close-up of the mask pattern is shown. Scanning Electron Microscopy (SEM) was used to image the unit cells and tungsten primary pixels of the same pattern as in Fig. 4.5. The filling factor and thereby grayscale level on the left is

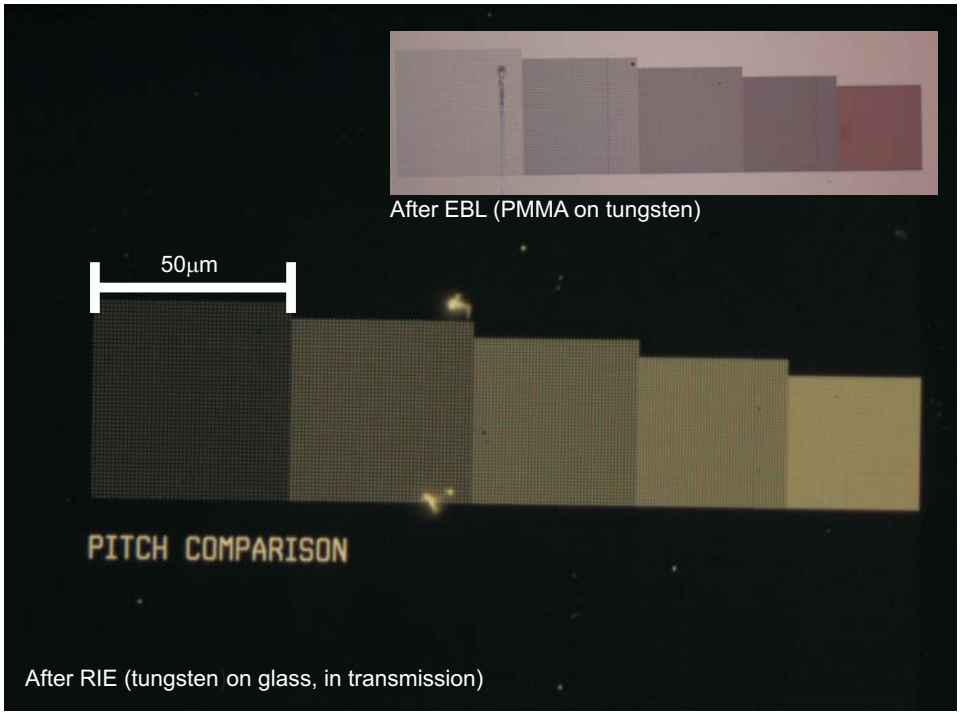

Figure 4.5: *Optical transmission micrograph of a grayscale pattern in tungsten after RIE. The pattern is used to test the effect of different values for unit cell pitch* P*. Inset shows the same pattern after development of PMMA, prior to RIE.*

smaller than on the right, while the unit cell pitch on the left is 0.9 μm compared to 0.8 μm on the right (insets). Depending on the actual resolution limit of the mask aligner used the unit cell outline should not be visible in the grayscale photoresist structures for P < resolution limit, resulting in smoother resist surfaces.

During development of the grayscale process it was found that the main step limiting mask fabrication was the dry-etching of the tungsten absorber layer. Tungsten layers thicker than 150 nm could not be etched with high enough resolution and selectivity towards the PMMA resist used. Replacing tungsten with a chrome-based absorber did not prove feasible, as chrome could not be dry etched in the RIE tool. Initial wet etch trials with sputter-deposited chrome showed similar lack of selectivity and were unable to replicate the primary pixels with sufficient resolution (minimum dimension ~100 nm) on the mask. An increase in hardbake time to enhance the durability of the PMMA resist layer towards the wet processing conditions did not show any significant improvement.

For masks containing combinations of grayscale patterns and channel designs writing the whole pattern on the Raith150 is not feasible due to excessive write times for

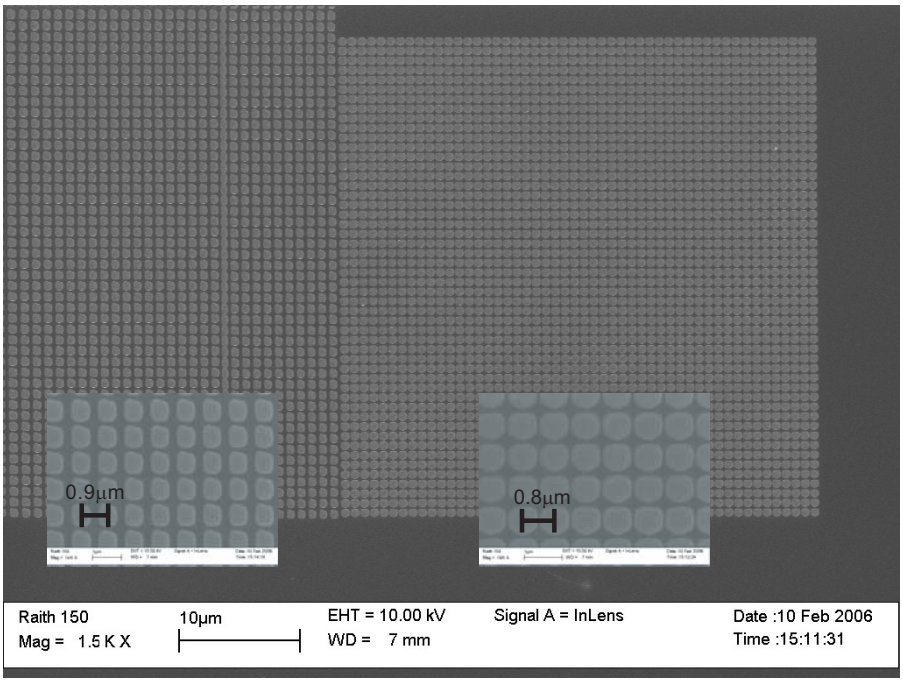

Figure 4.6: *SEM of the different filling factors and unit cell pitches (insets) on the grayscale test pattern mask.*

the binary channel parts of the pattern. To circumvent this limitation the two-step mask fabrication process based on printed foil masks was developed. First the grayscale pattern of the mask is fabricated as described above. Then the larger binary patterns of the channels are fabricated on the same mask as follows.

AZ1518 positive photoresist was applied after grayscale patterning onto the tungsten layer. The resist was spun on at 3000 rpm for 1 min followed by softbake of 1 min at 100°C on a hotplate. Channel masks were drawn using Corel Draw® graphics software and printed on transparent foil by a commercial high-resolution printer (Precision Lithographics, Christchurch NZ). A Süss MA6 mask aligner was used to align the printed masks with the grayscale pattern on the substrate and to expose the resist. Samples were then developed for 1 min in AZ MIF300 developer, rinsed with DI water and blow dried with nitrogen gas.

This was followed by a hardbake of 5min at 100°C on a hotplate. Pattern transfer was via RIE using the same etch recipe as for the grayscale process with a typical etch duration of 30 s. After RIE, remaining photoresist was stripped by immersion in acetone and applying ultrasound. Finally, masks were rinsed with methanol, followed by IPA and blow

drying with nitrogen gas. The transmission micrograph in Fig. 4.7 shows an example of a mask fabricated using this process. The larger channel structure in the lower part was aligned to the pattern after creation of the grayscale pattern and exposed using standard lithography, thereby significantly reducing the electron beam write time required.

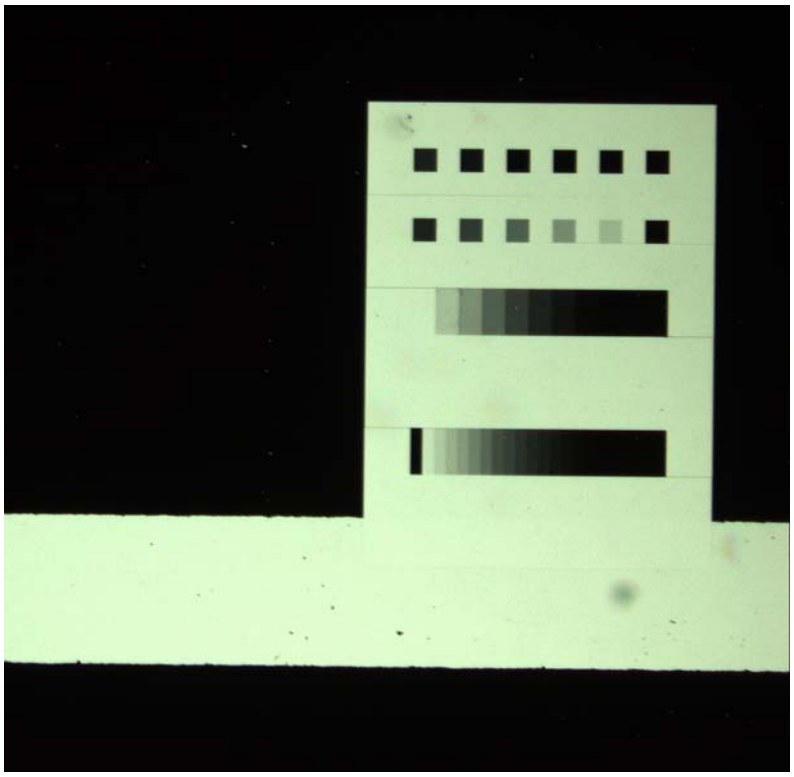

Figure 4.7: *Transmission micrograph of a grayscale mask fabricated by the two-step process with alignment to a larger channel pattern. Grayscale calibration regions are drawn in two rows above two different test channel structures.*

4.2.1.3 Optical Projection Grayscale Lithography in Photoresist

Fabricated grayscale masks were used for optical projection lithography in thick photoresist. Two choices of thick resists were investigated, namely SU-8 as the most popular negative resist currently in use for mold making in microfluidics and AZ4562 (both from Microchem) as one of the thickest positive resists available. Achievable thickness of the resist mold is an important parameter as this decides the depth of the final bioreactor and needs to be large enough to accommodate Hepatocyte cells (est. Ø~25 µm). SU-8 was available in preparations 2025, 2075 and 2100, where the latter can

be spun up to 300 µm thick in a single layer. Being an epoxy-based resist it has the potential to be used directly as a structural material for MEMS applications. AZ4562 can be applied up to 60 µm in a single spin coating, but requires a very stable processing environment in this thickness range.

As substrates, 22x22 mm coverslips and 10x10 mm diced Si wafer pieces were cleaned using acetone, followed by methanol and IPA. After blow drying with nitrogen gas, samples were dehydrated at 95°C in a convection oven for 1 h. Prior to application of resist samples were cooled to room temperature.

SU-8 Negative Resist

Fabricated grayscale masks were used to create sloped structures in SU-8 2075 photoresist with high aspect ratio as needed for microfluidic channels. Since SU-8 is a negative photoresist conventional frontside exposure through a grayscale mask would lead to peeling off of middle tone structures (see Fig. 4.4(f)). The process used in conventional front-side projection lithography has to be modified towards back-side exposure through a transparent substrate [98]. Figure 4.4(e) and (f) illustrate the difference between substrate penetration lithography (right) and standard frontside lithography (left) with a negative resist. If exposed from the front through a grayscale mask SU-8 or any other negative resist crosslinks only to a certain depth. This depth directly corresponds to the intensity modulation effect of the mask. If the crosslinking threshold of SU-8 is not reached polymerization will not reach the substrate surface and the resist structures will be free floating. During development middle and low tone structures lift-off as they are not in contact with the substrate underneath. In substrate penetration lithography, as shown on the right side of Fig. 4.4(e), SU-8 is spun onto a thin transparent substrate. Resist and substrate are inverted and placed on a spacer. The grayscale mask is then brought into contact with the backside of the substrate and exposed. Since, in this case, crosslinking starts from the substrate-resist interface features adhere after development. A further advantage of this process is that initial resist thickness, planarity and edgebead removal are no longer critical.

Thin clean coverslips (VWR, No. 0, thickness 100-120 µm) were treated with OMNICOAT adhesion promoter (Microchem). The promoter was applied by spinning 5 s

at 500 rpm (acceleration 84 rpm/s) followed by 30 s at 3000 rpm (acceleration 340 rpm/s) and hardbaking for 1 min at 200°C on a hotplate. After cooling to room temperature negative resist SU-8 2075 was applied to the coverslips with a final thickness of 100-200 µm by a two step spin-coating process. First resist was poured onto the coverslip and evenly distributed by rolling a clean glass rod over it. Then a spread cycle of 10 s at 500 rpm (acceleration 84 rpm/s) followed by a final cycle of 30 s at 1500 rpm (acceleration 10030 rpm/s[1]) were applied. This was followed by a softbake of 2 h at 95°C on a hotplate. Samples were inverted and placed on a rubber spacer in a custom holder. The tungsten side of the grayscale mask was aligned and brought into contact with the backside of the coverslip. Vacuum was applied to the holder in a Süss MA6 mask aligner. A HOYA-34 filter was place on top of the stack and exposed in multi-exposure mode, 25x with a 10 s exposure and 60 s wait step, in order to reduce resist heating during exposure. The exposure light intensity through the stack was measured to be 3.3 mW/cm^2 at a wavelength of 365 nm. After exposure a post exposure bake (PEB) was performed for 15 min at 95°C on a hotplate. Development was for 20 min in (1-Methoxy-2-Propyl)acetate on an orbital shaker. This was followed by rinsing with IPA and samples were blow dried with nitrogen gas. Grayscale resist structures were imaged using the Raith150 SEM function and a 10 nm sputter deposited layer of tungsten.

Figure 4.8 shows a SEM image of grayscale calibration pillars in SU-8 2075. The initially resist thickness after spin-coating was 200 µm. Patterns on the grayscale mask consisted of 100-by-100 µm squares of different transmission factors. The bottom row pillars correspond (from right to left) to 100%, 30%, 40%, 50% and then in 5% steps to 100% transmission on the mask. As can be seen from this image there is an obvious grayscale effect, however, compared to positive resist the surface is very rough. Also, it was observed that the remaining resist thickness vs. grayscale transmission (absorbed intensity) is rather nonlinear for SU-8 (see Fig. 4.9). This was also observed by Mori et al. [98] and is attributed to SU-8 being a negative resist chemically optimized for binary behavior. The resist will solidify above a certain energy threshold required for crosslinking. Figure 4.10 shows an example of this effect. Here, possibly due to

1.High acceleration is used to help break surface tension of the highly viscous SU-8 2075 or SU-8 2100 and assist spreading.

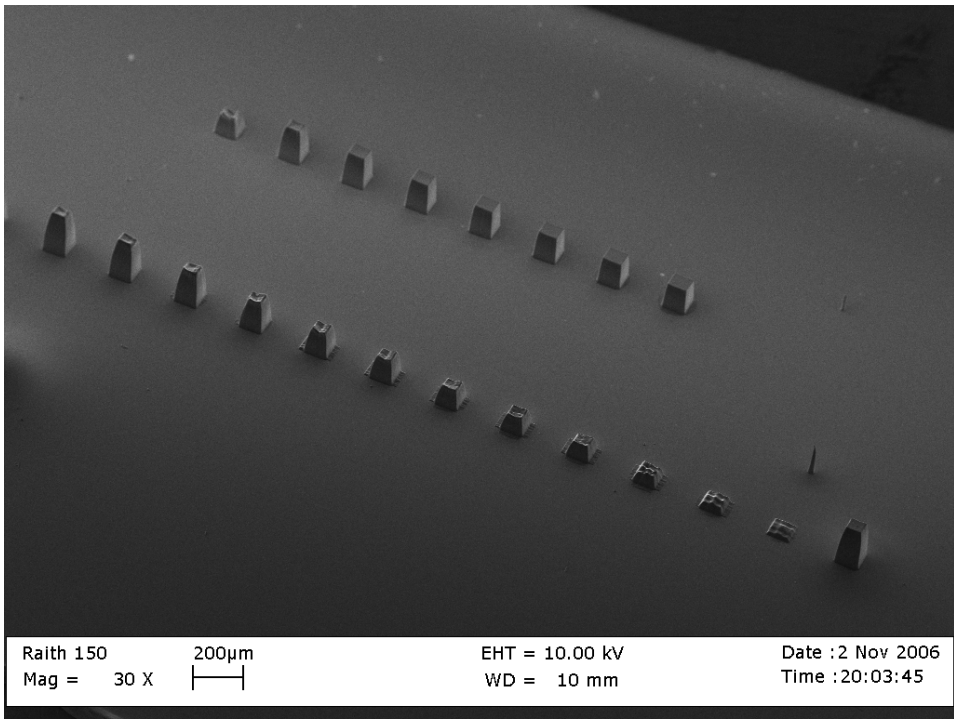

Figure 4.8: *SEM image of grayscale calibration pillars in SU-8 2075.*

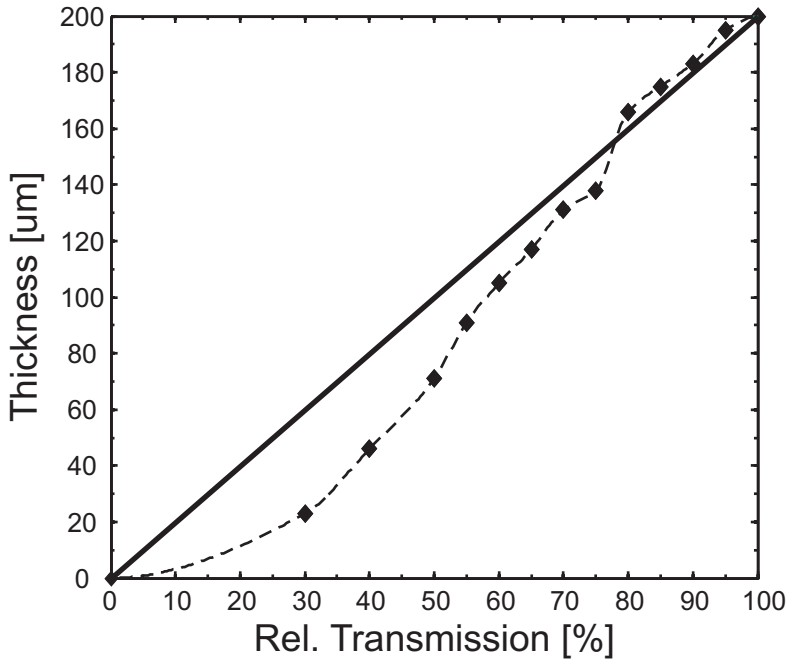

Figure 4.9: *Calibration curve recorded for grayscale in 200 µm thick SU-8 2075. Plotted is the remaining resist thickness as a function of relative mask transmission.*

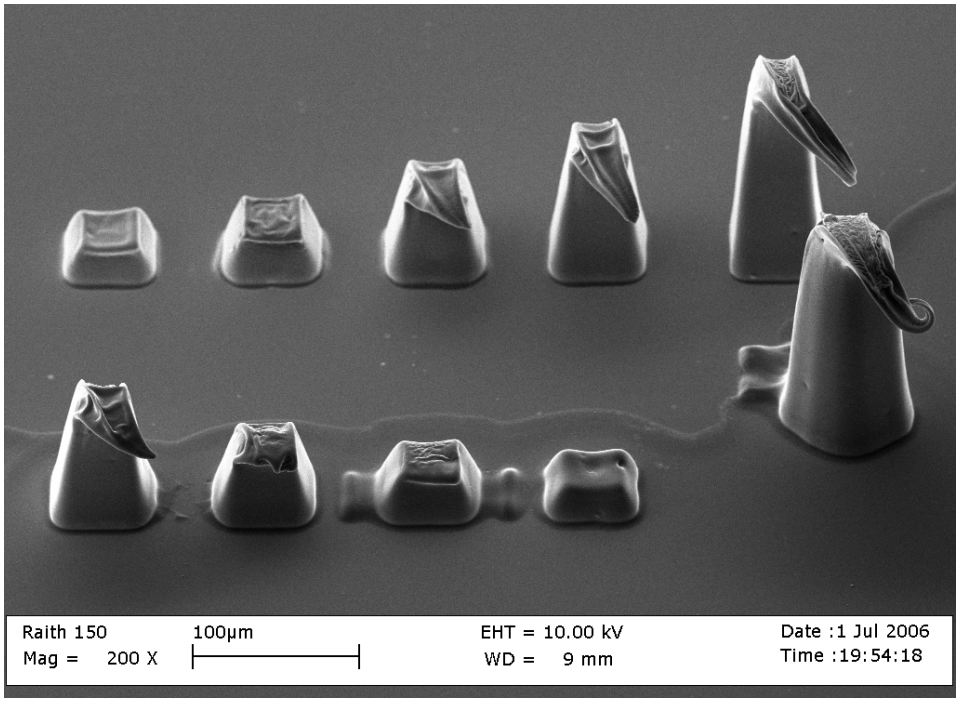

Figure 4.10: *SEM close-up of grayscale in SU-8 2075 showing collapsed empty tips not removed during resist development.*

diffraction on the mask pattern boundary, shell-like empty SU-8 tips remain above what should be flat pillars. Development is unable to remove these semi-crosslinked tips chemically. Only the two lowest pillars remain tip free, which might be due to mechanical collapse by agitation of the developer. In general, SU-8 seems to be only of limited applicability as mold material for this project. The limited window of resist height relative to exposure dose would make it very difficult to achieve the structural control necessary to produce smoothly tapering mold. Furthermore, surface roughness as observed in Fig. 4.10 can not be circumvented by a final bake as SU-8 and other negative resist in general show almost no reflow behavior due to polymer chain crosslinking.

AZ4562 Positive Resist

For this process, positive resist AZ4562 was applied to the coverslips with a final thickness of 60 µm by spinning 3 s at 2000 rpm. This was followed by a softbake of 1 h at 100°C on a hotplate. Grayscale masks and samples were aligned in a Süss MA6 mask aligner and exposed by alternating a 10 s exposure and 60 s wait step for a total of 250 s.

For development samples were immersed in 0.6% NaOH in DI[1] water for 6 mins, followed by rinsing with DI water and blow drying with nitrogen gas.

Grayscale resist structures were imaged using the Raith150 SEM function and a 10 nm sputter deposited layer of tungsten. Figure 4.11 shows a scanning electron micrograph of a high-aspect ratio structure in AZ4562 photoresist. Total resist thickness

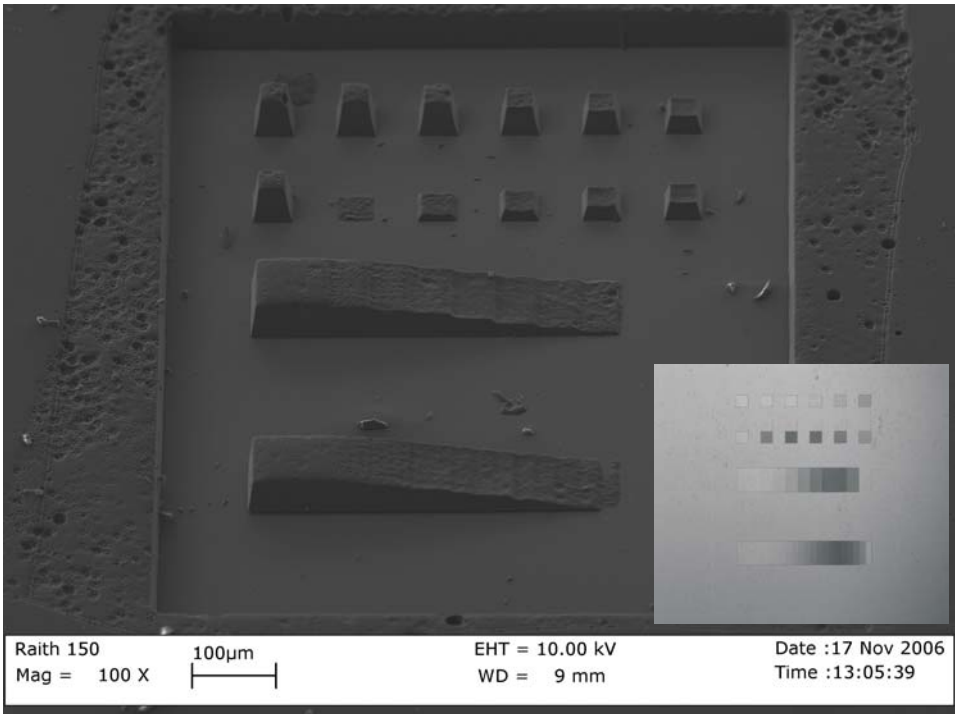

Figure 4.11: *SEM image of high aspect ratio grayscale structures in AZ4562. Inset shows a transmission micrograph of the grayscale mask used for exposure.*

was 60 µm on a 10x10 mm Prime N-type Si piece. The resist was exposed in Hard Contact mode on a Süss MA6 mask aligner in Multi-exposure mode. Exposure was 40x for 10 s each followed by a 60 s cooling step and recorded light intensity was 3.6 mW/cm^2 at 356 nm wavelength. The inset show a transmission micrograph of the grayscale mask used for exposure. After development the structure was characterized using surface profilometry on a DEKTAK profilometer. Figure 4.12 shows the results of this measurement as a grayscale calibration plot of remaining AZ4562 resist thickness vs. relative pattern transmission on the mask. Patterns on the mask for the top row of pillars

1.By recommendation from Microchem as the required developer AZ 351B was not available.

ranged from 100% to 50% in 10% steps (left to right) and 100% for the first pillar in the second row, followed by 10% to 50% (left to right). Height data shown in the insets in Fig. 4.12 was used to prepare the calibration plot. It is found that exposure dose and resist thickness are relatively close to a linear relationship for AZ4562, which is ideal for grayscale application.

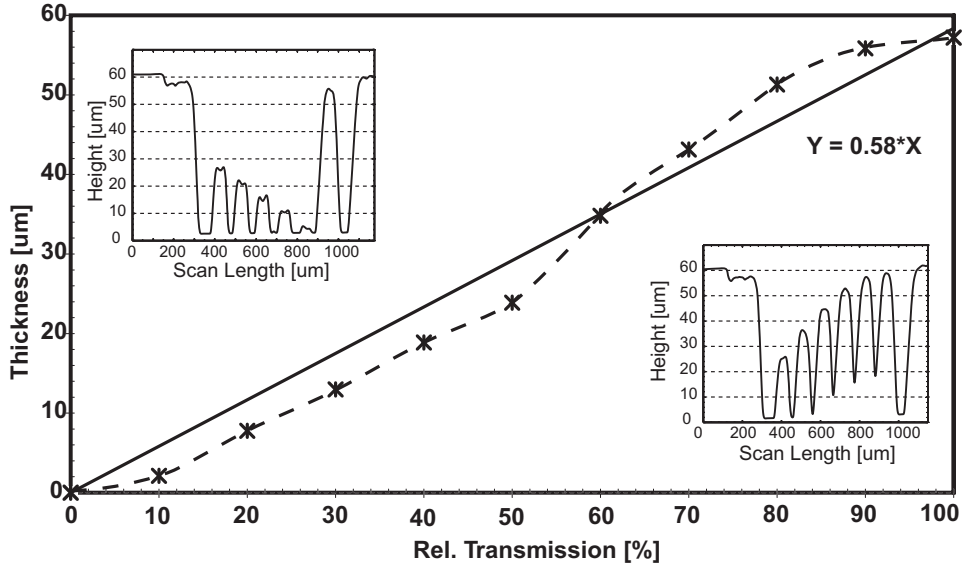

Figure 4.12: *Calibration curve recorded for grayscale in AZ4562. Plotted is the remaining resist thickness as a function of relative mask transmission. Insets show the profilometry scans used as raw data.*

However, as can further be seen in Fig. 4.11, with this combination of grayscale mask, resist thickness and development the process window is very small. The resist surface is extremely rough even on the areas covered by the mask. This is attributed to the upper limit of tungsten absorber layer thickness achievable in the mask fabrication process not being sufficient to absorb all incident light. The smoother area around the inner square was obtained by increasing the absorber layer thickness using a black waterproof marker pen. However, this is not feasible for the actual grayscale structures, which will therefore show increased surfaces roughness limiting their application for smoothly tapering molds. A possible solution to this problem is to investigate the reflow properties of AZ4562 [99]. By exposure to elevated temperatures after development the

resist can reflow and thereby be made to even-out existing surface roughness. Patterns defined through lithography prior to the reflow step have to be adjusted carefully to account for the change in dimensions during the resist flow. This leads to an unavoidable reduction in structural control and a very narrow process window.

Figure 4.13 illustrates the application of the mask process together with resist re-flow (~30 min at 150°C) to fabricate a vertically-tapered microchannel in AZ4562 resist. To fabricate this structure the binary pattern of the channel was combined with the grayscale part on the optical mask. The mask was then used to fabricate the structure by single exposure of the resist in the MA6 optical mask aligner. The vertical arrow (across channel) in Fig. 4.13(a) corresponds to the scan of the initial channel depth depicted on the left in Fig. 4.13(b). Plotted on the right in Fig. 4.13(b) is the scan along the channel length (horizontal arrow in Fig. 4.13(a)). The channel tapers vertically in six steps from the initial depth of 22 µm to a minimum of 7 µm over a length of 1 mm. After hardbake the structure can be directly used as microchannel by sealing it with an appropriate lid. Alternatively, the structure can be used as inverse mold for replication in PDMS or a similar elastomer. While this example demonstrated the general applicability of the process developed, the essential precise control required to reproduce the final tapering shape, as given by the solution of the analytical model, could not be achieved in thick resist.

To retain the advantages of lithography-based microfabrication and to circumvent the problems encountered with grayscale lithography an alternative planar bioreactor design was developed. The design uses laminar flow characteristics to obtain the same shear inducing effect with a symmetric planar arrangement of the initial tapering shape function. By turning the tapering geometry into the horizontal plane standard lithography can be used for pattern transfer, as is described in the second part of this chapter.

4.3 Constant Depth, Tapering Width Bioreactor

The reactor shape of Design B is indirectly derived from the results provided by the analytical model. Cell seeding can be on one or both the top and bottom surface of the channel. Since evaluation of the tapering effect on oxygen concentration requires the

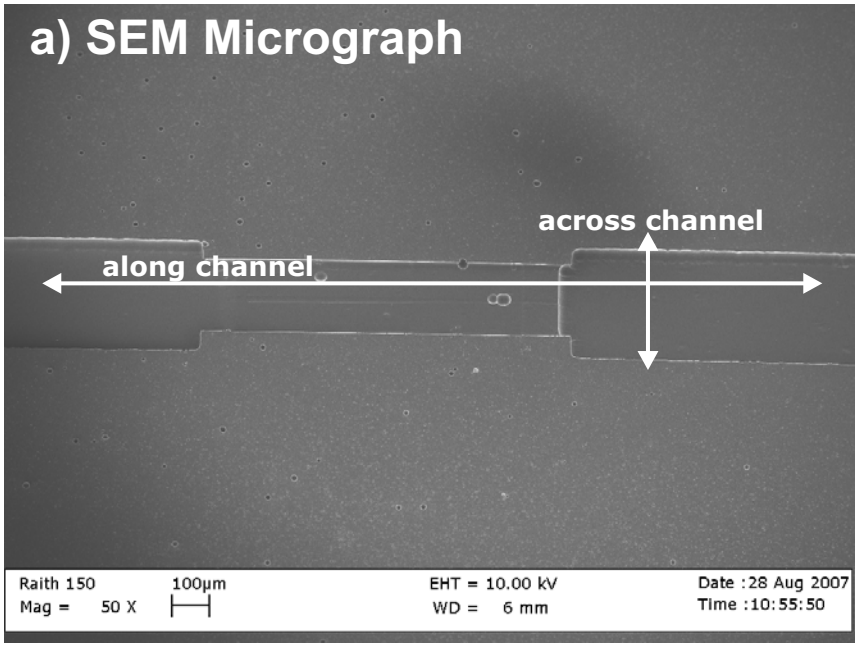

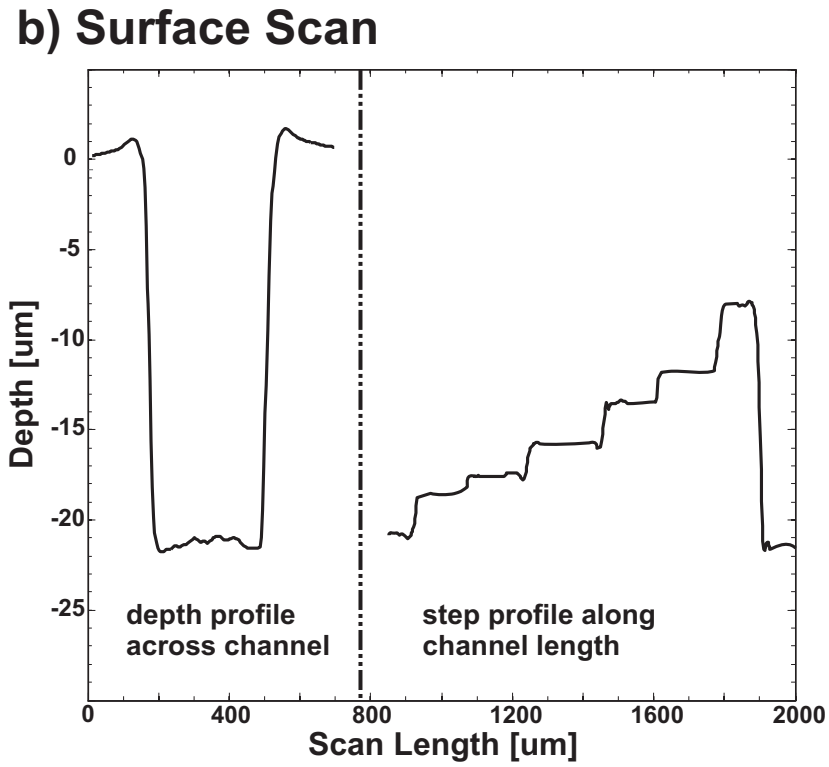

Figure 4.13: *Application example of the combined binary and grayscale mask process to fabricate a microchannel with an integrated feature tapering stepwise along the channel length. (a) Micrograph of the tapered channel indicating the profilometer scan directions. (b) Surface scan graph showing the rectangular depth profile across the channel and the stepwise tapering along its length.*

integration of a sensor, cells will only be cultured on one surface for the experimental measurement. The tapering shape of half the channel width can again be calculated using the analytical model and is mirrored for symmetry to provide constant oxygen concentration on the bottom surface over the channel length. Figure 4.14 shows a 3D rendering of Design B as used in FEMLAB to simulate fluid flow and species transport properties.

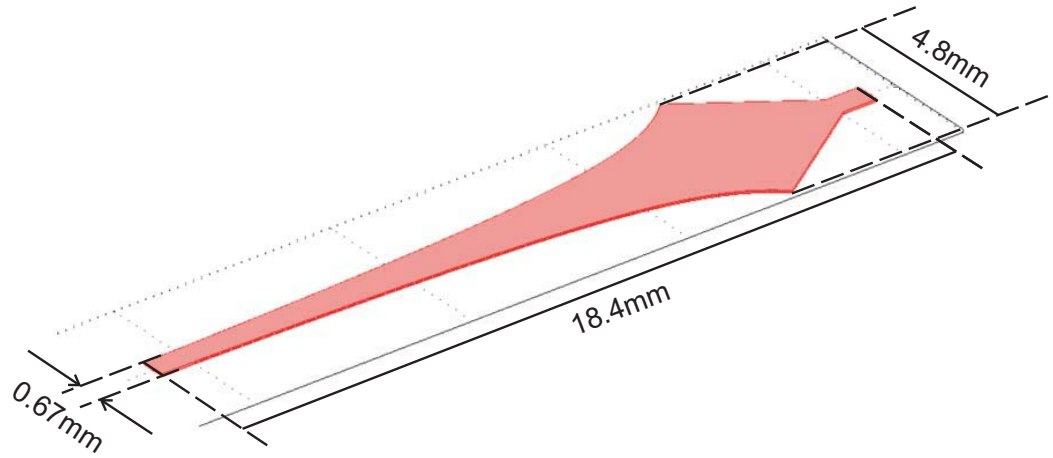

Figure 4.14: *FEMLAB model of Design B, reactor depth is constant (200 μm).*

4.3.1 Fabrication of the Mold

Fabricating a planar mold with lateral tapering is significantly easier, as standard lithography can be used compared to grayscale lithography. No modulation of exposure light dose is necessary on the mask. Common printed foil masks, as well as glass masks, can therefore be used in simple projection mode. Furthermore, using this technique negative SU-8 resist can be exposed in direct contact mode from the resist side, making the creation of multi layer molds feasible [8].

4.3.1.1 Custom-shaped Bioreactors

In all cases standard (mechanical or test grade) 4 inch Si wafers were used as mold support. The substrates were cleaned for 20 min in Piranha solution (5:1 H_2SO_4:H_2O_2), rinsed with DI water and blow dried with nitrogen gas. Silicon wafers were dehydrated in

a convection oven at 185°C for a minimum of 24 h prior to use. For the creation of the photoresist mold wafers were taken out of the oven and cooled to RT. This was followed by application of a thin adhesion layer of SU-8 2025. Without this layer successive processing of thick SU-8 2075 exhibits very low yields. Structures were observed to peel of after development possibly due to surface moisture and thermal stress during processing. SU-8 2025 was applied using a two-step spin-coating program with a spread cycle of 10 s at 500 rpm (acceleration 85 rpm/s) followed by 30 s at 4000 rpm (acceleration 340 rpm/s). Excess resist was cleaned from the wafer underside using a cleanroom wipe covered in acetone. Next, the resist was softbaked for 1 h at 95°C on a contact hotplate and allowed to slowly cool back to RT on the plate. Exposure was performed on a Süss MA6 mask aligner. To crosslink the whole adhesion layer the wafer was exposed in flood mode through a 10x10 mm Kopp 9345 (Newport Glass) filter[1] for three times 10 s plus a 60 s wait period in between each exposure step to reduce thermal stress. This was followed by a PEB for 1 h at 95°C on a hotplate and cooling down to RT.

As structural layer SU-8 2075 was applied on top of the SU-8 2025 adhesion layer in one or more spin coatings depending on the desired final thickness and mold design. Typically a two step spin-coating program was used. First SU-8 2075 was poured on to the wafer, spread using a cycle of 10 s at 500 rpm (acceleration 85 rpm/s) and spun to final thickness for 30 s at 1000 rpm (acceleration 10030 rpm/s). After cleaning the substrate underside, remaining solvent in the resist was removed during a 4 h softbake at 95°C on a hotplate and consecutive slow cooling to RT. Desired structures were then formed in the resist by exposure in the Süss MA6. A printed mask of the design was taped to a blank glass mask and placed in the mask aligner. Exposure was through the filter in “Hard Contact” and “Multi-Exposure” mode for 30x 10 s exposure interspersed with 60 s wait cycles. PEB was performed for 1 h at 95°C on a hotplate. Should a thicker layer or an integrated interconnect layer be required the whole process starting from spinning SU-8 2075 can be repeated. Exposure was then either in a long final cycle through the same mask or by aligning a second layer mask to the structures underneath followed by a final PEB.

Finally, samples were developed in (1-Methoxy-2-Propyl)acetate (Merck) on an

1.Used to filter out excessive energy below 350 nm for straighter sidewalls.

orbital shaker for 20 min and an additional 10 min in fresh developer depending on structural thickness. After rinsing with IPA and blow drying with nitrogen gas, samples were given a final 4 h exposure to UV light in a custom UV-box and a hardbake for 1 h at 100°C on a hotplate to allow for full crosslinking. Figure 4.15 shows a photograph of a two layer mold in SU-8 on a Si wafer. The bottom layer consists of the actual bioreactor shape, while a top layer defines vertical fluidic interconnects with a second device. The round ring surrounding the design has the thickness of both layers and is used to created a PDMS mold with openings on top and bottom [100].

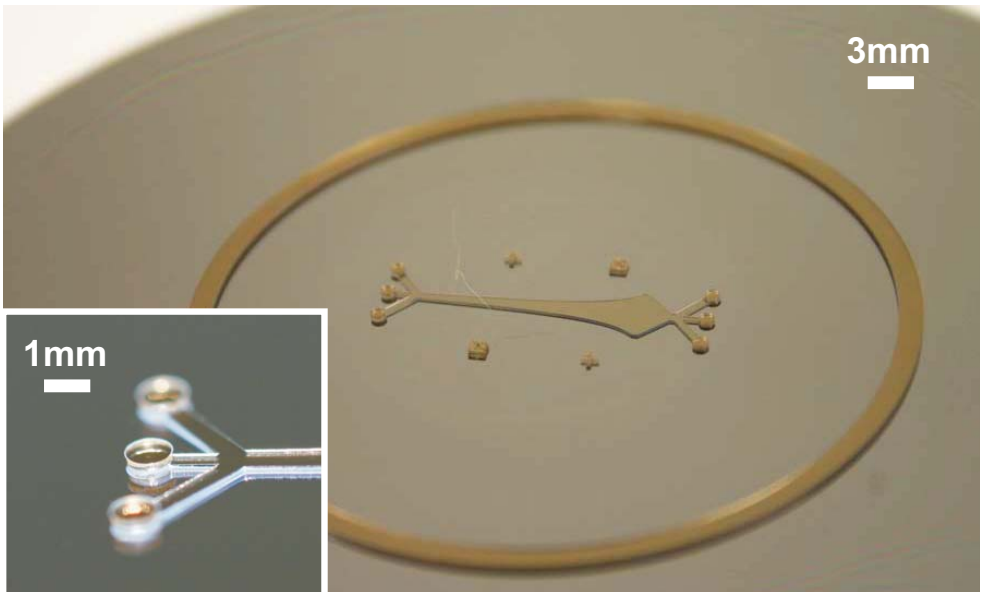

Figure 4.15: *Photograph of dual layer SU-8 mold. The bottom layer defines the reactor shape and the second layer provides vertical fluidic interconnects.*

4.3.1.2 Application of Release Layer

Mold creation was followed by the application of a fluoro-polymer based release layer on the Si/SU-8 mold. While PDMS is rather easily de-molded from SU-8 the lifetime of the master can be significantly increased by applying a release layer. Typically this is achieved by using the C_4F_8 deposition process in a DRIE etcher (Bosch Process [101]). Here a process based on the available Oxford PlasmaLab 80Plus RIE system and CHF_3 as gas was developed. After performing a standard clean of the RIE system master wafers were loaded and the chamber pumped down to ~10^{-6} mbar. For deposition Forward Power

was set to 100 W, etching pressure to 0.22 torr at 295K and CHF_3 flow rate to 50 sccm for 20 min. Wafers were hardbaked for 20 min at 95°C on a hotplate following deposition. Figure 4.16 shows a photograph of a SU-8 mold with release layer. Structures on the master are for definition of the sensor and collagen placement on the bioreactor substrate.

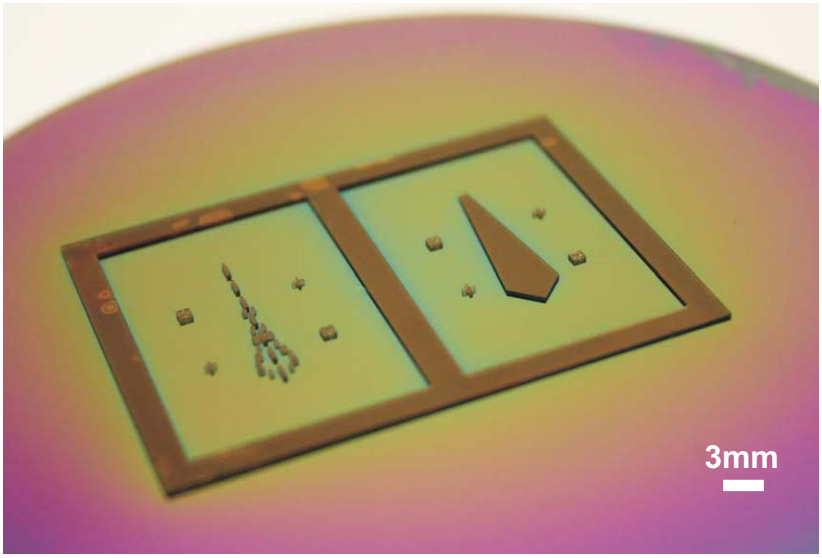

Figure 4.16: *Photograph of SU-8 mold for sensor fabrication after plasma deposition of release layer.*

4.3.1.3 Casting of PDMS Devices

After fabrication of the master mold, PDMS (Sylgard 184, Dow Corning) is used to create the actual channel and reactor structures. Figure 4.17 depicts the main steps of the multi-layer fabrication process. PDMS is a biocompatible silicone elastomer supplied as separate base and curing agent. To prepare the silicone for molding, 10:1 base:curing agent was weighed on a laboratory scale and mixed thoroughly by stirring with a glass rod. The mixture was then placed in a desiccator for 1 h to remove trapped air bubbles. Meanwhile the master mold was placed on polyethylene (PE) overhead foils on a hotplate. After degassing the mixture was carefully poured onto the master avoiding the formation of bubbles. A further foil was rolled onto the silicone and covered with a rubber sheet. To form top/bottom open layers using the double layer mold masters a heavy weight (~5 kg) was placed on top of the stack. The PDMS was then thermally cured at 70°C for a minimum of 1 h on the hotplate. After cooling down to RT the silicone was left

overnight to increase curing. Finally the device was peeled off the mold and placed on a PE sheet for storage. For fluidic sealing both the silicone and a glass microscope slide were exposed to 1 sccm oxygen plasma at 500 W for 10 s in a PlasmaFab wafer asher and brought into contact creating an irreversible seal. Visualization of channels and bioreactors was performed by infusion of DI water with a food color dye. Figure 4.18 shows an assembled linearly increasing wall shear stress bioreactor with a top layer providing interconnection to external tubing. Moving the external interfacing to the sides of the device allows for easier access during microscopy.

4.4 Bioreactor Scale-Up Study

To show the feasibility of system scale-up a multi-reactor demonstrator emulating a bioartificial liver device was fabricated. Roy et al. [88] stated a seeding density of 250,000 hepatocytes per 5.65 cm^2 for rat hepatocytes. Processing this data it can be deduced that up to 13,000 hepatocytes could grow in the $29.257x10^{-2}$ cm^2 available in the single reactor prototype. The fraction of liver mass that is necessary for patient survival has been estimated to between 2-12% of total liver mass. It has been reported that a BAL containing as little as 600 million hepatocytes (3-5%) [27] significantly increases the survival of pigs with induced liver failure. Using the seeding density given for rat hepatocytes, a bioartificial liver would therefore require a minimum of 46,200 single reactors to provide survival enhancing vital functions. This number can potentially be reduced to 23,100 by culturing cell on both bottom and top surface of the developed bioreactor. Furthermore, bioreactors can be combined to form larger patterns as observed in the liver itself. In the following, two prototype devices are introduced demonstrating the feasibility of device scale-up using the elastomer-based bioreactors described in this chapter.

4.4.1 First Prototype

Figure 4.19 shows a SU-8 mold master of 18 radially aligned bioreactors joined at a central core. Using this layout single PDMS layers were fabricated and bonded to a glass substrate. In Fig. 4.20 such a device is shown with all 18 reactors filled with dye-colored

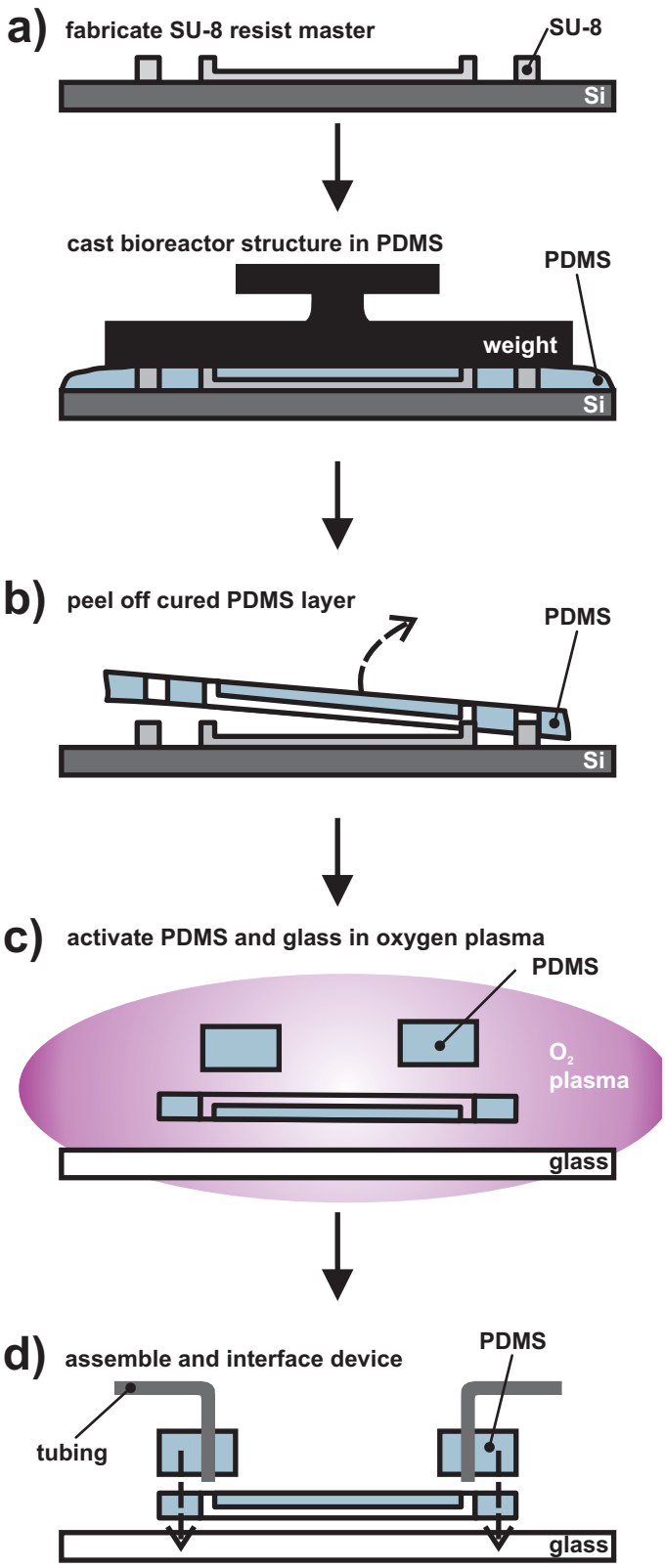

Figure 4.17: *Main fabrication steps of the multi-layer PDMS bioreactor process*

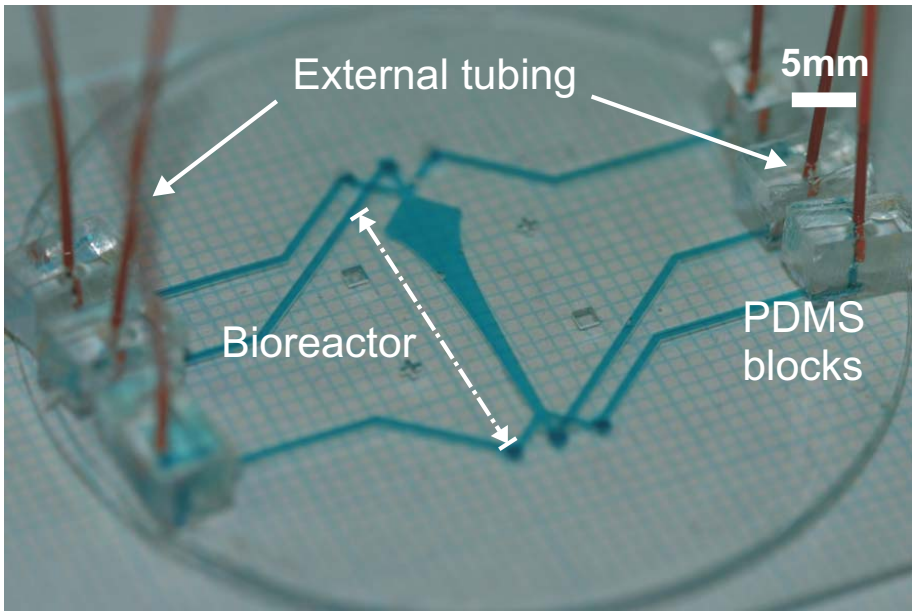

Figure 4.18: *Photograph of a single linearly-increasing wall shear stress bioreactor bonded onto a glass substrate. A second layer provides interconnection to external tubing (orange) via small blocks of PDMS.*

DI water. This design would require 1,300 devices to provide enough seeding area to replace a fully grown liver. Vertical interconnect in this early example were fabricated by manually coring holes with a hollow needle tip. Future designs will employ the single layer PDMS integrated interface technology described above, where vertical interconnects are an integral part of the mold. The speciality of the master mold technique is, that once the master is fabricated, a large number of silicone devices can be cheaply reproduced. Therefore, to increase the seeding area for cells several of the device layers can be vertically stacked and sealed via PDMS-PDMS bonding.

Figure 4.21 shows an example of two such devices bonded on top of each other. First the bottom layer was bonded to a glass substrate and the vertical holes cut using sharpened stainless steel dispensing needles (Farnell). Then the first and second layer were exposed to 1 sccm oxygen plasma at 500 W for 10 s in a PlasmaFab Asher and aligned using methanol. The methanol protects the activated surface from re-oxidation during manual alignment and allows for bonding once evaporated [100].

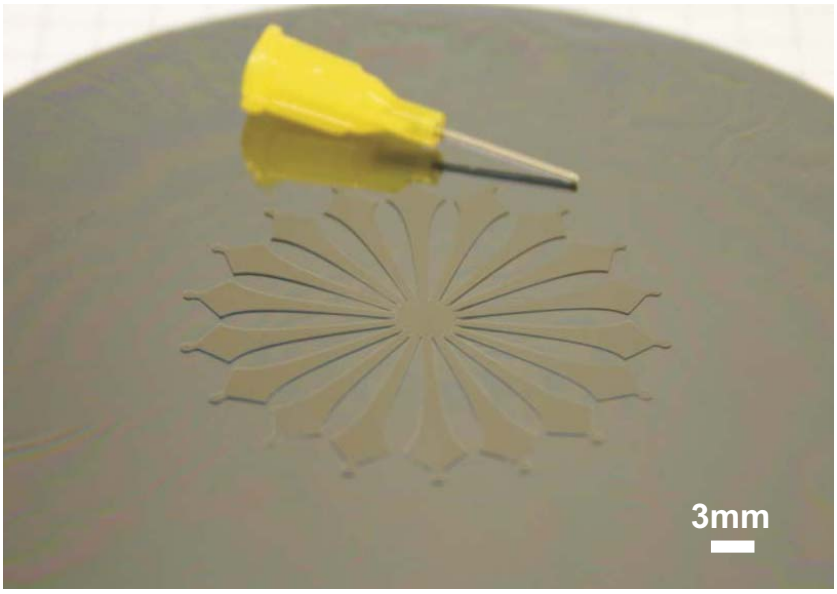

Figure 4.19: *Photograph of 18 radially arranged bioreactors in SU-8 mold for system scale-up study.*

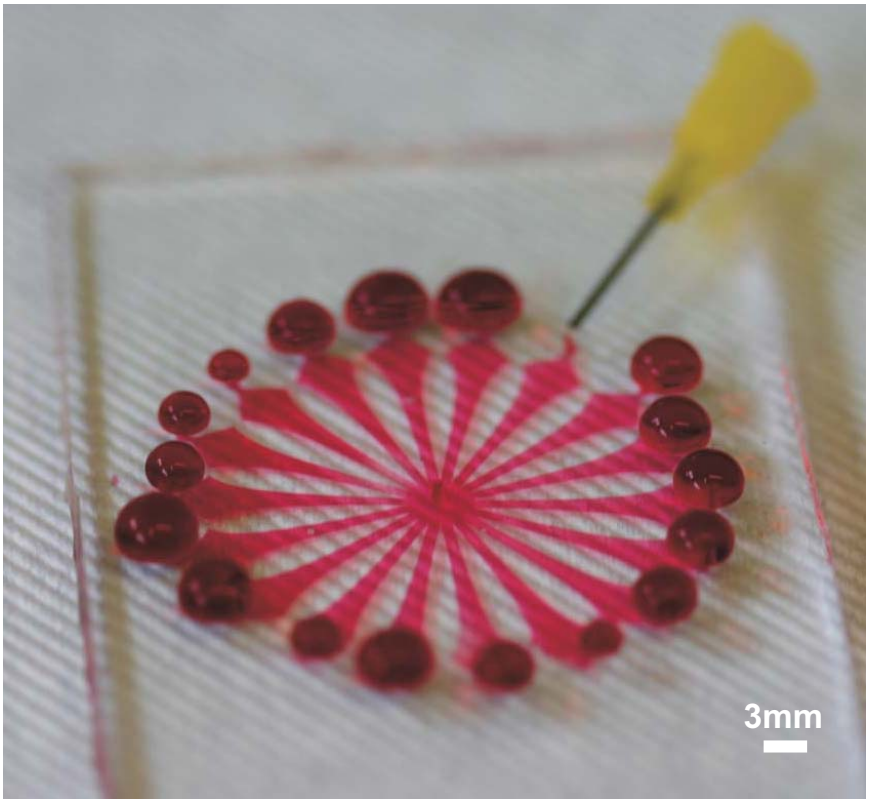

Figure 4.20: *Single layer replica of PDMS bonded on to a glass substrate. All 18 bioreactors are filled with dye-colored DI water from a central opening.*

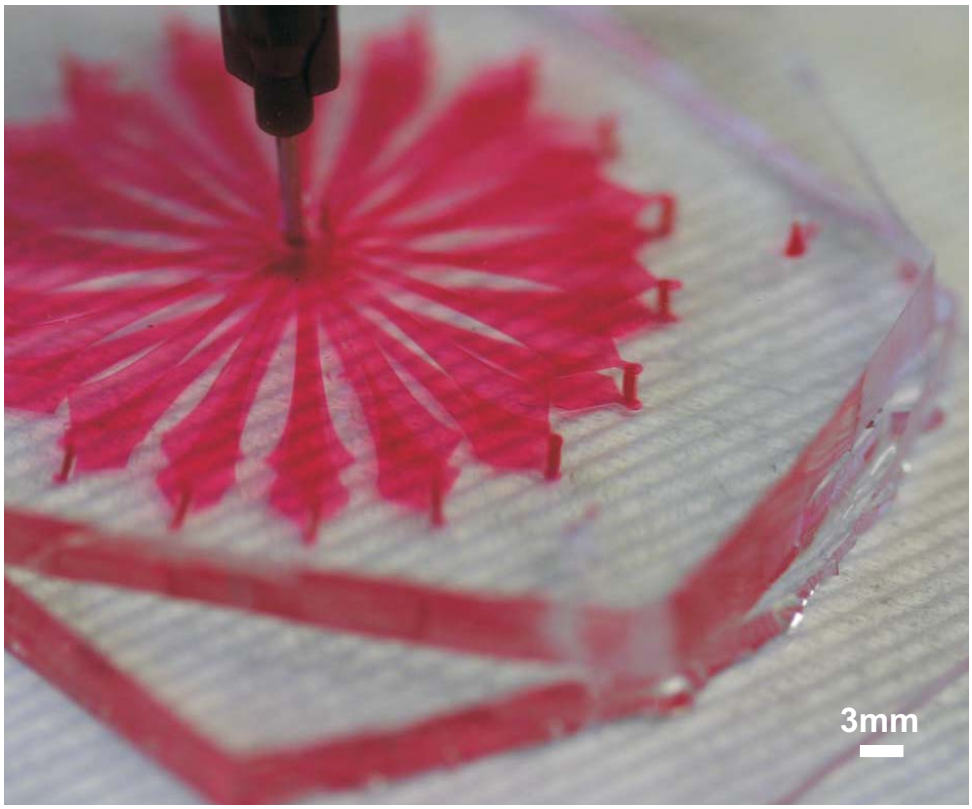

Figure 4.21: *Two-layer PDMS device with a total of 36 bioreactors in two layers. Vertical fluidic interconnects between the two layers are visible on the right.*

4.4.2 Second Prototype

Encouraged by results from the first two-layer prototype, the SU-8 molds were redesigned for a second prototype. This time the molds were to incorporate all fluidic features so that no manual handling would be required during fabrication and assembly. All features crossing between the individual layers, like vertical interconnects, were included in the corresponding mold masters by use of multi-layer SU-8 features as mold material. A total of three different mold masters were required, two for the top and bottom liquid interconnect and distribution layers and one for the functional layer containing the 18 radially arranged bioreactors.

One of each top and bottom layers, as well as seven of the functional layers, were cast in a 10:1 PDMS mixture and thermally cured as described before. Upon release from the mold, layers were bonded using oxygen plasma surface activation. First, the bottom interconnect layer was bonded to a glass substrate and then the first of the seven

successive functional layers was bonded onto this stack. After a rest period of 24 h to strengthen the previous bond, the resulting stack was again exposed to oxygen plasma, this time together with the next functional layer. This process was repeated for all layers including the attachment of a square PDMS connector block to the final top layer. Alignment of individual layers in between bonding was performed manually by applying a thin layer of methanol to the activated surface of the stack. The new layer was then inverted onto the stack and manually aligned using the vertical through holes and special alignment marks integrated in the initial design. Manual alignment of the layers to be bonded could easily be replaced by an automatic tool similar to a wafer bonder in a future commercial fabrication process. External interfacing concluded the prototype fabrication and was performed by coring into the square connector block with a syringe needle.

After assembly of the nine layers into a single device, liquid handling was tested by pumping dye-colored DI water through the stack. Figure 4.22 shows a photograph of the device with close-ups depicting the general layout. A total of 126 bioreactors are integrated over seven layers, with each layer containing 18 individual reactors. Liquid is injected through the central inlet (Fig. 4.22(a)) on the top and travels down a centre column to the top distribution layer. Here the flow is separated into 18 horizontal channels leading to the vertical columns on the outside perimeter (Fig. 4.22(b)). These columns each feed one bioreactor per layer, running all the way from the top of the device to the bottom. After travelling through a reactor the fluid drains into a vertical central column. This column drains via a horizontal outlet channel on the bottom layer and a further vertical column connected to a hole on the topside (Fig. 4.22(c)).

With PDMS-based microfluidic devices the hydrophobic nature of surfaces has to be taken into account when filling a device for the first time. Priming (pre-filling) with another liquid is sometimes used to overcome the initial flow resistance. In case of the prototype priming was not necessary to achieve filling of all the individual fluidic parts. However, it was observed that the slight offset in vertical alignment of the different layers and their interconnecting structures due to manual handling reduced the inherent symmetry of the device. This unbalances the flow resistance along the different parallel flow branches and leads to preferential filling of certain areas prior to others relative to the central inlet. A solution to this problem would be to use automatic handling and

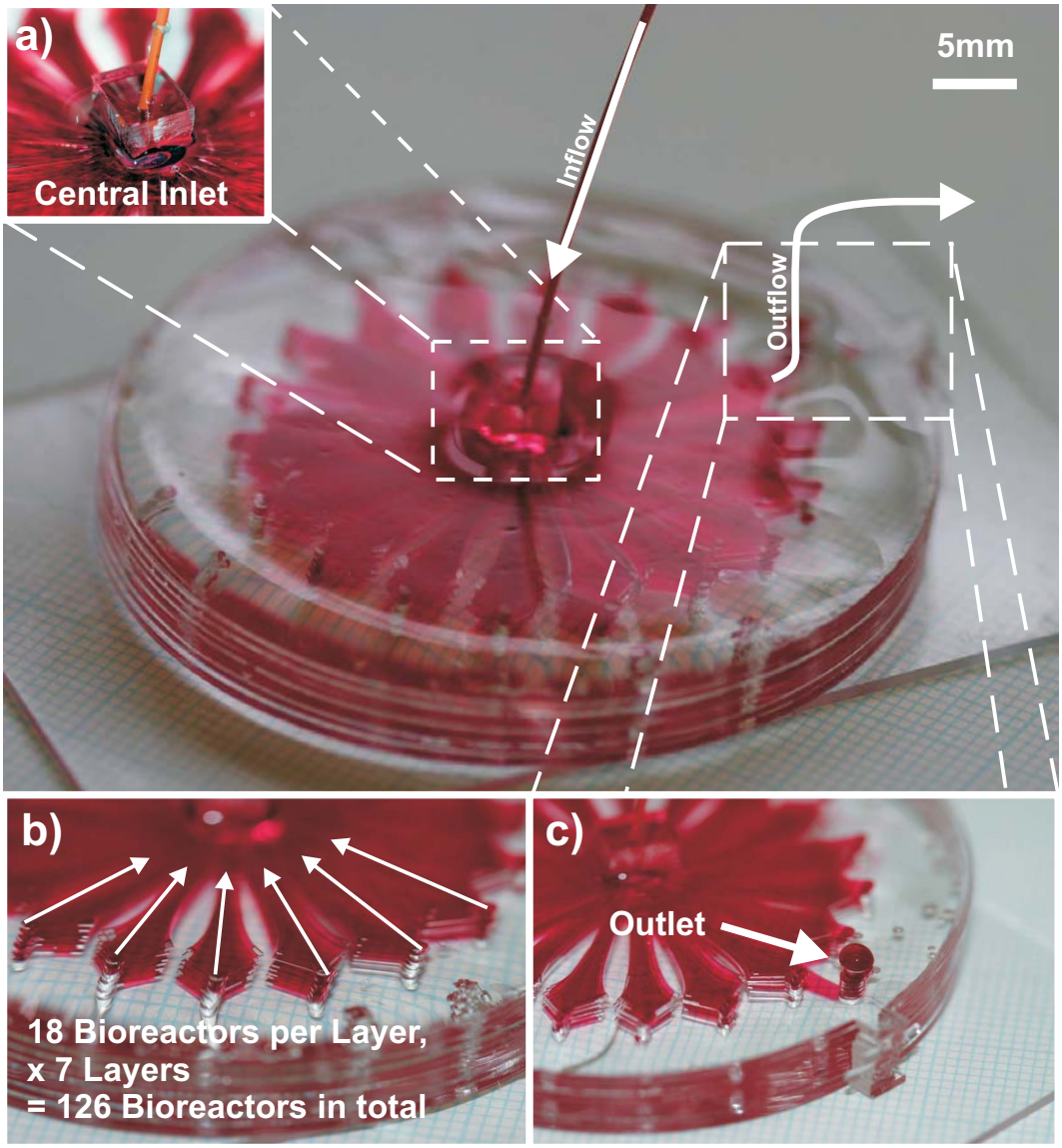

Figure 4.22: *Second prototype demonstrating the feasibility of device scale-up: The multi-layer design in PDMS integrates 126 bioreactors on seven layers around a central inlet (a) and common outlet (c). The number of layers in this prototype is only limited by the reproducibility of the manual alignment. Device was filled with dye-colored water for visualization.*

alignment of layers during fabrication or to produce a single homogenous device by injection molding. The latter would also eliminate potential sealing problems between layers. Although observed to be very reliable and repeatable, especially despite the large number of individual layers, oxygen plasma bonding of PDMS requires careful handling and environmental control to produce good sealing. For a total of 9 bonded layers the

device showed only one small delamination between two functional layers close to the outlet. This however, could be enough to render the device unusable if it leads to major leakage and thereby pressure loss. One possible way to strengthen the PDMS-to-PDMS bond is to initially produce only partially cured layers by reducing the recommended baking time during molding and then to add a final curing bake after the assembly of the complete device to enhance the interstitial bond between adjacent layers.

4.5 SUMMARY

In house grayscale lithography was investigated as a means of fabricating microfluidic bioreactors. A process for mask fabrication was developed and used to create master molds in positive and negative tone photoresist. However, features produced using grayscale lithography were observed to exhibit excessive surface roughness, which in turn would affect fluid flow in channels replicated from these molds. At the current stage further work into process optimization would be needed to achieve a significantly lower surface roughness. To alleviate this problem it would need to be investigated whether a final reflow bake could be used to reduce surface roughness. This technique is often used to produce rounded master structures in resist. It is however, not applicable to high-aspect ratio, epoxy-based photoresists such as SU-8, and is associated with a certain loss of control over structural feature size. In terms of time constraints and overall project goals it was therefore chosen to concentrate further development on Design B. This potentially provides the same effect as the tapering depth Design A, with the added advantage of using standard fabrication technology available at the Nanofabrication Laboratory. In summary, the full fabrication process from mold making to final device sealing for Design B has been demonstrated in this chapter. The fabrication process allows for a fast and flexible device prototyping and potential scale-up to the automated fabrication of a full bioartificial liver device. The following chapters will focus on the integration of oxygen sensing and cell-culture into the bioreactor chip.

When I'm working on a problem, I never think about beauty. I think only how to solve the problem. But when I have finished, if the solution is not beautiful, I know it is wrong.

R. Buckminster Fuller
1895-1983, American Architect,
Author, Futurist, Inventor and Visionary

CHAPTER 5

Oxygen Sensor Integration

One of the central ideas behind the use of channel geometry is to control and improve species transport to cells cultured within. To determine whether the analytical model developed specifically for oxygen transport to liver cells is valid requires a means of measuring the concentration gradient of dissolved oxygen (DO) inside the bioreactor device. Since the gradient produced by the geometry is not ideally constant and specific non-constant gradients can be of biological interest, simply measuring the inlet/outlet concentrations will not be sufficient.

A potential sensor has to be easily integrated into the confined space of the chamber without influencing the flow characteristics of the reactor. It further needs to have sufficient sensitivity to allow for detection of the minute changes in oxygen concentration exhibited by live cells. This chapter therefore discusses the advantages and limitations of the two most common sensor technologies, amperometric and optical oxygen sensing, for the detection of DO in biological applications. Optical oxygen sensing is identified as most suited for use in the bioreactor device and a novel sensor fabrication process is developed to improve presently available methods. The deposition of sensor films, their patterning and signal optimization, as well as their integration into the PDMS-based

bioreactor device are discussed in detail [10]. This represents one of the major contributions of this thesis.

5.1 Oxygen Sensing in Biological Applications

Oxygen concentration is increasingly recognized as a central parameter in cellular studies. In a natural environment, such as in mammalian organs, cellular oxygen concentration is maintained to normoxic (12% to <0.5% O_2) conditions [102]. Regulation to within this relatively narrow range of normoxia is necessary in-vivo to prevent oxidative damage to the cell from excess oxygen (hyperoxia) and metabolic demise from insufficient oxygen (hypoxia) [1]. Absolute normoxic values for a specific cell are furthermore dependent on the cell localization within a particular organ like the liver. Here localization is exhibited in form of oxygen modulated zonation and gradients along the length of the sinusoid result in regionally dominant metabolic and detoxification functions [103]. This natural sensitivity to local oxygen concentration can be replicated *in-vitro* to selectively increase specific liver cell function like urea synthesis [73].

However, recent research has indicated that *in-vitro* cell-culture experiments performed in air (~21% O_2) may introduce excessive stress on cells due to exposure to unnaturally high oxygen concentrations [102]. Fibroblasts exposed to different oxygen concentrations were found to adjust to high oxygen levels by reversible growth inhibition and differentiation. For neural and other stem cells in comparison, hypoxic conditions were observed to promote growth and influence differentiation [104]. Measurement of oxygen concentration is therefore of special importance when comparing *in-vitro* results to cell behavior observed in-vivo.

In general it can be said that oxygen uptake of cells is a powerful marker for their metabolic status, health and response to exogenous and endogenous stimuli [105]. Beyond cell culture, oxygen consumption characteristics can also be used to determine the development status of higher organisms. For example, a direct link exists between oxygen consumption of pre-implantation mammalian embryo and their development status. This indicates that integrated oxygen detection, such as developed here, has the potential to provide biomedical applications and the agricultural industry with a reliable,

non-intrusive tool to investigate embryogenesis, gene manipulation, cloning, assisted reproduction and transgenic animals [106].

5.1.1 Principles of Oxygen Sensing

Traditional laboratory procedures for the measurement of oxygen in solution require the extraction of a sample volume for external analysis. This sampling approach is limited by the difficulty and time needed for extraction and analysis. With fluid volumes in the range of micro-liters and below, as found frequently in current microfluidic LOC devices, analyte sampling constitutes a major disturbance of the system to be measured. This is a particular problem for sensing of less stable solutes such as oxygen, where retrieval is likely to significantly alter the sample characteristics [107]. Alternative *in-situ* sensing approaches are therefore needed and two such potential candidates are introduced in the this section.

5.1.1.1 Amperometric vs. Optical Oxygen Sensing

Two main technologies, amperometric electrochemical and optical sensing currently constitute the bulk of integrated sensors for the measurement of DO in biological applications. Both are tolerant to liquid exposure and exhibit the high sensitivity needed to detect the small changes of oxygen encountered in the cellular environment. The first principle, amperometric electrochemical sensing, has been applied in a variety of biomedical LOC devices [106,108,109]. Despite continuous interest, several significant limitations have been identified concerning the use of amperometric sensors. When exposed to organic matter sensor lifetime has been found to decrease through membrane fouling. Oxidation of the electrode surface area after prolonged usage and electrolyte depletion can be responsible for inconsistency between measurement data. A second, more important concern relates to the fundamental method of operation of the amperometric electrode [111]. The Clarke sensor operates by reducing oxygen and, in a low flow rate environment like the bioreactor device, is prone to show signal dependence on flow rate. Additional problems are posed by miniaturization itself, mainly due to the need to integrate a reference electrode [107].

5.1.1.2 Optical Oxygen Sensing

By contrast, fluorescent dye-based optical sensing does not exhibit analyte depletion, and has therefore emerged as a promising alternative in biomedical applications. The principle of measurement with this type of sensors relies on the quenching of either the intensity or lifetime of light emitted by a fluorescent dye in the presence of molecular oxygen. Fluorescence occurs upon excitation of the dye molecule (fluorophore) to an exited state S^* and subsequent relaxation back to the ground state S_0 via the emission of light [110]:

$$S_0 + h \cdot \nu_{ex} \rightarrow S^* \quad excitation \tag{5.1}$$

$$S^* \rightarrow S_0 + h \cdot \nu_{em} \quad emission \tag{5.2}$$

$$S^* + O_2 \rightarrow S_0\big|_K \quad quenching \tag{5.3}$$

where h is *Planck's* constant and $\nu_{ex} > \nu_{em}$ are the frequencies of the excitation and emission light, respectively, and K the molecular rate constant for oxygen quenching. One pathway for relaxation from the exited state of the fluorophore is via interaction with a secondary molecule. In case of oxygen, fluorescence quenching has a pronounced effect on the quantum yield as a result of the triplet ground state of the O_2 molecule. The fluorescence intensity, I, and lifetime, τ, and can be obtained for dissolved or gaseous oxygen from the *Stern-Volmer* equation for intensity [112]:

$$\frac{I_0}{I} = \frac{\tau_0}{\tau} = 1 + K_{SV}{}^S \cdot [O_2] = 1 + K_{SV}{}^G \cdot pO_2 \tag{5.4}$$

where $K_{SV}{}^S$ and $K_{SV}{}^G$ are the Stern-Volmer constants for solution and gas, respectively, I_0 and τ_0 the reference values in absence of oxygen, $[O_2]$ is the oxygen concentration in solution and pO_2 is the gaseous partial pressure of oxygen. Figure 5.1 illustrates the principle of oxygen sensing based on fluorescence for intensity quenching using sensors developed in this work. The intensity signal of a sensor pattern with no oxygen present (0% O_2) decreases upon exposure to gaseous or dissolved oxygen molecules (100% O_2). This decrease in intensity is recorded and translated into oxygen concentration by comparison to a reference value. Since the fluorescence quenching is reversible, the

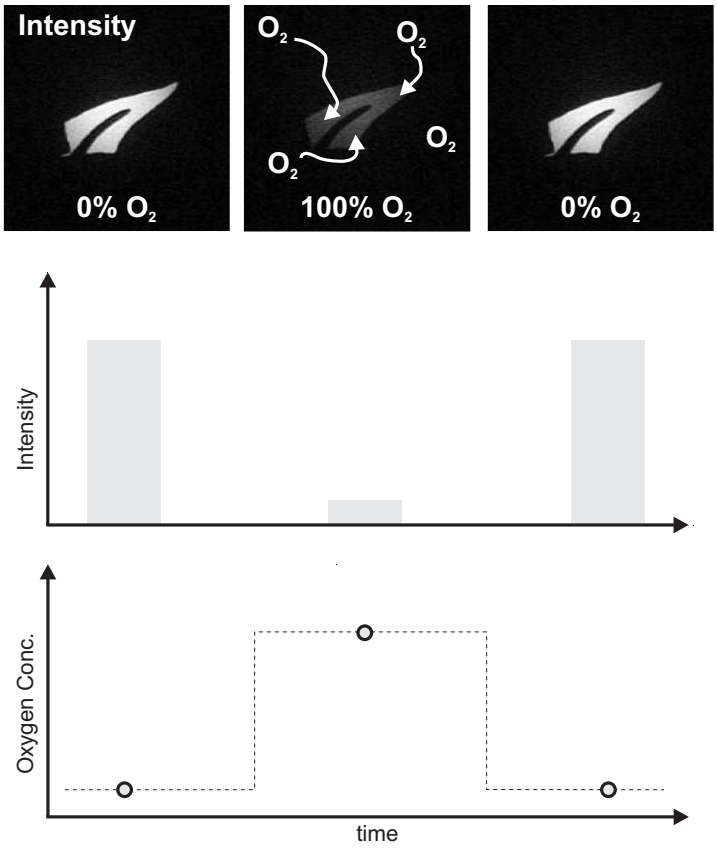

Figure 5.1: *Schematic depicting the principle of optical oxygen sensing. The fluorescence signal intensity of a sensor pattern (0% O_2) is reversibly quenched in presence of oxygen molecules (100% O_2). This signal decrease is translated into an oxygen concentration value relative to a reference intensity via a calibration curve.*

intensity reverses to its initial value once the oxygen is removed again (0% O_2). Should other effects (e.g. sensor film inhomogeneities) cause intensity fluctuations, fluorescence lifetime could be used to measure the oxygen concentration, however this requires a significantly more complicated experimental setup to modulate the excitation and extract spatial information.

5.1.1.3 Sensor Materials

While this characteristic quenching is exhibited by the majority of fluorescent dyes, a small subgroup has been found to be especially suited due to high sensitivity and long fluorescence lifetimes. These dyes are commonly categorized [112] into organic

luminescent or organometallic compound probes and used in solution [105,113,114] or immobilized on a support matrix [88,107,115-117] for the detection of dissolved oxygen. For use with low-cost LOCs, dye immobilization has the advantages of increasing the ease of handling and reducing the amount of fluorescent dye required. Table 5.1 gives a list of organometallic complexes used as oxygen sensors together with absorption/emission wavelengths, suitable solvents for immobilizing polymer films and relative intensity change.

Platinum(II) octaethylporphyrinketone (PtOEPK) suspended in a microporous polystyrene (PS) matrix has been identified as well suited for use in LOC devices due to its desirable optical properties, compatibility with standard optical components and it being readily available commercially. The PtOEPK dye molecule (Fig. 5.2) shows strong phosphorescence with a high quantum yield and long lifetime at room-temperature.

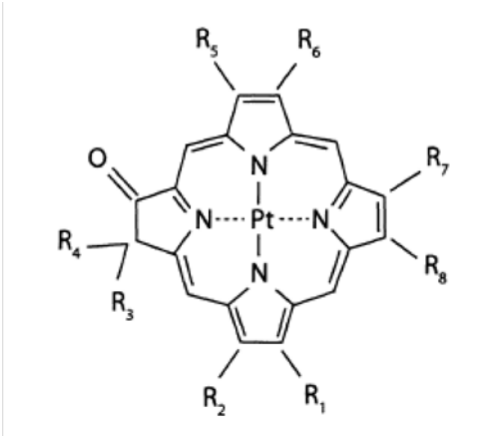

Figure 5.2: *Chemical structure of the PtOEPK molecule.*

Sensors immobilized in PS have been shown to diminish only 12% under continuous illumination for 18 h, detected by absorbance measurement [112]. It exhibits both a long-wave shift and an extended long-term photostability compared to other fluorescent dyes [118]. This allows for the use of standard optical filters and makes sample handling less critical. PS was chosen as polymer matrix because it provides good oxygen-permeability, bio-compatibility and low auto-fluorescence.

Probe	**λ_{max} (abs) [nm]**	**λ_{max} (em) [nm]**	**Suitable solvents for immobilizing polymer films**	**I_0/I_{100} in various polymer films**
$Ru(dpp)_3^{2+}$	337, 457	610	dichloromethane	4.4 in silicone film 1.1 in PS film 3.5 in PVC film
$Os(dpp)_3^{2+}$	454, 500, 580, 650	729	dichloromethane	4.5 in poly(DMS) film
$Os(phen)_3^{2+}$	432, 478, 660	720	dichloromethane	-
$Ir(ppy)_3$	376	512	THF, dichloromethane	1.2 in PS film
PtOEP	381, 535	646	toluene, THF, dichloromethane	4.5 in PS film
PtTFPP	395, 541	648	toluene, THF, dichloromethane	3.0 in PS film
PtOEPK	398, 592	758	toluene, chloroform	2.0 in PVC film 20 in PS film
PdOEP	393, 512, 546	663	toluene, THF, dichloromethane	11.5 in PS film
PdOEPK	410, 603	790	chloroform, toluene	8.0 in PVC film 28 in PS film

Table 5.1: *List of possible organometallic luminescence probes for optical oxygen sensing. Both Palladium OEPK and Platinum OEPK exhibit very high intensity ratios I_0/I_{100} immobilized in PS films (Adapted from [112]).*

5.2 SENSOR FABRICATION

The following sections discuss existing sensor fabrication processes and introduce the novel sensor-layer patterning process developed as part of this thesis. Whilst simple in concept (see Fig. 5.3), the details of the process required a significant amount of effort to allow for integration with the PDMS-based channels.

5.2.1 LIMITATIONS OF CURRENT FABRICATION PROCESSES

Beyond the advantages mentioned before, the PtOEPK/PS system shares one major limitation with most other fluorescence-based sensor materials, namely the challenge to fabricated micro-scale patterns and integrate them with commonly used PDMS devices. Organic solvents such as acetone readily dissolve PS, making it impossible to

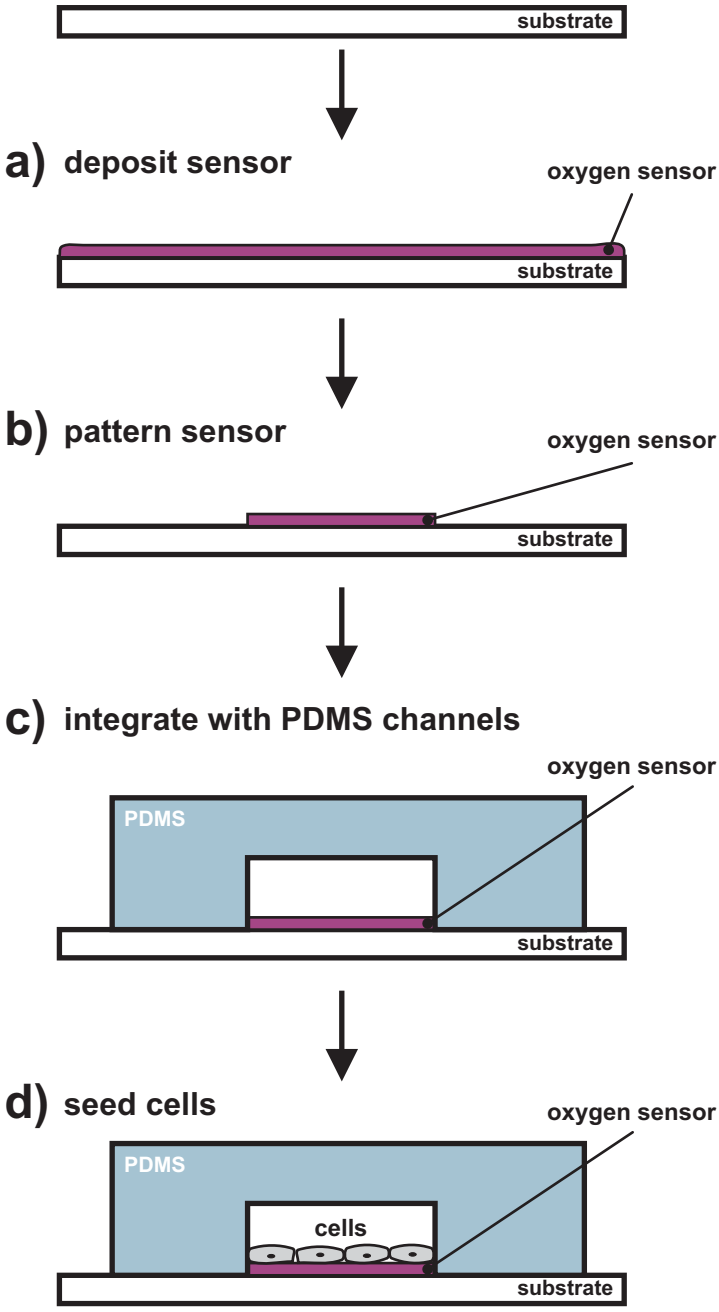

Figure 5.3: *Schematic of the sensor fabrication process. Starting with a substrate, a sensor film is deposited (a) and patterned (b) to a desired shape. This stack is then integrated (c) into PDMS-based microfluidic channels, providing the fluidic enclosure, and the structure is seeded with cells (d).*

subsequently apply photoresist on PtOEPK/PS films for standard lithographic patterning. In experiments performed with conventional positive tone resist (AZ1518, Microchemicals, Ulm, Germany) poor wetting of the resist on the PS film was observed. Figure 5.4 shows a photograph of a glass slide covered with PtOEPK/PS onto which photoresist was applied by spin-coating.

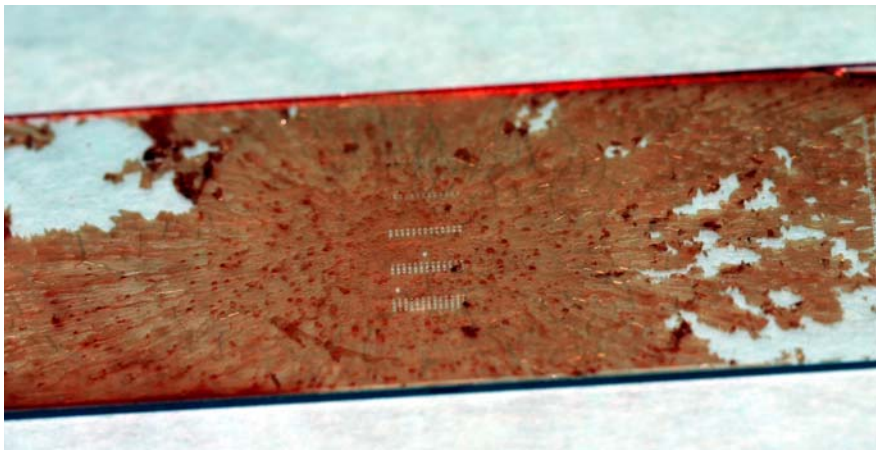

Figure 5.4: *Photograph showing de-wetting and adhesion failure of AZ1518 positive tone photoresist spin-coated onto a thin layer of PtOEPK/PS sensor material.*

As can be seen, during application the resist forms streak-shaped patterns due to solvent incompatibility and development in aqueous developer (AZ MIF300) leads to partial resist lift-off. Furthermore, removal of the photoresist with acetone after exposure and development, lead to the destruction of the underlaying PtOEPK/PS film surface.

Vollmer et al. [115] proposed photoresist lift-off in combination with pipetting of individual PtOEPK/PS patches through openings in the resist. They demonstrated an integrated oxygenator device with two large, manually deposited sensor patches and successively calibrated these for DO measurement. However, employing the same technique we were unable to obtain good sensor adhesion both on untreated and pre-etched glass substrates. Sensor membranes repeatedly lifted-off together with the photoresist mask, either due to the cohesive strength of the dried PtOEPK/PS film or due to delamination by the lift-off solvent used. The following discusses the method proposed in literature and compares it to an alternative method developed as part of this thesis.

5.2.2 Deposition of the Sensor Layer

5.2.2.1 Substrate Etch and Pipetting of Sensor Films

The application of a thin film of oxygen sensitive dye PtOEPK was tested on various substrates including PS Petri dishes, PDMS covered microscope slides and standard glass microscope slides. Glass microscope slides are the preferred substrate for two reasons: first, compatibility of glass with PDMS plasma bonding to form an irreversible seal between substrate and the PDMS-based bioreactor device, and second, because the glass substrate reduces oxygen diffusion to the sensor through the substrate to a minimum. This allows for faster equilibration of the sensor layer to the measurement environment.

For the sensor deposition experiments 5% and 7% w/w solution of PS without PtOEPK dye were prepared as a dummy sensor layer by dissolving PS (Sigma Aldrich, 200k M_W) in toluene. This was done to conserve the fluorescent dye since prior testing had not shown any significant difference in the surface properties of PS films with or without PtOEPK.

The first PS application method investigated is based on the method described by Vollmer et al. [115]. Hereby a commercial glass etch is used in combination with photoresist to provide a locally defined recess (7-10 µm deep) in the glass substrate. Due to export restrictions the particular etch (Armour etch) employed by Vollmer et al. was not available for use outside the United States of America. Buffered hydrofluoric acid (HF) was therefore used as a substitute etch for the following experiments. HF is known to produce rough surfaces when used to etch glass, similar as described by Vollmer et al. [115] for the Armour etch. This is important as it will increase adhesion of the PS layer to the glass substrate from which it might otherwise be lifted off when exposed to fluid flow inside the reactor[1].

First experiments were performed by spin coating AZ1518 photoresist for 30 s at 2040 rpm on a standard 25 x 75 mm glass microscope slide (ESCO Products, Oak Ridge, NJ, USA), followed by a softbake of 60 s at 100°C on a hotplate. The resist was then exposed 20 s in a Süss MA6 mask aligner using a printed foil mask. After 45 s development in AZ MIF300 and rinsing with DI water a 5 min hardbake at 100°C was

1.This is also the function of the recess in the substrate.

performed on a hotplate. Samples were then etched in buffered HF and rinsed thoroughly. Figure 5.5 shows the etch rate calibration data, from which an etch rate of 0.23 µm/min was determined. Samples were etched for 30 min to give an etch depth of 6.9 µm,

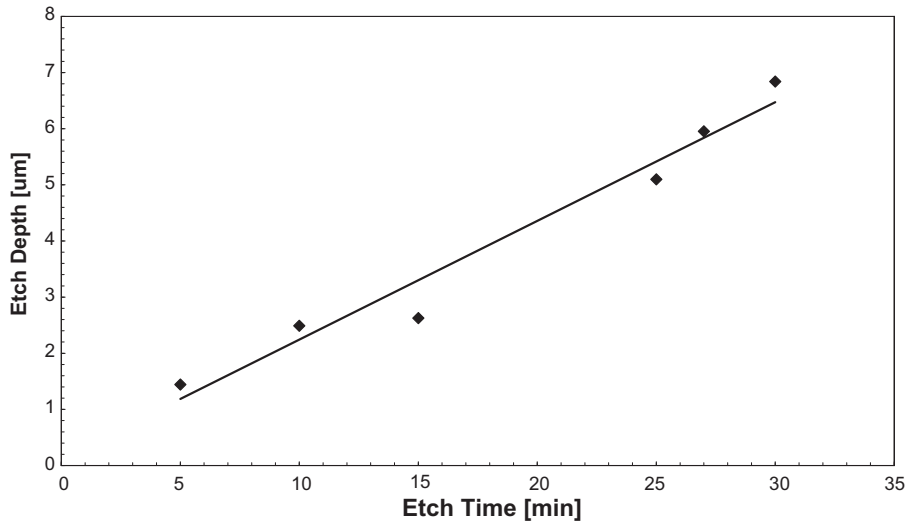

Figure 5.5: *Etch depth in glass slide for buffered HF with PDMS mask.*

approximately matching the value used by Vollmer et al. [115].

Remaining AZ1518 was stripped and re-applied as described above. The same mask was aligned to the etched pattern, the photoresist was re-exposed and developed. Depending on pattern size, 1 to 3 µl of PS solution were applied by pipetting to the exposed areas. Sensor patches were left to evaporate the toluene solvent overnight and the resist was stripped using acetone on the following day. It was observed that the majority of PS patches produced in this manner lifted-off completely with the photoresist. This was the case even in the dedicated sensor areas where resist was removed prior to PS application and the underlaying glass surface was pre-etched. Due to unavailability of the glass etch used by Vollmer et al. [115], it could not be determined whether this was due to a reduced roughness of the HF etch compared to Armour etch. Visual observation of the bottom of the etched patterns showed significant roughness (Fig. 5.6).

The same experiments were further repeated with bottom/top open PDMS stencils as etch masks to allow for extended etch times compared to AZ1518 photoresist. Stencils were created as described in Chapter 3 by molding against a resist master. For etching, the

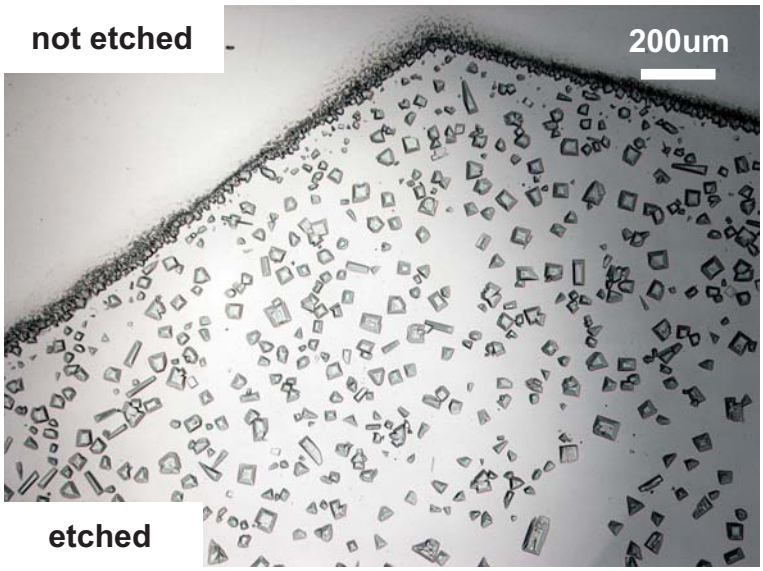

Figure 5.6: *Micrograph of a microscope slide surface etched in buffered HF for 30 min using a PDMS stamp as etch mask.*

stencils were brought into reversible contact with the glass substrate and the samples immersed in buffered HF for various times. After etching samples were rinsed thoroughly with DI water, immersed in DI water twice and rinsed again. Finally samples were dried using nitrogen gas and measured on a DEKTAK profilometer. As before the PS solution was applied by pipetting, however, in this case either with or without PDMS stamp attached. In the first case the resulting PS film was observed to peel of with the PDMS stamp after evaporation of toluene even if the film was confined to the glass recess only and not covering the PDMS. In the second case slightly better adhesion was observed, but the sensor confinement required greater care during application and showed large lateral thickness variation. Overall results from the above experiments indicated the need for a different, more reliable sensor fabrication method. While the advantages of the PtOEPK/PS material system for use as oxygen sensor are obvious, their integration into biological applications requires better control over sensor placement and film homogeneity than given by pipetting. To obtain high quality sensor films repeatable, a novel deposition method based on spin-coating was developed. The following section discusses this procedure and the properties of fabricated sensor films.

5.2.2.2 Spin-Coating of Sensor Films

The second PtOEPK/PS application method investigated is spin-coating, a standard industry process used for the application of thin films and photoresist to flat substrates. To deposit a film onto the substrate, the material of choice is dissolved in an appropriate solvent and the solution then spread over the rotating substrate by centrifugal force. Films applied by spin-coating exhibit high thickness uniformity and repeatability. The final film thickness is mainly controlled through the spin speed and duration, but it also depends on the concentration of the solution and the solvent used. Oxygen sensitive PtOEPK is readily dissolvable in a PS/toluene solution, making it well suited for application by spin-coating. Left at RT, spin-coated PtOEPK/PS forms solid films through evaporation of toluene.

The sensor material was prepared by dissolving PS pellets in toluene to yield 5% and 7% w/w solutions. Both solutions are based on PS purchased from Sigma Aldrich, with the 5% w/w solution corresponding to standard grade PS with a molecular weight (M_W) of 200.000 (Product No. 327786-1G), whereas the 7% w/w solution uses lower grade PS with an average M_W of 280.000 (Product No. 182427-25G). PtOEPK dye was added to the PS solution at 1 mg per 1 ml. Oxygen-permeable films of the PtOEPK/PS sensor material were prepared by pipetting approximately 200 µl of the solution onto clean 50 mm x 75 mm glass microscope slides and spinning for 30 s at different speeds on a standard spin-coater (WS-400B-6NPP-LITE, Laurell Technologies Corp., North Wales, PA, USA). After spin-coating, samples were left overnight at room temperature to evaporate the toluene. Thickness of the PtOEPK/PS layer was measured using a surface profilometer (Dektak, Veeco, Woodbury, NY, USA) at least 24 hrs after spin-coating. Figure 5.7 shows a plot of film thickness as a function of spin speed for the two solutions of PtOEPK in different M_W PS. The thickness was found to decrease linearly with increasing spin speeds. Optical inspection of the samples showed the formation of smooth, continuous films on the glass substrate. A quantitative test by blowing pressurized nitrogen onto the films further demonstrated good adherence of the sensor without the need to pre-etch the substrate. As discussed later, the optical properties of these spin-coated films were also very good.

With a reliable sensor deposition process in place it was then possible to develop a

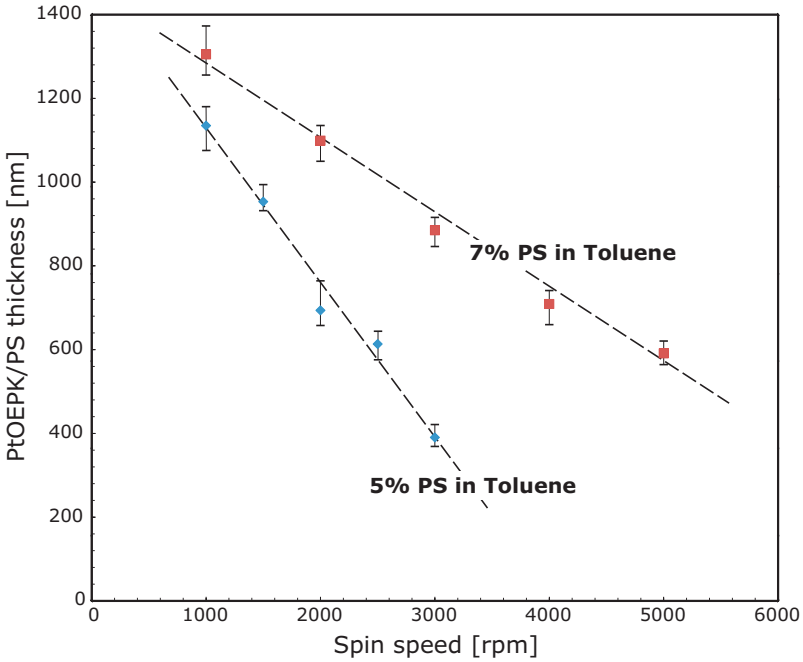

Figure 5.7: *Plot of sensor film thickness on glass microscope slides as a function of spin speed. Thickness was measured using a profilometer after spin-coating at the given speed for 30 s and evaporation of toluene (> 24 h at RT). For the 5% solution M_W 200.000 PS was used and for the 7% solution MW 280.000 PS, respectively.*

compatible patterning process, described in the next section. This process allows for the straightforward fabrication of laterally defined sensor structures and their integration at positions of interest within a PDMS-based microfluidic device.

5.3 Sensor Patterning

As discussed in the previous section, spin-coating can be used to fabricate high quality thin films of PtOEPK embedded in a PS matrix. Coated films exhibit excellent thickness homogeneity and repeatability due to the nature of the application process. When used as oxygen sensor these film properties lead to increased homogeneity and stability of the sensor signal intensity. Thus improved films, in turn, allow to implement fluorescent intensity-based, laterally resolved measurement of oxygen concentration. While spin-coated films can be applied to various substrates and directly used as sensors, their integration into microfluidic and PDMS-based devices in particular, requires a means to produce design specific sensor patterns. Due to differences in surface chemistry a

substrate fully covered in a PS thin film makes it significantly more difficult to achieve a permanent bond to a PDMS fluidic network with the established processes of surface activated PDMS-to-PDMS or PDMS-to-glass bonding. This problem can be avoided by limiting the PS sensor to areas within a particular fluidic feature such as a channel or reactor chamber. The PDMS device can thus be bonded to the exposed glass substrate surrounding the patterned sensor patches.

However, incompatibility of PS with common resist solvents, like acetone, makes it impractical to pattern the spin-coated films by photolithography. In experiments performed with conventional photoresist poor wetting of the resist on the PS film was observed (Fig. 5.4). Furthermore, removal of the photoresist with acetone after exposure and development lead to the destruction of the PS film surface. Hence, a different approach to sensor patterning was required. The process developed as part of this thesis and described in the following, relies on elastomer stamps for the definition of the pattern and oxygen plasma etching to transfer the pattern into the sensor layer, thus creating a completely “dry” patterning process.

PDMS was chosen as stamp material due to its material properties and ease of use. Pre-polymer mixtures of PDMS base and curing agent are routinely used in various applications to conformally replicate high resolution master patterns by a simple process of pouring, degassing and heat curing. The stiffness of the final stamp can, to a certain degree, be adjusted by increasing or decreasing the base/curing agent beyond the prescribed 10:1 w/w mixing ratio given in the Sylgard application notes [119]. For use as masks the stamps are brought (pattern side down) into conformal contact with the sensor film to be etched. After the etching step the stamps are peeled of the film and can be re-used. Figure 5.8 shows a schematic summarizing the main steps of the sensor fabrication process. Both positive and negative elastomer stamps can be fabricated.

The negative stamps (stencil masks) contain vertical vias for the RIE patterning, which can be problematic for isolated features. Hence the process was further extended to produce positive stamps supported on a PDMS substrate. The positive stamps contain a 100-200 µm thick pattern detail part and a thicker PDMS backing that laterally overhangs the pattern by several millimeters and simplifies the stamp handling during placement. The extent of this overhang is determined by cutting away excess PDMS around the

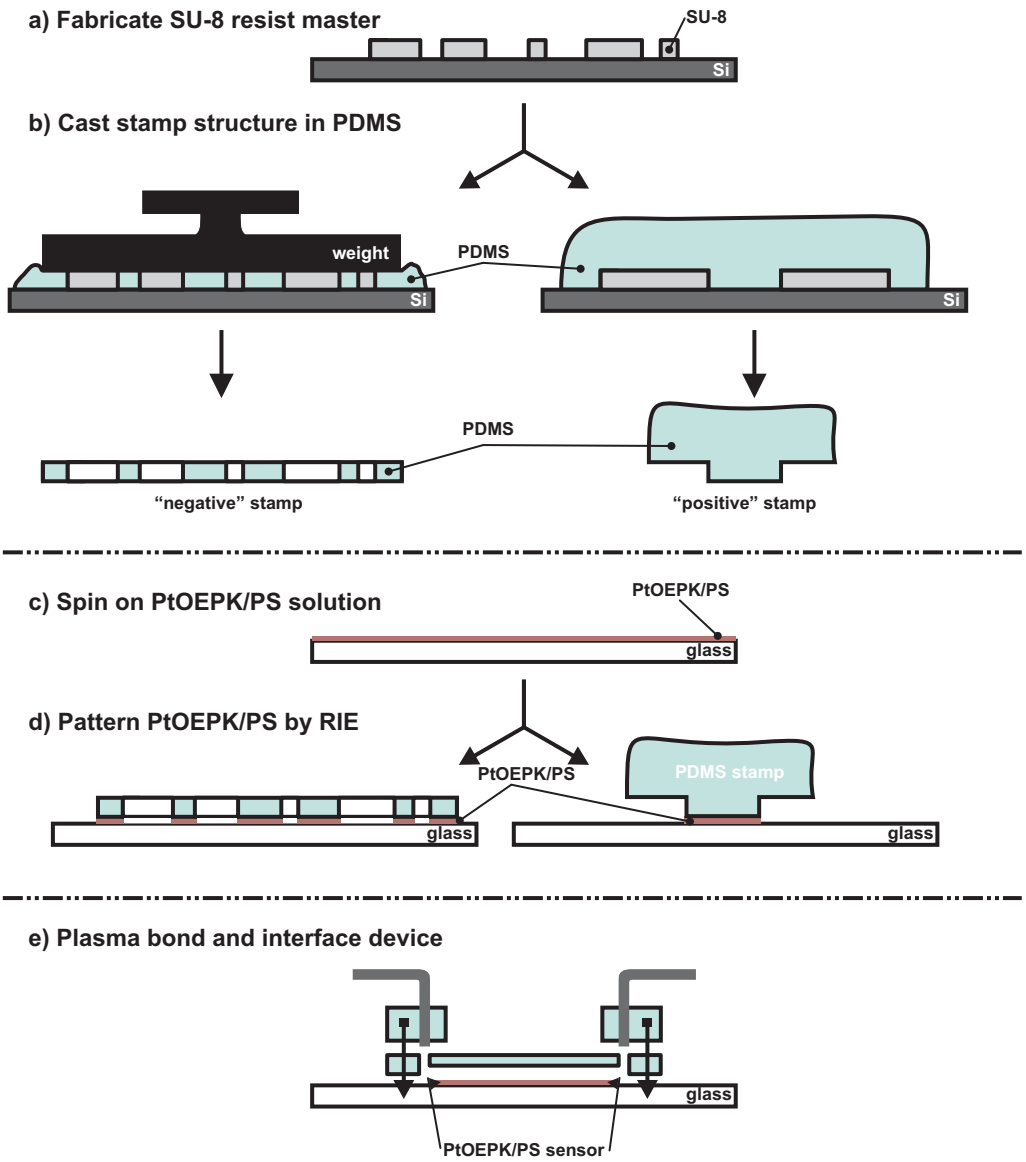

Figure 5.8: *Schematic depicting the main steps of the sensor patterning process: (a) A resist master of the negative or positive stamp pattern is fabricated in SU-8 photoresist, (b) the stamp is replicated in PDMS and released for use as mask. (c) PtOEPK/PS solution is spin-coated onto a clean glass slide and the solvent toluene is evaporated. (d) The stamp is brought into conformal contact with PtOEPK/PS film and the pattern is transferred into sensor layer by oxygen plasma etching. After etching the stamp is removed for possible re-use. (e) Finally, the sensor pattern on a glass substrate is integrated with a PDMS microfluidic device by plasma bonding.*

pattern areas. The patterning process, as well as experimental results for both stamps, will be discussed in the following. It will be shown that both positive and negative stamps can be successfully used for RIE-based pattern transfer despite the large backing structure.

5.3.1 Soft Lithography and Plasma Etching Process

PDMS stamps were produced by fabricating a master with the inverse of the desired sensor pattern in SU-8 negative tone photoresist on a 100 mm silicon wafer (Fig. 5.8(a)). As described in Chapter 4 the wafer is first covered with a thin, fully crosslinked SU-8 2025 adhesion layer. This is followed by applying a second, thicker layer of SU-8 2100. After a 2 h solvent removal bake at 95ºC on a contact hotplate, the layer was exposed through a mask containing the sensor pattern in a Süss MA6 mask aligner. This was follow by a post exposure bake of 40 min at 95ºC on a hotplate to activate resist cross-linking. Finally, development was performed by immersion in (1-methoxy-2-propyl)acetate and patterns were rinsed with isopropanol and blow-dried with nitrogen. To facilitate removal of the cured PDMS a fluoropolymer layer was deposited onto the resist mould. Meanwhile, liquid PDMS pre-polymer was prepared by thoroughly mixing 10:1 w/w base/curing agent. Prior to use the mixture was degassed in vacuum to remove any trapped air bubbles. The pre-polymer was then poured onto the resist master. It is then cured on a hotplate at 80ºC for 90 min. By using a weight to expel excess PDMS and the corresponding master, a negative stamp can be produced. To obtain a positive stamp the pattern detail replicated from the master is reinforced by a thick PDMS backing. The fabrication of a negative stamp is depicted on the left and that of a positive stamp on the right of Fig. 5.8(b). Once cured, the PDMS replica of the stamp pattern was carefully peeled off and the backing cut to size using a scalpel.

For patterning, the stamps were brought into conformal contact with the PtOEPK/PS layer formed on clean glass microscope slides by spin-coating and solvent evaporation (Fig. 5.8(c)). The stack was then placed in an Oxford Plasmalab 80Plus reactive ion etcher and the layer was etched using oxygen as the reactive species (Fig. 5.8(d)). The etching conditions used were 50 sccm O_2 flow rate, 0.55 Torr etch pressure and 200 W RF power applied for a typical etching time of 5 min or more depending on the film thickness of the spin-coated sensor layer. For a discussion of the plasma conditions and chosen etch pressure in relation to the successful use of “positive” stamps see the next section.

After plasma etching, PDMS stamps were peeled off and could be re-used. Prior to characterisation, sensors were stored in the dark to prevent possible long-term

photobleaching. PDMS stamps and PtOEPK/PS sensor patterns were imaged using SEM, optical microscopy and fluorescence microscopy. SEM micrographs were recorded using the imaging function of a Raith 150 electron beam lithography system, as described in detail in Chapter 4. Differential interference contrast (DIC) in reflected light on a Nikon Eclipse 80i fluorescence microscope with a 5x Nikon objective was used to record patterned sensor films. Due to the pattern size and amplification partial images were recorded and successively stitched on a PC running a freely available demo version of the *Autostitch* software package [120]. Fluorescent imaging was performed on the same microscope as used for DIC, but in combination with a Sony Digital Handycam in *Nightshot* mode for near infrared (NIR) image acquisition. A special filter combination with excitation/emission filters at 595/760 nm and a 620 nm dichroic mirror was purchased from Chroma (Rockingham, VT, USA).

5.3.2 Patterning Results

Following spin-coating, sensor films were patterned to micrometer resolution using elastomeric stamps and plasma-assisted RIE. When placed onto PtOEPK/PS films the PDMS stamp formed a conformal and reversible bond, protecting the area in contact from reactive species produced in the etch chamber. RIE with O_2 as reactive species was chosen as method of pattern transfer due to superior etch uniformity and the possibility of batch development. Wet etching with acetone or selective dissolution in the PS solvent toluene were discarded as possible alternatives due to excessive isotropy observed in initial trials.

Etching conditions for the RIE process were adapted from data published by Taylor et al. [121] for films of pure PS. The process parameters reported in this work indicated a vertical etch rate of 27 nm/min and 108 nm/min for PS using a etcher with barrel reactor (100 W, 0.55 Torr, 100 ml/min) and pancake reactor (75 W, 0.025 Torr, 30 ml/min), respectively. Using these parameters with both available dry-etching systems (Oxford Plasmalab 80i, pancake reactor, and plasma asher, barrel reactor) sufficient or comparable etch rates for PS or PtOEPK/PS films could not be reproduced. Due to this, and considering the large backing of the supported positive stamps, new etch parameters were

determined. Process development was focussed in particular on the RIE system as the pancake design allows for better control of the etch direction.

A higher etch pressure of 0.55 Torr was chosen mainly to allow for increased underetching of the thick stamp support through the resulting decrease in etching anisotropy. Furthermore, the increase in pressure also facilitates the transport of the significant amount of reactive species required for etching to occur under the stamp overhang. Simultaneously the etching power was increased to 200 W due to the insufficient etch rates observed in the initial test. Using these values, the general, unmasked vertical etch rate of PtOEPK/PS in the Oxford Plasmalab 80i reactive ion etcher was determined to be 150 nm/min at 200 W power and 50 sccm O_2 flow rate, compared to 108 nm/min reported for pure PS at 75 W and 30 sccm [121]. For positive masks, the removal of PtOEPK/PS underneath the stamp support was found to depend on the feature height of the stamp pattern. For 100 µm high features a stamp backing overhang in excess of 5 cm could be routinely cleared in a 10 min etch compared to 7 min for 200 µm features. Figure 5.9 shows DIC micrographs of typical patterns replicated with both positive (a) and negative (b) stamps. The insets in Fig. 5.9 show photographs of the corresponding PDMS stamps with the thick support backing (a) and vertical through-holes (b) visible for positive and negative stamps, respectively. In the former, stamps are turned pattern-side down for use, whereas for the latter stamps are used more resembling a layer of photoresist and film removal is through the opening in the stencil, as seen in the inset in Fig. 5.9(b).

Figure 5.10 shows micrographs of a test pattern as PDMS stamp with a feature height of 150 µm (a), replicated by dry-etching into a PtOEPK/PS film (b) and fluorescent sensor signal of the film when exposed to an excitation wavelength of 590 nm (c). The sensor signal was measured before and after patterning and no change in intensity due to the oxygen plasma could be observed. As can be seen from Fig. 5.10(b) and (c), complex patterns such as text with 100 µm line width can be replicated. The only exceptions are enclosed ring structures, as found in the letter O, where the stamp prevents reactive species from entering the inside of the shape. This limitation however can be prevented during design of the pattern or by leaving an opening, as can be seen in the fern shape on the left side of Fig. 5.10. A variety of regular and irregular patterns were replicated and

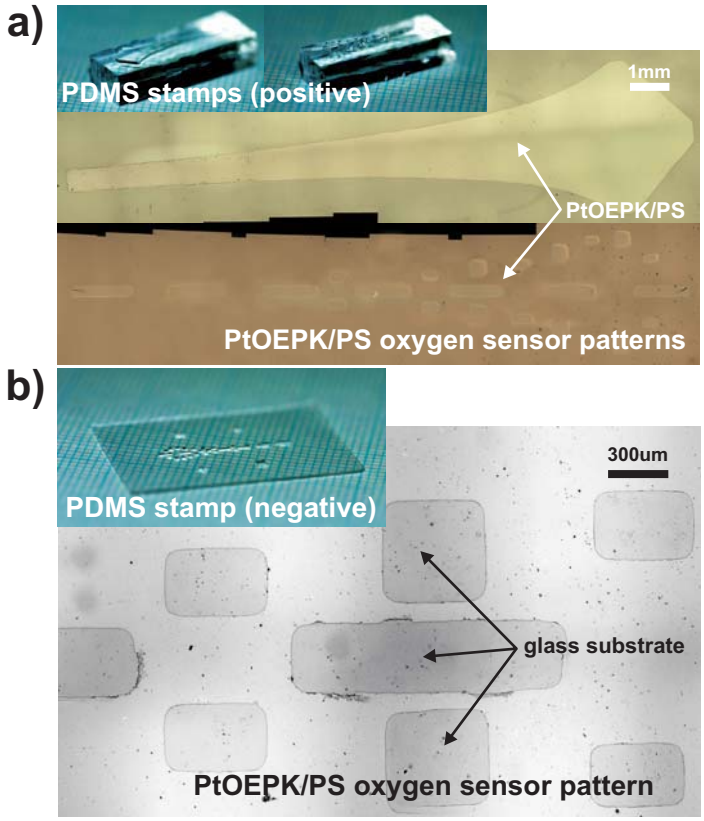

Figure 5.9: *DIC Micrographs of PtOEPK/PS patterns replicated by RIE with positive (a) and negative (b) PDMS stamps. The insets show photographs of the corresponding elastomer stamps used as etch masks.*

some are shown in Fig. 5.11. Minimum feature sizes in the range of 25 µm could be replicated with various different stamps and this could be repeated several times by re-using the same stamp. Pattern fidelity was found to be good and at the current stage resolution is mainly limited by stamp detail. This is due to the printed masks and their subsequent use in the SU-8 lithography. An example of a replication error is shown in form of missing sensor patches in the bottom pattern of Fig. 5.11. In this case, successive visual observation of the stamp and SU-8 mold showed that the errors were due to underdeveloped features on the resist master, which were then replicated in the stamp. In general, if greater stamp detail is needed, for example for single cell studies, master fabrication could easily be improved by use of glass masks. However, this would increase the process cost and decrease flexibility, while most PDMS-based LOC devices do not require higher resolution than provided with the current process.

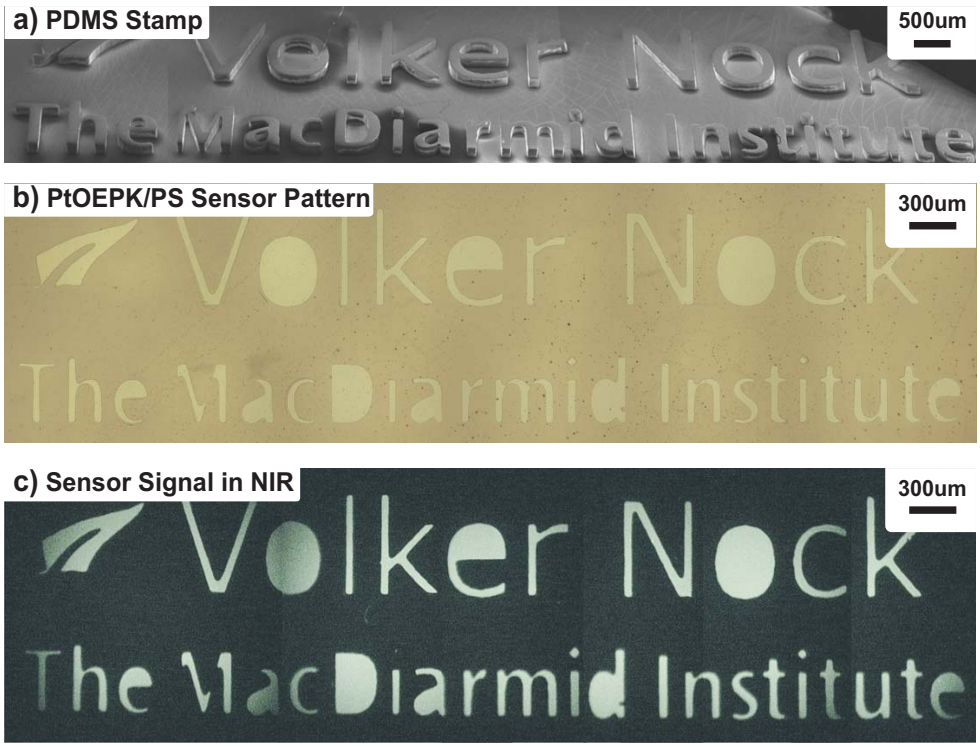

Figure 5.10: *Test pattern replicated in PtOEPK/PS by the fabrication process: (a) SEM micrograph of the PDMS stamp used as mask in the RIE step, (b) DIC image of the pattern in the PtOEPK/PS film after etching, and (c) fluorescent emission in the NIR from the same pattern under illumination with light of 590 nm wavelength.*

All the spin-coated PtOEPK/PS sensor films and individual patterns produced by RIE etching thereof exhibited excellent adherence under gas and liquid shear. From this observation it follows that no special pre-treatment of the substrate in terms of increasing the surface roughness or a recess is necessary. However, the fabrication process is applicable even in case of a substrate with pre-etched recesses. Figure 5.12 shows a micrograph of a 400 nm thin 5% w/w PtOEPK/PS film spin-coated onto a glass substrate at 3000 rpm. Prior to coating a 5 µm deep recess was etched using buffered HF. The etch was purposely chosen to produce a rough surface inside the recess for demonstration purpose. Spin-coating of PtOEPK/PS onto this substrate produced a continuos film covering the complete surface including the bottom of the recess. Using a PDMS stamp designed to the shape of the pre-etched cavity in combination with RIE the sensor pattern was confined to the part of the recess indicated in gray in Fig. 5.12. The thickness of the sensor layer was measured by performing a surface profilometry scan along the arrow

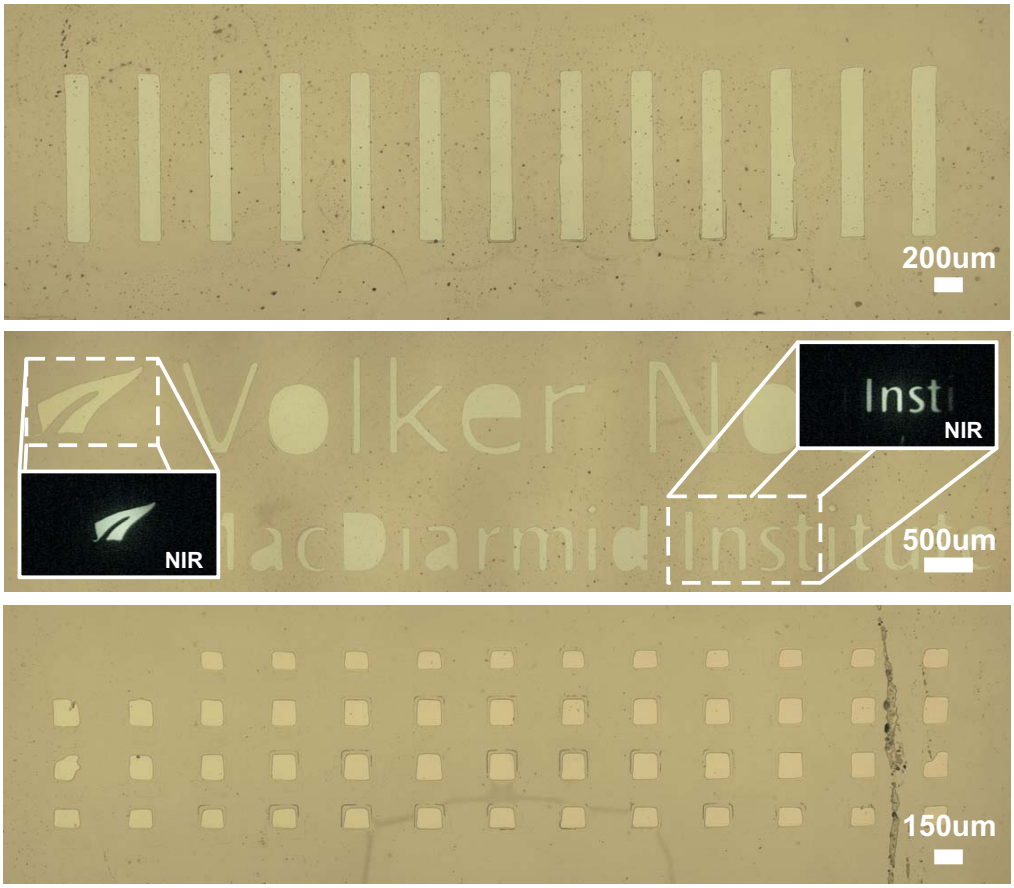

Figure 5.11: *Micrographs of oxygen sensor patterns fabricated by RIE. Pattern dimensions are defined using a positive PDMS stamp as mask. The insets show the sensor signal of the same pattern in NIR after RIE. Errors in the pattern transfer as visible in the bottom image are mainly due to defects in the PDMS stamp.*

labelled DEKTAK scan. As can be observed from the plot of the scan Fig. 5.12(a), a locally confined sensor pattern of constant thickness (~700 µm) was produced by the fabrication process inside the recess. This demonstrates the versatility of the process and its applicability to devices which require protection of the sensor layer and/or cells cultured on top of it from fluid shear.

With the demonstration of sensor film formation by spin-coating and high-resolution patterning, as shown above, the remaining step to a functioning device is integration of the sensor with a pre-fabricated PDMS microfluidic network. Since the patterning step not only produced locally confined sensor patches, but also removed excess PS of the substrate in regions unprotected by the stamp masks, it is now possible to apply oxygen plasma activation to the exposed glass surface and the PDMS channels for bonding. The

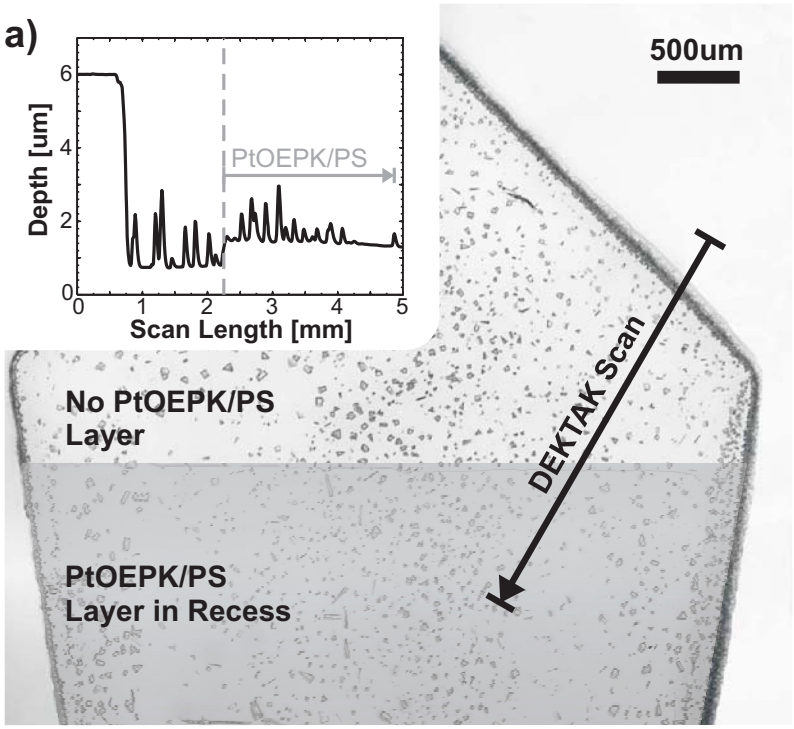

Figure 5.12: *Micrograph of a sensor pattern (gray) deposited onto a pre-etched recess in a glass substrate by spin-coating and RIE. The inset (a) on the top left shows a profilometer scan (arrow) indicating the 400 nm thick sensor layer.*

next section discusses the integration process and introduces a microfluidic chip for shear effect comparison. The chip features integrated oxygen sensors fabricated using a combination of the three process steps: PtOEPK/PS sensor spin-coating, patterning by RIE and integration via oxygen plasma bonding.

5.4 Sensor Pattern Integration

To demonstrate the complete fabrication process and its applicability to PDMS-based microfluidic devices, the two processes described in Section 5.2.2.2 and Section 5.3.1 were combined to produce a custom sensor pattern on a glass microscope slide. This slide was then irreversibly sealed to a corresponding fluidic channel structure in PDMS by oxygen plasma bonding (Fig. 5.8(e)). This process is the main method of producing irreversibly sealed microfluidic devices in PDMS. Both, the surface of the PDMS channel network and the glass substrate with the sensor pattern, were activated in the RIE using oxygen plasma, manually aligned and brought into conformal contact. Surface activation

was performed using the Oxford Plasmalab 80i RIE system with a 50 sccm O_2 flow rate, 75 mTorr etch pressure and 70 W RF power for a duration of 10 s [100]. Whilst not significant due to the very short application time, this surface activation step will lead to some etching of the sensor layer by the oxygen plasma.

A blunt needle was used to cut access ports and external fluidic interfacing was provided by insertion of *Microtight* tubing sleeves (Upchurch, Oak Harbour, WA, USA). For visualization the device was filled with red and blue dye-colored DI water. Measurement of the fluorescent sensor signal before and after oxygen plasma activation showed that the bonding process had no influence on signal intensity.

A plasma-bonded, fully assembled bioreactor device with external fluidic connections is shown in Fig. 5.13. Three cell culture chambers of different shapes and hence, different wall shear-stress profiles, are integrated on the chip. The lateral tapering of the middle chamber is specifically designed to generate a linearly increasing wall shear stress along its length. Sensor patterns in the individual chambers are restricted to the outlines by the patterning process described before. Flow direction through the device is from left to right, as indicated by the arrow in Fig. 5.13(a). A close-up of the middle PDMS chamber is shown in Fig. 5.13(b). The corresponding sensor pattern realized within the chamber was imaged in multiple, separate DIC images, which were then automatically overlaid to provide the complete micrograph shown in Fig. 5.13(c). Intensity images on the left and right of Fig. 5.13(c) show parts of the sensor response in NIR for exposure to air. The large sensor shape inside the chamber and the finer patterns in the in-/outflow channels were fabricated simultaneously with the same PDMS stamp, thus demonstrating the flexibility of the stamp patterning process.

Under certain circumstances, such as for characterisation of different substrates or sensor systems, it can be advantageous to be able to remove the channel structure from the substrate after use. In case of PDMS it is possible to obtain either a permanent seal by oxygen plasma bonding or a reversible seal by pressure clamping to the underlying substrate. For example, clamping was used to characterise several spin-coated oxygen sensor films for both gaseous and DO measurement with a single channel structure. After sensor signal measurement the reversible seal allows for removal and re-use of the channels.

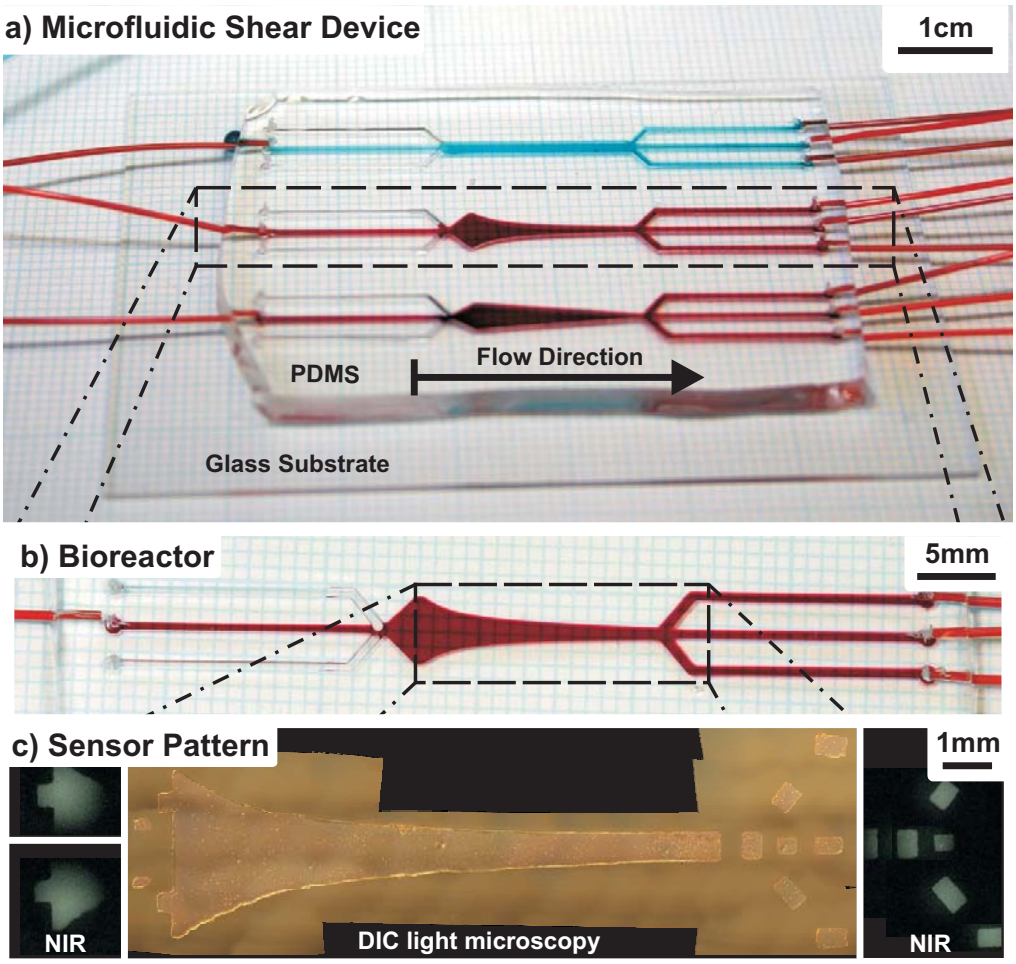

Figure 5.13: *(a) PDMS-based shear device with integrated oxygen sensors and external interfacing. Red and blue dye in DI water was flowed through the channels to aid visualization and to test fluidic sealing. (b) Close-up showing the central bioreactor device providing linearly increasing shear stress. (c) DIC light microscopy and NIR fluorescence images of the sensor patterns integrated into the bioreactor and inlet/outlet channels.*

To facilitate reversible clamping fluidic interconnects were machined into a transparent rectangular block of plexiglas. Tubing was inserted into the external holes and fixed with epoxy glue. Internal holes were machined to overlay the corresponding channel inlets on the PDMS device. A reversible seal was formed by sandwiching the glass substrate with oxygen sensor and the PDMS channel device between the Plexiglas block and the metal plate of a microscope stage warmer. The stack was secured using six screws, which could be individually adjusted to provide the best possible seal.

5.5 SUMMARY

This chapter has covered the development of a fabrication process to integrate polymer encapsulated fluorescent dye based oxygen sensors into PDMS microfluidic devices for in-situ DO detection. Integration of oxygen sensing into the devices introduced in Chapter 4 is essential to evaluate the species transport predictions made by the solution to the analytical model and CFD simulations in Chapter 3. Existing sensor fabrication methods proposed in literature were found to be unreliable and lacking in compatibility with layer-by-layer processing, as commonly used for fabrication of PDMS based microfluidic devices. Spin-coating of PtOEPK/PS sensor material was investigated as a robust alternative method for film formation. Sensor films deposited with this method were found to be well adhered without the need for a substrate pre-treatment. They further exhibited excellent thickness homogeneity and repeatability. Following film deposition, custom sensor patterns were fabricated using a newly-developed patterning process based on elastomer stamps and oxygen plasma etching. This process allowed to confine the sensors, initially spin-coated onto the whole substrate, to complex lateral shapes featuring high-resolution details. In the final step, patterned sensors were integrated with PDMS channel networks by oxygen plasma bonding to yield fully sealed devices with integrated optical oxygen sensors. Both oxygen plasma etching and bonding were found to have no influence on the sensor signal intensity.

With sensor integration completed, the following chapters cover the experimental procedures required for successful characterisation and calibration of oxygen measurement using the integrated PtOEPK/PS sensor system and their application to Lab-on-chip type devices. Since the spin-coating process produces very homogenous sensor films fluorescence intensity quenching was chosen as oxygen detection method for the following sensor characterisation experiments. As opposed to luminescent lifetime, intensity quenching has the ability to resolve laterally distributed oxygen concentrations within the device without the need for a complex scanning laser setup, resulting in a variety of potential novel applications for the sensors.

A theory is something nobody believes, except the person who made it. An experiment is something everybody believes, except the person who made it.

Albert Einstein
1879-1955, German-born
Theoretical Physicist

CHAPTER 6

Experimental Fluidic Setup

In the previous chapter a novel process for the integration of optical oxygen sensors into microfluidic devices was described. Prior to use the sensors have to be characterized and calibrated for measurement of gaseous or dissolved oxygen concentration inside the bioreactor. This is achieved by comparing the change in fluorescent sensor signal intensity for different solutions of oxygen concentration to a reference value provided by an external sensor. After recording the calibration graph, oxygen concentration is determined by comparing the change of sensor intensity for an unknown concentration to the corresponding value determined during calibration.

To facilitate sensor calibration, readout and successive use of the bioreactor devices for cell-based experiments an external fluidic setup has been designed. This chapter discusses the general requirements of the experimental setup and the individual components. The first section gives an overview of the experimental setup used for sensor calibration and characterisation. This is followed by a section on the main components of the fluidic circuit. The third section covers the generation and control of an oxygen reference source. Two alternative methods investigated for initial oxygenation of the carrier fluid are discussed in detail. The fourth and final section covers the optical sensor

readout and the data post-processing procedures used to generate the calibration for DO detection and in-situ measurement.

6.1 Overview of the Experimental Setup

Due to the non-contact nature of the optical sensing process readout of the bioreactor devices can be performed on any standard fluorescence microscope. The only adjustment required to the microscope for use with the PtOEPK dye is the addition of an appropriate filter cube and imaging device. The bioreactor device can be interfaced with common syringe or peristaltic pumps for external fluid actuation. Alternatively, on-chip fluid actuation could be realized by integration of microfluidic pumps and valves. For sensor calibration and for use in a cell-culture setup a gas-exchanger is integrated into the flow circuit to provide custom dissolved oxygen concentrations. Pressure driven flow (PDF) of controlled flow rate is generated using an external syringe pump. The pump is connected via tubing to a custom external or integrated gas-exchanger producing fluid flow with defined oxygen concentration. A bubble trap placed before the gas-exchanger and bioreactor chip removes potential bubbles in the fluidic circuit. The inlet oxygen concentration is determined using a flow through Clarke-type oxygen sensor and provides a reference value for calibration of the integrated oxygen sensor. The bioreactor chip itself is mounted on a temperature-controlled microscope stage of a conventional fluorescence microscope for oxygen sensor readout. An optional second Clarke-type sensor can be installed at the device outlet to provide a further reference value for the oxygen concentration after the liquid has passed over the cell culture inside. Finally, the liquid is collected in a waste container for biochemical analysis to determine cell function and metabolisms. The following sections provide a detailed introduction of the individual parts of the experimental setup.

6.2 Fluidic Circuit

Fluid actuation and generation of PDF in the flow circuit is provided by a dual push-pull syringe pump (PHD 2000, Harvard Apparatus, Holliston, MA, USA) in combination with standard 60 ml plastic syringes. The syringe pump, shown in Fig. 6.1, allows precise

control of the fluid flow rate from 0.0001 µl/hr to 220.82 ml/min with an accuracy of ±1%. This covers the entire projected range of inlet velocities required to investigate the effect of wall shear stress on species transport inside the bioreactor. In addition, due to the capability of using two syringes in parallel, the pump allows one to simultaneously generate multiple flows of different oxygen concentrations when used with multiple gas exchangers. Initial sensor calibration experiments were performed using DI water as oxygen transport medium. For final application in conjunction with live cells pure DI water was replaced with Dulbecco's Modified Eagle's Medium (DMEM) as carrier fluid. DMEM is a variation of Eagle's Minimal Essential Medium and is based on pure water supplemented with various amino acids, inorganic salts (potassium chloride, magnesium sulfate, sodium chloride, and sodium dihydrogen phosphate), glucose and vitamins (folic acid, nicotinamide, riboflavin, B-12), among others [122].

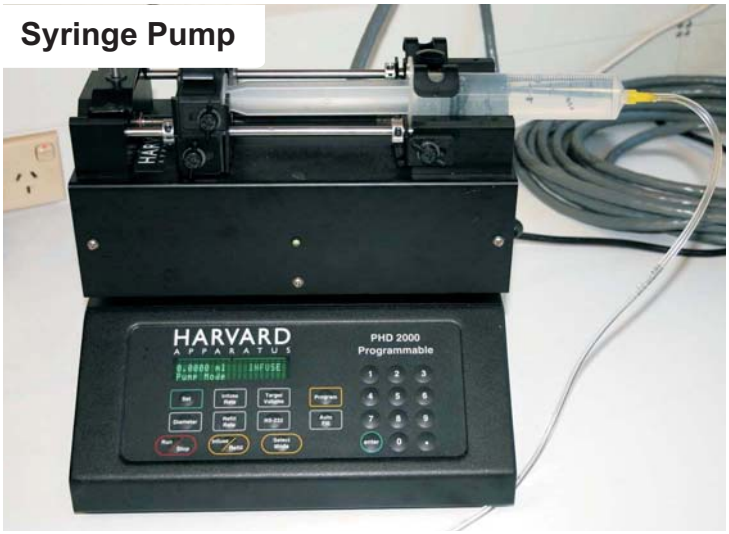

Figure 6.1: *Photograph of the syringe pump used to provide PDF with constant flow rate.*

From the pump the fluid is transported through transparent *Masterflex* tubing (Tygon Lab, Cole-Parmer, Vernon Hills, IL, USA) with an internal diameter of 1.6 mm to a custom bubble trap. The Tygon-type tubing was chosen because of its relatively low gas permeability of 80 and $40*10^{10}$ cc*mm/(cm^2*s*mmHg) in relation to oxygen and nitrogen, respectively [123]. Figure 6.2 shows a photograph of the trap used to remove air bubbles from the fluidic circuit.These bubbles can be introduced by initial filling of the

syringe. In the trap, bubbles entering through a short inlet tube rise up and are thereby prevented from leaving the device through the longer, lower outlet tube. Removal of the bubbles from the fluid is essential, as trapped air could influence measurement results by introducing local oxygen variations. Furthermore, the excessive shear stress created by the air-liquid interface transition of enclosed air bubbles over cells cultured inside the bioreactor device has the potential to rupture cell membranes [124] and ultimately cause cell lysis.

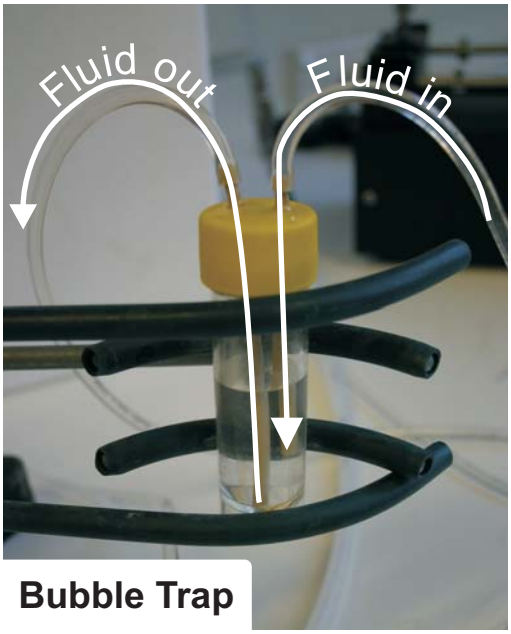

Figure 6.2: *Photograph of the custom bubble trap used to remove bubbles from the fluidic circuit.*

6.3 Oxygen Reference

Since the integrated oxygen sensor patterns are to be used for detection of an unknown DO concentration, sensor response has to be measured for exposure to liquid flow of different, known oxygen concentrations. The resulting calibration curve can then be used to correlate sensor intensity to oxygen concentration. This initial calibration therefore requires a device capable of transferring gas molecules from their gaseous state into solution form in a controlled manner. One method commonly used for this is to bubble the gas of interest directly into the fluid while it passes through an enclosed container. The

main disadvantages of this method are the relatively large quantity of liquid needed to prime the container and the potential introduction of bubbles into the microfluidic circuit. Both issues can be critical in conjunction with biomedical applications. If used in a dialysis-like system, the former can lead to a drop in blood pressure in a patient attached to the device due to the limited total blood volume available in the human body, whereas the latter has the potential to induce stress on cells in culture. To avoid these problems two versions of diffusion-based gas exchangers, external macro-scale and integrated micro-scale types, were constructed and investigated. Controlled oxygenation of the carrier fluid via a gas exchanger relies on several parameters in these devices. The following section introduces these parameters and a brief derivation of the theoretical model for oxygen solubility.

6.3.1 Oxygen Solubility

In microfluidic applications and BAL and cell-culture devices in particular, oxygen supply is limited by the solubility of oxygen in the carrier fluid. Oxygenation of a liquid, such as water, is related to the general solubility of the gas in the respective liquid. This solubility, and thereby maximum concentration of DO obtainable, is dependent primarily on the three variables pressure, temperature and concentration of dissolved salts. For a constant temperature the solubility in water can be described by Henry's law[1]:

$$f_{oxygen} = k \cdot x_{oxygen}, \tag{6.1}$$

where f_{oxygen} is the fugacity, x_{oxygen} the mole fraction of the solute and k is a proportionality constant. When taking in account temperature and pressure, this simple equation can be extended to a more generalized expression for oxygen solubility in air-saturated water:

$$S' = 3.936 \times 10^{-4} \cdot \alpha \cdot (P_T - p_1) mg/l, \tag{6.2}$$

1.Formulated by William Henry, 1775-1836.

where *S'* is the oxygen solubility, α is the Bunsen absorption coefficient, P_T the total pressure and p_1 the water vapor pressure [125].

Table 6.1 lists a selection of solubility values of oxygen in water for certain salt concentrations and temperatures, including 37.4°C for cell-culture conditions, at a total pressure of 760 torr. As can be seen from Table 6.1, oxygen solubility decreases with both increasing water temperature and salinity. Additional values dependent on salt concentration, temperature and pressure are tabulated in [125] or can be obtained graphically from the nomogram reproduced in Appendix F. From this decrease in oxygen solubility with salt concentration follows that the maximum amount of DO dissolved in physiological salines, such as blood plasma and nutrient solutions used in cell-culture, will be lower. If not otherwise indicated, calibration and oxygen measurement results in the following sections relate to data for pure DI water.

Cl^- [g/1000 g]	0	8	20
Temperature [°C]	**Oxygen Solubility [mg/l]**		
0	14.5	13.3	11.3
10	11.3	10.4	9.0
20	9.1	8.5	7.4
30	7.5	7.0	6.1
37.4	6.7	6.4	5.9

Table 6.1: *Solubility of oxygen in water as a function of temperature and salt concentration for a pressure of p_T = 760 torr (Adapted from [125]).*

6.3.2 Reference Oxygen Sensor

The DO concentration in the fluid after the gas exchanger is monitored via a reference oxygen sensor (DO-166FT, Lazar Research, Los Angeles, CA, USA). This amperometric sensor is based on a Clarke-microelectrode inserted into a flow-through housing made from acrylic. Figure 6.3 shows the individual components of the reference sensor: control electronics housing the signal amplifier with zero-point and calibration adjustment

screws (a), the voltage meter showing the oxygen concentration in millivolt (b), and the flow-through cell with inserted microelectrode (c).

Prior to use as reference the DO-166FT sensor is calibrated using a two-point calibration procedure. The first point corresponding to zero DO concentration is obtained by using the microfluidic circuit to flow nitrogenated water through the sensor and by adjusting the amplifier to zero millivolt output signal. For the second point, air-saturated water is flowed through the sensor chamber. The calibration value of the amplifier is then adjusted to coincide with the corresponding DO concentration previously calculated for the local temperature and partial pressure using Equation (6.2). Following oxygenation in the gas exchanger and measurement of the DO concentration in the reference microelectrode sensor, the fluid enters the bioreactor device placed on the stage of a fluorescence microscope through further Tygon tubing.

6.3.3 Macro-scale Gas Exchanger

The first, macro-scale gas exchanger was constructed as a hollow fiber flow-through device based on a design proposed by Hamilton et al. [126]. The device utilizes the gas-permeability of silicone-based tubing to diffuse gas molecules from a pressurized gaseous environment to a fluid flowing through the tubing coiled inside the container. This design reduces the amount of liquid needed to prime the device to the volume contained inside the tubing. Depending on length and diameter of the tubing this volume can be adjusted to meet the constraints of the perfusion experiment.

Figure 6.4 shows a photograph of the external gas exchanger and the lid providing fluid and gaseous interfacing. The main compartment of the device is formed by a 1 l Pyrex bottle (Dow Corning, Midland, MI, USA) with a linerless polypropylene plug seal cap. Inside the container silicone tubing (Silastic, EW-96115-06, Cole-Parmer, Vernon Hills, IL, USA) is loosely coiled to provide maximum exposure to the introduced gases. Gas and fluid interfaces were integrated into the cap by drilling and insertion of stainless steel push-in fittings (Norgren, Auckland, New Zealand) and coned ports (Upchurch, Oak Harbor, WA, USA), respectively. After insertion, the ports and a closeable pressure relief opening were sealed to the lid with two-part epoxy glue. Tygon tubing was used to

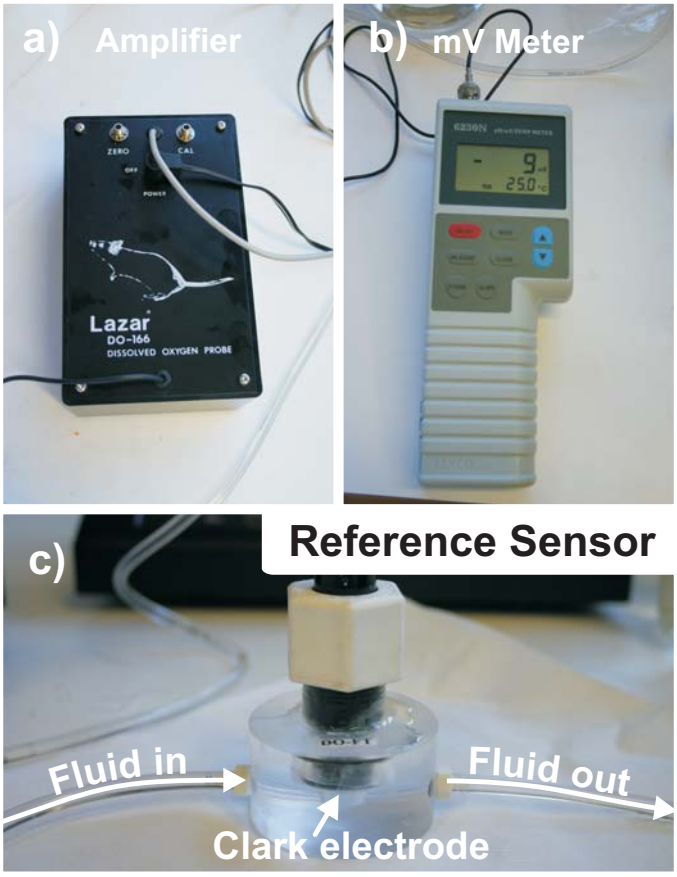

Figure 6.3: *Photograph of the flow-through Clarke-electrode. This sensor was used to provide DO reference values for calibration and monitor the bioreactor inlet concentration. The signal amplifier (a), voltage meter (b) and microelectrode sensor housing with fluid interfacing (c) are shown.*

connect ports on the gas exchanger to the bubble trap and the adjacent flow-through reference oxygen sensor. The gas fittings were connected via pressure regulators to nitrogen (oxygen-free) and oxygen (industrial grade) cylinders (BOC, Auckland, New Zealand). During experiments the Pyrex container was enclosed in a styrofoam box with a temperature sensor to provide stable environmental conditions. Prior to use of the gas exchanger, its oxygenation capability was measured using the Clarke-electrode reference sensor described before. At a flow rate of 0.5 ml/min the macro-scale gas exchanger was able to provide a maximum DO concentration of 18.4 mg/l or parts-per-million (ppm) in DI water while using pure oxygen gas for perfusion.

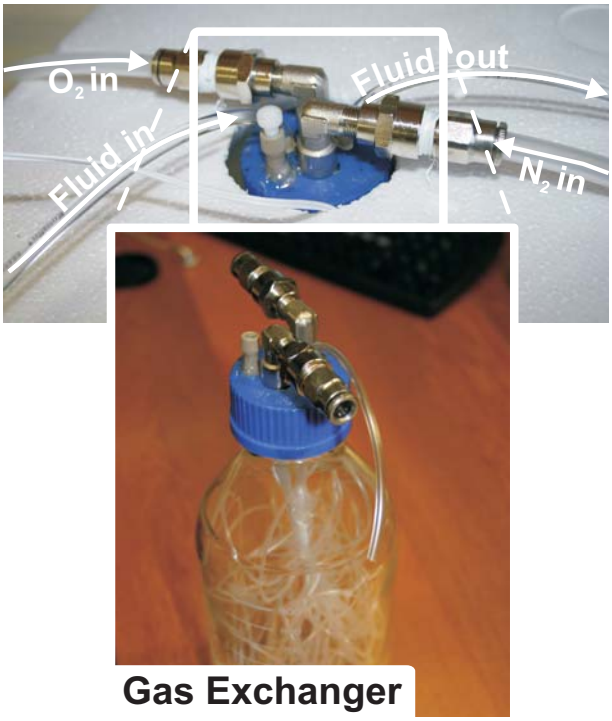

Figure 6.4: *Photograph of the macro-scale flow-through gas exchanger used to produce fluid flow of defined DO concentration. Top close-up shows the fluidic and gas interfacing.*

It should be noted at this point that mg/l is technically not a dimensionless number as required by the definition of the parts-per notation. However, ppm will be used instead of mg/l in the following to denote concentrations of a species in water to allow for easier comparison with data published in literature. While this use of ppm for water with a density of $\rho = 1000$ kg/m^3 is not uncommon, concentrations in other liquids will be given in SI-compliant units to avoid confusion.

6.3.4 Integrated Gas Exchanger

Dead fluid volume is a major constraint in biomedical applications. The total blood volume in a human patient is limited and any amount of blood removed from the body to fill an external system has the potential to further destabilize an already critical patient. In a bid to minimize the dead volume of the overall fluidic system, integration of the external gas exchanger on-chip was investigated using PDMS technology. Besides reducing the amount of tubing volume, this approach has the additional advantage that it reduces the

distance between the bioreactor and the gas exchanger. Oxygen concentration changes of the fluid bulk in the bioreactor can thus be realized faster due to the shorter distance. This could potentially enable the experimental observation of dynamic cell function in relation to changes of DO concentration.

The integrated gas-exchanger is based on a design proposed by Vollmer et al. [115]. In this design two layers of parallel channels are separated by a thin membrane of gas-permeable PDMS. The membrane allows gas molecules, and oxygen in particular, to diffuse from the top channels pressurized with the respective gas to the fluid flowing through the channels underneath. As mentioned above, this continuous diffusion-based gas transfer into the fluid prevents the introduction of gas bubbles, a problem commonly observed when actively bubbling gas through a fluid. PDMS exhibits high diffusivity for oxygen and other gases and is therefore well suited as membrane material. Table 6.2 lists the diffusivity of hydrogen, oxygen, nitrogen and carbon dioxide as observed for cured PDMS.

Penetrant	**D_{O2} x10^6 [cm^2/s]**
H_2	**140 ± 5**
O_2	**34 ± 1**
N_2	**34 ± 1**
CO_2	**22 ± 1**

Table 6.2: *Diffusivity of hydrogen, oxygen, nitrogen and carbon dioxide in PDMS at 35ºC (Adapted from [127]).*

Figure 6.5(a) shows a photograph of a single gas exchanger with 64 parallel channels. Incoming fluid is distributed to the individual channels from a single inlet, while gas moves through a meandering channel exactly overlaying the fluidic layer. The device was fabricated by replica molding of two 100 µm thick SU-8 molds on Si wafer. The first mold incorporates the structure of the fluid layer and was spin-coated with PDMS pre-polymer (Sylgard 184, 10:1 w/w base:curing agent, 1500 rpm for 30 s) to form the fluidic channel and the thin membrane separating gas from fluid. Simultaneously a second mold with the

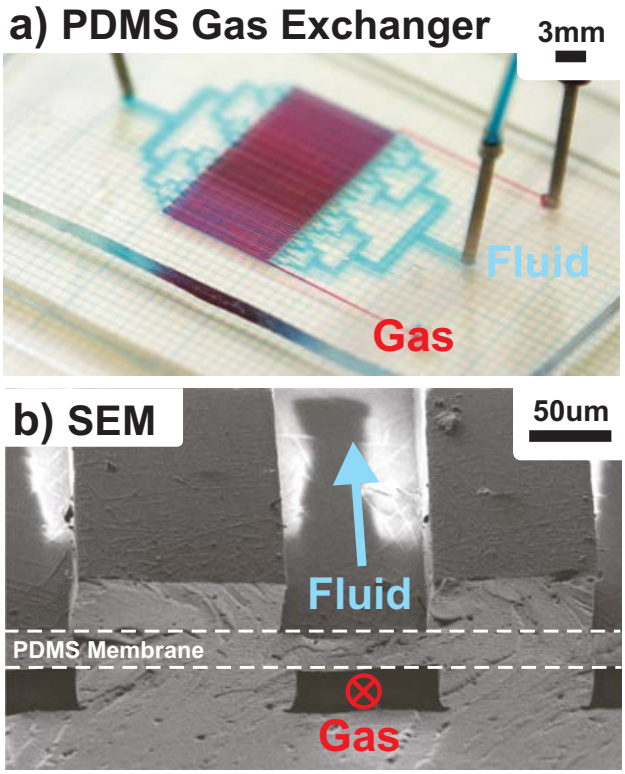

Figure 6.5: *Photograph of the integrated gas-exchanger in dual-layer PDMS. (a) A fluidic layer containing 64 parallel channels is bonded onto a glass substrate. Overlaying this is a second layer with the same number of channels for the respective gas. (b) SEM image of a cut through the device showing the two layers of channels. Both layers are separated by a gas-permeable PDMS membrane, allowing gas molecules to diffuse into the fluid underneath.*

gaseous layer design was replica-molded by pouring PDMS to a thickness of 10 mm. Both layers were partially cured for 20 min at 80ºC. The gaseous layer was then peeled off the second mold and both, the first mold and the gaseous layer were activated in oxygen plasma (500 W DC for 10 s). Following activation, both layers were manually aligned, brought into contact and left 24 h at room temperature to fully cure. A SEM image of a cross-cut through the fluidic layer is shown in Fig. 6.5(b). The fluid is transported through the upper channel while oxygen or nitrogen are applied to the lower channel and diffuse through the PDMS membrane indicated by the dashed lines. In the final device, shown in Fig. 6.5(a), this structure is inverted and plasma bonded onto a glass microscope slide to

provide fluidic sealing. For visualization the gaseous layer was filled with red and the fluidic layer with blue-colored DI water.

At a flow rate of 0.5 ml/min the integrated gas exchanger was able to provide a maximum DO concentration of 34 mg/l in DI water by flowing pure oxygen gas (industrial grade) through the top layer. While this is almost double the concentration of 18.4 mg/l, as obtained with the external gas-exchanger described in the previous section, the maximum value is lower than the 42.5 mg/l reported by Vollmer et al. [115] for a similar integrated device. However, the SEM image in Fig. 6.5(b) also shows that the membrane realized with the process described above is approximately 10 µm thicker than reported by Vollmer et al. This, in conjunction with a potentially different oxygen gas pressure in the gaseous layer, might explain the difference in DO between the two designs. If needed, the maximum value for DO can be further optimized by reducing the thickness of the remaining PDMS membrane during the spin-coating process or increasing the device area/number of channels.

6.3.5 Waste Collection

After passage through the microfluidic device the fluid enters further Tygon tubing and is transported to a Pyrex bottle. Depending on the device layout and application several bottles can be used for each bioreactor. Up to three outlets per reactor are realized in the current design. By utilizing the laminar flow regime this outlet layout allows to isolate individual parallel flow streams in the reactor after passage through the device. Each collected outflow can then be analyzed separately for biochemical markers and cell function indicators in relation to the respective oxygen concentration of the stream passing over the cells.

6.4 Optical Pick-up

Excitation and detection of the oxygen-dependent dye response are performed via standard epi-fluorescence microscopy. Central to the optical setup is a Nikon Eclipse 80i fluorescence microscope (Nikon, Lidcombe, Australia) providing the platform for sensor control and image acquisition. Figure 6.6 shows a photograph of the optical setup used for

flow experiments (a) and a close-up of the bioreactor device on the microscope stage (b). For measurement the bioreactor device is secured to the microscope stage and interfaced with Tygon inlet and outlet tubing. Depending on the device under test this is performed by either small, bonded PDMS blocks or a pre-machined plate of clear acrylic. The PDMS blocks and the acrylic plate allow rotation of the external tubing and syringes used as connectors by 90 degrees from vertical to parallel with the stage, thereby increasing the space available over the device for the microscope objectives. The stage of the microscope is augmented with a LEC059 microprocessor-controlled stage heater (LEC, Scoresby, Australia) consisting of a metal heat spreader with power resistor and external control electronics. This stage allows the sample under test to be maintained at a preset temperature of 37.4ºC during measurements. Keeping the temperature constant not only increases the repeatability of the calibration and stability of measurement, but also helps to provide the environmental conditions required for cell culture within the bioreactor. For use with the acrylic interconnect plate, the bioreactor device is sandwiched between the plate and stage holder. In this case the fluidic outlet holes on the PDMS chip are aligned with conduits pre-drilled into the acrylic plate and the sandwiching pressure can be adjusted via six screws from the plate to the metal stage holder.

Since the PtOEPK sensor layer exhibits an excitation peak at 590 nm in the visible range of the spectrum, it is illuminated through a custom filter cube using the high-power mercury light source of the Eclipse microscope. Light emitted from PtOEPK is shifted to a peak around 760 nm, detectable by Silicon-based semiconductors, such as CCD cameras. The long excitation/emission shift of PtOEPK allows for effective filtering using standard filter components. As a technique fluorescence-based oxygen sensing builds upon the basic principles of standard fluorescence microscopy. As shown in Fig. 6.7, the sensor is illuminated with its excitation wavelength range (blue) and, in return, emits in the range shifted relative to its excitation wavelength (red). A dichromatic mirror or beam splitter (green) acts as a high pass and prevents the excitation light from passing through to the detection system. Both wavelength regions are fitted to the absorption and emission spectra of the PtOEPK dye used and are defined by filters placed in the respective light path.

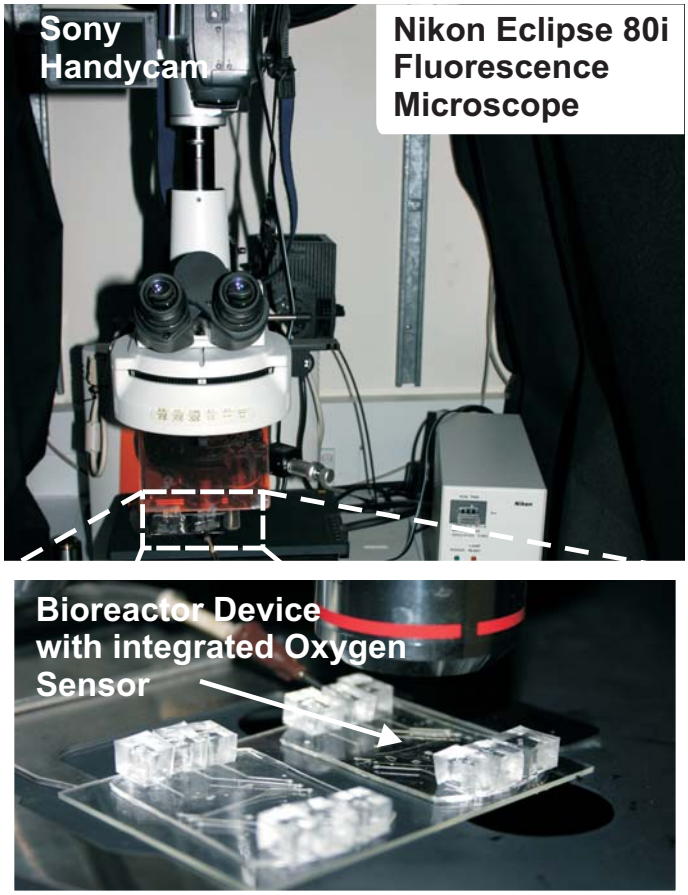

Figure 6.6: *Photograph of the optical setup for detection of the sensor signal and close-up of the bioreactor device on the microscope stage.*

An example of a filter cube arrangement is shown as inset in Fig. 6.7. The graph corresponds to a custom filter combination designed for use with PtOEPK with excitation/emission filters at 595/760 nm and a dichroic mirror with a cut-off wavelength of 620 nm (Chroma, Rockingham, VT, USA). The intensity information transmitted through the filter cube from the sensor pattern is recorded using a standard digital camera (DCR TRV520E Handycam, Sony, Tokyo, Japan), shown in the top part of Fig. 6.6(a). This camera is fitted with a *Nightsho*t mode, which allows to extend the usual imaging range from visible to NIR wavelengths. While the microscope comes fitted with a 5-megapixel high-resolution cooled color digital camera (DS-5Mc, Nikon), the integrated IR filters on this and other common microscope cameras prevent their use for NIR applications. Images are saved either in uncompressed JPEG-format color images

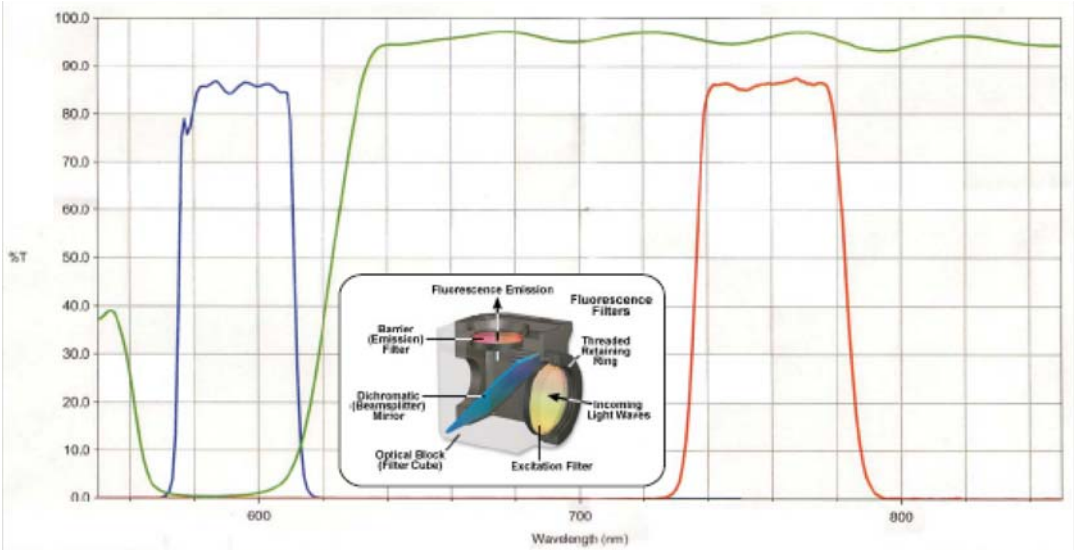

Figure 6.7: *Excitation and emission spectra of the filter set used for imaging PtOEPK sensors with the transmission curves of excitation filter (blue), emission filter (red) and dichromatic mirror (green) shown. The inset depicts a typical filter cube arrangement (Adapted from [128]).*

(640x480 pixels) on a *Memorystick* digital memory card or as film on a *Digital8* magnetic tape. Data captured as film was exported to a PC via the *Firewire* interface of the camera and snapshots were transcoded to BMP-format grayscale files (720x576 pixels) for intensity analysis.

Alternatively to the Sony camera, a dedicated NIR camera (Guppy F-038B NIR, Allied Vision Technologies, Stadtroda, Germany) was used. The Guppy camera features a firewire interface and is controlled directly via a PC running the AVT FirePackage software kit supplied with the camera. Grayscale images recorded through this software were saved as uncompressed Tiff files. Raw data from all image sources was imported into the Matlab (Mathworks, Natick, MA, USA) software package and processed for analysis using the integrated image processing toolbox.

6.5 SUMMARY

As with any sensor system, the right measurement setup plays an essential role in the quality of data obtained from the sensor itself. This chapter has introduced the external setup and all components used in conjunction with the integrated sensor film. Centered

around fluorescent microscopy as a non-contact sensor readout, the setup can be easily replicated using standard equipment available in biological laboratories. The main differences to conventional plate-based culture systems is the adoption of a fluidic circuit to provide continuous flow, the insertion of a custom filter cube, and the use of an IR camera. While the PtOEPK/PS sensor films can be used in static, non-flow systems, the current setup was developed deliberately to allow flow conditions for testing the target BAL devices.

The true delight is in the finding out rather than in the knowing.

Isaac Asimov
1920-1992, Russian-born American
Author and Professor in Biochemistry

CHAPTER 7

Oxygen Measurement

Use of the oxygen sensors for measurement of DO concentration requires initial calibration of the sensor film intensity response to certain, known oxygen concentrations. This chapter covers the use of the experimental setup, developed and described in the previous chapter, for characterisation and calibration of the integrated oxygen sensor patterns. The first section of this chapter describes the device interfacing together with data acquisition and post-processing. With this process in place, the second section summarizes experimental results for the detection of gaseous oxygen. Both, static calibration and dynamic sensor behavior for changes in oxygen concentration are outlined. As result from the initial sensor characterisation for exposure to gaseous oxygen, several parameters affecting sensor sensitivity were identified. These parameters and their optimization using the fabrication process are discussed in the third section. The fourth section covers the calibration of DO measurement in fluid flow and determines the dynamic operating range for use of the PtOEPK/PS sensor patterns at different flow rates. This is supplemented by a fifth section discussing the general application of the oxygen sensors to Lab-on-a-Chip devices via a demonstration of oxygen visualization, transverse graduation of the concentration profile and measurement of the coefficient of diffusion for oxygen.

7.1 SENSOR CHARACTERISATION

After fabrication, individual sensor pattern response was first characterized by exposure to different gaseous oxygen concentration for film comparison and to ascertain the suitability of the fabrication process. Successively patterns were then calibrated and used to measure the concentration of oxygen dissolved in a carrier fluid, such as water. To acquire the calibration curve, the microfluidic device was connected with the experimental setup and the fluorescence microscope was used to record the sensor response. Figure 7.1 shows a schematic of the experimental setup developed for calibration of dissolved oxygen measurements. First, an image with closed shutter was

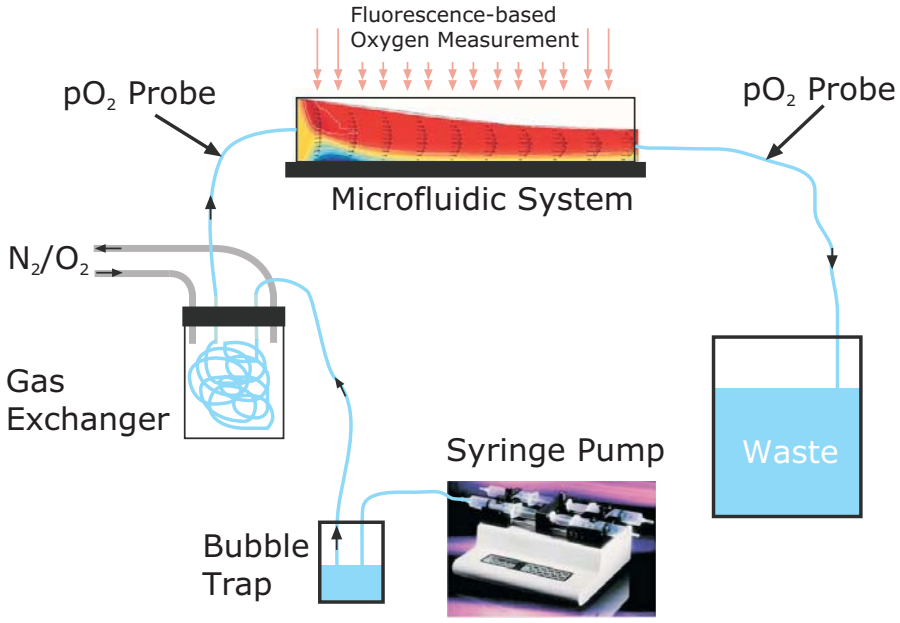

Figure 7.1: *Schematic of the external experimental setup used for the characterisation of local oxygen concentration measurement inside the microfluidic device. Sensor readout from the microfluidic system is performed by means of a fluorescent microscope and image capturing.*

recorded with the Sony microscope camera to eliminate CCD background effects and stray lighting. Following this, the lamp shutter was opened and images for the different gaseous oxygen concentrations were recorded. The images were then transferred to a PC in video or JPG file format, converted to grayscale and imported into Matlab using the

image processing toolbox. Intensity was averaged over a region of interest (ROI) within the complete image by use of a custom m-file script. Finally, the value obtained from this ROI was compared to the chosen reference intensity (pure oxygen-free nitrogen, I_0 ~ 0% O_2) and plotted versus the relative gaseous oxygen concentration.

The ratio I_0/I_{100}, in conjunction with the Stern-Volmer constant ${K_{SV}}^G$ or ${K_{SV}}^S$, is commonly used as an indicator of the sensitivity of the sensing film [129,130]. For reasons of better comparability of different sensor material systems, and as proposed by Amao [112], this ratio was chosen as a general measure of sensor sensitivity for the following experiments. Sensor materials with an intensity ratio I_0/I_{100} larger than 3.0 are commonly considered suitable for oxygen-sensing devices [131].

7.2 Gaseous Oxygen Detection

Before individual patterns and sensor films can be used to detect an unknown oxygen concentration, the change of fluorescent signal intensity has to be calibrated for exposure to a reference concentration. While the final goal is to use the sensors for detection of oxygen concentration in a liquid medium, initial calibration was performed for exposure to gaseous oxygen to better understand sensor characteristics and dynamics. This is especially useful since calibration with gaseous media has the advantage of reduced requirements on the experimental setup. Compared to liquid media, sealing is less critical and pumping is simplified by use of a pressurized gas source as supply, such as a standard gas cylinder. Devices do not have to be permanently sealed and switching between different oxygen concentrations (or gases) can be performed almost instantaneously. In addition to providing first data on sensor characteristics, experiments using gaseous oxygen also demonstrate the suitability of the patterned PtOEPK/PS sensors for gas-based detection applications, such as in food packaging [132]. The following two sections summarize results for static and dynamic gaseous oxygen measurements with sensor films and integrated sensor patterns [94].

For characterisation of sensor signal change in presence of gaseous oxygen the sensor patterns were exposed to pure industrial grade oxygen, oxygen-free nitrogen, air and mixtures of the three. All oxygen and nitrogen used in the following experiments was

supplied by BOC (Auckland, New Zealand) in standard D and G-sized gas cylinders fitted with the corresponding pressure regulators. The air used in experiments corresponded to a well ventilated room. Room temperature and atmospheric pressure were monitored for all experiments. Gases were applied to the sensor films and patterns either with or without PDMS channels bonded or clamped on top. The temperature of all sensor substrates, and thereby the sensor films, under test was kept at 37.4ºC using the microscope stage heater described in Section 6.4.

7.2.1 Static Gaseous Oxygen

For the calibration of static gaseous oxygen detection single images were recorded after equilibration with oxygen and the change of sensor intensity was analyzed using the image processing module of Matlab. Figure 7.2 shows a plot of 1/(fluorescent intensity) as a function of relative gaseous oxygen partial pressure for sensor patterns realized in a 400 nm thick PtOEPK/PS layer on a glass microscope slide as substrate. For this measurement PtOEPK was dissolved in a 5% w/w solution of PS (standard grade, 200k M_W), spin-coated and plasma patterned, as described in Chapter 5. The effect of intensity quenching by molecular oxygen leads to a significant increase in sensor intensity from the presence of pure oxygen (100% O_2) to air (~21% O_2) and to pure nitrogen (0% O_2), as is demonstrated by the intensity images on the right in Fig. 7.2. Superposition of the Stern-Volmer model, given in Equation (5.4), onto the data in graph in Fig. 7.2 indicates good agreement with linear sensor behavior for the region of interest. While this 3-point measurement is relatively crude and does not qualify as a comprehensive calibration, it nevertheless is useful to demonstrate sensor function and to determine sensor performance (in form of the sensor ratio I_0/I_{100}).

7.2.2 Dynamic Gaseous Oxygen

Dynamic sensor response to gaseous oxygen was measured by continuously recording sensor intensity for a total duration of 20 min. During this time the sensor layer was exposed to different oxygen concentration. Applied gases were switched between 0%, 21% and 100% relative gaseous oxygen concentration using a inline valve. The resulting

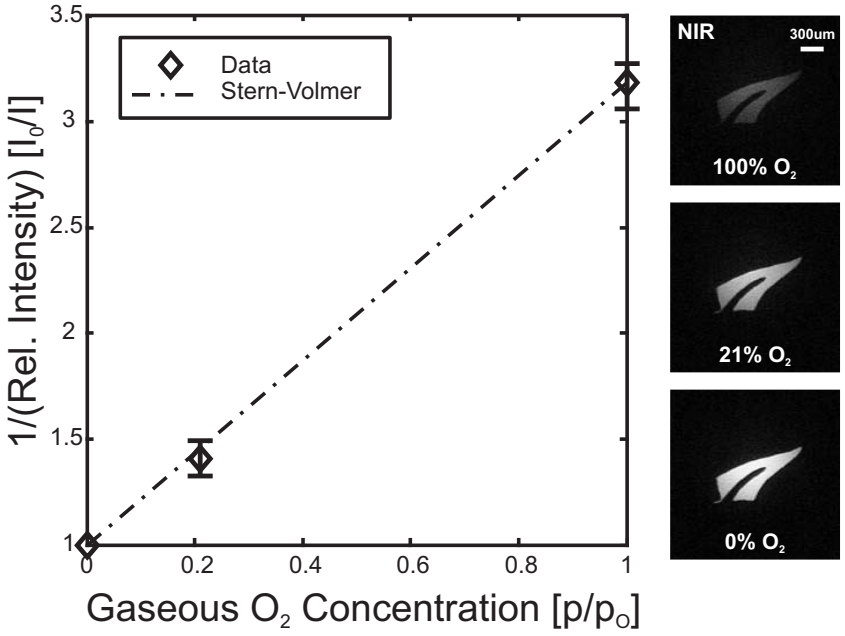

Figure 7.2: *Three-point calibration curve for the detection of gaseous oxygen with a 400 nm thick 5% w/w PtOEPK/PS sensor film pattern. The dashed line indicates the linear Stern-Volmer model. Fluorescence images on the right show the change in signal intensity in presence of oxygen from 100% O_2 to 0% O_2 (top to bottom).*

video of the sensor intensity change was then digitized and the change was analyzed on a single image, frame-by-frame basis in Matlab, as described above for static measurements. For all dynamic gaseous oxygen measurements no reduction of the sensor intensity due to photobleaching by the excitation source could be detected during the exposure period. This is a further demonstration of the excellent photostability of the PtOEPK fluorescent dye, as mentioned previously in Section 5.1.1.3.

Figure 7.3 plots 1/(fluorescent intensity) versus time for a section of data recorded for an unpatterned 1.1 µm thick layer of PtOEPK/PS. For this measurement PtOEPK was dissolved in a 7% w/w solution of PS (280k M_W) and spin-coated onto a glass microscope slide, as described in Section 5.2.2. The dashed lines in Fig. 7.3 indicate the intensity levels corresponding to 100% oxygen (O_2), ~21% oxygen (Air) and 0% oxygen (N_2). As can be seen, the intensity change follows the change in oxygen concentration almost instantaneously with an average rate of change of ~2.1 s^{-1}, making the PtOEPK/PS sensor

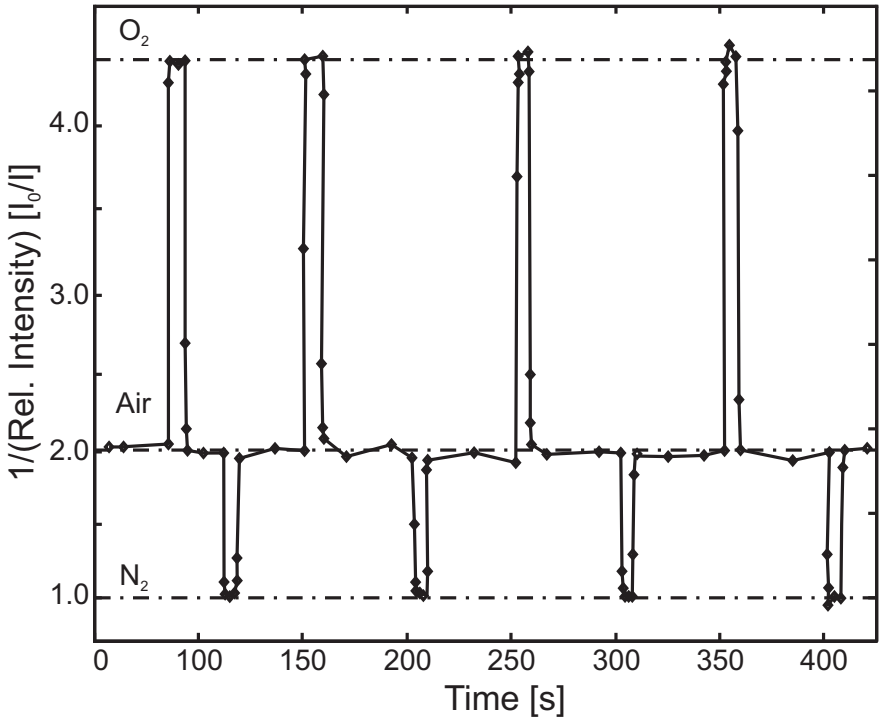

Figure 7.3: *Dynamic sensor response (relative intensity, I_0/I) for the detection of varying gaseous oxygen concentration. The sensor was exposed to different oxygen concentrations by alternating between oxygen-free nitrogen (0% O_2), air (~21% O_2) and industrial-grade oxygen (100% O_2), indicated in the graph by the dashed lines.*

system ideal for fast detection of changes in gaseous oxygen. The system further exhibits excellent repeatability over multiple cycles of switching between different concentrations, while retaining a high fluorescent signal intensity ratio I_0/I_{100}.

7.3 Sensor Signal Optimization

As explained above, the sensor signal intensity I of the different PtOEPK/PS films was measured for exposure to different gaseous oxygen concentrations just after spin-coating and patterning. Partial oxygen pressures of 0% (I_0) and 100% (I_{100}) were produced by blowing oxygen-free nitrogen and industrial grade oxygen, respectively, through the device and onto the sensor patterns. During this initial testing of the sensors it was observed that several parameters affect the final sensor signal ratio [10]. These parameters included both, molecular weight (MW) of the PS used, as well as the PS concentration

(% w/w) in the initial toluene solution. The strongest influence on the fluorescent signal intensity ratio I_0/I_{100} however, was found to be related to sensor film thickness. From an engineering point-of-view this is of great advantage, as the final thickness can be easily adjusted via the spin-speed during spin-coating of the sensor layer. The relationship between speed and sensor film thickness for different PtOEPK/PS solutions was discussed previously in Chapter 5. As was shown in Fig. 5.7, the film thickness decreased linearly with increasing spin-speed.

Using this relationship several samples with PtOEPK/PS films of different thicknesses were produced. Comparing the intensity ratios of these films revealed that the sensor signal ratio increases with decreasing film thickness. Figure 7.4 summarizes the corresponding results for two PtOEPK/PS mixtures at various thicknesses. The plot

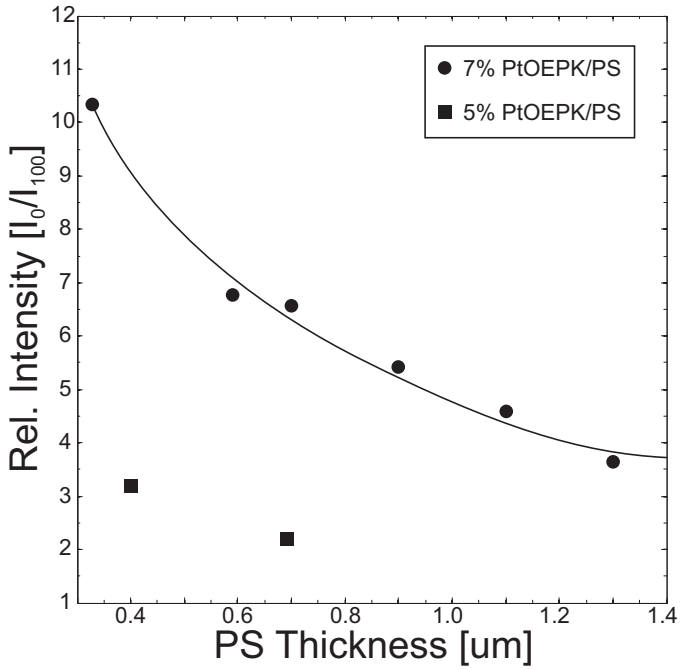

Figure 7.4: *Plot of the sensor intensity ratio I_0/I_{100} vs. film thickness for two PtOEPK/PS solutions (I_0 corresponds to 0% and I_{100} to 100% gaseous oxygen).*

shows the intensity ratio as a function of film thickness measured for the 5% and 7% PS solutions used in Section 5.2. For the 7% PS solution I_0/I_{100} increases almost two-fold from 3.6 at 1.3 µm film thickness to 6.8 at 0.6 µm. One possible explanation for this

increase in intensity ratio is the increase in the surface area-to-volume ratio. With decreasing film thickness the overall intensity contribution of dye close to the surface will increase, due to the fact that the permeability-limited intensity contribution from dye molecules in the PS bulk is reduced. The second observation from Fig. 7.4 is the dependence of the increase in intensity ratio on PS solution. A 0.7 µm thick film in 7% PS solution (MW = 280k) shows a three-fold increase in I_0/I_{100} compared to a 5% PS solution (MW = 200k) of equal thickness. This significant difference is mainly attributed to the higher molecular weight PS used in the 7% solution. During solvent evaporation the system of PS chains strives to attain a state of minimal energy by contraction. Molecules above the entanglement molecular weight of PS ($M_{e,PS}$ = 18k) are thought to contract more slowly with increasing molecular weight and to be frozen in place before complete solvent evaporation [133]. This formation of disordered molecule chains can lead to an increase in oxygen-permeability in PS films of higher MW.

Although preliminary, these results indicate further possibility for optimization of the sensor sensitivity through the use of thinner films and PS of different molecular weight. A fourth possible parameter not investigated here is the influence of the substrate material on sensor signal intensity. The maximum intensity ratio of 11 (average 10.4) for a 350 nm thick 7% PtOEPK/PS film is the highest reported on a LOC-compatible glass substrate. However, even higher values have been reported for films on a different substrate. Hartmann and Trettnak [134] observed an I_0/I_{100} ratio of 20 for a 20 µm thick (wet-layer thickness) PtOPEK/PS film on a mylar substrate. This indicates that the choice of substrate material could provide an additional parameter in optimizing the intensity ratio. In regards of device fabrication, especially for PDMS-based devices, some substrate materials might provide a high intensity ratio, however their use might be limited if the material is not compatible with commonly used processes, such as surface-activated plasma bonding. Notwithstanding the potential for further optimization, it should be noted that all the 7% PtOEPK/PS devices presented here exceed the intensity ratio of 3 required to be suitable for use as oxygen sensor.

7.4 Dissolved Oxygen Detection

The main application for the sensors develop as part of this work is the measurement of oxygen dissolved in aqueous media, such as full blood or blood plasma. In humans blood performs important transport functions for nutrients, oxygen and the removal of waste. It further acts as an essential part of the self-repair mechanisms of the body, conveys messaging functions and the regulates temperature. About 55% of the blood volume in an average human is made up of blood plasma, which in turn consists mostly (~90%) of water and some dissolved proteins, glucose, clotting factors, mineral ions, hormones and carbon dioxide.

Oxygen saturation in such an aquatic environment is a relative measure of the amount of oxygen dissolved in the water. For example, in freshwater under atmospheric pressure at 20°C, O_2 saturation is 9.1 mg/l. In addition to temperature and pressure, this value is also affected by the chloride (salt) concentration in the water and the maximum saturation decreases with increasing Cl^-. The latter gains further importance when biologically relevant solutions, such as cell-culture media, are considered. These usually contain multiple additives including amino acids, salts, glucose and vitamins depending on the formulation used. As with detection of gaseous oxygen, sensor response to DO has to be calibrated prior to use for DO measurement. The following two sections introduce the calibration procedure and give typical results for the calibration of intensity change vs. DO concentration and the measured operating range of the sensors in relation to flow rate [102].

7.4.1 Sensor Calibration for Measurement of DO Concentration

PtOEPK/PS sensor patterns were calibrated for DO measurement in aqueous media by flowing DI water of calibrated oxygen concentration through a bioreactor device, such as the one shown in Fig. 5.13. Characterisation experiments were performed with the microfluidic chip equilibrated to a temperature of 37.4ºC to ensure compatibility of the sensor test with cell-culture conditions. A sensor pattern, as depicted in Fig. 5.13(c), was fabricated by spin-coating and RIE patterning in 600 nm thick 7% w/w PtOEPK/PS on a glass substrate. The PDMS-based microfluidic part was manually aligned with the sensor

patterns and clamped using a block of plexi- glas for fluidic interfacing. Intensity images for the calibration were recorded on a rectangular sensor patch at the bioreactor exit. DO detection was successively calibrated with DI water of five different oxygen concentrations produced by the external PDMS oxygenator and determined using the Clark-electrode reference sensor. Figure 7.5 shows a typical calibration plot of relative intensity as a function of DO concentration at a constant flow rate of 1 ml/min. The

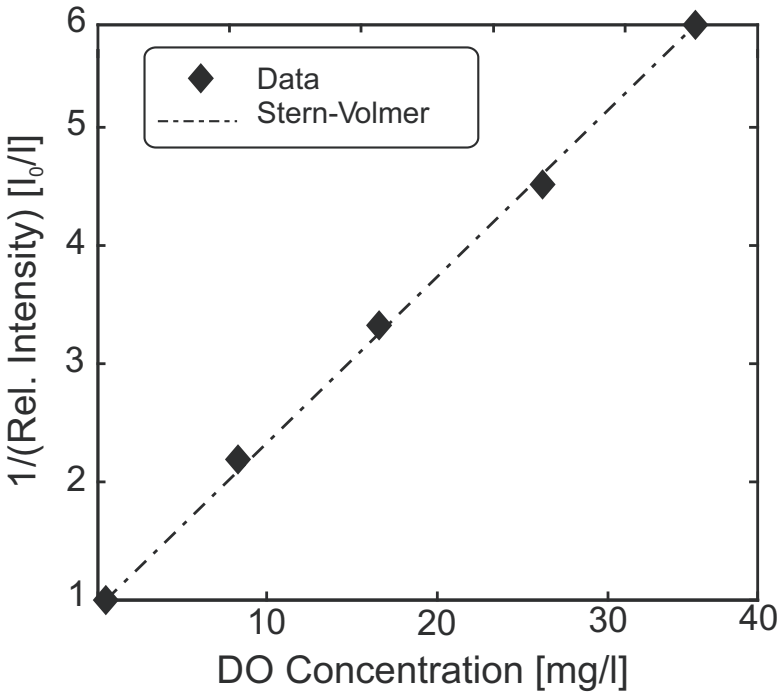

Figure 7.5: *Stern-Volmer calibration curve for detection of dissolved oxygen in DI water with a 600 nm thick 7% w/w PtOEPK/PS sensor at a flow rate of Q = 1 ml/min (T = 37.4*ºC*).*

maximum DO concentration of 34 mg/l produced by the external oxygenator caused a factor of 6.1 change in total fluorescent intensity. The sensor was found to follow the linear Stern-Volmer model (Equation (5.4)) with an intensity ratio value I_0/I_{100} of 6.1 at this flow rate.

7.4.2 Sensor Dynamic Operating Range

Calibration experiments were further extended to determine the dynamic operating range of the sensor. For this the sensor intensity for exposure to nitrogenated and oxygenated water was recorded at different flow rates. Sensor response was tested for flow rates from 0.05 to 2 ml/min applied via the syringe pump and corresponding to the shear-stress range of interest in the final device application. Simultaneous visual observation of potential effects of shear stress on film adherence found the films to remain strongly attached up to the highest flow rate tested (2 ml/min).

Figure 7.6 plots the measured absolute sensor intensity of oxygenated (~100% O_2) and nitrogenated (~0% O_2) DI water as a function of flow rate. The full-scale operating range of the sensor is reached at a flow rate of about 0.5 ml/min and remains constant thereafter. For flow rates below this value the operating range decreases slightly with decreasing flow rate. A similar effect was observed by Vollmer et al. [115] and attributed to parasitic convective losses to the surrounding PDMS matrix. Depending on the initial concentration entering the device, oxygen is either added or removed from the fluid by mass transfer through walls of the device. This effect is mainly due to the high oxygen permeability of PDMS. Since the permeation coefficient of N_2 in PDMS has been found to be approximately a factor of two smaller[1] than that of O_2 (800 Barrer for O_2 compared to 400 Barrer for N_2) [127,135,136], the signal decrease for nitrogenated water is larger than that for oxygenated water at lower flow rates. If critical, loss of dissolved gases to the surrounding material can be reduced by encapsulation of the final device or by use of a less permeable polymer for the channel structure. Such an alternative material has been proposed for use in microfluidics in form of thermoset polyester (TPE) [137]. Previously, fabrication of devices with this material required an additional step after formation of photoresist molds and PDMS replication [138]. Recent improvements [139] to the fabrication process however, have lead to direct TPE rapid-prototyping becoming a valid alternative to the use of PDMS for applications requiring more stable surface properties and when solvent-based fluids are involved.

1.Mainly due to the difference in solubility factors of O_2 and N_2 in PDMS

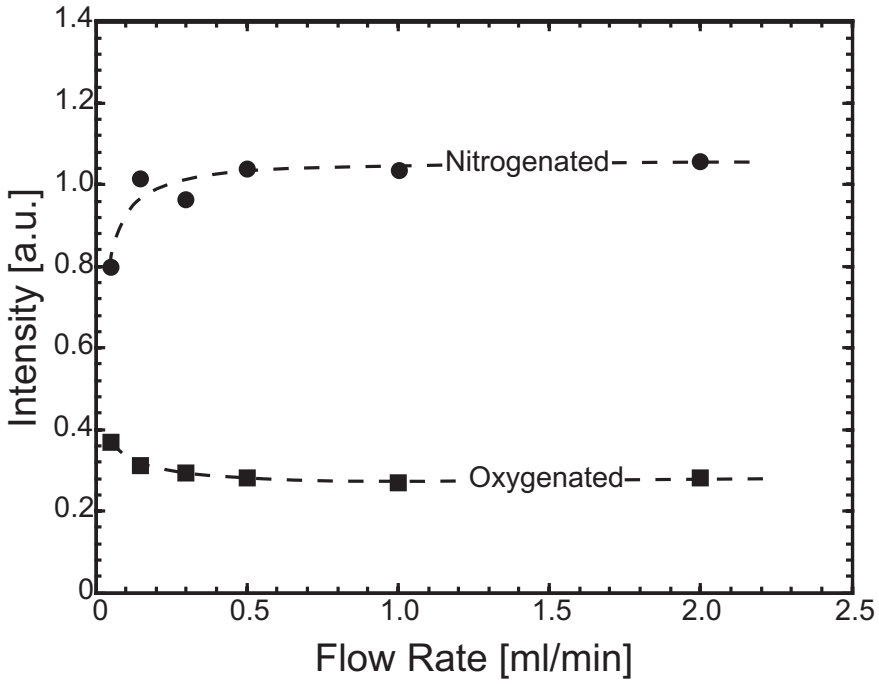

Figure 7.6: *Plot of the sensor intensity data corresponding to flows of nitrogenated and oxygenated water across the tested dynamic operating range. At low flow rates the operating range decreases slightly due to parasitic convective losses to the surrounding PDMS matrix.*

7.5 Sensor Application

This section introduces the application of the oxygen sensor inside a LOC-type microfluidic device by demonstrating visualization of oxygen concentration and measurement of the diffusion coefficient of oxygen in water. In Chapter 3 it was demonstrated how channel geometry can be used to control the fluid shear stress and oxygen gradient experienced by cells cultured within a parallel-plate flow-through bioreactor chamber. The analytical model introduced requires only a single inlet stream with an initial oxygen concentration and was validated for the example of linear and constant gradients using computational fluid dynamics. In this section the bioreactor is modified by use of further inlets to yield an additional transverse graduation of DO levels. Dissolved oxygen sensors are integrated into the device using the process described in Chapter 5 and successively used to visualize oxygen concentration and determine the cross-stream diffusion coefficient of oxygen in water. The first part gives a brief

introduction to oxygen sensing in LOC applications. This is followed by an introduction of the two microfluidic devices designed and results obtained for transverse oxygen graduation. The final part illustrates the use of the device and analytical procedure for the measurement of the coefficient of diffusion.

7.5.1 Oxygen Sensing for Lab-on-a-Chip Applications

Due to the absence of convective mixing at low Reynolds numbers[1] diffusion is the predominant transport mechanism between two or more parallel input streams. Several schemes for solute sorting and detection, such as the H-Filter and T-Sensor [140,141], operate using this principle. The T-Sensor in particular has been used extensively to measure the diffusion coefficients of solutes from and to adjacent flow streams [140,142]. Using the oxygen sensing technology developed here and a channel setup similar to the T-Sensor allowed the investigation of oxygen transport and cross-stream diffusion in different liquid media. In the following sections generation and visualization of flow streams with laterally-varying oxygen concentrations is demonstrated.

Furthermore, laminar flow, as observed in the device, has been shown to allow for partial treatment of cell-cultures and individual cells with biochemical reagents without the need for physically separated culture chambers [143,144]. This technique provides a powerful tool for studies in cell biology. However, it does not account for the local oxygen concentration, a further parameter with significant effect on cell behavior. As previously discussed in Section 5.1, dissolved oxygen concentration has been found to be intimately linked to cell survival, metabolism and function [88,94,102-104]. These results demonstrate the need to precisely control DO levels to increase the relevance of *in-vitro* experiments for cell biological studies and assays. The two experimental examples introduced in the following sections represent, in their own right, a novel method to expose a single cell or multiple cells in culture to different oxygen concentrations in a single flow chamber. In addition, the device can be used to control the DO level of individual flow streams used to apply different biochemical agents to cells and thus increase the validity of *in-vitro* experiments.

1.Re smaller than Re_{crit} ~ 2400 for a circular tube.

7.5.2 BIOREACTOR DEVICES

Two different devices and experimental setups were constructed and used to demonstrate transverse graduation by multi-stream flow and oxygen visualization/measurement in LOC devices. The first example introduced in the following is based on a PDMS microfluidic device and external gas-exchangers using macro-scale containers and gas-permeable silicone tubing for oxygenation, as described in detail in Section 6.3.3. For the second setup discussed here the gas-exchanger was integrated onto the chip using a design based on a thin gas-permeable PDMS membrane. Additional PDMS exchangers were fabricated (without the bioreactor structure) on separate glass substrates and were connected to the integrated device via tubing when required. These devices are referred to as external PDMS gas-exchanger in the following.

7.5.2.1 Bioreactor with External Gas-Exchanger

Measurement of locally varying oxygen concentrations inside a microfluidic channel is one possible application for the sensors produced by the patterning process [10]. To demonstrate this two inlet flows of differing oxygen concentration were applied to the device and the change in intensity of an integrated sensor film was recorded. A set of two identical external oxygenators, of the type described in Section 6.3.3, was used to provide aerated (Air), nitrogenated (N_2) or oxygenated (O_2) flow of DI water via two inlets. The flow rate of both inlets was kept constant at 0.5 ml/min by use of two equal syringes in the syringe pump. The two inlets lead to a rectangular reactor chamber (depth 0.2 mm, width 2 mm, length 18 mm) and exit through an outlet at the end of the chamber.

Figure 7.7 shows a photograph of the device and the corresponding intensity images at the inlet, the midpoint of reactor and the outlet. For illustration purposes this device was filled with blue dye-colored DI water. Intensity images in Fig. 7.7(b,d,e) correspond to the sensor signal at the bioreactor inlet for combinations of nitrogenated-oxygenated (b), nitrogenated-nitrogenated (d) and aerated-aerated (e) streams of water. As can be observed, no convective mixing takes place over the reactor length due to laminar flow conditions (Re ~ 80). The nitrogenated and oxygenated flow streams remain parallel and easy to distinguish from reactor inlet to outlet. Figure 7.7(c) plots the relative signal

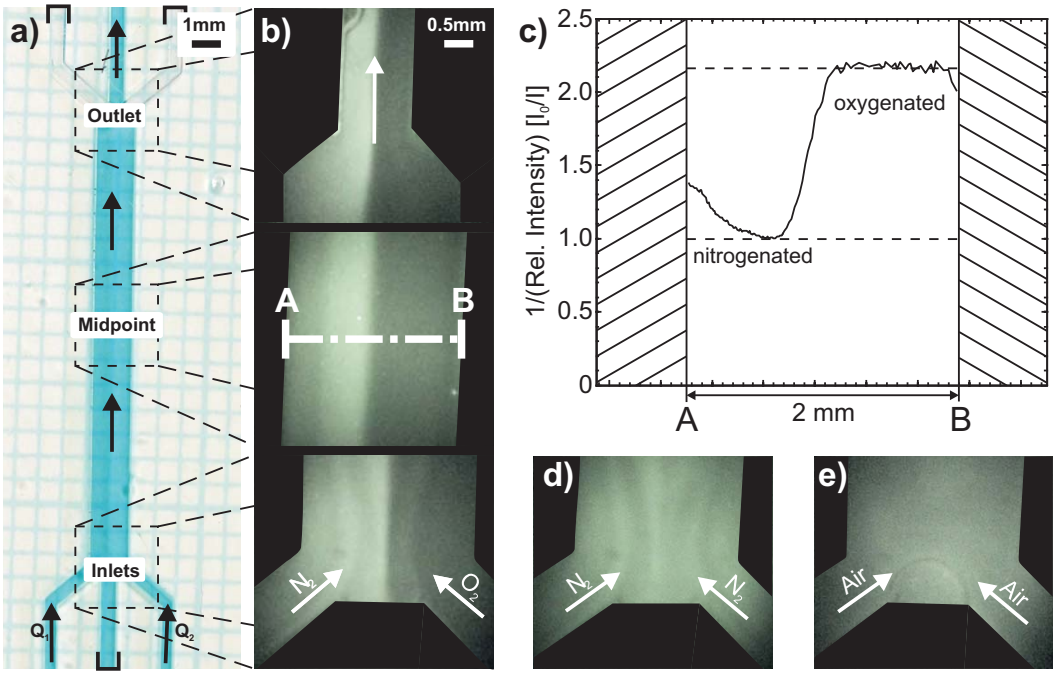

Figure 7.7: *Detection of laterally varying oxygen concentrations inside a microfluidic device: (a) Photograph of the rectangular bioreactor with integrated oxygen sensor film and filled with colored DI water for illustration. The two inlets at the bottom were used to provide flows of differing oxygen concentration into the device, $Q_1 = Q_2 = 0.5$ ml/min. (b) Intensity images for dual flow of nitrogenated (N_2) and oxygenated (O_2) water at the device inlet, midpoint and outlet. No convective mixing is observed due to laminar flow conditions. (c) Plot of the relative intensity signal across the reactor width at the midpoint (A - B) showing a clear transition between the two flow lines. (d,e) Intensity images for the device inlet after switching both inlets to nitrogenated and aerated water.*

intensity across the channel width (A-B) for the two parallel nitrogenated-oxygenated flows at the reactor midpoint. A clear transition of oxygen concentration between the two flows can be observed along the reactor centreline. The deviation of the plot shape from a stepwise function increases along the reactor length due to diffusive transport of oxygen from the oxygenated flow on the right to the nitrogenated flow on the left. As shown in the next section, this can be used to determine the constant of diffusion for oxygen in different media. The increase in signal towards the left boundary of the nitrogenated flow was attributed to flow instabilities induced by slight leakage at the tubing-PDMS interface of the left inlet port.

7.5.2.2 Bioreactor with Integrated Gas-Exchanger

The previous example for parallel flow with two different oxygen concentrations can be further extended towards a full LOC device. Miniaturization based on PDMS microfabrication allows for additional inlets and gas-exchangers to be integrated on-chip. Combining oxygenation and detection on the same substrate has the advantage that, due to the reduced fluid volume, concentration changes can be realized faster. The integration of the fluidic network onto the chip further increases system stability and thereby improves the experimental procedure.

To demonstrate this a device was designed with three inlet flows of different oxygen concentrations provided by on-chip PDMS-based gas-exchangers [11]. The individual flows were supplied to a bioreactor in the device and the change in intensity of the integrated PtOEPK/PS sensor film was recorded. A set of three identical integrated oxygenators was used to provide aerated (8.6 ppm O_2), nitrogenated (0 ppm O_2) or oxygenated (34 ppm O_2) flow of DI water via three inlets. Figure 7.8 shows a photograph of the assembled device. The gas-exchangers are based on the design introduced in

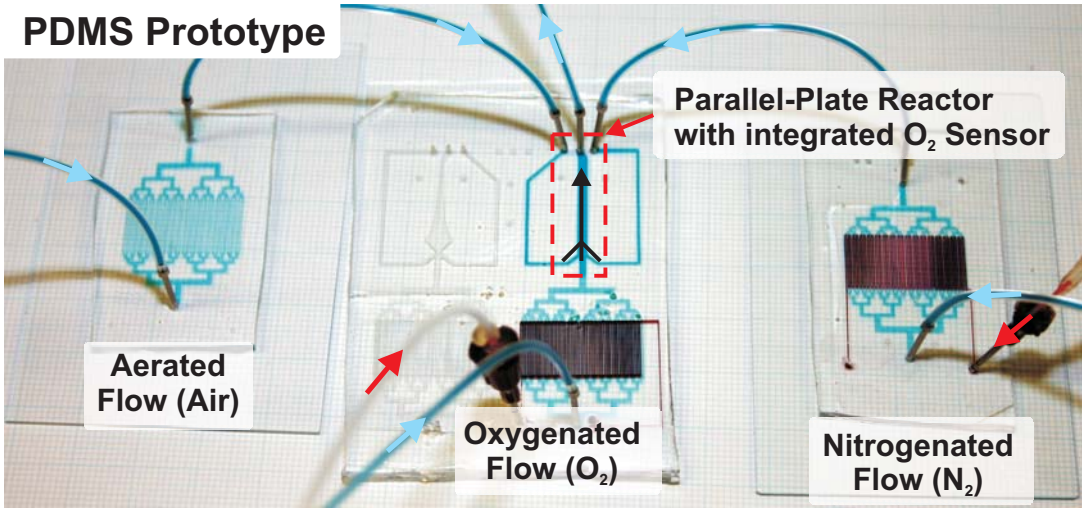

Figure 7.8: *Photograph of the complete PDMS Prototype with three gas-exchangers and the two central parallel-plate bioreactors with integrated oxygen sensors. For visualization purposes the rectangular bioreactor and fluidic interconnects were filled with blue water and the gas layer with red dye-colored water. The gas-exchanger for aerated flow (left) is a dummy device with no second gas layer and relies on equilibration of the fluid via air diffusion from the local environment.*

Section 6.3.4. A central one is integrated with the bioreactor on one substrate, while the other two are realized on separate substrates. This provides a modular system, where additional inlet streams can be created by simply connecting further gas-exchangers via short tubing. Alternatively, the unused inlet ports could be used to introduce cells into the reactor chamber or flush the device. The gas-exchanger for aerated flow is realized as a dummy device to provide the same fluidic resistance, but without second gas layer. It relies on equilibration of the fluid via air diffusion from the local environment. Oxygenated flow was produced by flowing gaseous oxygen (industrial grade) through the top layer of the central gas-exchanger. Similarly, nitrogenated flow was produced in the right gas-exchanger by flowing nitrogen (oxygen-free) through the top layer. The flow rate of the three inlets was kept constant at 0.1 ml/min for each inlet by use of the dual syringe pump. The dimensions of the rectangular and tapered bioreactor chambers were the same as in the previous example. Visualization and measurement results obtained using this device are discussed in the following sections.

7.5.3 Visualization of DO Concentration

To demonstrate device applicability the resulting flow of laterally-varying oxygen concentration was imaged using the oxygen sensors integrated on the bottom of the chamber. Upon entering the reactor the parallel streams remain separated due to the predominant laminar flow regime. This results in three distinct oxygen concentration levels across the width of the chamber. Figure 7.9 shows the intensity images and oxygen concentration plots for the rectangular bioreactor chamber. The images from left to right in Fig. 7.9(a) correspond to reactor inlet, mid-point and outlet. Aerated water enters the chamber through the top inlet, oxygenated through the central and nitrogenated through the bottom inlet. The individual streams are easily discernible and remain stable over the full 18 mm length of the device.

Oxygen concentration across the reactor is analyzed in the areas indicated by the dashed rectangles, A-B and C-D for the inlet and outlet, respectively. The two measurement points are separated along the length of the reactor by a distance of 16.4 mm. Figure 7.9(b) shows the cross-width plots of the DO concentration at inlet and

outlet obtained from the intensity images. The oxygen concentration levels of 34 ppm (oxygenated), 8.6 ppm (aerated) and 0 ppm (nitrogenated) indicated by the dashed lines in the plots in Fig. 7.9(b) were determined through calibration of the sensor prior to measurement. As can be observed, the width of the individual streams or oxygen levels varies over the reactor length. These differences in level width from inlet to outlet of the individual streams can partially be attributed to lateral diffusion of oxygen from the oxygen-rich central stream. However, in addition to the diffusion contribution, the flow rate of the nitrogenated stream (bottom in intensity images, right in concentration plot) was found to be slightly less than the inlet flow rate of 0.1 ml/min pre-set via the syringe pump. The difference originated in the uneven number of inlets, where one of the two syringes on the pump was used to supply two inlets each via a y-junction in the tubing. Although the second half of flow from the syringe, providing the nitrogenated stream, was connected to an additional dummy gas-exchanger for fluidic resistance equilibration, combining only one of these two streams in the reactor lead to the aforementioned differences in stream width. If perceived critical, this minor problem could be mitigated by use of a triple syringe pump with one single syringe per stream or by a device design with only even number of inlets.

The most important observation from Fig. 7.9 however, is the significant decrease in slope of the transition between the centre stream and the two outlaying ones from inlet to outlet plot. This is indicative of lateral diffusion of oxygen from the oxygen-rich region (central oxygenated stream) to regions of lower oxygen concentration (aerated and nitrogenated streams). Since the device dimensions, initial oxygen concentrations of the three streams and the flow conditions are known, this phenomenon can be used to deduce the diffusion coefficient of oxygen in the fluid. This is an important parameter for BAL devices at which this work is aimed at, in particular since diffusion constants in different media, such as biological salines and plasma, are largely unknown or may differ from batch to batch. An integrated non-contact measurement system for the diffusion coefficient based on a H-filter device, as presented in this thesis, could allow for inline calibration on-chip prior to the bioreactor.

7.5.4 Measurement of Diffusion Coefficients

In the following sections the diffusion theory required for the analysis is introduced and applicability of the device, integrated oxygen sensor and measurement procedure is demonstrated by calculation of the diffusion coefficient of oxygen in water.

7.5.4.1 Diffusion Theory

Diffusion is the spontaneous movement of particles from an area of high concentration to an area of low concentration in a given volume of fluid. As the statistical outcome of random motion, diffusion increases entropy, decreasing Gibbs free energy, and therefore is thermodynamically favorable operating within the boundaries of the Second Law of Thermodynamics. Diffusion is mathematically described by Fick's law, which states that the net movement of diffusing substance per unit area of section is proportional to the concentration gradient and directed towards lower concentration. Thus, there will be no net motion if the concentration is uniform. For steady-state diffusion Fick's first law is given by

$$\bar{J} = -D \cdot \nabla c \,, \tag{7.1}$$

where $\bar{J}$ is the flux, c the concentration, and $D = k_B T/(6\pi\eta r)$ the diffusion coefficient. The latter depends on the diffusing species and the material through which diffusion occurs. For a normal diffusion process the total number of particles is constant and the flux of particles into one region must be the sum of particle flux flowing out of the surrounding regions. This is described by the following equation of continuity:

$$\frac{\partial c}{\partial t} + \nabla \cdot \bar{J} = 0 \,. \tag{7.2}$$

If the diffusion coefficient D is constant in space, substitution of Fick's first law into Equation (7.2) leads to the diffusion equation, which describes the relationship between the spatial and temporal behavior of the concentration, as

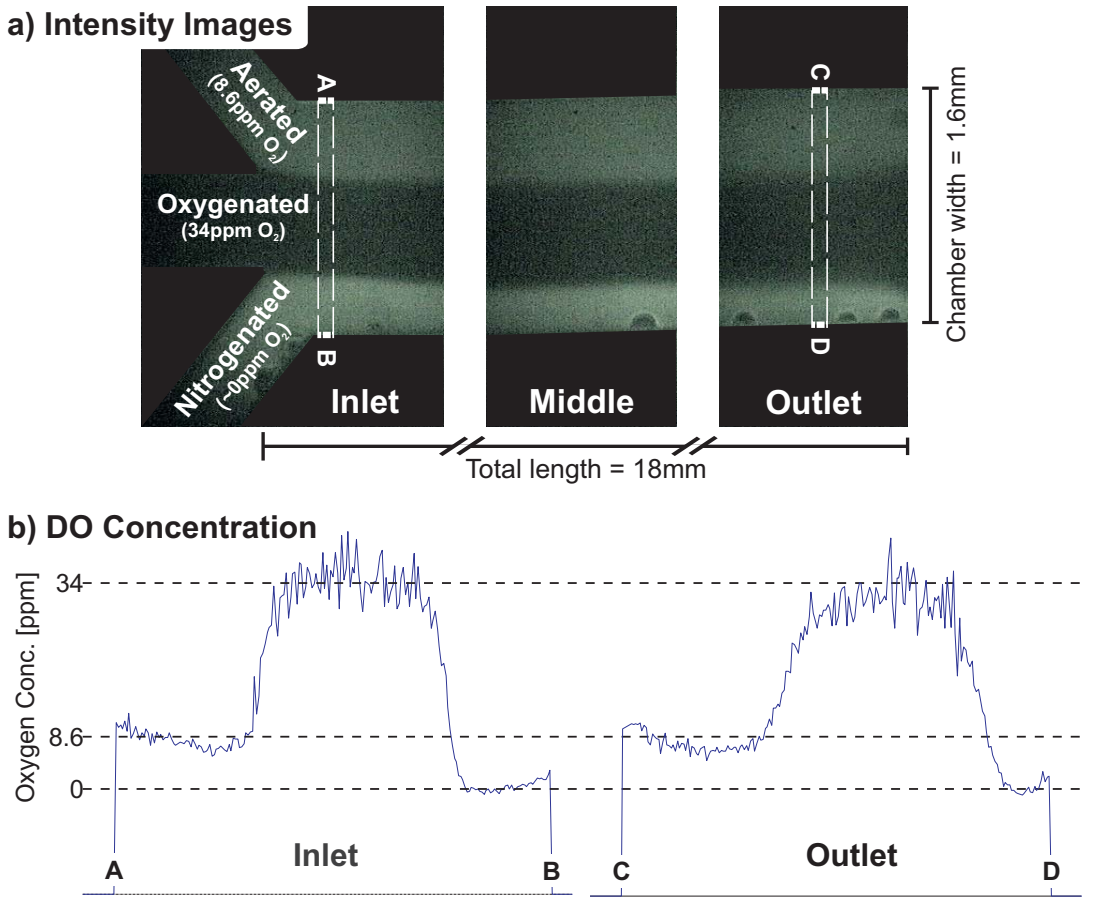

Figure 7.9: *Detection and analysis of laminar flow with three different oxygen concentrations. (a) Intensity images of three positions along the rectangular bioreactor with integrated oxygen sensor film. The three inlets on the right provide flows of DI water with 8.6 ppm (aerated), 34 ppm (oxygenated) and 0 ppm (nitrogenated) concentration of DO. The flow rate for each inlet was kept constant at Q_1, Q_2, Q3= 0.1 ml/min. (b) Plot of the DO concentration profiles across the reactor width at inlet (A-B) and outlet (C-D).*

$$\frac{\partial c}{\partial t} = D \cdot \nabla^2 c \,. \tag{7.3}$$

For a simple case of diffusion in a semi-infinite region and with concentration *c(x,t)* maintained at a value *c(0)* for $x = 0$, the solution to the diffusion equation is of the form

$$c(x,t) = c(0) \cdot erfc\left(\frac{x}{\sqrt{4Dt}}\right), \tag{7.4}$$

where *erfc* is the complementary error function, x is the distance and t the time. The characteristic length

$$x = \sqrt{4Dt} = L_d \tag{7.5}$$

is called the diffusion length and provides a measure of how far the concentration has propagated in the *x*-direction by diffusion in time *t*. In the next section it will be demonstrated how the relationship in Equation (7.5) can be used to extract the diffusion coefficient for oxygen in DI water, or any other carrier fluid, from the triple flow experiment described above.

7.5.4.2 Analysis of Triple Flow Data

The data acquired during the triple flow experiment was used to calculate the diffusion coefficient of oxygen in DI water. Due to laminar flow in the rectangular bioreactor no convective mixing occurs between the three flows of different oxygen concentration. However, oxygen molecules will diffuse from regions of high concentration (e.g. the middle oxygenated stream) to regions of lower concentration (e.g. aerated and nitrogenated streams). This diffusive transport from the central stream is approximated by the solution described in Equation (7.4) and reflected in Fig. 7.9 by a flattening-out of the concentration profiles towards the bioreactor outlet.

Figure 7.10 shows a schematic of the procedure used to calculate the diffusion coefficient of oxygen in water from the experimental results. The total flow rate into the reactor is $Q_{Bioreactor}$ = 0.3 ml/min. Using this, together with the bioreactor geometry depicted in Fig. 7.10(a) and a channel depth of 200 µm, an average fluid velocity of $v_{Bioreactor} = Q_{Bioreactor}/\textit{cross-sectional area} = 1.56\text{x}10^{-2}$ ms^{-1} can be calculated. With a length of approximately 16.5 mm between the two measurement points *Inlet* and *Outlet*, a plug of fluid will spend the time $t = \textit{measurement length}/v_{Bioreactor}$ = 1.05 s traversing this distance. Through the diffusion coefficient *D* the residence time *t* is directly related to the distance the oxygen molecules can diffuse in lateral direction. If the diffusion distance is known, *t* can be used, in conjunction with Equation (7.5), to calculate the diffusion coefficient for oxygen. Figure 7.10(b) indicates how the diffusion distance can be deduced from the slope of the slope of the concentration profile. The analysis of the

plot in Fig. 7.10(c) yields a distance $\Delta x_{aerated}$ = 105 µm and $\Delta x_{nitrogenated}$ = 103 µm for diffusion into the aerated and nitrogenated streams, respectively. Using these values to solve Equation (7.5) for the diffusion coefficient

$$D_{O2} = \frac{x^2}{4 \cdot t}, \tag{7.6}$$

yields a diffusion coefficient for oxygen in water $D_{O2inH2O}$ of 2.57×10^{-5} $cm^2 s^{-1}$ at a stage temperature of 37.4ºC. This value compares well with oxygen diffusion coefficients of 2.52×10^{-5} $cm^2 s^{-1}$ at 35.1ºC and 2.78×10^{-5} $cm^2 s^{-1}$ at 40.1ºC for water published in literature [145].

To validate the applicability of the diffusion model the measured diffusion coefficient was used to solve a 2D CFD model of the bioreactor and flow conditions in Comsol Multiphysics. The model geometry was set up to be equivalent to that shown in Fig. 7.10(a) with a reactor depth of 200 µm. Flow conditions were modelled using the Navier-Stokes application mode with three parallel inlet streams of equal flow rate Q = 0.1ml/min each. The pressure at the outlet was set to p = 0. Liquid properties used were those of freshwater with a dynamic viscosity $\eta = 1 \times 10^{-3}$ Pa*s and density $\rho = 1 \times 10^3$ kg/m^3. Species transport was modelled using the Convection and Diffusion application mode. The measured D_{O2} of 2.57×10^{-9} $m^2 s^{-1}$ was used as isotropic diffusion coefficient of the liquid. Each inlet was assigned a constant species concentration of 0, 0.538 and 2.125 mol/m^3, respectively. The boundary condition of the outlet was set to convective flux and the two application modes were coupled via the fluid velocity u, parallel to the long axis of the reactor chamber. Automated meshing and refinement yielded a 90.000 element mesh, which was solved using the GMRES linear system solver. Simulated oxygen concentration profiles across the chamber width were evaluated at the two points indicated in Fig. 7.10(a) as inlet and outlet. Figure 7.10(d) plots an overlay of the measured oxygen profiles and the corresponding simulation results (dotted lines) at these two positions. As can be seen, there is a good agreement between experimental and simulation results considering the noise on the measured data. The slope of the measured and simulated profiles coincide, indicating the validity of the diffusion model for analysis, as well as the value of the diffusion coefficient measured using the fluorescent sensor.

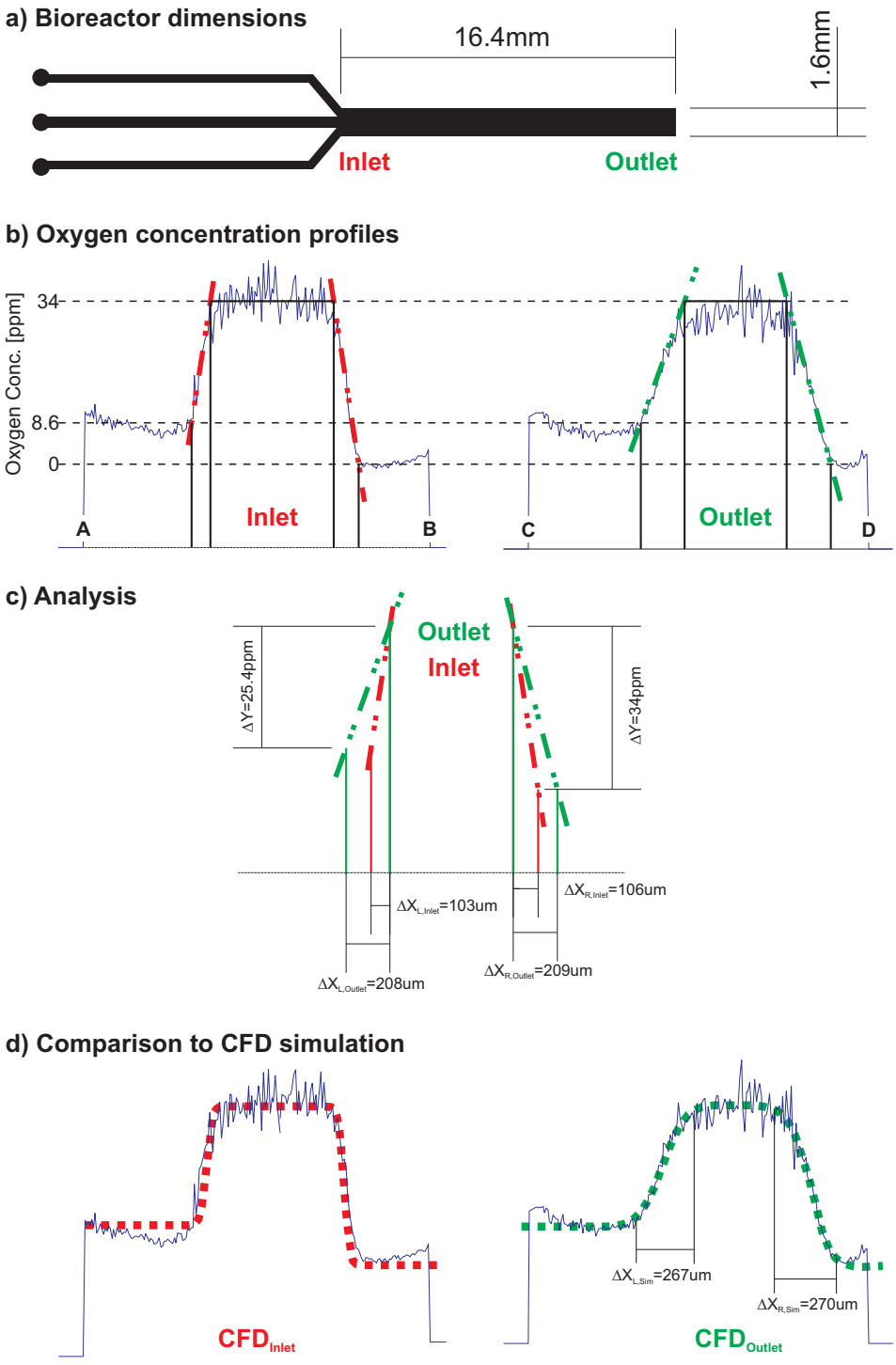

Figure 7.10: *Schematic of the procedure used to calculate the diffusion coefficient D_{O2} of oxygen in water from the experimental data. (a) Bioreactor dimensions, (b) lateral oxygen concentration profiles, (c) analysis of the diffusion distance from the slope of the concentration profiles and (d) comparison of measured oxygen profile with CFD simulation results (dotted lines) for a D_{O2} in water of $2.57x10^{-5}$ cm^2/s.*

7.6 SUMMARY

Both, for use with gaseous oxygen and to measure dissolved concentrations, calibration of the sensor prior to application is essential. This chapter has introduced the two calibration methods used for the detection of the oxygen concentration in gaseous and liquid media. As a result of the sensor calibration measurements several parameters influencing the total sensor fluorescent intensity ratio were discovered. These include PS molecular weight, percentage of PS in solution, substrate material and film thickness. In following experiments the latter dependency was used to optimize the fluorescent ratio of PtOEPK films on glass substrates. Reducing the film thickness down to several hundred nanometers by increasing the spin-coating speed yielded maximum intensity ratios I_0/I_{100} of 11 for gaseous and 6.1 for oxygen dissolved in water. In case of measurement of DO concentration, calibration can be performed using the same experimental set-up as for measurement by simply adding a reference sensor, such as a flow-through Clark electrode sensor, to the device inlet. The main difference between gaseous and dissolved oxygen measurements was found to be the reduced dynamics for switching of concentrations in the latter case. While sensor response to changes in concentration remains nearly instantaneous, as observed for gaseous samples, generation and fluidic transport of these different liquid samples to the sensor limits the recording of a dynamic sensor response. In general however, DO operation of the PtOEPK/PS sensors was found to be very stable with very homogeneous laterally resolved intensity response and independent of media flow rate in the region of interest for the desired application. Building on the sensor calibration, the application of the sensor inside a LOC-type microfluidic device was demonstrated by visualizing oxygen concentration and measuring the diffusion coefficient of oxygen in water. Dissolved oxygen concentration is an important parameter in biological systems. Microfluidics-based devices are leading the way towards miniaturization and integration of a multitude of previously macro-scale biological processes into LOCs. Oxygen sensing and concentration control constitute two key elements in such microdevices. This chapter has demonstrated the application of the developed oxygen sensor and flow system to the visualization and measurement of DO in PDMS-based microfluidic devices. The importance of oxygen sensing and control was

discussed and their potential to improve microfluidic devices based on laminar flow was brought into context with existing approaches. Several examples of typical LOC applications were discussed. In a first example an external hollow-fiber gas-exchanger was used to demonstrate visualization of various DO concentrations inside a PDMS bioreactor with integrated oxygen sensor layer. In a second step, multiple parallel streams of water with different oxygen concentrations were generated, combined and visualized simultaneously in a single bioreactor chamber. This was performed both with external and on-chip PDMS-based gas-exchangers to show the applicability of the design for further integration. The final example demonstrated how lateral oxygen concentration profiles recorded with the latter setup can be analyzed to measure the coefficient of diffusion of oxygen in a liquid medium. While not exhaustive, the examples presented in this chapter manage to illustrate the multitude of possible novel applications for the PtOEPK/PS sensor system in LOCs and cell-culture devices, such as BAL bioreactors. The next chapter brings together the integrated oxygen sensor of the developed microfluidic platform with *in-vitro* cell-culture and introduces a concept of a cellular waste drainage system specifically designed for BALs. This is followed by the last chapter with final conclusions and recommendations for future work.

The essence of life is statistical improbability on a colossal scale.

Richard Dawkins
1941, British Ethologist,
Evolutionary Biologist and Writer

CHAPTER 8

Cell Integration

Parallel to device integration initial cell-culturing experiments have been undertaken, as well as investigations of other enabling technologies relating to a planar BAL bioreactor device. These experiments include microstructuring of cell adhesion and cell-culture and relating protocols, as well as determining their potential influence on sensor function. Integration of the PS sensor and PDMS bioreactor shape require lateral control over cell adhesion to facilitate hepatocyte seeding and sensor readout. The first section reviews existing methods used to pattern cell adhesion promoting extracellular matrix (ECM) proteins, such as collagen. This is followed by a discussion of the methods investigated to promote localization of cell adhesion and the influence of substrate material on cell-culture. Following this, the procedures for integration of cell culture into the microfluidic shear device are discussed and sensor function is demonstrated in a cancer cell culture. The last section introduces initial investigations on the use of highly aligned vertical carbon nanotube (CNT) membranes as a conduit for an integrated bile drainage system.

8.1 CELL ADHESION

Further evaluation of the oxygen control principle requires the integration of live cells into the bioreactor device introduced in the previous chapters. Figure 8.1 shows a schematic

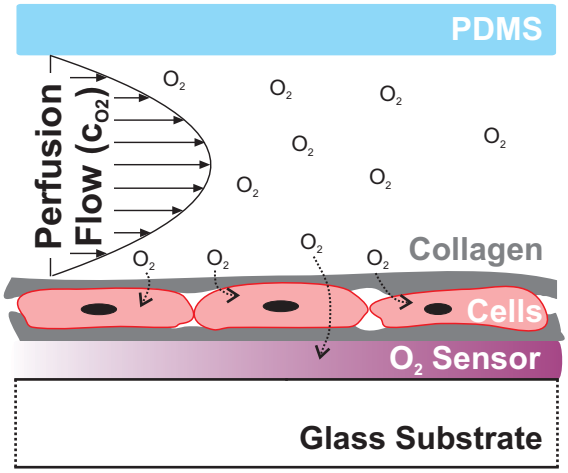

Figure 8.1: *Schematic side view of the bioreactor chamber indicating the individual layers of the final device (layer thickness not to scale).*

of the individual layers inside the bioreactor chamber. Structural support is provided by a glass substrate, such as a microscope slide, onto which the oxygen sensor layer is applied. The sensor is then covered with a layer of adhesion promoting protein, such as collagen. Cells are allowed to attach to this film and are covered by a further layer of collagen to promote expression of natural polarity. Finally, the complete stack is aligned with a layer of PDMS containing the corresponding fluidic features.

To facilitate the integration of cells into the oxygen sensor device, the attachment of cells has to be controlled and restricted to the regions with underlying oxygen sensor layer. Several different approaches have been proposed to control selective cell adhesion in cultures. Bhatia et al. [75] used photolithography for adhesion protein patterning. Commercial photoresist was structured using a mask and cell-specific adhesion protein was deposited onto the resist. After binding of the protein to the substrate, the remaining photoresist was lifted-off, producing localized patches of protein. Using this method patterned co-cultures of hepatocytes and 3T3 fibroblasts were demonstrated. A second approach proposed by Powers and Griffith [146] used affinity-specific cell morphology to influence cell layer formation. Different cell types were observed to form differing morphologies depending on the concentration of the adhesion protein deposited on a substrate and cell-substratum affinity in general. By varying protein concentration and substrate affinity this approach was used to produce hepatocyte and endothelial cell

co-cultures with pre-determined morphology.

Recently, advances in microfabrication techniques based on silicone elastomers such as PDMS have seen the introduction of several novel protein patterning approaches. As demonstrated in Chapter 5, PDMS provides an excellent material for the high-resolution replication of a stencil pattern into polymer thin films. The use of these stamps is not limited to dry-patterning of polymers, but can also be extended to bio-materials such as cell adhesion promoting protein films. With micro-contact printing, stencil stamps and a combination of the two, three different approaches to pattern protein films with PDMS stamps have been proposed. De Silva et al. [147] demonstrated localization of cell adhesion by micro-contact printing. A PDMS stamp was coated with adhesion-promoting biomolecules and brought into contact with a substrate forming a biomolecule pattern. Both collagen and laminin patterns were fabricated and cells were found to preferentially adhere to the biomolecule patterns. Zinchenko and Coger [148] used PDMS to create a stencil-type template of the desired cell pattern. Openings in the stencil allowed the deposition of proteins onto an underlaying substrate. After removal of the stencil hepatocytes and Kupffer cells were successfully co-cultured by localizing the hepatocytes to the pre-defined collagen patterns. Finally, Rhee et al. [149] proposed a combination of a PDMS stamp pattern with dry-etching for selective cell adhesion. This approach is similar to the process developed for sensor patterning in Section 5.3. PDMS stamps with the desired pattern are brought into conformal contact with a bare PS or poly-L-lysine coated substrate. When placed in a plasma etcher the stamp pattern in contact with the substrate protects the underlaying material. As a result protein patterns or selectively oxidized PS is obtained. Thus modified substrates were successfully used to demonstrate patterned cell cultures of human umbilical vein endothelial cells, MDA-MB-231 human breast cancer cells, NIH 3T3 mouse fibroblasts and primary rat cortical neurons.

8.2 Localization of Cell Adhesion by Microstructuring of Collagen

Two methods for producing patterned collagen films were investigated. The first approach builds on the similarity of the technique proposed by Rhee et al. [149] and the process introduced in for sensor patterning Chapter 5. PDMS stamps in combination with

RIE in oxygen plasma were adapted for the micro-structuring of cell adhesion promoters. This method allows the bioreactor shape to be bonded in the same plasma exposure step as used for structuring of the collagen film. Furthermore, oxygen sensor and collagen patterning can be performed as part of the same fabrication step. The second method uses PDMS stencils, as compared to stamps, to form the collagen pattern. Solution is pipetted directly into the stencil opening, which defines the final shape of the pattern. Although simpler, this method is limited in realizable shapes, as discussed in Chapter 5 for sensor patterning. To implement both techniques 25 mg type I collagen (rat tail, Prod. No. C7661, Sigma Aldrich, St. Louis, MO, USA) was purchased and PDMS stamps with the required bioreactor shape were fabricated according to the processes described in Chapter 4.

8.2.1 Collagen Film Preparation

Water-free glacial acetic acid (17 mol/l) was diluted in two steps to obtain 0.1 mol/l acetic acid. First, glacial acetic acid was blended 1:16 with DI water and stirred for 2 h resulting in 1 mol/l acetic acid. This was again diluted 1:9 with DI water and stirred for further 2 h. A 0.1% (w/v) main stock solution of type I collagen was prepared according to the product information provided [150] by weighing 10 mg of collagen and adding 10 ml of 0.1 mol/l acetic acid. Dissolution was performed by agitating in US over 1 h. A second working stock solution of 0.01% (w/v) collagen was prepared by diluting the stock solution tenfold.

In general, collagen films were deposited onto bare glass microscope slides and slides pre-coated with PtOEPK/PS films by pipetting from the second working stock. After deposition the solution was left to incubate in a fume hood at room temperature for a typical duration of 8 hrs overnight. In case of pre-coated PtOEPK/PS films a short (10 s, 500 W O_2) plasma treatment of the substrate was performed prior to pipetting of the collagen solution. This allows for continuous wetting of the otherwise hydrophobic PS surface and thereby a more homogenous collagen film. Following incubation, excess collagen solution was rinsed off with DI water and the film was carefully blow-dried using N_2.

8.2.2 Collagen Patterning by RIE

Patterning by RIE requires a pre-deposited layer of ECM on a flat substrate. For testing of the procedure, 50x75 mm glass microscope slides were spin-coated with PtOEPK/PS solution and left to dry. Collagen was deposited onto the sensor layer by use of a large stencil-like PDMS gasket cut to the size of the substrate. For deposition of an ECM monolayer previously described stock collagen solution was pipetted into this gasket and left to incubate at RT overnight. Excess solution was rinsed off the following day and the sample was carefully dried using N_2. As described for patterning of the oxygen sensor in Chapter 5, a PDMS stamp of the desired sensor and collagen shape was then brought into conformal contact with the surface. The pattern was then transferred into both layers in a single RIE etch step.

An example of a collagen layer patterned using this method is shown in Fig. 8.2. The complete replicated pattern corresponds to that previously introduced in Fig. 5.13(c). Square patches to the right of the pattern and close-ups are depicted as DIC micrographs in Fig. 8.2. The insets (a) to (c) show the fine structure of the top collagen patch at different enlargements. A continuous layer of collagen can be observed and overall dimensions of the replicated pattern agree well with the stamp. Pattern fidelity seems to be slightly reduced around the shape boundaries due to the rough protein surface, which might limit the conformity of the contact between PDMS stamp and the collagen during etching. However, the resolution obtained using this method is more than sufficient for localization of cell adhesion inside the bioreactor device.

8.2.3 Collagen patterning by PDMS Stencil

The second method investigated for patterning of the collagen layer uses a thin (~200 µm) version of the PDMS stencil for deposition and pattern definition. Openings in the stencil corresponds to the desired collagen patches and solution is deposited directly into the holes onto the substrate underneath. For use with an underlaying oxygen sensor the stencil is first aligned during stencil placement. Figure 8.3 shows a composite DIC micrograph of a collagen pattern fabricated by use of a PDMS stencil. The pattern has the shape of the bioreactor design and can be used to limit cell adhesion to the active area of the reactor

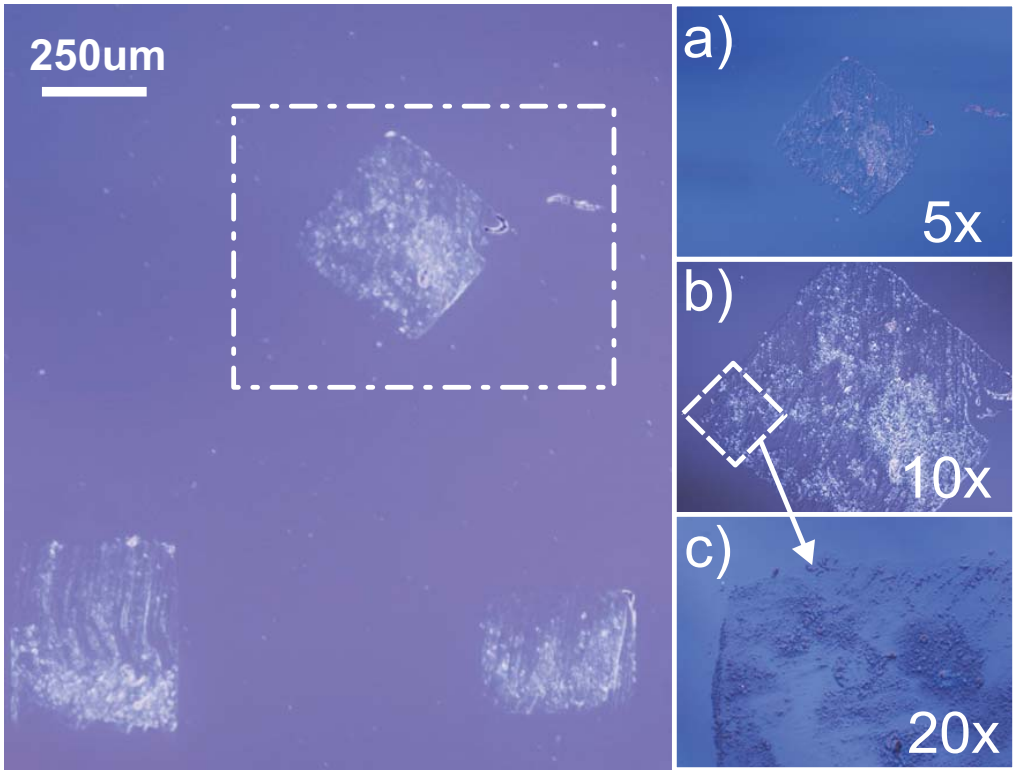

Figure 8.2: *DIC micrographs of a plasma patterned type I collagen layer on a glass microscope slide. The pattern was replicated with the same PDMS stamp as used for oxygen sensor patterning. The images on the right (a, b and c) show the indicated pattern detail in 5, 10 and 20x enlargement, respectively. A continuous layer of collagen can be observed, but pattern fidelity seems to be reduced due to the rough protein surface limiting conformal PDMS contact during etching.*

only. This is of advantage if additional sensor patches without collagen and cell-cover are required in the inlet and outlet channels for example. While this method of patterning is experimentally simple and fast once the stencil is fabricated, it was observed that collagen films deposited this way tend to exhibit less thickness uniformity than those fabricated using RIE. As this phenomenon is especially pronounced towards the boundaries of the pattern, hydrophobicity of the stencil is a likely cause. In fact, prior treatment of the PDMS with a plasma wand (BD-20AC laboratory corona treater, Electro-Technic Products Inc., Chicago, IL, USA) for a short (~30 s) period of time lead to significantly better wetting of the collagen solution and successively more homogeneous films.

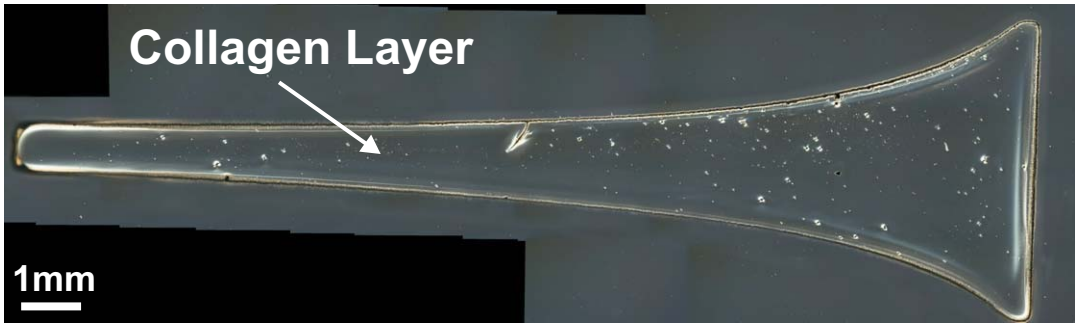

Figure 8.3: *Composite DIC micrograph of a full bioreactor shape replicated in type I collagen by use of a PDMS stencil. The collagen solution was pipetted into the stencil pattern placed onto the substrate and left to evaporate to form a solid film.*

8.2.4 Influence of Collagen on Sensor Films

The cell-adhesion promoting ECM constitutes a biomaterial, as it is sourced from rat tails and consists mainly of glycoproteins. In form of the collagen layer it is in direct contact with the PS matrix containing the PtOEPK oxygen sensor dye molecules. Thus it is important to determine potential degrading effects of the proteins on sensor function. To test this, samples of glass substrates with a spin-coated PtOEPK/PS layer were covered with a film of type I collagen, as described in the previous section, and the intensity response was monitored daily over a duration of two weeks [151]. For measurement of the intensity ratio the sensor was exposed to 100% gaseous oxygen and 100% nitrogen (0% O_2) once per day. In between measurements sensor films were stored in darkness and at 37.4ºC to exclude photobleaching and temperature effects.

Figure 8.4 shows a plot of the sensor intensity ratio I_0/I_{100} as a function of time in days for a typical 600 nm thick sensor patch of PtOEPK/PS covered with collagen by evaporation of 200 µl of 0.01% collagen solution. As can be observed, the initial value for I_0/I_{100} of 6.05 is somewhat lower than for pure PtOEPK/PS (I_0/I_{100} ~6.8), but remains nearly constant over the first 4 days. In total, the ratio decreases by only 8% over the measurement time of 14 days. During this period the sensor film was illuminated for an accumulated duration of 5 hrs, corresponding to ~20 mins per day. The result indicates that the collagen film does not significantly affect the sensor. Furthermore, taking into account photobleaching and measurement accuracy, it can be said that the reduction of intensity is small enough to make the sensor suitable for long-term observation of oxygen

concentration. Due to its applicability as adhesion promoter for hepatocytes, only collagen was tested in conjunction with the sensor. If other cell lines requiring a different ECM are to be used with the PtOEPK/PS sensor, these should be re-tested prior to use.

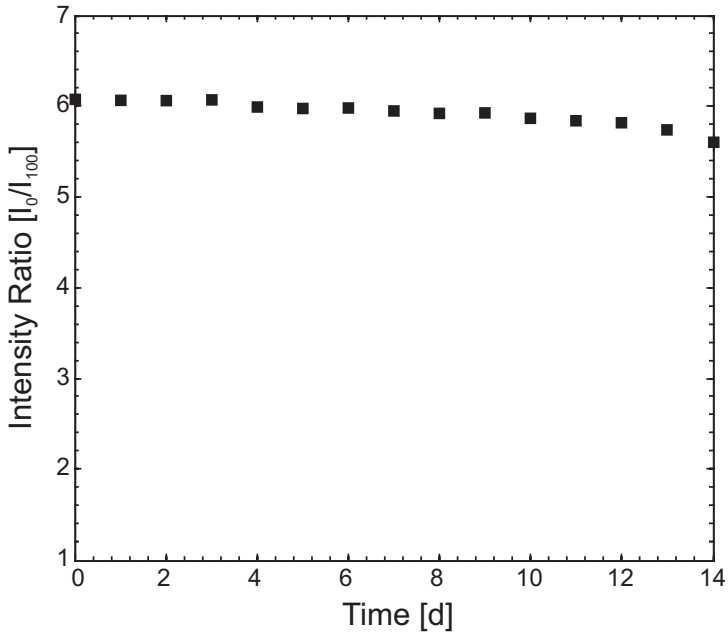

Figure 8.4: *Plot of the sensor intensity ratio as function of time (days) for a PtOEPK/PS film covered with a layer of type I collagen. The intensity was measured once daily for exposure to gaseous oxygen and nitrogen over a period of two weeks.*

8.3 Sensor Use with Live Cells

As demonstrated in the previous section, the oxygen sensor function of the PtOEPK/PS layer remains unaffected when covered with collagen. However, the application of the sensor in this form is only an intermediate step on the way to its use in conjunction with live cells. Ideally, cells are either cultured in an alternating pattern with interspersed sensor stripes or directly on top of the collagen-covered PtOEPK/PS layer. In both cases chemicals secreted by the cells as part of metabolisms and signalling have the potential for biofouling of the sensors. In addition, diffusion of oxygen through the cell/collagen sandwich (as formed in the latter case) to the sensor layer underneath may be reduced due to oxygen uptake of the cells. This has to be evaluated during calibration and accounted

for during measurement. In the following sensor function in conjuction with cells is demonstrated and initial results of oxygen measurement are given.

8.3.1 Cell Culture Preparations

Ideally, hepatocytes would have been used for the next phase of the work, however this proved to be difficult so another cell type was employed instead. Ethical approval to procure rat liver cells (Hepatocytes) was obtained from the University of Otago's Christchurch School of Medicine and Health Sciences (CSMHS) with the help of Prof. John Evans. A dedicated laboratory for handling of cells has been put in place within the Department for Electrical and Computer Engineering at the University of Canterbury and awaits PCR-2 biological safety certification. However, at the time of this work no other research relating to rat liver cells was being performed at the CSMHS so protocols for cell harvesting and culture were not in place. Other cell sources were available for immediate use so these were used instead.

In addition initial contacts were established with Prof. Mehmet Toner's group at the Harvard Medical School (HMS) in Boston, USA regarding the use of liver cells. Agreement was obtained for the author to undertake work in Prof. Toner's laboratory, however the current HMS protocols did not permit pre-PhD researchers to be processed for admission as visitors - an unfortunate chicken-and-egg situation.

For these reasons, immediate testing of the sensor and as proof of concept in conjunction with live cells, it was decided to use human *Ishikawa* endometrial carcinoma cells instead of hepatocytes. This cell line and related protocols were readily available at the CSMHS.

8.3.1.1 Cell-Culture Supplies and Protocol

The nutrient solution and supplements necessary to culture the cells were acquired from Sigma Aldrich according to the solution used by Dunn et al. [152] and others for rat hepatocytes. This included Dulbecco's Modified Eagle's Medium (DMEM, Prod. No. D5796) and insulin (Pro. No. I6634), glucagon (Prod. No. G2044), epidermal growth factor (Prod. No. E4127), hydrocortisone (Prod. No. H0888) and penicillin/streptomycin

(Prod. No. P4333) nutrient supplements. Plain DMEM was used as perfusion medium for cancer cell trials.

Cells were obtained from Cryo-storage at -80ºC in a freezer or in liquid nitrogen. Cell dispersion was carried out under aseptic conditions. Preparation was performed in a laminar flow cell culture hood (EMAIL Air Handling Biological Safety Cabinet Class II). All glassware used for cell preparation was autoclaved before use and together with all the solutions were sterilized with ethanol. All cells (in cryo-vial) and solutions were first pre-warmed to 37ºC before use. Minimum Essential Medium αMedium (αMEM) supplemented with a 10% of Fetal Bovine Serum Medium was used culture medium. Once the cells were ready, they were transferred into culture flasks (50 ml with carted neck) and 10 ml of the αMEM was added to each flask. Then the cells were stored in an incubator (37ºC, 0.5% CO_2) for at least 1 - 2 days to allow the cells to adhere to the surface. Culture medium was changed after 1 -2 days and replaced with another 10 ml of (αMEM + FBS 10%).

When cells had reached a confluent state, they were split in preparation for further use. Cultures that had become confluent were placed in the cell-culture hood, where the cell culture media was removed by aspiration. Pre-warmed 10 ml of Phosphate Buffered Saline (10x PBS pH7.4) at 37ºC was used to wash the cells. The PBS was then removed and the wash step was repeated twice more. Following the final aspiration of the PBS from the flask, 2.5% trypsin in PBS was added to the cells. Cells were dislodged by light tapping onto the side of the flask. The split cells were transferred into a larger multi-welled or culturing plate for different experiments. A small sample of a prepared cell suspension was removed, and used to perform a cell count with a haemocytometer. Cells were then centrifuged at 1500 rpm for 5 minutes at room temperature. After that, the supernatant was aspirated and the media (αMEM + FBS 10%) was added, with the volume dependent on the cell count performed earlier, the size of the plate and the concentration of cells required. The plate was then stored in the incubator for 2 - 6 days depending on the type of experiment.

8.3.1.2 Substrate Material for Cell-Culture

The choice of substrates for testing of the sensor in cell-culture was based on the materials making up the bioreactor device. Large 50x75 mm glass microscope slides were used as base substrate. Slides were used either plain, treated or coated with a variety of sensor films and cell adhesion promoters. Commercially available, sterile PS cell-culture dishes (OmniTray, Nalge Nunc Int., Rochester, NY, USA) acted as control substrate and carrier for the sensor substrates. Glass slides were mounted inside the carrier by use of double-sided adhesive tape. Table 8.1 lists the different substrates and material combinations prepared for cell adhesion and culture experiments. To limit the exposed surface area a PDMS stencil containing the three (rectangular, intermediate and optimized) bioreactor shapes was placed on each of the substrates. For samples with pre-patterned sensor films the patterns of the stencil were manually aligned with the underlaying identical PtOEPK/PS pattern. For samples covered by a Type I collagen layer the sensor was exposed to a short (~30 s) atmospheric pressure plasma using the plasma wand to assist wetting of the film. Immediately after treatment the collagen solution was applied by pipette and left to dry overnight at RT. Excess solution was rinsed off with DI water. Samples were stored in the dark and transported in lightproof containers to prevent photobleaching.

8.3.2 Cell-Culture of Human Cancer Cells

The cell line *Ishikawa* was established from an endometrial adenocarcinoma from a 39-year-old Asian woman [153]. It originated from a well differentiated human endometrial carcinoma and bears both estrogen and progesterone receptors. The cells have been used in numerous basic research areas such as reproductive biology and molecular science. Being carcinomic, this type of cell is able to divide in culture and thus form confluent layers on a substrate from a seed stock. Hepatocytes on the other hand, do not readily divide in culture and need to be re-harvested and re-seeded for each experiment. For the following experiment cells were prepared as described before, transferred to the substrate to be tested and incubated for a certain period prior to use.

Figure 8.5 shows DIC micrographs of *Ishikawa* cells after 3 days in culture on a glass

No.	Substrate	Layer	Treatment	Conditions
1	glass slide	plain	untreated	NA
2	cell culture dish PS	plain	untreated	sterile
3	glass slide	PtOEPK/PS (7% w/w)	untreated	spin-coated 30 s @ 6000 rpm
4	glass slide	PtOEPK/PS (7% w/w)	RIE patterned	spin-coated 30 s @ 6000 rpm
5	glass slide	PtOEPK/PS (7% w/w) Type I collagen (0.01%)	no RIE, O_2 plasma for wetting	spin-coated 30 s @ 6000 rpm 200 µl in square PDMS for 4 h @ 37.4ºC
6	glass slide	PtOEPK/PS (7% w/w) Type I collagen (0.01%)	RIE patterned, O_2 plasma for wetting	spin-coated 30 s @ 6000 rpm 200 µl in square PDMS for 4 h @ 37.4ºC

Table 8.1: *Substrates, adhesion layers and corresponding surface treatments for cell-adhesion trials.*

substrate used as control. The cells were confined to a bioreactor-shaped pattern of type I collagen during culture using a PDMS stencil. As can be observed in Fig. 8.5(a), after the stencil is peeled off, cell coverage is concentrated inside the area defined by the stencil opening, which is indicated by the white dashed line. Cells were observed to form dense clusters, shown in Fig. 8.5(b) and (c), on top of the collagen-covered glass surface. After 3 days incubation roughly 70% of the surface area of the patch was covered with cells. Simultaneously to this sample, cells were cultured on a second substrate with a PtOEPK/PS sensor layer between the glass base and the collagen film. For this example the shape of the sensor and collagen was again pre-patterned using the developed RIE process and a removable PDMS stencil was used to confine the cells during culture. The following section discusses measurement of oxygen using this sample.

8.3.3 Oxygen Sensing in Cancer Cell Culture

To demonstrate the compatibility of the PtOEPK/PS oxygen sensor with direct cell culture, oxygen measurement was performed with cancer cells seeded onto a sensor layer. Figure 8.6 shows oxygen calibration results of a PtOEPK/PS sensor patch seeded with *Ishikawa* human endometrial cancer cells after 3 days in culture. Prior to testing of sensor

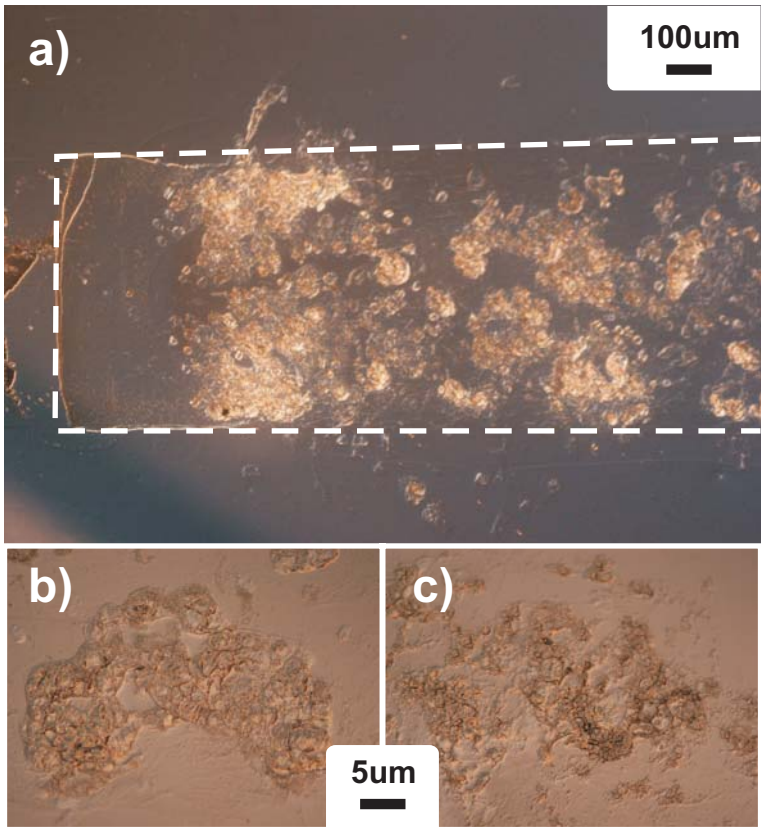

Figure 8.5: *DIC micrographs of Ishikawa human endometrial cancer cells after 3 days in culture. The white dashed line in (a) indicates the outline of the bioreactor shape defined by the PDMS stencil during culture. (b) and (c) show close-ups of cell clusters.*

function remaining culture solution was rinsed off the sample with fresh DMEM and the surface was carefully dried using N_2. DIC and fluorescent micrograph images of a region of the bioreactor-shaped sensor, indicated by the schematic on the top right, are displayed on the left in Fig. 8.6(a) to (f). Starting from the top, Fig. 8.6(a) shows the area of interest in DIC light microscopy indicating clusters of cancer cells before measurement. The following four images (b to e) show the fluorescent intensity response of the underlaying sensor layer for exposure to air (~21% O_2), nitrogen (0% O_2), oxygen (100% O_2) and back to air, respectively. The final image, Fig. 8.6(f), shows the same area again as a DIC micrograph after measurement.

A graph of the relative intensity I_0/I versus the relative gaseous oxygen concentration p/p_0 for the sensor sample is plotted on the bottom right. The measured intensity ratio I_0/I_{100} exhibited by the sensor when covered with a film of type I collagen and cancer cells

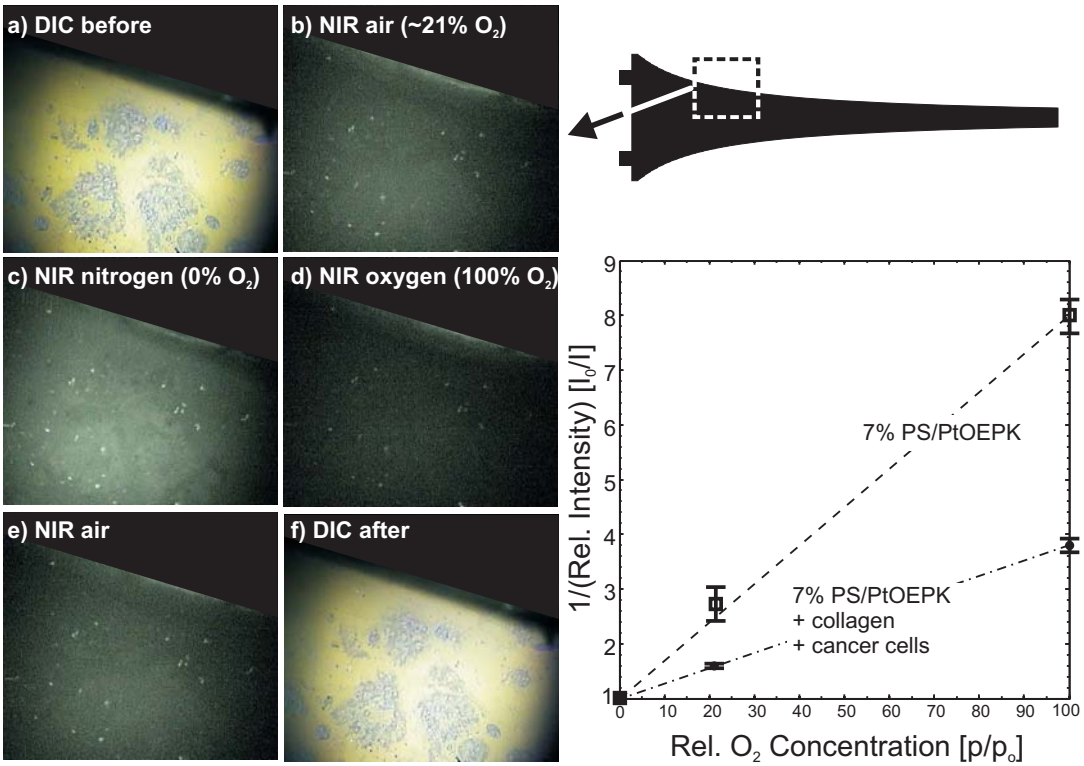

Figure 8.6: *PtOEPK/PS oxygen sensor function with cancer cells cultured on top. Micrographs on the left show a region of the bioreactor indicated by the schematic on the top right. (a) DIC microscopy of cancer cells growing on the sensor film prior to application of O_2. Consecutive images of fluorescent sensor response of the same area in (b) air (~21% O_2), (c) pure nitrogen (0% O_2), (d) pure oxygen (100% O_2) and (e) air. (f) DIC micrograph of the area after sensing. The graph on the right shows a plot of relative intensity as a function of oxygen concentration before and after cell-culture. (T=37.4°C)*

is 3.8. The second line in the plot indicates the sensor calibration 60 days prior to collagen deposition and cell-culture. In this case the I_0/I_{100} is 8.2, approximately double the value recorded with cells and collagen. Despite this difference, this successful use of the sensor layer in cell-culture demonstrates the applicability of the PtOEPK/PS sensor films to the in-situ measurement of oxygen in active biological environments. It further indicates that sensor function remains viable even when covered with biofilms and live cells for extended periods (~ days). As can be observed, the measured intensity ratio is smaller than for uncovered sensor patches, which might be related to both the extended storage time prior to cell seeding and the potentially reduced diffusion of oxygen through the cell/collagen sandwich.

Acquisition of the results given above conclude the study presented in this thesis.

Oxygen measurement under medium flow could not be performed as CSMHS protocols required a shut-down of all cell-incubation experiments over the summer holiday period. To continue work on the oxygen gradient hypothesis will require further cell sources, preferably the establishment of hepatocyte harvesting and culture protocols, and the certification of the biological containment facility in the Electrical Engineering Department to allow flow experiments to be set up under stable culture conditions. The last section in this chapter briefly introduces initial investigations into an auxiliary technology related to waste removal from hepatocytes cultured in a bioreactor, which has the potential to further improve BAL devices.

8.4 Bile Drainage System

An additional anatomical feature specific to the liver microstructure is the system of bile canaliculi and ductule formed to remove bile fluid from the hepatocytes to the gallbladder and intestines. The function of bile in the hepatic system and the human body were introduced in Section 2.1.2.3. Briefly, the major constituents of the bile are bile acids, cholesterol, water, bilirubin and other organic waste substances. To this day, removal of bile from the main perfusion flow has not been addressed by any of the existing BAL bioreactor devices. Currently bile fluid produced by the hepatocytes in culture is re-introduced into the main flow and potential effects of this on metabolic function of hepatocytes seeded further down-stream in the bioreactor are not yet fully understood [154]. In humans, blockage of the bile duct by a cancer, gallstones, or scarring from injury prevents the bile from being transported to the intestines. This leads to the active ingredient in the bile (bilirubin) accumulating in the blood stream and the resulting condition is called jaundice.

8.4.1 Conceptual Design

Bile canaliculi are formed as grooves on some of the lateral faces of hepatocytes in contact other hepatocytes. The canaliculi merge and form bile ductules, which eventually become the common hepatic duct. Formation of this micro anatomy is a function of inter-cellular arrangement and related to the matrix the cells are cultured on [155]. Typical materials

used for this are ECM proteins and hydrogels. However, recently preparations of CNTs and membranes based on these have started to gain increased interest as a novel cell-culture substrate due to excellent cell-adhesion and proliferation properties [157]. Furthermore, separate investigations into the transport mechanism of liquid through CNTs, which is predicted to be similar to naturally occurring ion channels, have shown it to be ultra-efficient and magnitudes faster than through pores of comparable size [158]. The discovery of one particular form of CNTs, commonly called vertically aligned carbon nanotubes (VACNT), has made it possible to grow both vertically and laterally defined mats of highly ordered tubes [156]. Currently the main application of these patterned tube arrays is their use as microelectrodes, but great potential exist for applications in nanofluidics such as vertical conduits and as membrane material.

The promising existing findings on nanotube properties in relation to cell-culture and fluidic transport lead to the design and initial investigations of a conceptual bile drainage system. Figure 8.7 shows a schematic of two possible versions of a potential bile drainage system based on capillary flow through a membrane of CNT bundles.The first example, shown on the left in Fig. 8.7, is based on bundles of CNTs embedded in a thin PDMS film. In this case the cells are cultured on a layer of collagen and the embedded bundles act as localized vertical fluidic interconnects to a drainage channel. The second example shown on the right uses a mat of VACNTs as direct cell-culture substrate and fluidic conduit. This variation in particular allows to utilize potentially advantageous morphological cell-substrate interactions.

8.4.2 Initial CNT Experiments

A schematic of the fabrication process used for the CNT/PDMS membranes is shown in Fig. 8.8. CNT bundles were grown on a pyrolyzed photoresist film (PPF)-covered substrate using a thermal chemical vapor deposition process [156]. Lateral confinement of the bundles was achieved by deposition through a shadow mask type stencil. The substrate was then covered in a thin layer of PDMS by spin-coating to the vertical length of the CNT bundles and the top of the CNTs was cleared of remaining PDMS using RIE. After thermal curing of the polymer a pre-fabricated second layer of PDMS containing

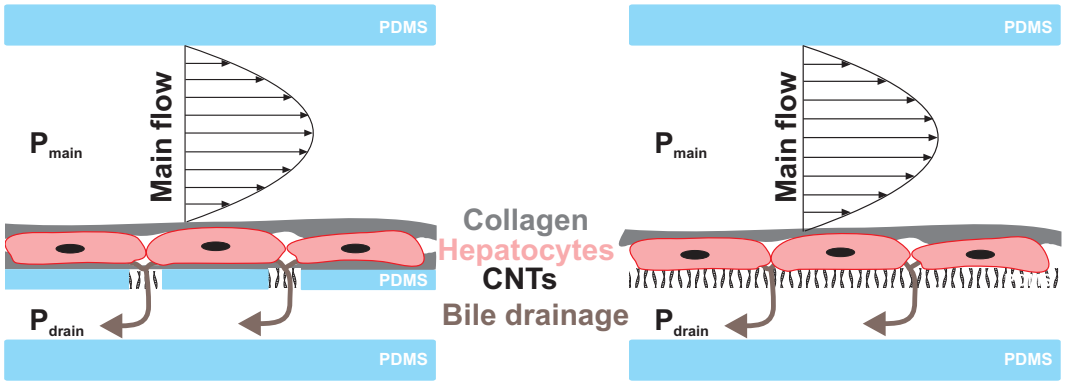

Figure 8.7: *Schematic of two possible versions of the direct bile drainage system for the BAL device. Hepatocytes are cultured as a monolayer on a liquid-permeable CNT membrane with underlaying drainage channel. By maintaining the pressure in the drainage channel* $P_{drain}<P_{main}$*, bile fluid is allowed to drain from the system to an external reservoir.*

fluidic interconnects was aligned to the bundles and irreversibly bonded to the membrane using oxygen plasma activation. This sandwich could be carefully peeled off the PPF substrate complete with the embedded CNT bundles. It was then bonded to a third PDMS layer with further fluidic interconnects to the backside of the bundles and a glass substrate for mechanical stability.

Figure 8.9 shows optical and SEM micrographs of the experimental bile drainage system. An optical micrograph of the assembled test chip is displayed in the main image. Both, top and bottom fluidic interconnects are visible and three channels are partially filled with dye-colored water. CNT bundles are visible as darker areas in the middle of the round channel ends and a SEM micrograph of the bundle array is shown in Fig. 8.9(a) prior to spin-coating of PDMS and release from the substrate. The close-up optical micrograph in Fig. 8.9(b) focuses on the top end of a single CNT bundle inside the PDMS channel, demonstrating that the CNT tips were cleared of PDMS during RIE. Initial experiments with water gave inconclusive results for pressure-driven flow. Liquid was observed to move from the top channels to the bottom channels through some of the CNT bundles. With the current setup it was not possible to determine whether this transport occurred through individual nanotubes or via conduits formed by the potentially imperfect PDMS-CNT interface. However, the work carried out here does demonstrate the viability of the process.

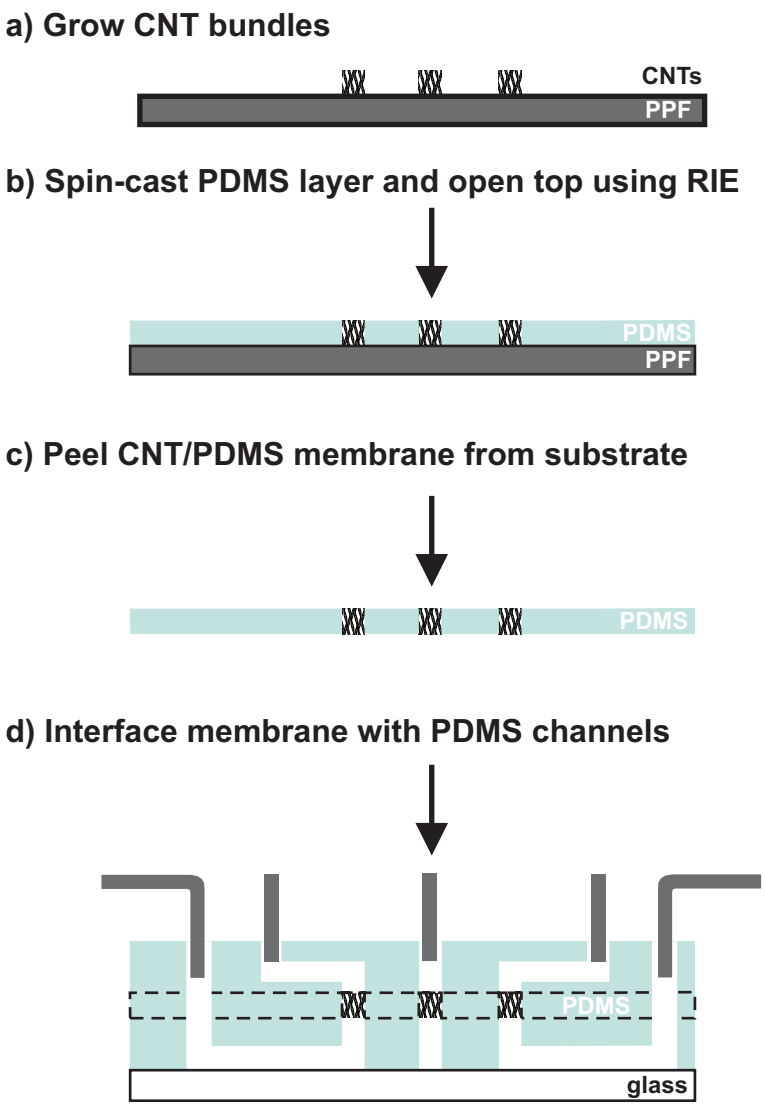

Figure 8.8: *Schematic of the fabrication process of the CNT/PDMS membrane devices.*

8.5 SUMMARY

In this chapter several additional processes and issues relating to *in-vitro* cell-culture in the developed bioreactor device have been addressed. The potential influence of biomaterials found in culture media and that of the ECM and cells themselves on sensor performance was investigated. A process to pattern a collagen cell-adhesion film simultaneously with the oxygen sensor layer was developed and demonstrated for selective cell localization. Collagen type I deposited onto the PS/PtOEPK film was found

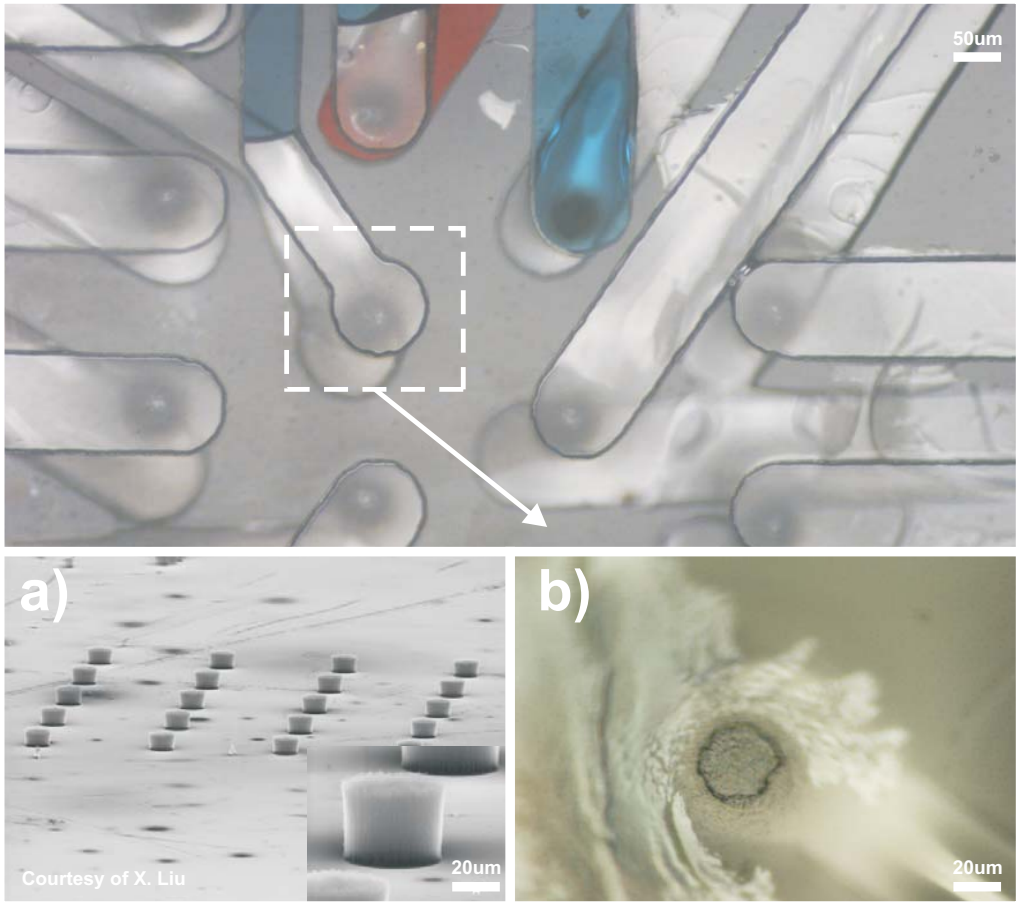

Figure 8.9: *Optical and SEM micrographs showing the initial experiments related to the use of CNT bundles for fluid transport. The main image shows the fluidic interfacing of the PDMS-encapsulated bundles with top and bottom channels. (a) SEM micrograph of the array of CNT bundles on PPF prior to encapsulation in PDMS and release from the substrate (Courtesy of X. Liu). (b) Optical micrograph close-up of an encapsulated CNT bundle inside the fluidic channel showing the top of the nanotubes free of PDMS.*

to have no detectable influence on the sensor intensity ratio over a period of two weeks. Oxygen sensing with cells was demonstrated by culturing human cancer cells directly on top of the sensor with an intermediate collagen film. The sensor showed a slightly reduced intensity ratio after 3 days in culture compared to the pure film measured 60 days prior. However, the ratio I_0/I_{100} remains larger than 3, which is the commonly agreed value above which a sensor is suitable for oxygen-sensing devices. As a final notion, a novel concept of an auxiliary bile drainage system for BAL devices was introduced. The design is based on a novel material combination of bundles of VACNTs embedded in a thin PDMS film. Fabrication of a prototype was demonstrated and initial fluid flow through

the membrane was observed. However, more testing is required to determine the feasibility of the concept.

In summary, the results discussed in the first part of this chapter, together with the techniques described in the previous chapters, provide a complete toolbox enabling the use of the bioreactor with integrated sensor system for cell-culture applications. The second part brings forward a novel concept combining fluidic conduits and cell substrate in a single promising material for future potential use in a BAL bile drainage system. The next chapter will provide conclusions to the work presented in this thesis and recommend directions for future work based on the results.

...the end of all our exploring will be to arrive where we started, and know the place for the first time.

T. S. Elliot
1888-1965, Anglo-American Poet, Dramatist, Literary critic

CHAPTER 9

Conclusions and Future Work

This chapter summarizes the main contributions made by this thesis and draws conclusions from the research performed. Recommendations are then made concerning future work in the area.

9.1 THESIS SUMMARY AND CONCLUSIONS

The work described in this thesis contributes to the understanding of oxygen concentrations in microfluidic cell-culture devices. In particular, it provides the tools necessary to generate, control and measure the dissolved oxygen concentration in continuously perfused BAL bioreactors, thereby helping to overcome existing fundamental transport limitations in parallel-plate designs. The development of the model-based bioreactor shape together with the process for the integration of a cell-culture compatible oxygen sensor provide these tools. Numerical evaluation of the bioreactor shows that the transport model, in conjunction with cell oxygen uptake, can be used to design the lateral bioreactor shape to yield custom concentration gradients. This is especially useful to maintain a certain, constant oxygen level over the full length of a cell-culture as demonstrated by the tapered bioreactor.

The bioreactor device is unique in that it can maintain a specific concentration gradient without the need for additional membrane-based oxygen input. This is achieved simply by implementing the corresponding reactor outline resulting from the model equations and providing inlet flow with the desired initial oxygen concentration. However, this advantage is gained at the cost of increasing shear-stress over the chamber length compared to conventional designs with constant width. Nevertheless, by adjusting the inlet flow rate the value of the shear stress experienced by the perfused cells can be maintained at physiological levels. Furthermore, in case of application with hepatocytes shear-stress constitutes an additional parameter determining cellular function and thus the bioreactor can provide a closer match to in-vivo sinusoids than conventional designs.

Simultaneously, the integrated oxygen sensor allows for non-contact *in-situ* monitoring of the concentration throughout the whole chamber and inlet and outlet ports if required. The novel fabrication process developed for the highly sensitive and versatile PS/PtOEPK fluorescent oxygen sensor system allows very homogeneous films to be deposited and integrated into common microfluidic devices. PS/PtOEPK itself is not new a new material, however, the combination of spin-coating and RIE-etching with PDMS stencils for fabrication allows for the first time large-scale custom shaped sensor patterns to be produced while retaining film quality. Unlike existing techniques, such as deposition by manual pipetting, the new process provides excellent control over sensor film thickness via the spin-speed. In addition, since patterning is performed after film formation and on a wafer-level, both pattern reproducibility and fabrication throughput are significantly increased. Sensor patterns with feature sizes in the lower micrometer range have been demonstrated. While this is sufficient for cell-based applications, potential for future pattern miniaturization using this approach exists.

A further discovery in relation to the PS/PtOEPK sensor films, which was directly facilitated by the thickness control inherent to the deposition method, is the inverse dependence of the fluorescent intensity ratio I_0/I_{100} on film thickness. This ratio is a measure of the sensitivity of the sensor layer and could be more than tripled by reducing the film thickness from 1.3 µm down to around 300 nm. Through this, the highest reported sensitivity ratio for PS/PtOEPK on glass substrates has been achieved.

The observed homogeneity of the spin-coated sensor films also implies that intensity quenching instead of fluorescent lifetime can be used to measure the oxygen concentration. This simplifies the required excitation and detection setup to a conventional fluorescence microscope with attached CCD sensor and enables low-cost, spatially-resolved oxygen profiling. To demonstrate the latter, and device applicability in general, lateral oxygen profiling was for the first time ever used to visualize parallel multi-stream flow of different dissolved oxygen concentrations and with stable laminar interfaces in a single bioreactor. Inlet stream oxygenation based on PDMS membrane gas-exchangers was integrated on-chip to provide multiple inlet streams and thereby add a second dimension to graduation. Changes of *in-situ* oxygen concentration inside the device could be imaged in real-time and the profile of the transverse graduation of concentration levels across flow streams measured at various points along the device length. This technique provides a powerful new tool to increase the significance of studies in cell biology based on partial treatment of cell-cultures and individual cells with biochemical reagents by adding oxygen control.

In addition, and comparable to use of the T-sensor, it was shown how the device can provide an experimental tool to determine the coefficient of diffusion of oxygen in a liquid medium. This was demonstrated for the diffusion of oxygen in water and the measured coefficient agrees well with data published in literature. Using the obtained diffusivity, the shape of the recorded cross-stream concentration profiles could be validated by means of CFD simulation.

One of the biggest advantages of the present system in relation to use with biological samples and cells is the solid state nature of the sensor. This not only significantly reduces the amount of dye needed compared to dissolved sensors, it also means that there is practically no contact between biomaterials and sensor. A layer of the ECM protein collagen deposited directly on top of the sensor film was shown to have no discernible effect on the oxygen sensing capabilities even after an extended period of incubation. Initial test with human cancer cells cultured on the sensor layer demonstrated sensor function after several days in culture, thus indicating the potential of *in-situ* oxygen

measurement. Whilst a reduction in relative fluorescence intensity was observed, the measured I_0/I_{100} ratio remains adequate to make the system a candidate for use as an embedded oxygen sensor layer in cell-culture.

9.2 Suggested Future Work

As well as the development of the bioreactor device for oxygen control and detection, this thesis has introduced the laminar flow-based oxygen transport model and several related phenomena. Given an ample source of hepatocytes and the resources to perform controlled cell-culture, there are now a number of experiments that could be performed based on the developed set-up.

First and foremost should be the establishment of a source of hepatocytes and the corresponding protocols for their extraction, culture and seeding into the bioreactor device. This would allow for direct experimental verification of the shear-based oxygen transport model using the developed sensor system. By demonstrating spatially resolved oxygen measurement inside the bioreactor the groundwork has been laid for the demonstration of the effect of chamber geometry on concentration profile. The first test should include a direct comparison between the tapered design derived in this thesis and a conventional straight bioreactor, as realized in the prototype chip, to ascertain the resulting oxygen gradients along the device length. Initial contacts towards the procurement of cells from the Otago School of Medicine have been established and ethical approval to harvest hepatocytes from rat liver cells has been obtained. Furthermore, a dedicated laboratory for the handling of biological samples, such as liver cells, has been set up in the Electrical and Computer Engineering Department and is currently undergoing certification. Whilst there is some disappointment that the author could not undertake these important experiments himself, significant steps have been taken along the way and the scope of the work is now more in Biological Sciences than Electrical Engineering.

The feasibility of seeding cells directly onto the oxygen sensor layer was demonstrated to some extent in Section 8.3. However, cancer cells and not hepatocytes were used in this example and, although successful, some decrease of sensor sensitivity due to the cell cover was observed.

Two primary areas of further research ensue from this. The first area would cover more thorough testing of sensor function with perfused hepatocytes and other attached cell lines and in comparison to plain control samples. This should help to determine in more detail whether the observed reduction of intensity is due only to the reduced diffusion of oxygen through the cell-sensor sandwich or whether there is an optical or biological influence of the cells on the sensing mechanism in this configuration.

The second area relates to the developed sensor and ECM patterning process. Should it emerge that seeding certain cells of interest directly onto the sensor does not provide the required intensity change and detection sensitivity, cell-adhesion patterning can be employed. Several methods of selective localization of cell attachment have been published [146-149] and can be used together with the results on collagen patterning in Section 8.2 as a starting point to investigate the use of repeating patterns of cell patches and sensor stripes. This would result in uncovered PS/PtOEPK sensing areas and could alleviate the potential problems observed with the sandwich configuration while still providing spatial concentration information.

From a more general point of view, the sensor patterning process and sensor application themselves provide multiple avenues for additional research. For example, further reduction in sensor pattern feature size and increase in level of reproducible detail could be achieved by using the nanoimprint lithography technique, as described by Mohamed et al. [159], for sensor fabrication. The initially soft nature of the freshly spin-coated PS/PtOEPK films makes them an ideal candidate for imprinting. Nanoscale patterns producible with this technique make it potentially feasible to integrate whole arrays of sensor patches underneath a single cell. Also, due to the described improvements in the sensor fabrication and integration process, PS/PtOEPK films should be investigated for other oxygen visualization applications. One such example could be the demonstration of purely diffusive spatial oxygen gradients on-chip based on the novel device recently proposed for chemical gradients by Atencia et al. [160].

Beyond the continuation of system development, device application for cell biology studies should be explored further, in particular in context with the introduced multi-stream configuration. An excellent starting point for the use of the developed system in this area is the previously mentioned ground-breaking work by Takayama et al. [143,144] on partial chemical treatment of cells using laminar streams. The work presented in Chapter 8 of this thesis allows similar experiments to be performed on molecular cell-biology, however, now these can be extended in relation to defined local variations in oxygen concentration. An additional enhancement of the parallel stream concept would be to demonstrate hydrodynamically-focussed media streams of controlled oxygen concentration. These would allow one to even more precisely target single cells or maybe even specific areas on a cell surface to determine the influence of oxygen on cell function. As work by Yu et al. [161,162] suggests, with increasing use of microfluidic devices for cell-culture, understanding inter-cellular signalling and the external factors involved in this process becomes more and more important regarding comparison with *in-vivo* observations. Through its capability to virtually compartmentalize areas in the bioreactor via the individual streams and control the cross-stream diffusion via the flow rate the device provides great potential to study these phenomena.

Of secondary importance, it could be of interest to further develop the fabrication process for the vertically tapered bioreactor. In this configuration the resulting concentration profile on the bottom chamber surface corresponds directly to the 2D analytical model, as opposed to the horizontally tapered designed where the profile has to be established via 3D simulation. As mentioned in Section 4.2 and demonstrated by Ruffieux et al. [99], a carefully controlled reflow bake of the AZ4562 resist could alleviate the surface roughness resulting from the grayscale process. In this context it should also be mentioned that an extension of the analytical model to a horizontally tapering geometry would be worth investigating.

9.3 Final Comments

The focus of this thesis has been on the initial development of the prototype system rather than its optimisation for use as a BAL bioreactor or scale-up to a clinically relevant size. These are major areas that require further study. This is exemplified by the initial investigations into a bile drainage system summarized in Section 8.4, which should be investigated in more detail. It should be of special interest to investigate the use of the novel VACNT films as cell-culture substrate, as it might positively influence hepatocyte morphology and formation of bile canaliculi.

The author is often asked if this device will eventually lead to an implantable liver replacement. Although this is unlikely due to the large surface area required to seed the necessary number of cells for a full liver replacement, it is still of great interest to continue investigations relating to miniaturization and integration for an external device. The multi-layer device introduced in Section 4.4, as well as the vision presented in [163] are recommended as a good starting points for this.

Today's scientists have substituted mathematics for experiments, and they wander off through equation after equation, and eventually build a structure which has no relation to reality.

Nikola Tesla
1856-1953, Austrian-born American
Inventor, Mechanical and Electrical Engineer

APPENDIX

A NONDIMENSIONALISATION OF THE CONCENTRATION CONSERVATION EQUATION

The steady-state 2D conservation of concentration equation is given as

$$\tilde{u}\cdot\frac{\partial\tilde{c}_i}{\partial\tilde{x}}+\tilde{v}\cdot\frac{\partial\tilde{c}_i}{\partial\tilde{y}}=D_i\cdot\left[\frac{\partial^2\tilde{c}_i}{\partial\tilde{y}^2}\right]. \tag{A.1}$$

Characteristic scales for mass fraction $c_{i,\infty}$, length L and velocity U_∞ are

$$x=\frac{\tilde{x}}{L};y=\frac{\tilde{y}}{L};u=\frac{\tilde{u}}{U_\infty};v=\frac{\tilde{v}}{U_\infty};c_i=\frac{\tilde{c}_i}{c_{i,\infty}} \quad . \tag{A.2}$$

Substitution of Equation (A.2) into Equation (A.1) leads to

$$u\cdot U_\infty\cdot\frac{\partial}{\partial xL}c_i\cdot c_{i,\infty}+v\cdot U_\infty\cdot\frac{\partial}{\partial yL}c_i\cdot c_{i,\infty}=D_i\cdot\left[\frac{\partial^2}{\partial y^2\cdot L^2}c_i\cdot c_{i,\infty}\right], \tag{A.3}$$

After rearranging, this results in

$$L\cdot U_\infty\cdot\left(u\cdot\frac{\partial}{\partial x}c_i\cdot c_{i,\infty}+v\cdot\frac{\partial}{\partial y}c_i\cdot c_{i,\infty}\right)=D_i\cdot\left[\frac{\partial^2}{\partial y^2}c_i\cdot c_{i,\infty}\right] \tag{A.4}$$

and

$$L \cdot U_\infty \cdot \left(u \cdot \frac{\partial c_i}{\partial x} + v \cdot \frac{\partial c_i}{\partial y} \right) = D_i \cdot \left[\frac{\partial^2 c_i}{\partial y^2} \right] \tag{A.5}$$

respectively. Further rearranging and introduction of the Peclet number gives

$$u \cdot \frac{\partial c_i}{\partial x} + v \cdot \frac{\partial c_i}{\partial y} = \frac{D_i}{L \cdot U_\infty} \cdot \frac{\partial^2 c_i}{\partial y^2} = \frac{1}{Pe} \cdot \frac{\partial^2 c_i}{\partial y^2}. \tag{A.6}$$

B TRANSFORMATION OF THE CONSERVATION INTO THE O.D.E. BY SIMILARITY VARIABLE

The transformation process is shown by David et al. [88] for cylindrical co-ordinates. Here it is adopted to the cartesian co-ordinate system of the parallel-plate channel model depicted in Figure 3.3. Given the non-dimensionalised conservation Equation (A.6)

$$u \cdot \frac{\partial c_i}{\partial x} + v \cdot \frac{\partial c_i}{\partial y} = \frac{1}{Pe} \cdot \frac{\partial^2 c_i}{\partial y^2} \tag{B.1}$$

and the assumption of a linear velocity profile due to a small ratio of mass transfer boundary layer thickness to the viscous boundary layer thickness, a stream function is defined as

$$\tilde{\psi}(\tilde{x}, \tilde{y}) = \frac{1}{2} \cdot \frac{\tilde{v}_o^{\,2}}{\nu} \cdot \tilde{y}^2, \tag{B.2}$$

where $\tilde{v}_o$ is the 'friction' velocity ($[m/s]$) defined by

$$\tilde{v}_o = \left(\frac{\tilde{\tau}_w(\tilde{y} = 0)}{\rho} \right)^{1/2}. \tag{B.3}$$

The wall shear stress function $\tilde{\tau}_w$ is know a priori and non-dimensionalised as follows

$$\tau_w = \frac{\tilde{\tau}_w}{\rho \cdot U_\infty^{\,2}}. \tag{B.4}$$

Using Equation (B.2) the velocity components can then be written as

$$\tilde{u} = \frac{\partial}{\partial \tilde{y}}\tilde{\psi} = \frac{\tilde{v}_o^2}{\nu}\cdot\tilde{y}\,;\ \tilde{v} = -\frac{\partial}{\partial \tilde{x}}\tilde{\psi} = -\frac{1}{2}\cdot\frac{\tilde{y}^2}{\nu}\cdot\frac{\partial}{\partial \tilde{x}}(\tilde{v}_o^2) \tag{B.5}$$

and non-dimensionalised to

$$u = v_o^2\cdot y\cdot Re\,,\ v = -\frac{1}{2}\cdot y^2\cdot Re\cdot\frac{\partial}{\partial x}(v_o^2)\,, \tag{B.6}$$

by use of

$$x = \frac{\tilde{x}}{L}; y = \frac{\tilde{y}}{L}; u = \frac{\tilde{u}}{U_\infty}; v = \frac{\tilde{v}}{U_\infty}; v_o = \frac{\tilde{v}_o}{U_\infty} \quad , \tag{B.7}$$

where the Reynolds Number Re is defined as

$$Re = \frac{U_\infty\cdot L}{\nu}\,. \tag{B.8}$$

Substituting u, v into Equation (B.1) leads to

$$v_o^2\cdot y\cdot Re\cdot\frac{\partial c_i}{\partial x} - \frac{1}{2}\cdot y^2\cdot Re\cdot\frac{\partial}{\partial x}(v_o^2)\cdot\frac{\partial c_i}{\partial y} = \frac{1}{Pe}\cdot\frac{\partial^2 c_i}{\partial y^2} \tag{B.9}$$

$$v_o^2\cdot y\cdot\frac{\partial c_i}{\partial x} - \frac{1}{2}\cdot y^2\cdot\frac{\partial}{\partial x}(v_o^2)\cdot\frac{\partial c_i}{\partial y} = \frac{1}{Pe\cdot Re}\cdot\frac{\partial^2 c_i}{\partial y^2}\,. \tag{B.10}$$

We introduce two new variables

$$\zeta = x\,,\ \xi = v_o\cdot y\cdot Re \Leftrightarrow y = \frac{\xi}{v_o\cdot Re} \Leftrightarrow v_o = \frac{\xi}{y\cdot Re}\,; \tag{B.11}$$

$$\frac{\partial c_i}{\partial x} = \frac{\partial c_i}{\partial \zeta} + \frac{\partial c_i}{\partial \xi}\cdot\frac{\partial \xi}{\partial x} = \frac{\partial c_i}{\partial \zeta} + \frac{\partial c_i}{\partial \xi}\cdot Re\cdot y\cdot\frac{\partial v_o}{\partial x}\,; \tag{B.12}$$

$$\frac{\partial c_i}{\partial y} = \frac{\partial c_i}{\partial \zeta} \cdot v_o \cdot Re \Rightarrow \frac{\partial^2 c_i}{\partial y^2} = \frac{\partial^2 c_i}{\partial \zeta^2} \cdot v_o^2 \cdot Re^2 . \tag{B.13}$$

Thus by substitution of Equations (B.11), (B.12) and (B.13) into Equation (B.10) we obtain

$$\Rightarrow \frac{\xi}{v_o} \cdot \frac{\partial c_i}{\partial \zeta} = \frac{Re^2}{Pe} \cdot \frac{\partial^2 c_i}{\partial \xi^2} . \tag{B.14}$$

Through variables

$$\sigma = \xi \cdot \left(\frac{Pe}{Re^2}\right)^{1/3}, \ \chi = \int_{\zeta_0}^{\zeta} v_o d\zeta, \ \eta = \frac{\sigma}{(9\chi)^{1/3}}, \tag{B.15}$$

Equation (B.14) can then be transformed from a two-variable equation into a one-variable equation

$$\Rightarrow \quad \frac{\sigma \cdot \left(\frac{Pe}{Re^2}\right)^{-1/3}}{v_o} \cdot \frac{\partial c_i}{\partial \zeta} = \frac{Re^2}{Pe} \cdot \frac{\partial^2 c_i}{\partial \sigma^2 \cdot \left(\frac{Pe}{Re^2}\right)^{-2/3}} \tag{B.16}$$

$$\Rightarrow \frac{\sigma \cdot \left(\frac{Pe}{Re^2}\right)^{-1}}{v_o} \cdot \frac{\partial c_i}{\partial \zeta} = \frac{Re^2}{Pe} \cdot \frac{\partial^2 c_i}{\partial \sigma^2} \tag{B.17}$$

$$\Rightarrow \frac{\eta \cdot (9\chi)^{1/3} \cdot Re^2}{v_o \cdot Pe} \cdot \frac{\partial c_i}{\partial \zeta} = \frac{Re^2}{Pe} \cdot \frac{\partial^2 c_i}{\partial \eta^2 \cdot (9\chi)^{2/3}} \tag{B.18}$$

$$\Rightarrow \frac{\eta \cdot 9\chi}{v_o} \cdot \frac{\partial c_i}{\partial \zeta} = \frac{\partial^2 c_i}{\partial \eta^2} \tag{B.19}$$

$$\Rightarrow \frac{\partial^2 c_i}{\partial \eta^2} + 3\eta^2 \cdot \frac{\partial c_i}{\partial \eta} = 0 \tag{B.20}$$

In terms of the initial variables

$$\eta = \frac{\sigma}{(9\chi)^{1/3}} \tag{B.21}$$

$$\Rightarrow \eta = \frac{\xi \cdot \left(\frac{Pe}{Re^2}\right)^{1/3}}{\left(9\int_{\zeta_0}^{\zeta} v_o d\zeta\right)^{1/3}} \tag{B.22}$$

$$\Rightarrow \eta = \frac{v_o \cdot y \cdot Re \cdot \left(\frac{Pe}{Re^2}\right)^{1/3}}{\left(9\int_{x_0}^{x} v_o d\gamma\right)^{1/3}} \tag{B.23}$$

$$\Rightarrow \eta = \frac{\sqrt{\tau_w(x)} \cdot \left(\frac{Pe \cdot Re^3}{Re^2}\right)^{1/3}}{\left(9\int_{x_0}^{x} \sqrt{\tau_w(\gamma)} d\gamma\right)^{1/3}} \cdot y \tag{B.24}$$

the similarity variable η can now be written as

$$\eta = \frac{(Pe \cdot Re)^{1/3} \cdot \sqrt{\tau(x)}}{(9\int_{x_0}^{x} \sqrt{\tau(\gamma)} d\gamma)^{1/3}} \cdot y = \beta(x) \cdot y\,. \tag{B.25}$$

C SOLUTION OF THE O.D.E

The general solution to the ordinary differential equation

$$\frac{\mathrm{d}^2 c}{\mathrm{d}\eta^2} + 3\eta^2 \cdot \frac{\mathrm{d}c}{\mathrm{d}\eta} = 0 \tag{C.1}$$

is

$$c(\eta) = A \cdot \int_0^{\eta} e^{-\gamma^3} d\gamma + B, \tag{C.2}$$

with A and B constants to be determined via boundary conditions.

$$\frac{\mathrm{d}}{\mathrm{d}\eta} c(\eta) = A \cdot e^{-\eta^3} \tag{C.3}$$

$$\frac{\mathrm{d}^2}{\mathrm{d}\eta^2} c(\eta) = -3 \cdot \eta^2 \cdot A \cdot e^{-\eta^3} \tag{C.4}$$

$$\frac{\mathrm{d}^2}{\mathrm{d}\eta^2} c(\eta) = -3 \cdot \eta^2 \cdot \frac{\mathrm{d}}{\mathrm{d}\eta} c(\eta) \Rightarrow -3 \cdot \eta^2 \cdot A \cdot e^{-\eta^3} \equiv -3 \cdot \eta^2 \cdot A \cdot e^{-\eta^3}. \tag{C.5}$$

At the surface oxygen uptake is balanced by diffusive transport of oxygen to the surface. Hence the surface flux boundary condition is of the form

$$\frac{D_i \cdot c_\infty}{L} \cdot \left.\frac{\partial c}{\partial y}\right|_{y=0} = \frac{D_i \cdot c_\infty}{L} \cdot \beta(x) \cdot \left.\frac{\partial c}{\partial \eta}\right|_{\eta=0} = \frac{c(x,0) \cdot \kappa \cdot V_{max}}{K_m + c(x,0)} \tag{C.6}$$

$$\left.\frac{\partial c}{\partial \eta}\right|_{\eta=0} = \frac{c(x,0)}{K_m + c(x,0)} \cdot \frac{\kappa \cdot V_{max} \cdot L}{D_i \cdot c_\infty} \cdot \frac{1}{\beta(x)} = \frac{c(x,0)}{K_m + c(x,0)} \cdot \frac{Da}{\beta(x)}, \tag{C.7}$$

where Da is the non-dimensional Damkohler number. Using Equation (C.3) constant A is found to be

$$\left.\frac{\partial c}{\partial \eta}\right|_{\eta=0} = A \cdot e^{-\eta^3}\Big|_{\eta=0} \Rightarrow A = \frac{c(x,0)}{K_m + c(x,0)} \cdot \frac{Da}{\beta(x)}. \tag{C.8}$$

Using Equation (C.2) and Equation (C.8) constant B is found to be

$$c(0) \rightarrow c(x,0) = \frac{c(x,0)}{K_m + c(x,0)} \cdot \frac{Da}{\beta(x)} \cdot \int_0^0 e^{-\gamma^3} d\gamma + B, \tag{C.9}$$

$$B = c(x,0). \tag{C.10}$$

The full solution to Equation (C.1) then becomes

$$c(\eta) = \frac{c(x,0)}{K_m + c(x,0)} \cdot \frac{Da}{\beta(x)} \cdot \int_0^\eta e^{-\gamma^3} d\gamma + c(x,0). \tag{C.11}$$

D BOUNDARY CONCENTRATION

Using Equation (C.11) and $\eta \to \infty; \tilde{c}(\eta) \to \tilde{c}_\infty$

$$c(\infty) \to 1 = \frac{c(x,0)}{K_m + c(x,0)} \cdot \frac{Da}{\beta(x)} \cdot \int_0^\infty e^{-\gamma^3} d\gamma + c(x,0), \tag{D.1}$$

with [89]

$$\int_0^\infty e^{-\gamma^3} d\gamma = \frac{\Gamma(1/3)}{3}. \tag{D.2}$$

Rearranging leads to the following quadratic function

$$c(x,0)^2 + c(x,0) \cdot (K_m - 1 + \Delta) - K_m = 0, \tag{D.3}$$

where Δ is

$$\Delta = \frac{Da}{\beta(x)} \cdot \frac{\Gamma(1/3)}{3}. \tag{D.4}$$

The solution to Equation (C.11) is found to be [89]

$$c(x,0) = \frac{1}{2} \cdot [(1 - \Delta - K_m) + \sqrt{(\Delta + K_m - 1)^2 + 4 \cdot K_m}]. \tag{D.5}$$

E LINEARLY INCREASING SHEAR STRESS AND THE SIMILARITY VARIABLE

This calculation is to show that, given a linearly increasing shear stress as in

$$\tau(x) = a \cdot x, \tag{E.1}$$

where a is a constant, the similarity variable η or $\beta(x)$ introduced in Equation (3.25) becomes independent of x, i.e. constant.

$$\beta(x) = \frac{(Pe \cdot Re)^{1/3} \cdot \sqrt{\tau(x)}}{(9\int_0^x \sqrt{\tau(\gamma)}d\gamma)^{1/3}} \tag{E.2}$$

$$= \frac{(Pe \cdot Re)^{1/3} \cdot \sqrt{a \cdot x}}{(9\int_0^x \sqrt{a \cdot \gamma}d\gamma)^{1/3}}$$

$$= \frac{(Pe \cdot Re)^{1/3} \cdot (a \cdot x)^{1/2}}{9^{1/3} \cdot a^{1/6}(\int_0^x \gamma^{1/2}d\gamma)^{1/3}}$$

$$= \frac{(Pe \cdot Re)^{1/3} \cdot (a \cdot x)^{1/2}}{9^{1/3} \cdot a^{1/6}\left(\left[\frac{2}{3} \cdot \gamma^{3/2}\right]_0^x\right)^{1/3}}$$

$$= \frac{(Pe \cdot Re)^{1/3} \cdot (a \cdot x)^{1/2}}{9^{1/3} \cdot a^{1/6} \cdot \left(\frac{2}{3}\right)^{1/3} \cdot x^{1/2}}$$

$$= \frac{(Pe \cdot Re)^{1/3} \cdot a^{1/3}}{6^{1/3}}$$

F SOLUBILITY OF OXYGEN IN AIR-SATURATED WATER

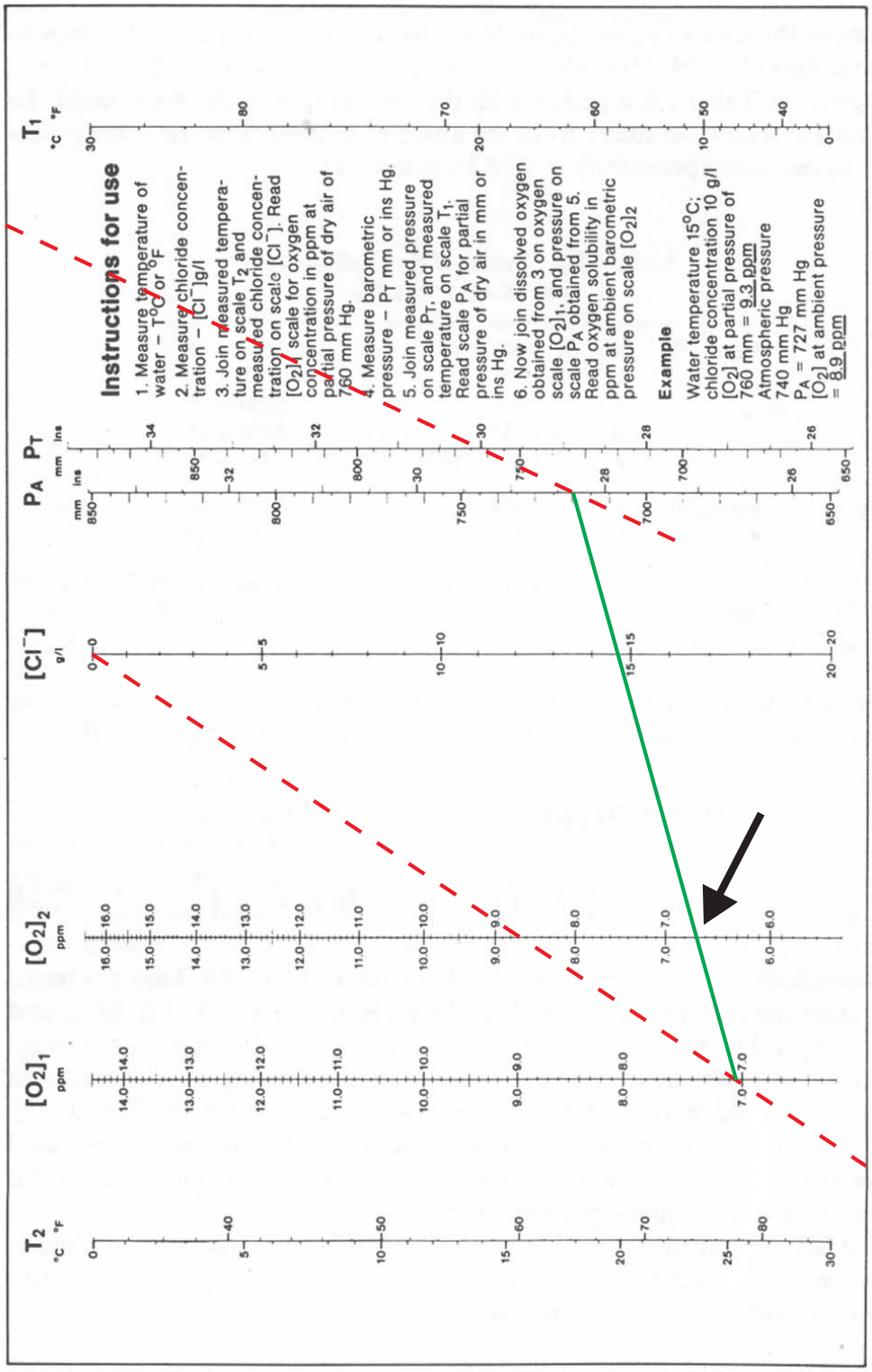

Figure F.1: *Nomogram of oxygen solubility in air-saturated freshwater showing the example determination of the dissolved O_2 concentration in DI water at 37.4*°C, 760 torr and 0 g/l Cl^-. *Adapted from [125].*

REFERENCES

[1] G. L. Semenza, "HIF-1, O2, and the 3 PHDs: How Animal Cells Signal Hypoxia to the Nucleus", *Cell (2001)*, Vol. 107, No. 1, pp. 1-3.

[2] N. S. Chandel and G. R. S. Budinger, "The cellular basis for diverse responses to oxygen", *Free Radical Biology and Medicine (2007)*, Vol. 42, No. 2, pp. 165-174.

[3] H. Zhang and G. Semenza, "The expanding universe of hypoxia", Journal of Molecular Medicine (2008), Vol. 86, No. 7, pp. 739-746.

[4] R. Fukuda, H. Zhang, J.-W. Kim, L. Shimoda, C. V. Dang and Gregg L. Semenza, "HIF-1 Regulates Cytochrome Oxidase Subunits to Optimize Efficiency of Respiration in Hypoxic Cells", *Cell (2007)*, Vol. 129, No. 1, pp. 111-122.

[5] L. C. U. Junqueira, J. Carneiro and R. O. Kelley, "Basic Histology", McGraw-Hill Medical, New York, USA, 2005.

[6] V. Nock, R. J. Blaikie, and T. David, "Micro-patterning of Polymer-based Optical Oxygen Sensors for Lab-on-Chip Applications", *Proceedings of SPIE (2007)*, Vol. 6799, DOI: 10.1117/12.759023.

[7] V. Nock, R. J. Blaikie, and T. David, "Microfluidics for Bioartificial Livers", *New Zealand Medical Journal (2007)*, Vol. 120, No. 1252, pp. 2-3.

[8] T. David, S. Thomas, and P. G. Walker, "Platelet deposition in stagnation point flow: an analytical and computational simulation", *Medical Engineering & Physics (2001)*, Vol. 23, pp. 299-312.

[9] V. Nock and R. J. Blaikie, "Fabrication of optical grayscale masks for tapered microfluidic devices", *Microelectronic Engineering (2008)*, Vol. 85, No. 5-6, pp. 1077-1082.

[10] V. Nock, R. J. Blaikie, and T. David, "Patterning, integration and characterisation of polymer optical oxygen sensors", *Lab on a Chip (2008)*, Vol. 8, No. 8, pp. 1300-1307, DOI: 10.1039/b801879k.

[11] V. Nock, R. J. Blaikie, and T. David, "Generation and detection of laminar flow with laterally-varying oxygen concentration levels", *Proceedings of the 12th International Conference on Miniaturized Systems for Chemistry and Life Sciences MicroTAS (2008)*, Vol. 1, pp. 299-301.

[12] R. Fraser, “The liver in health, and disease”, *New Zealand Pharmacy (June 2002)*, pp. 36-41

[13] S. Sherlock, “The Human Liver”, *Carolina Biology Readers 72 (1978)*, Carolina Biological Supply Company.

[14] R. A. Freitas Jr., “Nanomedicine, Vol. IIA: Biocompatibility”, Landes Bioscience, Georgetown, USA, 2003.

[15] A. C. Guyton, “Textbook of Medical Physiology”, 8th edition, Saunders, Philadelphia, USA, 1991.

[16] R. Fraser, B. R. Dobbs, and G. W. T. Rogers, “Lipoproteins and the Liver Sieve: The Role of the Fenestrated Sinusoidal Endothelium in Lipoprotein Metabolism, Atherosclerosis, and Cirrhosis”, *Hepatology (1995)*, Vol. 21, No.3, pp. 863-874.

[17] Department of Pathology, University of Otago, Christchurch School of Medicine & Health Sciences, accessed January 2009, <http://www.chmeds.ac.nz/research/liversieve/background.htm#5>

[18] K. R. Prasad and J. P. A. Lodge, “ABC of diseases of liver, pancreas, and biliary system: Transplantation of the liver and pancreas”, *British Medical Journal (2001)*, Vol. 322, pp. 845-847.

[19] M. I. Prince and M. Hudson, “Liver transplantation for chronic liver disease: advances and controversies in an era of organ shortages”, *Postgraduate Medical Journal (2002)*, Vol. 78 (917) pp. 135-141.

[20] Organ Procurement and Transplantation Network, accessed December 2008, <http://www.optn.org>

[21] J. F. Trotter, “Living donor liver transplantation: is the hype over?”, *Journal of Hepatology (2005)*, Vol. 42, Issue 1, pp. 20-25.

[22] H. V. Melendez and N. D. Heaton, “Understanding ‘marginal’ liver grafts”, Transplantation (1999), Vol. 68, Issue 4, pp. 469-471.

[23] J. A. Lowell, S. E. Taranto, G. G. Singer, S. B. Miller, R. Ghalib, C. Caldwell, S. Shenoy, S. Dolan, M. Peters, T. K. Howard, and D. C. Brennan, “Transplant recipients as organ donors: the domino transplant”, *Transplantation Proceedings (1997)*, Vol. 29, Issue 8, pp. 3392-3393.

[24] R. W. Busuttil and J. A. Goss, “Split liver transplantation”, *Annals of Surgery (1999)*, Vol. 229, Issue 3, pp. 313-321.

[25] J. W. Allen, T. Hassanein, and S. N. Bhatia, “Advances in Bioartificial Liver Devices”, *Hepatology (2001)*, Vol. 34, No. 3, pp. 447-455.

[26] C. Selden and H. Hodgson, “Cellular therapies for liver replacement”, *Transplant Immunology (2004)*, Vol. 12, Issues 3-4, pp. 273-288.

[27] C. Chan, F. Berthiaume, B. D. Nath, A. W. Tilles, M. Toner, and M. L. Yarmush, “Hepatic Tissue Engineering for Adjunct and Temporary Liver Support: Critical Technologies”, *Liver Transplantation (2004)*, Vol. 10, No. 11, pp. 1331-1342.

[28] J. W. Allen and S. N. Bhatia, “Engineering liver therapies for the future”, *Tissue Engineering (2002)*, Vol. 8, Issue 5, pp. 725–737.

[29] A. J. Tector, M. Berho, J. A. Fridell, A. DiCarlo, S. Liu, C. Soderland, J. S. Barkun, P. Metrakos, and J. I. Tchervenkov, “Rejection of pig liver xenografts in patients with liver failure: implications for xenotransplantation”, *Liver Transplantation (2001)*, Vol. 7, Issue 2, pp. 82-89.

[30] J.-K. Park and D.-H. Lee, “Bioartificial Liver Systems: Current Status and Future Perspective”, *Journal of Bioscience and Bioengineering (2005)*, Vol. 99, No. 4, pp. 311-319.

[31] T. Hui, J. Rozga and A. A. Demetriou, “Bioartificial liver support”, *Journal of Hepatobiliary Pancreatic Surgery (2001)*, Vol. 8, pp. 1-15.

[32] N. R. Barshes, A. N. Gay, B. Williams, A. J. Patel, and S. S. Awad, “Support for the Acutely Failing Liver: A Comprehensive Review of Historic and Contemporary Strategies”, *Journal of the American College of Surgeons (2005)*, Vol. 201, No.3, pp. 458-476.

[33] Gambro AB, accessed January 2009, <http://www.gambro.com/int/Treatment-offerings/Hepatic-Care/MARS-system/>

[34] Fresenius Medical Care AG, accessed January 2009, <http://www.fresenius.se/internet/fag/com/faginpub.nsf/Content/Liver+Support+Therapy>

[35] K. Rifai, T. Ernst, U. Kretschmer, M. J. Bahr, A. Schneider, C. Hafer, H. Haller, M. P. Manns, and D. Fliser, “Prometheus - a new extracorporeal system for the treatment of liver failure”, *Journal of Hepatology (2003)*, Vol. 39, Issue 6, pp.984-990.

[36] M. N. Berry and D. S. Friend, “High-Yield Preparation of Isolated Rat Liver Parenchymal Cells: A Biochemical and Fine Structural Study”, *Journal of Cell Biology (1969)*, Vol. 43, Issue 3, pp. 506-520.

[37] C. F. W. Wolf and B. E. Munkelt, “Bilirubin conjugation by an artificial liver composed of cultured cells and synthetic capillaries”, *ASAIO Transactions (1975)*, Vol. 21, pp.16-26.

[38] J. C. Hager, R. Carmann, R. Stoller, G. Panol, E. G. Ledue, W. R. Thayer, L. E. Porter, and P. M. Galletti, P. Calabresi, “A prototype for a hybrid artificial liver”, *ASAIO Transactions (1978)*, Vol. 24, pp. 250–253.

[39] J. C. Hager, R. Carmann, L. E. Porter, P. M. Galletti, and P. Valabresi, “Neonatal hepatocyte culture on artificial capillaries. A model for drug metabolism and artificial liver”, *ASAIO Journal (1983)*, Vol. 6, pp. 26–35.

[40] Y. L. Xue, S. F. Zhao, Y. Luo, X. J. Li, Z. P. Duan, X. P. Chen, W. G. Li, X. Q. Huang, Y. L. Li, X. Cui, D. B. Zhong, Z. Y. Zhang, and Z. Q. Huang, “TECA hybrid artificial liver support system in treatment of acute liver failure”, World Journal of Gastroenterology (2001), Vol. 7, pp. 826–829.

[41] Y. T. Ding, Y. D. Qiu, Z. Chen, Q. X. Xu, H. Y. Zhang, Q. Tang, and D. C. Yu, “The development of a new bioartificial liver and its application in 12 acute liver failure patients”, *World Journal of Gastroenterology (2003)*, Vol. 9, pp. 829–832.

[42] A. Donini, U. Baccarani, A. Risaliti, A. Degrassi, and F. Bresadola, “Temporary neurological improvement in a patient with acute or chronic liver failure treated with a bioartificial liver device”, *American Journal of Gastroenterology (2000)*, Vol. 95, pp. 1102-1104.

[43] Arbios Systems, Inc., accessed January 2009, <http://www.arbios.com/>

[44] J. Rozga, A. A. Demetriou, E. Morsiani, E. Lepage, A. D. Moscioni, and T. Giorgio, “Isolated hepatocytes in a bioartificial liver: single group view and experience”, *Biotechnology and Bioengineering (1994)*, Vol. 43, pp. 645-653

[45] Vital Therapies, Inc., accessed January 2009, <http://vitaltherapies.com/>

[46] N. L. Sussman and J. H. Kelly, “Improved liver function following treatment with extracorporeal liver assist device”, *Artificial Organs (1993)*, Vol. 18, pp. 27-30.

[47] N. L. Sussman, G. T. Gislason, C. A. Conlin, and J. H. Kelly, “The Hepatix extracorporeal liver assist device: initial clinical experience”, *Artificial Organs (1994)*, Vol. 18, pp. 390-396.

[48] J. M. Millis, D. C. Cronin, R. Johnson, H. Conjeevaram, C. Conlin, S. Trevino, and P. Maguire, “Initial experience with the modified extracorporeal liver-assist device for patients with fulminant hepatic failure: system modifications and clinical impact”, *Transplantation (2002)*, Vol. 74, Issue 12, pp.1735-1746.

[49] J. C. Gerlach, “Development of a hybrid liver support system: a review”, *International Journal of Artificial Organs (1996)*, Vol. 19, pp. 645-654.

[50] I. M. Sauer, N. Obermeyer, D. Kardassis, T. Theruvath, and J. C. Gerlach, “Development of a hybrid liver support system”, *Annals of the New York Academy of Sciences (2001)*, Vol. 944, pp. 308–319.

[51] I. M. Sauer, K. Zeilinger, N. Obermayer, G. Pless, A. Grunwald, A. Pascher, T. Mieder, S. Roth, M. Goetz, D. Kardassis, A. Mas, P. Neuhaus, and J. C. Gerlach, “Primary human liver cells as source for modular extracorporeal liver support — a preliminary report”, *International Journal of Artificial Organs (2002)*, Vol. 25, pp. 1001–1005.

[52] Hybrid Organ GMBH, accessed January 2009, <http://www.hybrid-organ.com/>

[53] Excorp Medical Inc., accessed January 2009, <http://www.excorp.com/html/product.html>

[54] J. F. Patzer II, G. V. Mazariegos, and R. Lopez, “Bioartificial liver program investigators. Preclinical evaluation of the Excorp Medical, Inc., bioartificial liver support system”, *Journal of the American College of Surgeons (2002)*, Vol. 195, pp. 299-310.

[55] G. V. Mazariegos, J. F. Patzer II, R. C. Lopez, M. Giraldo, M. E. deVera, T. A. Grogan, Y. Zhu, M. L. Fulmer, B. P. Amiot, and D. J. Kramer, “First Clinical Use of a Novel Bioartificial Liver Support System (BLSS)”, *American Journal of Transplantation (2002)*, Vol. 2, pp. 260–266.

[56] E. Morsiani, M. Brogli, D. Galavotti, T. Bellini, D. Ricci, P. Pazzi, and A. C. Puviani, “Long-term expression of highly differentiated functions by isolated porcine hepatocytes perfused in a radial-flow bioreactor”, *Artificial Organs (2001)*, Vol. 25, pp. 740-748.

[57] E. Morsiani, P. Pazzi, A. C. Puviani, M. Brogli, L. Valieri, P. Gorini, P. Scoletta, E. Marangoni, R. Ragazzi, G. Azzena, and other 10 authors, “Early experiences with a porcine hepatocyte-based bioartificial liver in acute hepatic failure patients”, *International Journal of Artificial Organs (2002)*, Vol. 25, pp. 192-202.

[58] L. M. Flendrig, J. W. La Soe, G. G. Jorning, A. Steenbeek, O. T. Karlsen, W. M. Bovee, N. C. Ladiges, A. A. te Velde, and R. A. Chamuleau, "*In-vitro* evaluation of a novel bioreactor based on an integral oxygenator and a spirally wound nonwoven polyester matrix for hepatocyte culture as small aggregates", *Journal of Hepatology (1997)*, Vol. 26, pp. 1379-1392.

[59] W. S. Hu, J. R. Friend, F. J. Wu, T. Sielaff, M. V. Peshwa, A. Lazer, S. L. Nygerg, R. P. Remmel, and F. B. Cerra, "Development of a bioartificial liver employing xenogenic hepatocytes", *Cytotechnology (1997)*, Vol. 23, pp. 29-38.

[60] I. Jasmund, A. Langsch, R. Simmoteit, and A. Bader, "Cultivation of primary porcine hepatocytes in an OXY-HFB for use as a bioartificial liver device", *Biotechnology Progress (2002)*, Vol. 18, pp. 839-846.

[61] I. Jasmund, "Entwicklung und Funktionsprüfung eines oxygenierenden Hohlfaserreaktors zur Kultivierung von Leberzellen", *Ph.D. Thesis (2003)*, in German, Technical University Carolo-Wilhelmina, Braunschweig, Germany.

[62] H. Mizumoto and K. Funatsu, "Liver regeneration using a hybrid artificial liver support system", *Artificial Organs (2004)*, Vol. 28, pp. 53-57.

[63] K. Nakazawa, H. Ijima, J. Fukuda, R. Sakiyama, Y. Yamashita, M. Shimada, K. Shirabe, E. Tsujita, K. Sugimachi, and K. Funatsu, "Development of a hybrid artificial liver using polyurethane foam/hepatocyte spheroid culture in a preclinical pig experiment", *International Journal of Artificial Organs (2002)*, Vol. 25, pp. 51-60.

[64] Y. Yamashita, M. Shimada, H. Ijima, K. Nakazawa, K. Funatsu, and K Sugimachi, "Hybrid-artificial liver support system", *Surgery (2002)*, Vol. 131, No. 1, pp. 334-340.

[65] V. Dixit and G. Gitnick, "The bioartificial liver: state-of-the-art", *European Journal of Surgery (1998)*, Vol. 164 (Suppl. 582), pp. 71-76.

[66] D. H. Lee, H. H. Yoon, and J. K. Park, "Hepatocyte culture technology and its application to bioartificial liver", *Korean Chemical Engineering Research (2004)*, Vol. 42, pp. 129-138.

[67] L. De Bartolo, G. Jarosch-Von Schweder, A. Haverich, and A. Bader, "A novel full-scale flat membrane bioreactor utilizing porcine hepatocytes: cell viability and tissue-specific functions", *Biotechnology Progress (2000)*, Vol. 16, pp. 102-108.

[68] M. Shito, A. W. Tilles, R. G. Tompkins, M. L. Yarmush, and M. Toner, "Efficacy of an extracorporeal flat-plate bioartificial liver in treating fulminant hepatic failure", *Journal of Surgical Research (2003)*, Vol. 111, pp. 53-62.

[69] M. Shito, N. H. Kim, H. Baskaran, A. W. Tilles, R. G. Tompkins, M. L. Yarmush, and M. Toner, "*In-Vitro* Evaluation of Albumin Synthesis Rate of Porcine Hepatocytes in a Flat-Plate Bioreactor", *Artificial Organs (2001)*, Vol. 25, Issue 7, pp. 571-578.

[70] E. Lagasse, H. Connors, M. Al-Dhalimy, M. Reitsma, M. Dohse, L. Osborne, X. Wang, M. Finegold, I. L. Weissman, and M. Grompe, "Purified hematopoietic stem cells can differentiate into hepatocytes *in vivo*", *Nature Medicine (2000)*, Vol. 6. No. 11, pp. 1229-1234.

[71] N. Harimoto, A. Taketomi, D. Kitagawa, Y. Kuroda, S. Itoh, T. Gion, S. Tanaka, K. Shirabe, M. Shimada, and Y. Maehara, "The newly established human hepatocyte cell line: application for the bioartificial liver", *Journal of Hepatology (2005)*, Vol. 42, pp. 557-564.

[72] A. J. Strain and J. M. Neuberger, "A Bioartificial Liver - State of the Art", *Science (2002)*, Vol. 295, pp. 1005-1009.

[73] J. W. Allen and S. N. Bhatia, "Formation of Steady-State Oxygen Gradients in Vitro", *Biotechnology and Bioengineering (2003)*, Vol. 82, No. 3, pp. 253-262.

[74] J. W. Allen, S. R. Khetani, and S. N. Bhatia, "*In Vitro* Zonation and Toxicity in a Hepatocyte Bioreactor", *Toxicological Sciences (2005)*, Vol. 84, pp. 110-119.

[75] S. N. Bhatia, M. L. Yarmush, and M. Toner, "Controlling cell interactions by micropatterning in co-cultures: Hepatocytes and 3T3 fibroblasts", *Journal of Biomedical Materials Research (1997)*, Vol. 34, pp. 189-199.

[76] M. N. De Silva, R. Desai, and D. J. Odde, "Micro-Patterning of Animal Cells on PDMS Substrates in the Presence of Serum without Use of Adhesion Inhibitors", *Biomedical Microdevices (2004)*, Vol. 6, No. 3, pp. 219-222.

[77] T. A. Broughan, R. Naukam, C. Tan, C. J. Van De Wiele, H. Refai and T. K. Teague, "Effects of Hepatic Zonal Oxygen Levels on Hepatocyte Stress Responses", *Journal of Surgical Research (2008)*, Vol. 145, No. 1, pp. 150-160.

[78] Y. Nahmias, Y. Kramvis, L. Barbe, M. Casali, F. Berthiaume and M. L. Yarmush, "A novel formulation of oxygen-carrying matrix enhances liver-specific function of cultured hepatocytes", *FASEB Journal (2006)*, Vol. 20, No. 14, pp. 2531-2533.

[79] B. J. Kane, M. J. Zinner, M. L. Yarmush and M. Toner, "Liver-Specific Functional Studies in a Microfluidic Array of Primary Mammalian Hepatocytes", *Analytical Chemistry (2006)*, Vol. 78, No. 13, pp. 4291-4298.

[80] P. J. Lee, T. A. Gaige, N. Ghorashian and P. J. Hung, “Microfluidic Tissue Model for Live Cell Screening”, *Biotechnology Progress (2007)*, Vol. 23, No. 4, pp. 946-951.

[81] M. Zhang, P. Lee, P. Hung, T. Johnson, L. Lee and M. Mofrad, “Microfluidic environment for high density hepatocyte culture”, *Biomedical Microdevices (2008)*, Vol. 10, No. 1, pp. 117-121.

[82] M. R. Neumann, “Biomedical Sensors”, T*he Biomedical Engineering Handbook: Second Edition*, CRC Press, Boca Raton, USA, 2000.

[83] N.-T. Nguyen and Z. Wu, “Micromixers - a review”, *Journal of Micromechanics and Microengineering (2005)*, Vol. 15, No. 2, pp. R1-R16.

[84] J. Holder, R. Ellison, and R. Lee, “Research, Development and Feasibility Study for Bio-Artificial Liver”, *Final Year Project Report (2003)*, Department of Mechanical Engineering, University of Canterbury, Christchurch, New Zealand.

[85] J. Happel and H. Brenner, “Low Reynolds Number Hydrodynamics with Special Applications to Particulate Media”, Prentice-Hall, Englewood Cliffs, USA, 1965.

[86] W. J. Beek and K. M. K. Muttzall, “Transport Phenomena”, Wiley, London, GB, 1975.

[87] T. David, “Wall Shear Stress Modulation of ATP/ADP Concentration at the Endothelium”, *Annals of Biomedical Engineering (2003)*, Vol. 31, pp. 1231-1237.

[88] P. Roy, H. Baskaran, A. W. Tilles, M. L. Yarmush, and M. Toner, “Analysis of Oxygen Transport to Hepatocytes in a Flat-Plate Microchannel Bioreactor”, *Annals of Biomedical Engineering (2001)*, Vol. 29, pp. 947-955.

[89] D. Zwillinger, “CRC - Standard Mathematical Tables and Formulae”, 30th edition, CRC, Boca Raton, USA, 1996.

[90] S. Usami, H.-H. Chen, Y. Zhao, S. Chien, and R. Skalak, “Design and Construction of a Linear Shear Stress Flow Chamber”, *Annals of Biomedical Engineering (1993)*, Vol. 21, pp. 77-83.

[91] Multiphysics© version 3.4, COMSOL AB, Stockholm, Sweden <http://www.comsol.com>

[92] Mathematica© version 5.2, Wolfram Research Inc., Champaign, USA.

[93] Matlab© version R14 SP3, The Mathworks Inc., USA.

[94] A. W. Tilles, H. Baskaran, P. Roy, M. L. Yarmush, and M. Toner, “Effects of Oxygenation and Flow on the Viability and Function of Rat Hepatocytes Co-cultured in a Microchannel Flat-Plate Bioreactor”, *Biotechnology and Bioengineering (2001)*, Vol. 73, No. 5, pp. 379-389.

[95] Y. Xia and G. M. Whitesides, “Soft Lithography”, *Angewandte Chemie International Edition (1998)*, Vol. 37, pp. 550-575.

[96] W. Henke, W. Hoppe, H. J. Quenzer, P. Staudt-Fischbach, and B. Wagner, “Simulation and experimental study of gray-tone lithography for the fabrication of arbitrarily shaped surfaces”, *Proceedings of the IEEE Workshop on MEMS (1994)*, pp. 205-210.

[97] C. M. Waits, A. Modafe, and R. Ghodssi, “Investigation of gray-scale technology for large area 3D silicon MEMS structures”, *Journal of Micromechanics and Microengineering (2003)*, Vol. 13, pp. 170-177.

[98] R. Mori, K. Hanai, and Y. Matsumoto, “Three Dimensional Micro Machining of SU-8 and Application for PDMS Micro Capillaries”, *Proceedings of the 8th International Conference on Miniaturized Systems for Chemistry and Life Sciences MicroTAS (2004)*, pp. 333-335.

[99] P. Ruffieux, T. Scharf, I. Philipoussis, H. P. Herzig, R. Voelkel and K. J. Weible, “Two step process for the fabrication of diffraction limited concave microlens arrays”, *Opt. Express (2008)*, Vol. 16, No. 24, pp. 19541-19549.

[100] B. H. Jo, L. M. Van Lerberghe, K. M. Motsegood, and D. J. Beebe, “Three-dimensional micro-channel fabrication in polydimethylsiloxane (PDMS) elastomer”, *Journal of Microelectromechanical Systems (2000)*, Vol. 9, No. 1, pp. 76-81.

[101] F. Laerme, A. Schilp, K. Funk, and M. A. O. M. Offenberg, “Bosch deep silicon etching: improving uniformity and etch rate for advanced MEMS applications”, *Technical Digest of the 12th IEEE International Conference on Micro Electro Mechanical Systems MEMS (1999)*.

[102] S. Roy, S. Khanna, A. A. Bickerstaff, S. V. Subramanian, M. Atalay, M. Bierl, S. Pendyala, D. Levy, N. Sharma, M. Venojarvi, A. Strauch, C. G. Orosz, and C. K. Sen, “Oxygen Sensing by Primary Cardiac Fibroblasts: A Key Role of p21Waf1/Cip1/Sdi1”, *Circulation Research (2003)*, Vol. 92, No. 3, pp. 264-271.

[103] T. Kietzmann and K. Jungermann, “Modulation by oxygen of zonal gene expression in liver studied in primary rat hepatocyte cultures”, *Cell Biology and Toxicology (1997)*, Vol. 13, No. 4, pp. 243-255.

[104] L.-L. Zhu, L.-Y. Wu, D. Yew, and M. Fan, “Effects of hypoxia on the proliferation and differentiation of NSCs”, *Molecular Neurobiology (2005)*, Vol. 31, No. 1, pp. 231-242.

[105] F. C. O'Mahony, C. O'Donovan, J. Hynes, T. Moore, J. Davenport, and D. B. Papkovsky, “Optical Oxygen Microrespirometry as a Platform for Environmental Toxicology and Animal Model Studies”, *Environmental Science and Technology (2005)*, Vol. 39, No. 13, pp. 5010-5014.

[106] C.-C. Wu, T. Saito, T. Yasukawa, H. Shiku, H. Abe, H. Hoshi, and T. Matsue, “Microfluidic chip integrated with amperometric detector array for in situ estimating oxygen consumption characteristics of single bovine embryos”, *Sensors and Actuators, B: Chemical Sensors and Materials (2007)*, Vol. 125, No. 2, pp. 680-687.

[107] D. A. Chang-Yen and B. K. Gale, “An integrated optical oxygen sensor fabricated using rapid-prototyping techniques”, *Lab on a Chip (2003)*, Vol. 3, No. 4, pp. 297-301.

[108] J. Karasinski, L. White, Y. C. Zhang, E. Wang, S. Andreescu, O. A. Sadik, B. K. Lavine, and M. Vora, “Detection and identification of bacteria using antibiotic susceptibility and a multi-array electrochemical sensor with pattern recognition”, *Biosensors and Bioelectronics (2007)*, Vol. 22, No. 11, pp. 2643-2649.

[109] E. Akyilmaz, A. Erdogan, R. Ozturk, and I. Yasa, “Sensitive determination of L-lysine with a new amperometric microbial biosensor based on Saccharomyces cerevisiae yeast cells”, *Biosensors and Bioelectronics (2007)*, Vol. 22, No. 6, pp. 1055-1060.

[110] S. Fischkoff and J. M. Vanderkooi, “Oxygen diffusion in biological and artificial membranes determined by the fluorochrome pyrene”, *Journal of General Physiology (1975)*, Vol. 65, No. 5, pp. 663-676.

[111] H. Chuang and M. A. Arnold, “Radioluminescent sources for optical chemical sensors”, *Pure Applied Chemistry (1999)*, Vol. 71, pp. 803-810.

[112] Y. Amao, “Probes and Polymers for Optical Sensing of Oxygen”, *Microchimica Acta (2003)*, Vol. 143, pp. 1-12.

[113] J. Alderman, J. Hynes, S. M. Floyd, J. Kruger, R. O'Connor, and D. B. Papkovsky, “A low-volume platform for cell-respirometric screening based on quenched-luminescence oxygen sensing”, *Biosensors and Bioelectronics (2004)*, Vol. 19, No. 11, pp. 1529-1535.

[114] D. Sud, G. Mehta, K. Mehta, J. Linderman, S. Takayama, and M.-A. Mycek, “Optical imaging in microfluidic bioreactors enables oxygen monitoring for continuous cell culture”, *Journal of Biomedical Optics (2006)*, Vol. 11, No. 5, pp. 050504-3.

[115] A. P. Vollmer, R. F. Probstein, R. Gilbert, and T. Thorsen, “Development of an integrated microfluidic platform for dynamic oxygen sensing and delivery in a flowing medium”, *Lab on a Chip (2005)*, Vol. 5, pp. 1059-1066.

[116] X. Xiong, D. Xiao, and M. M. F. Choi, “Dissolved oxygen sensor based on fluorescence quenching of oxygen-sensitive ruthenium complex immobilized on silica-Ni-P composite coating”, *Sensors and Actuators B: Chemical (2006)*, Vol. 117, No. 1, pp. 172-176.

[117] S. Lee, B. L. Ibey, G. L. Cote, and M. V. Pishko, “Measurement of pH and dissolved oxygen within cell culture media using a hydrogel microarray sensor”, *Sensors and Actuators B: Chemical (2008)*, Vol. 128, No. 2, pp. 388-398.

[118] D. B. Papkovsky, G. V. Ponomarev, W. Trettnak, and P. O'Leary, “Phosphorescent Complexes of Porphyrin Ketones: Optical Properties and Application to Oxygen Sensing”, *Anal. Chem. (1995)*, Vol. 67, No. 22, pp. 4112-4117.

[119] Sylgard 184 Datasheet, “*Information about Dow Corning brand Silicone Encapsulants*”, Dow Corning (2005).

[120] M. Brown, Autostitch, Demo Version, accessed January 2009, <http://www.cs.ubc.ca/~mbrown/autostitch/autostitch.html>

[121] G. N. Taylor, T. M. Wolf, and J. M. Moran, “Organosilicon monomers for plasma-developed x-ray resists”, *Journal of Vacuum Science and Technology (1981)*, Vol. 19, No. 4, pp. 872-880.

[122] Media Formulations for Cell Culture, “DME”, Sigma Aldrich (2008).

[123] Product Catalogue, Cole-Parmer (2001/02), p. 1306.

[124] Y. Chisti, “Animal-cell damage in sparged bioreactors”, *Trends in Biotechnology (2000)*, Vol. 18, No. 10, pp. 420-432.

[125] M. L. Hitchman, “Measurement of dissolved oxygen”, Wiley, New York, USA, 1978.

[126] R.L. Hamilton, M.N. Berry, M.C. Williams, and E.M. Severinghaus, “A simple and inexpensive membrane “lung” for small organ perfusion”, *Journal of Lipid Research (1974)*, Vol. 15, No. 2, pp. 182-186.

[127] T. C. Merkel, V. I. Bondar, K. Nagai, B. D. Freeman and I. Pinnau, “Gas sorption, diffusion, and permeation in poly(dimethylsiloxane)”, *Journal of Polymer Science Part B: Polymer Physics (2000)*, Vol. 38, No. 3, pp. 415-434.

[128] Nikon MicroscopyU, accessed January 2009, <http://www.microscopyu.com>

[129] A. Mills, “Controlling the sensitivity of optical oxygen sensors”, *Sensors and Actuators B: Chemical (1998)*, Vol. 51, No. 1-3, pp. 60-68.

[130] Y. Fujiwara and Y. Amao, “Optimizing oxygen-sensitivity of optical sensor using pyrene carboxylic acid by myristic acid co-chemisorption onto anodic oxidized aluminium plate”, *Talanta (2004)*, Vol. 62, No. 3, pp. 655-660.

[131] B. D. MacCraith, C. M. McDonagh, G. O'Keeffe, E. T. Keyes, J. G. Vos, B. O'Kelly, and J. F. McGilp, “Fibre optic oxygen sensor based on fluorescence quenching of evanescent-wave excited ruthenium complexes in sol–gel derived porous coatings”, *The Analyst (1993)*, Vol. 118, No. pp. 385 - 388.

[132] M. Smiddy, N. Papkovskaia, D.B. Papkovsky, and J.P. Kerry, “Use of oxygen sensors for the non-destructive measurement of the oxygen content in modified atmosphere and vacuum packs of cooked chicken patties; impact of oxygen content on lipid oxidation”, *Food Research International (2002)*, Vol. 35, No. 6, pp. 577-584.

[133] J. Zhao, S. Jiang, Q. Wang, X. Liu, X. Ji, and B. Jiang, “Effects of molecular weight, solvent and substrate on the de-wetting morphology of polystyrene films”, *Applied Surface Science (2004)*, Vol. 236, No. 1-4, pp. 131-140.

[134] P. Hartmann, and W. Trettnak, “Effects of Polymer Matrices on Calibration Functions of Luminescent Oxygen Sensors Based on Porphyrin Ketone Complexes”, *Analytical Chemistry (1996)*, Vol. 68, No. 15, pp. 2615-2620.

[135] M. Ohyanagi, H. Nishide, K. Suenaga, and E. Tsuchida, “Oxygen-permselectivity in new type polyorganosiloxanes with carboxyl group on the side chain”, *Polymer Bulletin (1990)*, Vol. 23, No. 6, pp. 637-642.

[136] H.-X. Rao, F.-N. Liu and Z.-Y. Zhang, “Preparation and oxygen/nitrogen permeability of PDMS crosslinked membrane and PDMS/tetraethoxysilicone hybrid membrane”, *Journal of Membrane Science (2007)*, Vol. 303, No. 1-2, pp. 132-139.

[137] G. S. Fiorini, G. D. M. Jeffries, D. S. W. Lim, C. L. Kuyper and D. T. Chiu, “Fabrication of thermoset polyester microfluidic devices and embossing masters using rapid prototyped polydimethylsiloxane molds”, *Lab on a Chip (2003)*, Vol. 3, No. 3, pp. 158-163.

[138] G. S. Fiorini, R. M. Lorenz, J. S. Kuo and D. T. Chiu, "Rapid Prototyping of Thermoset Polyester Microfluidic Devices", *Anal. Chem. (2004)*, Vol. 76, No. 16, pp. 4697-4704.

[139] G. S. Fiorini, M. Yim, G. D. M. Jeffries, P. G. Schiro, S. A. Mutch, R. M. Lorenz and D. T. Chiu, "Fabrication improvements for thermoset polyester (TPE) microfluidic devices", *Lab on a Chip (2007)*, Vol. 7, No. 7, pp. 923-926.

[140] A. E. Kamholz, E. A. Schilling, and P. Yager, "Optical Measurement of Transverse Molecular Diffusion in a Microchannel", *Biophysical Journal (2001)*, Vol. 80, No. 4, pp. 1967-1972.

[141] A. E. Kamholz, and P. Yager, "Theoretical Analysis of Molecular Diffusion in Pressure-Driven Laminar Flow in Microfluidic Channels", *Biophysical Journal (2001)*, Vol. 80, No. 1, pp. 155-160.

[142] M. S. Munson, K. R. Hawkins, M. S. Hasenbank and P. Yager, "Diffusion based analysis in a sheath flow microchannel: the sheath flow T-sensor", *Lab on a Chip (2005)*, Vol. 5, No. 8, pp. 856-862.

[143] S. Takayama, E. Ostuni, P. LeDuc, K. Naruse, D. E. Ingber and G. M. Whitesides, "Laminar flows: Subcellular positioning of small molecules", *Nature (2001)*, Vol. 411, No. 6841, pp. 1016-1016.

[144] S. Takayama, E. Ostuni, P. LeDuc, K. Naruse, D. E. Ingber and G. M. Whitesides, "Selective Chemical Treatment of Cellular Microdomains Using Multiple Laminar Streams", *Chemistry & Biology (2003)*, Vol. 10, No. 2, pp. 123-130.

[145] P. Han and D. M. Bartels, "Temperature Dependence of Oxygen Diffusion in H2O and D2O", *Journal of Physical Chemistry (1996)*, Vol. 100, No. 13, pp. 5597-5602.

[146] M. J. Powers, L. G. Griffith, "Adhesion-guided *in-vitro* morphogenesis in pure and mixed cell cultures", *Microscopy Research and Technique (1998)*, Vol. 43, No. 5, pp. 379-384.

[147] M. N. De Silva, R. Desai and D. J. Odde, "Micro-patterning of animal cells on PDMS substrates in the presence of serum without use of adhesion inhibitors", *Biomedical Microdevices* (2004), Vol. 6, No. 3, pp. 219-222.

[148] Y. S. Zinchenko, and R. N. Coger, "Engineering micropatterned surfaces for the coculture of hepatocytes and Kupffer cells", *Journal of Biomedical Materials Research Part A* (2005), Vol. 75A, No. 1, pp. 242-248.

[149] S. W. Rhee, A. M. Taylor, C. H. Tu, D. H. Cribbs, C. W. Cotman, and N. L. Jeon, "Patterned cell culture inside microfluidic devices", *Lab on a Chip (2005)*, Vol. 5, pp. 102-107.

[150] Type I Collagen Product Information, "*Collagens for Cell Culture*", Sigma Aldrich (2007).

[151] V. Nock, R. J. Blaikie, and T. David, "In-situ Optical Oxygen Sensing for Bioartificial Liver Bioreactors", *Proceedings of ICBME (2008)*, **in press.**

[152] M. Shito, A. W. Tilles, R. G. Tompkins, M. L. Yarmush and M. Toner, "Efficacy of an extracorporeal flat-plate bioartificial liver in treating fulminant hepatic failure", *Journal of Surgical Research (2003)*, Vol. 111, No. 1, pp. 53-62.

[153] M. Nishida, "The Ishikawa Cells from Birth to the Present", *Human Cell (2002)*, Vol. 15, No. 3, pp. 104-117.

[154] S. Erlinger, "Hepatocyte bile secretion: Current views and controversies", *Hepatology (1981)*, Vol. 1, No. 4, pp. 352-359.

[155] J. C. Y. Dunn, R. G. Tompkins and M. L. Yarmush, "Long-term in vitro function of adult hepatocytes in a collagen sandwich configuration", *Biotechnology Progress (1991)*, Vol. 7, No. 3, pp. 237-245.

[156] X. Liu, K. H. R. Baronian and A. J. Downard, "Patterned Arrays of Vertically Aligned Carbon Nanotube Microelectrodes on Carbon Films Prepared by Thermal Chemical Vapor Deposition", *Analytical Chemistry (2008)*, Vol. 80, No. 22, pp. 8835-8839.

[157] N. Aoki, A. Yokoyama, Y. Nodasaka, T. Akasaka, M. Uo, Y. Sato, K. Tohji and F. Watari, "Cell Culture on a Carbon Nanotube Scaffold", *Journal of Biomedical Nanotechnology (2005)*, Vol. 1, No. pp. 402-405.

[158] A. Noy, H. G. Park, F. Fornasiero, J. K. Holt, C. P. Grigoropoulos and O. Bakajin, "Nanofluidics in carbon nanotubes", *Nano Today (2007)*, Vol. 2, No. 6, pp. 22-29.

[159] K. Mohamed, M. M. Alkaisi and R. J. Blaikie, "The replication of three dimensional structures using UV curable nanoimprint lithography", *Journal of Vacuum Science & Technology B (2008)*, Vol. 26, No. 6, pp. 2500-2503.

[160] J. Atencia, J. Morrow and L. E. Locascio, "The "Microfluidic Palette": Generation of Stable and Purely Diffusive Chemical Gradients inside a Microfluidic Chamber", *Proceedings of the Twelfth International Conference on Miniaturized Systems for Chemistry and Life Sciences (2008)*, San Diego, California, USA, pp. 1332-1334.

[161] H. Yu, I. Meyvantsson, I. A. Shkel and D. J. Beebe, “Diffusion dependent cell behavior in microenvironments”, *Lab on a Chip (2005)*, Vol. 5, No. pp. 1089 - 1095.

[162] H. Yu, C. M. Alexander and D. J. Beebe, “Understanding microchannel culture: parameters involved in soluble factor signaling”, *Lab on a Chip (2007)*, Vol. 7, No. pp. 726 - 730.

[163] C. E. Webb, “The Body Shops”, *IEEE Spectrum (2005)*, February, pp. 35-39.